Università di Napoli Federico II

Dipartimento di Ingegneria Industriale

Doctorate Thesis

EXPERIMENTAL AND NUMERICAL ANALYSIS OF THE THERMAL PERFORMANCE OF PCM IN A SOLAR SYSTEM WITH ENHANCEMENT PCM THERMAL CONDUCTIVITY METHODS

Abolfazl Nematpourkeshteli

Supervisors,

Prof. Nicola Bianco

Prof. Giuseppe Langella

Co supervisor,

Dr. Marcello Iasiello

Università degli Studi di Napoli Federico II

School of Doctorate in Industrial Engineering (Cycle 36)

Doctorate Thesis

EXPERIMENTAL AND NUMERICAL ANALYSIS OF THE THERMAL PERFORMANCE OF PCM IN A SOLAR SYSTEM WITH ENHANCEMENT PCM THERMAL CONDUCTIVITY METHODS

Doctorate Program Coordinator

Prof. Michele Grassi

Advisors

Prof. Nicola Bianco

Prof. Giuseppe Langella

Dr. Marcello Iasiello

Candidate

Abolfazl Nematpourkeshteli

To my sister

I dedicate this thesis to the cherished memory of my dear sister, ELHAM, whose presence profoundly enriched my life, leaving an enduring imprint on my heart and soul. Although she is no longer with us, her spirit and the invaluable lessons she imparted continue to kindle my inspiration each day.

ELHAM possessed an unwavering belief in my abilities and aspirations. Her unwavering encouragement and support served as my guiding light during the most arduous junctures of this academic journey. She instilled in me the significance of persistence, kindness, and the pursuit of one's dreams, even when faced with adversity.

As I pen down this thesis, I am reminded of her unwavering strength and resilience in the face of life's challenges-qualities that continue to motivate me. I am forever grateful for the time we shared and the profound impact she had on my life. Although her physical presence is no longer with us, her memory endures in the dedication and passion I pour into this work.

I dedicate this thesis to my sister, with boundless love and gratitude, as a testament to the profound influence she had on my life and as a tribute to the everlasting inspiration she embodies.

In loving memory of ELHAM.

ACKNOWLEDGMENTS

I want to thank:

- The Dipartimento di Ingegneria Industriale (DII) of the Università degli Studi di Napoli Federico II,

- Dr. Marcello Iasiello of the University of UniNA deserves my heartfelt gratitude for her steadfast and sincere support, which has been instrumental in guiding me through every step of this journey,

- The UniNA, that financially supported my stay at the University of University of Twente (UT),

- The University of Twente (UT) for its contribution on experimental work at chemical and Kleinhorst labartory, and Dr. Amir Mahmoudi to have had the opportunity and the honor to work with him at UT,

Finally, I would like to express my sincere and profound appreciation to Prof. Nicola Bianco and Prof. Giuseppe Langella for their invaluable support and mentorship, which have played a pivotal role in enabling me to undertake and complete my doctoral project over the span of these enriching and formative three years. Their guidance, encouragement, and expertise have been instrumental in shaping my academic journey and fostering my growth as a researcher.

NOMENCLATURE			
A_m	Constant of mushy zone ($kg/m^3 s$)	$\dot{m}$	Mass flow rate (kg/s)
A_{sf}	Interfacial surface area (1/m)	p	Effective pressure (Pa)
C	Specific heat capacity (J/kg K)	p_L	Rate of heat storage/recovery (W)
d_l	ligament diameter (m)	Q	Energy (J)
d_p	Pore size (m)	t	Time (s)
D	Pipe Diameter (m)	t_m	Melting time (s)
g	Gravity acceleration (m/s^2)	t_s	Solidification time (s)
h_{sf}	Interfacial heat transfer coefficient (W/m^2 K)	T	Temperature (°C or K)
k	Thermal conductivity (W/m K)	T_{ini}	Initial temperature (°C or K)
K	Permeability of porous foam (m^2)	u	x-direction velocity (m/s)
L	Pipe length (m)	v	y-direction velocity (m/s)
L_f	Latent heat (J/kg)	w	z-direction velocity (m/s)
m_{pcm}	PCM mass (kg)		
Greek letters			
ρ	Density of fluid (kg/m^3)	ω	Pore density (PPI)
φ	Volume fraction of nanoparticles (%)	α	Thermal diffusivity (m^2/s)
λ	Liquid fraction	ν	Kinematic viscosity (m^2/s)
β	Coefficient of thermal expansion (1/K)	T_{avg}	Average PCM temperature (°C or K)
μ	Dynamic viscosity (kg/m s)	T_e	Endpoint temperature (°C or K)
ε	Porous foam porosity		
Subscripts			

Summary

f	Liquid nanoPCM	*s*	Porous foam
fe	Fluid effective value	*se*	Solid effective value
ini	Initial		
Acronyms			
Al_2O_3	Aluminum Oxide	NP-HNF-MF	Metal Foam /Hybrid Nanofluid/ NanoPCM /Pure PCM
CFD	Computational Fluid Dynamics	NP-MF	Metal Foam / NanoPCM /Pure PCM
CENG	Compressed Expanded Natural Graphite	PP-MF	Metal Foam/Pure PCM
CPC	Compound Parabolic Concentrator	Ste*	Modified Stefan numbers
CFD	Computational Fluid Dynamics	MWCNT	Multi-Walled Carbon Nanotubes
CSP	Concentrated Colar Power	NEPCM	Nano-Enhanced Phase Change Material
CuO	Copper Oxide	NC	Natural convection
DAQ	Data Acquisition System	OP	Optimization Systems
DSC	Differential scanning calorimetry	MFP	PCM-metal foam composite
DPHX	Double-Pipe Heat Exchanger	NP	PCM-nanoparticle composite
E	Energy Storage	MFNP	PCM-nanoparticle-metal foam composite
ESS	Energy Storage System	PVT	Photovoltaic thermal
ETC	Evacuated Tube Collector	PMF	Porous Metal Foam
FEM	Finite Element Method	PPI	Pores Per Inch
FV	Finite Volume	PP	Pure PCM
FPSCs	Flat Plate Solar Collectors	Re	Reynolds
Gr	Graphite	SSPCMs	Shape Stabilized PCMs
HX	Heat Exchanger	SiO_2	Silicon Dioxide
HTF	Heat Transfer Fluid	SAH	Solar Air Heater

(PL,m and PL,m*)	Heat Transfer Rates	(DPSAH)	Solar Air Heater
(HVAC)	Heating, Ventilation, and Air Conditioning	(SDHW)	Solar Domestic Hot Water heating
(HNEPCM)	Hybrid Nano-Enhanced Phase Change Material	(SWHS)	Solar Water Heating System
(HNP)	Hybrid Nanoparticles	(Ste)	Stefan
(HNF)	Hybrid Nano-Fluid	(TTHX)	Triplex Tube Heat Exchanger
(NP-HNF)	Hybrid Nanofluid/ NanoPCM /Pure PCM	(%)	Time-Saving
(PP-HNF)	Hybrid Nanofluid/Pure PCM	(TPSAH)	Triple-Pass Solar Air Heater
(LES)	Latent Energy Storage	(TES)	Thermal Energy Dtorage
(LHTES)	Latent Heat Thermal Energy Storage	(TC)	Thermal Conductivity
(LF)	Liquid Fraction	(UTHX)	U-Shaped-Tube Heat Exchanger
(LTNE)	Local Thermal Non-Equilibrium	(VAT)	Volume Averaging Technique
(LDPHX)	Lobed Dobule Pipe Heat Exchanger	(Micro-CT)	X-ray computed microtomography
(MF)	Metal Foam	(ZnO)	Zinc Oxide

ABSTRACT

Solar energy, well-known for its inexhaustible and ecologically beneficial features, is one of the most promising energy sources. Solar energy is often captured in the form of heat by a heat medium Heat Transfer Fluid (HTF) and then transmitted to manufacturing and human usage. Solar heating or power supply devices based on Thermal Energy Storage (TES) components that can work constantly and without interruption are required due to the problems of varying weather, climate, and seasons. Latent Heat Thermal Energy Storage (LHTES) employs Phase Change Materials (PCMs) to store and release heat, effectively mitigating the discrepancy between energy availability and demand. Nevertheless, conventional PCMs with low Thermal Conductivity (TC) suffer from prolonged energy storage and release durations, significantly compromising the efficiency of TES components.

The primary objective of this doctoral dissertation is to investigate the thermal behavior of a solar system integrated with a composite PCMs. This investigation will employ a combination of experimental and numerical techniques, incorporating Porous Metal Foam (PMF), Nanoparticles (NP), and Optimization Systems (OP). The model incorporates the enthalpy-porosity technique to account for phase change phenomena, while considering the local thermal non-equilibrium assumption for the utilization of foam, and a single-phase equivalent assumption is used for nanoparticles.

The research outcomes indicate that the integration of PMF, NP, and OP methodologies can significantly reduce the overall duration required for both charging and discharging the PCM. Simultaneously, these approaches lead to an accelerated rate of energy storage and release. After comparing the numerical outcomes with the experiments herein run, data are shown in terms of liquid fraction, temperature evolution, stored energy, rate of energy storage charge, and a dimensionless parameter that characterizes the phase change process. The findings suggest that the proposed methods for enhancing heat transfer can enhance the thermal efficiency of systems. In one of experimental trials, the results indicate that incorporating the methods nanoparticle, metal foam, and metal foam with nanoparticles, each with porosities of 0.4% and 0.94%, leads to a reduction in melting time by 13.39%, 60.77%, and 71.93%, respectively, compared to pure PCM.

Keywords: Thermal energy storage, Energy efficiency, Solar collector, Heat exchanger, Phase change materials, Nano powder, Porous metal foam

Chapter 1.

GENERAL INTRODUCTION

1.1. Thesis Structure

In **Chapter 1** of this thesis, an in-depth exploration is conducted, delving into a comprehensive review of the current body of literature surrounding the multifaceted realm of thermal energy storage. This analysis encompasses a thorough examination of general information pertaining to the utilization of thermal energy storage, including its applications across various domains, nuanced limitations encountered in practical scenarios, and the diverse methods employed in harnessing and optimizing this crucial aspect of energy management. Through a meticulous examination of existing research and scholarly works, this chapter aims to provide a robust foundation for understanding the intricacies and advancements in thermal energy storage, setting the stage for subsequent chapters that delve into more specific aspects and contributions of this vital field.

Chapter 2 of this thesis entails an extensive review and numerical study of the existing literature concerning the utilization of metal foams, nanoparticles, and finned surfaces within the framework of triplex tube heat exchangers and PCM composites. composites within the field of thermal engineering. The primary objective of this study is to establish a comprehensive understanding of the most optimal choice between single-PCM and multilayer-PCM configurations, a comparative analysis not previously explored in current scholarly works. Additionally, the chapter provides an overarching overview of the practical applications of PCM, metal foams, and nanoparticles in thermal energy storage and thermal management, encompassing areas such as solar energy utilization, energy-efficient building systems, domestic applications, energy storage, and transport, etc.

In **chapter 3**, the effects of heat and contact conditions on the thermal performance of PCM composite for thermal energy storage are considered. Increasing melting and solidification performances of a phase change material-based flat plate solar collector equipped with metal foams, nanoparticles, and wavy wall-Y shaped surface. Based on the volume-averaged method, the equilibrium temperature energy model is used to investigate the thermal characteristics of composite PCM under different heating and contact conditions, in which the thermal characteristics include solid-liquid interface, liquid fraction, velocity, total melting time and average heat storage rate.

Chapter 4 of this thesis has unveiled a range of strategic enhancements for LHTES-DPHX (Latent Heat Thermal Energy Storage- Double-Pipe Heat Exchangers) systems, with a specific focus on the optimization of the charging and discharging processes. In the context of the current solar concentrating unit coupled with a thermal storage and harvesting system, four distinct strategies

have been implemented to expedite the melting and solidification processes, effectively reducing the time required for charging and discharging, while simultaneously augmenting the rate of energy storage and retrieval. These strategies are as follows: 1) Improving the heat exchanger geometry (lobed pipe); 2) Dispersing Al_2O_3 nano-sized powders into paraffin (RT82); 3) Dispersing Al_2O_3-MWCNT nano-sized powders into H_2O; 4) Adding metal foam with different porosity (aluminum foam).

Chapter 5 of this thesis has unveiled experimental and numerical thermal enhancement techniques for thermal storage systems. First objective of this study is to investigate the effectiveness of various techniques for enhancing the heat transfer performance of PCMs during both melting and solidification processes. Specifically, the study aims to compare the performance of four different types of composite materials, namely Pure PCM (PP), PCM-nanoparticle composite (NP), PCM-metal foam composite (MFP), and PCM-nanoparticle-metal foam composite (NPMF), in terms of their heat transfer properties. Second objective of this project is to develop a storage-integrated solar thermal collector that has a compact design and is equipped with a compatible PP and MFP. To achieve this goal, the project begins with an experimental study of a simple collector to analyze the behavior of the developed PCM and metal foam as light absorbers and storage mediums. The results of the experiment are then compared with the predicted outcomes, and a validated model is established to investigate the heat transfer characteristics of a solar collector with PCM and metal foam. In third objective we investigate the effect of a U-shaped heat exchanger and porous material on accelerating the energy-storing process in PCMs through experimental analysis. For practical applications, it is crucial to increase the charge/discharge rate of the TES unit initially, followed by a lower rate for optimal usage. Although previous studies have shown remarkable improvements in heat storage, managing the release of stored heat based on system requirements is equally important. In some applications, the duration of the charge/discharge process is critical, and it can be regulated by controlling heat storage. Thus, it is necessary to evaluate heat storage management methods experimentally, which has not been done before. To address this issue, we propose a novel design for a multi-purpose TES unit with two energy storage regions featuring different charge/discharge rates. This design allows for better control of energy storage and usage. Specifically, we designed a U-shaped Heat Exchanger (HX) TES unit with two separate LHTES regions: a region with porous metal foam and another with pure PCM and/or nanoPCM. Both regions are in contact with the copper pipe, and their charge/discharge rates can support the required energy based on its need.

In the end, the conclusions of this thesis are summarized, and some perspectives are provided for future studies. A comprehensive summary of all the chapters has been provided:

Chapter 1: General Introduction;
Chapter 2: Enhancing PCMs Thermal Conductivity;
Chapter 3: Using Enhancements Method in Solar Systems;
Chapter 4: Optimizing Energy Storage;
Chapter 5: Experimental and Numerical Study;
Chapter 6: Conclusion and Future Study.

1.2. Introduction

Thermal energy is an encouraging source to drive many practical applications. Renewable energy resources particularly solar energy is most important source of thermal energy. Energy storage from such systems plays vital role to meet the energy requirements. Thermal Energy Storage (TES) is defined as the temporary holding of thermal energy in the form of hot or cold substances for later utilization. Energy demands vary on daily, weekly and seasonal bases. These demands can be matched with the help of TES systems that operate synergistically, and deal with the storage of energy by cooling, heating, melting, solidifying or vaporizing a material and the thermal energy becomes available when the process is reversed. TES is a significant technology in systems involving renewable energies as well as other energy resources as it can make their operation more efficient, particularly by bridging the period between periods when energy is harvested and periods when it is needed. That is, TES is helpful for balancing between the supply and demand of energy.

1.3. Thermal Energy Storage

Thermal energy storage comes in various forms, including sensible, chemical (such as sorption and thermochemical processes), and latent heat storage, as depicted in **Figure 1.1** [1-2]. Among these, the primary categories are sensible and latent heat storage. Sensible thermal energy storage relies on altering the temperature of the storage medium, which can include substances like water, brine, rocks, or soil. On the other hand, latent heat storage systems store energy by utilizing phase changes, such as the freezing and melting of water/ice for cold storage and the use of paraffin waxes for heat storage. Latent heat storage units are generally more compact in comparison to sensible storage systems. Additionally, it is worth noting that latent heat storage offers higher thermal energy storage density when compared to sensible heat storage [2–3]. For instance, paraffin wax is a prime example of a latent heat storage material. It boasts a significant heat capacity, which allows for substantial energy storage capacity. Furthermore, its low melting point enables it to release and store energy efficiently even when there are minor temperature differences, as illustrated in **Figure 1.2**. Therefore, it is imperative to harness the solidification-melting (solid-liquid) process of paraffin wax for effective thermal energy storage.

In efficient TES systems, the process of storing or releasing energy involves the heating or cooling of a liquid or solid storage substance through a heat exchange mechanism. The total energy added to a TES in a sensible heat system depends on factors like the quantity of storage material, its heat-holding

capacity, and the temperature differential between the storage medium's initial and final states. This transfer of heat, denoted as Q, can be mathematically represented as follows:

$$Q = mC_p \Delta T \quad (1)$$

where m and C_p denote the mass and specific heat of the storage material and ΔT is the temperature difference before and after the storage operation. Examples of materials typically used as a storage medium are water, air, oil, rocks, brine, concrete, sand and soil.

Latent heat refers to the energy exchange that occurs when a substance transitions from one phase to another at a constant temperature. In latent TES systems, energy is stored or released during these phase transitions, such as melting, evaporation, or crystallization. This is because of the inherent properties of the storage material, like its specific heat and the significant enthalpy change that occurs during a phase transition. Typically, the latent heat change tends to be larger than the sensible heat change for a given system size. Latent heat storage materials are most effective within a limited temperature range.

$$Q = mL \quad (2)$$

m denotes the mass, and *L* represents the specific latent heat associated with Phase Change Materials (PCMs). PCMs, such as water/ice, paraffin, and eutectic salts, exemplify substances capable of undergoing phase changes. One notable industrial PCM is the hand warmer, specifically sodium acetate trihydrate. These PCMs are typically contained within various structures, such as tubes, plastic capsules, wall panels, and ceilings, and are predominantly available in three primary forms: powder, granulate, and board.

Latent Heat Thermal Energy Storage (LHTES) systems revolve around the phase change process, maintaining nearly constant temperatures as solids transform into liquids and vice versa. PCMs play a crucial role in storing and releasing significant amounts of heat during melting and solidification phases. To be effective in various applications, PCMs should possess high latent heat capacity, excellent thermal conductivity, and minimal volume expansion. These materials manifest in various categories, with eutectic, organic, and inorganic forms being the most prevalent. LHTES systems find broad application in diverse fields, contributing to both heating and cooling solutions and serving as a reservoir for potential electrical energy conversion. Cooling applications span electronic cooling, air conditioning, refrigeration systems, lithium-ion battery cooling, and cold food packaging. In heating applications, they support building heating, waste heat recovery (e.g., car exhaust and industrial facilities), and

solar food drying equipment. Furthermore, LHTES systems are deployed for energy storage purposes, notably in solar power storage systems, including Concentrated Colar Power (CSP) generation setups. Additionally, medical applications, such as smart textiles, enable temperature regulation to either heat or cool individuals as required.

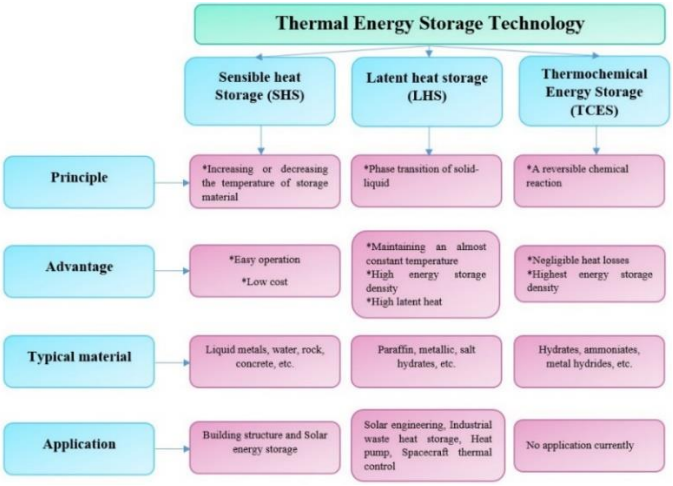

Fig. 1.1. Categorization of thermal energy storage technologies using the factors of energy storage material state, operating principle, benefits, Common materials, and field of application [1-2]

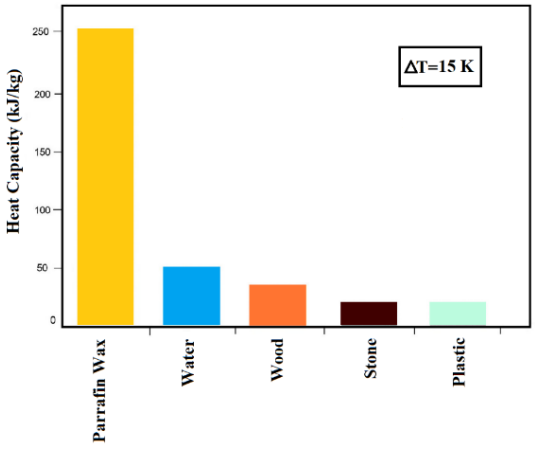

Fig 1.2. Heat capacity of different materials compared to PCMs [4,5]

1.4. PCMs and Their Different Types

Phase change materials, commonly referred to as PCMs, encompass both organic and inorganic compounds designed to absorb substantial amounts of heat energy. The essence of thermal energy storage within these materials revolves around the process of transitioning between phases. Specifically, these materials adeptly assimilate and release thermal energy to their surroundings during the shifts from solid to liquid and liquid to solid states, respectively. A distinctive attribute of PCMs lies in their ability to preserve latent heat energy over numerous phase change cycles, enduring these transitions without any significant alterations. When employed in indoor settings, they engage in a series of heat exchanges with the environment, especially in response to notable fluctuations in air temperature, such as the transition from night to day. This continuous process ultimately contributes to maintaining a more stable indoor temperature. As PCMs are heated, they accumulate energy, progressively approaching their melting point, at which they transform from a solid to a liquid state. A pivotal characteristic of PCMs is their capacity to maintain a constant temperature during the phase change, even when subjected to environmental temperature fluctuations. This unique property allows them to synchronize their temperature with the surroundings during the heating process, preventing any further temperature increase beyond the phase change point. Consequently, during this phase, which often extends over several hours, PCMs efficiently capture substantial amounts of ambient heat without undergoing a temperature increase themselves.

To assist in the selection of the appropriate PCM, researchers have devised criteria, as illustrated in **Figure 1.3**. The process of PCM melting involves a chronological progression from a solid to a semi-solid and eventually a liquid state. Conversely, the freezing process follows the reverse trajectory, necessitating six distinct stages to complete the thermal cycle. At each of these stages, heat transfer takes place through mechanisms such as convection and conduction. **Figure 1.4** showcases various methodologies employed in the investigation of PCMs.

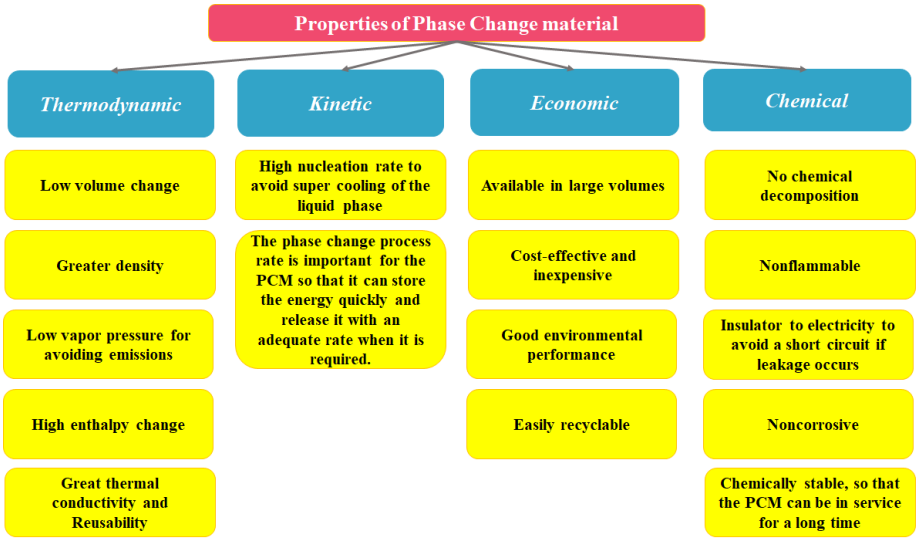

Fig. 1.3. Chemical, kinetic, economic and thermophysical properties of PCMs [4,5]

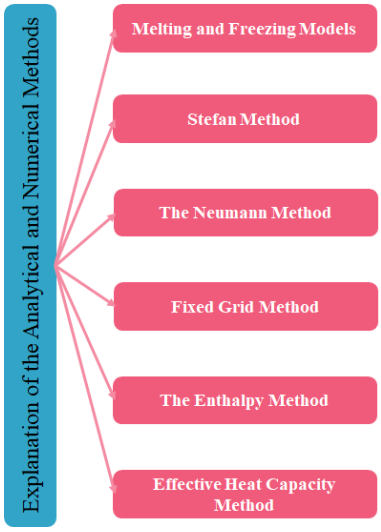

Fig. 1.4. Different methods for investigating PCMs [4,5]

1.5. Application of PCM composite in thermal energy Storage

In recent years, the growing energy crisis and worsening environmental pollution have sparked increased interest in renewable energy sources and the sustainable development of low-carbon eco-cities. Consequently, there has been a significant focus on the advancement of renewable energy technologies, with thermal energy storage playing a crucial role in the efficient storage and release

of energy. PCMs have garnered widespread attention due to their high energy storage capacity and excellent thermal stability, making them a popular choice in various TES applications, including solar energy, energy-efficient building design, and waste heat recovery. To illustrate the utility of PCMs, **Table 1.1** outlines their common advantages, disadvantages, and the challenges associated with their use in diverse fields, such as batteries, central processing units (CPUs), solar photovoltaics (PV), and capacitors.

Table 1.1. Advantages, disadvantages, and challenges of using PCM in certain areas.

Type	Advantages	Disadvantages	Challenges	Ref
Batteries	• Better temperature uniformity	• Heat accumulation • Additional weight	• Melting point in the desired operating temperature range	[6,7,8]
	• Reduced peak temperature	• Undesirable thermal inertia	• Changes in density to avoid problems with the storage tank	
	• Reduced system volume			
CPU	• Reduced need for reliance on measures • Throttling of component power	• Adds weight • Design complexity	• Small unit size • Long-term chemical stability	[9,10]
Solar PV	• Delay temperature rise • Reduced loss in electric efficiency • Low vapor pressure	• Undesirable thermal inertia	• Latent heat should be as high as possible to minimize the physical size of the heat storage	[11,12,13]
Capacitors	• Improved thermal behavior • Reduced peak temperature	• Design complexity	• Long-term chemical stability	[8,14]
Thermally regulated textiles	• Reduced temperature variance • Improved thermal properties	• Reduced thermal conductivity of PCM • Flammability of organic PCM	• Improve thermal conductivity of PCM microcapsules as well as their shell	[15,16]

Thermal protection	• Suitable PCMs can be used to reduce the rise of temperature in high-heat flux objects	• Design complexity • Additional weight	• Small unit size •Long-term chemical stability • Health & safety and disposal	[9,10]
Air-conditioning	• Reduced CO_2 emissions • Selectable melting temperature for work with standard heat pumps for each application • Mitigate fluctuating availability of solar energy • Defrosting solution for air-conditioning equipment	• Low heat transfer between HTF and PCM due to the low thermal conductivity of PCM • Cost of implementation	• Low heat transfer greatly affects the charging time of the PCM storage systems • Thermo-physical properties and the geometry of encapsulation of PCMs must be considered and improved • Charging and discharging of PCM	[17,18, 19]
Solar heating system	• Heat is stored and released at an almost constant temperature • PCMs can be used for both active and passive space heating and cooling systems • Stored energy can be utilized when energy is not available • Reduced peak demand • PCMs overcome the problem of temporal unavailability of sunlight • Positive environmental impact	• Heat loss in two ways: Inside the device and between the device and users • Poor thermal conductivity • Slow thermal diffusion • Reduced storage capability	• Melting point of storage material • PCM mass • PCM phase separation • PCM should keep its original configuration and composition under • Various external factors • Thermophysical properties of PCM should not • Change after repeated cycles	[20, 21, 22]
Building thermal comfort	• Reduced energy consumption, reduce temperature and temperature fluctuations • Wide application possibilities	• Cost • PCM performance affected by ambient conditions	• Climate conditions • Damage to the bearing capacity of construction materials	[23,24,25]

PCMs offer several universal benefits across various applications, primarily aimed at lowering peak temperatures and enhancing thermal performance. Nevertheless, their integration can pose intricate design challenges and lead to added weight in the system. It is imperative to focus on critical application considerations, such as ensuring their protection within devices, ensuring long-term chemical stability, and addressing health and safety concerns associated with disposal.

1.5.1. Thermal energy storage in the heat exchanger

TES materials have found diverse applications in various heat exchange systems, including solar domestic hot water systems, building heating systems, and storage tanks commonly referred to as "heat banks." Recent research has investigated heat exchangers designed to leverage both sensible and latent energy storage materials. **Table 1.2** outlines key findings from published studies that explore the utilization of TES materials in heat exchange applications. This section specifically delves into heat exchangers integrated within heat banks, while heat exchanger designs for traditional solar applications are addressed separately. The discussion encompasses various heat exchanger configurations, such as packed beds for sensible and latent heat storage, bulk storage solutions for sensible and latent storage, and modular storage options. In particular, the discussion extends to the usage of storage modules, including flat plate modules, shell and tube (pipe modules), and shell and tube (cylinder modules).

Table 1.2. Energy storage materials in heat exchangers.

Heat exchanger	Material	Remark	Ref
PCM packed bed	• Paraffin granules, fatty acid, and hydrated salt	• 89% of the cooling load is accumulated overnight in the packed bed granules • Ventilation load is reduced by about 62.8% • TES systems with 1 m3of PCM can potentially reduce cooling energy in the evaporator by 21–38%	[26, 27, 28, 29]
Circular fin	• Paraffin	• The charging and discharging time reduction for the m-PCM system is 30% for non-uniform fin distribution and 9% for PCM block length ratio optimization	[30]
Spiral fin	• PCM	• The melting and solidification time of PCM can be reduced by 57.6% and 74.1% compared to the axial fins	[31, 32]

		• Reduction of charging and discharging time by 41.5% and 22.2%, respectively.	
Axial fin	• Paraffin RT50, Water	• 2.85% of longitudinal fins of total annulus volume can reduce melting time by 34%	[32, 33]
Plate fin	• Paraffin RT30	• The effectiveness of plate fins is increased up to 3 times • Conduction is improved 3 times	[34]

1.5.2. Solar energy

Solar energy stands out as a promising renewable resource, valued for its cleanliness and widespread availability in many regions (as illustrated in **Fig. 1.5**). However, given the intermittent nature of solar energy, the integration of thermal energy storage systems is essential to extend the operational hours of solar energy systems. In this context, latent heat storage represents a common method of thermal energy storage, with particular attention being drawn to its application in solar energy systems. This heightened interest can be attributed to its compact nature, high energy storage capacity, and stable operating temperatures. Therefore PCMs, recognized for their potential in energy storage, find utility in latent heat energy storage within solar energy applications, including solar water heating and solar collectors. Solar water heaters are widely employed for solar energy collection due to their affordability and simplicity in both production and maintenance. Notably, these systems harness the latent heat capacity of PCMs to store solar energy. In the operation of a solar water heater, hot water is extracted, and in its place, cold water is introduced, absorbing energy from the PCM. As a result of this energy transfer, the PCM undergoes a phase change from liquid to solid, facilitating energy storage.

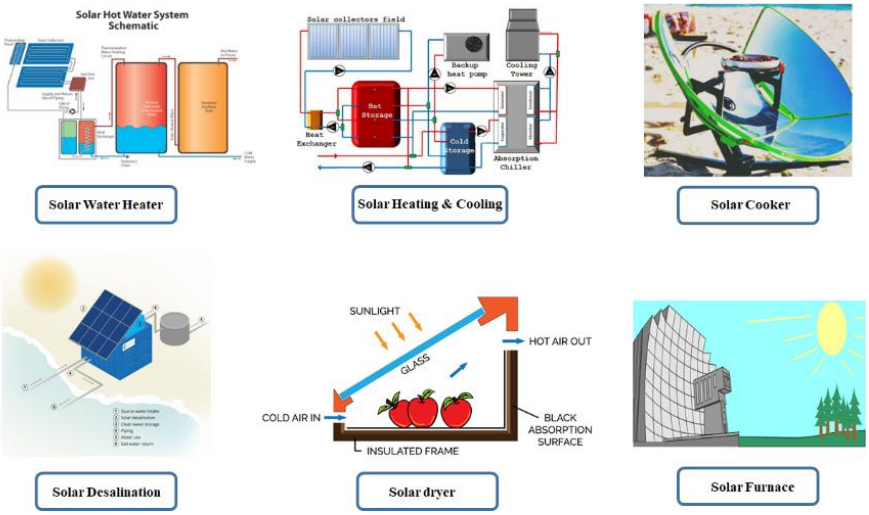

Fig. 1.5 Solar energy applications (non-power plant application) [4,5]

1.5.3. Building

Before 1980, PCMs found use in thermal storage within the construction industry due to their advantageous properties, including a high latent heat capacity and stable chemical characteristics. PCMs could be seamlessly integrated into various building components such as wallboards, ceiling boards, and floors through microencapsulation and other methods. The primary purpose of employing PCMs in building design revolves around the storage and controlled release of energy to meet specific requirements.

The utilization of PCMs in buildings encompasses both passive and active TES integration applications. Passive applications are geared towards enhancing building comfort by mitigating peak temperatures, reducing energy consumption, and minimizing the need for extensive heating and cooling systems during peak demand periods. To ensure the successful and widespread adoption of efficient heating and cooling systems in buildings, it is essential to incorporate dependable, sustainable, and low-carbon energy solutions based on TES materials. In engineering applications, the capacity to store and release energy is pivotal in aligning energy availability with demand, considering factors such as time and power requirements. For an overview of materials applied in passive building design, refer to **Table 1.3**, which provides insights into typical outcomes related to PCM usage.

Table 1.3. Illustration of the results for passive heating

Application	Material	Ref

Building envelope	PCM, Brick	[35]
Building envelope	Paraffin wax (melting point 44 °C)	[36]
Building envelope	PCM	[37]
Wall	PCM, Brick	[38]
	Bricks, n-Eicosane, n-Octadecane, P116	[39]
Wallboard		[40]
Night ventilation	Paraffin	[41]
Hybrid cooling	shape-stabilized PCMs	[42]
Floor	Paraffin granules (Packed bed)	[43]
Glazing system	Paraffin wax (melting point 26 °C)	[44,45,46]

1.6. Improvement of the thermal performance of PCMs

The primary issue associated with PCMs lies in their insufficient thermal conductivity, resulting in extended melting and solidification durations. To address this concern, numerous strategies for augmenting PCM thermal conductivity have been devised, aiming to expedite the charging and discharging processes within LHTES systems. These techniques are designed to enhance system efficiency without requiring additional energy input. Prominent passive enhancement methods encompass integrating heat pipes and fins, infusing PCMs with highly conductive Porous Metal Foam (PMF), employing multiple PCMs, and dispersing highly conductive Nanoparticles (NPs) throughout the PCM matrix. Furthermore, certain investigations have explored additional factors, including system orientation, as well as temperature and flow rate adjustments in the Heat Transfer Fluid (HTF).

PCMs possess several desirable attributes; however, a significant drawback lies in their suboptimal heat transfer characteristics. The heat transfer process within PCMs is frequently sluggish, particularly when they exist in a solid state. This sluggish heat transfer hinders the energy storage operation, namely the charging phase of PCMs, where they transition from a solid to a liquid state. Moreover, solidifying PCMs in proximity to a heat sink obstructs the efficient dissipation of thermal energy from other regions to the heat sink during the discharging phase. Often, PCMs struggle to deliver thermal energy at the pace required by end-users. The core concept behind enhancing the thermal performance of PCM-based Latent Heat Energy Storage (LHES) systems involves the integration of a secondary material with high thermal conductivity. This secondary material primarily serves to expedite heat transport to various sections of the energy storage unit. Increasing the quantity of this high-conductivity material in the system enhances the overall heat transfer rate, albeit at the expense of reduced energy storage capacity due to a lower amount of PCM in the system.

Examining the contact interface between PCM and materials with high thermal conductivity is a crucial aspect in the development of such systems. Among the key parameters, employing metal foam structures stands out as an effective means to enhance the thermal conductivity of PCM-based energy storage devices. Metal foams are characterized by their high porosity and metallic composition, resulting in a lightweight structure with a substantial surface area. Various geometries of metal foam structures, ranging from ordered arrays of cells to irregular configurations with randomly dispersed pores, can be fabricated. These metal foam structures may have numerous pores embedded within a metallic substrate when low porosity is desired, or they may take on a more intricate network of metallic wires when high porosity is the goal. The manufacturing process plays a significant role in determining the final characteristics of metal foam structures. The introduction of foaming agents generates gas bubbles during the solidification of metal from a molten state or by the introduction of a foaming gas during the solidification process, leading to variable geometries with pores of different sizes interwoven. Techniques like direct molding or additive manufacturing are utilized to create metal foam structures with regular geometries. To address the inherent drawback of PCM systems, various methods for enhancing heat transfer have been developed. Two widely adopted and effective approaches involve incorporating nanoparticles and metal foam into the PCM. However, these methods are not without their limitations. Elevated concentrations of nanoparticles within the PCM can enhance thermal properties but can also compromise the stability of the composite. In contrast, the incorporation of metal foams significantly enhances the heat transfer properties of PCMs, primarily by augmenting the overall thermal conductivity of the PCM unit. The present research aims to investigate the thermal behavior of composite materials consisting of porous metal foam and PCM, along with the integration of nanoparticles, with the goal of optimizing the energy storage and release performance of the composite. **Figure 1.6** visually illustrates the classification of performance enhancement techniques for latent heat thermal systems.

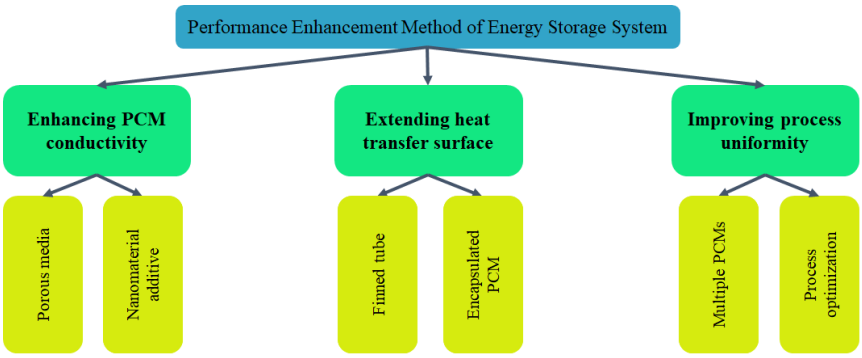

Fig. 1.6. Classifications of performance enhancement methods for latent heat thermal systems [4,5]

Materials with a cellular structure composed of foams exhibit a diverse range of physical and mechanical characteristics. These include the unique ability to possess high stiffness while maintaining an exceptionally low specific weight, or combining high gas permeability with elevated thermal conductivity. Consequently, cellular materials are frequently employed in nature for both structural and functional purposes, as evidenced by the use of wood or bones. Within the realm of man-made cellular materials, polymeric foams stand out as the predominant variety, boasting extensive utilization across various technological sectors. It is worth noting that metals and alloys can also be engineered to assume a cellular structure akin to foams, and these materials exhibit intriguing properties, promising innovative applications in the near future.

Metal foams are renowned for their exceptional physical and mechanical attributes, which encompass their low weight, elevated specific strength, remarkable stiffness, improved high-temperature endurance, and impressive capacity for absorbing energy even at very low plateau stress levels. These remarkable properties make metal foams highly versatile and sought after in an array of industries, including shipbuilding, aerospace, PVT systems, and the automotive sector, owing to their diverse qualities. Furthermore, they find utility as the core material in sandwich panels, effectively enhancing the structural components' rigidity and strength without contributing to additional weight. The selection of foams for specific applications is driven by the distinct requirements of each use case.

Metal foam represents a cellular composition composed of solid metal with a substantial proportion of gas-filled voids. These voids come in two varieties: they can be either sealed (designated as closed-cell foam) or interconnected (referred to as open-cell foam). The term "metal foams" is used when describing

closed-cell foam, whereas open-cell foams are simply termed porous metals, as illustrated in **Figure 1.7** [47]. Generally, foam is defined as the homogeneous dispersion of gas bubbles within a liquid or solid medium. The specific morphology of such foams is typically obtained through the process of allowing the liquid to solidify, resulting in what is termed "solid foams." Metallic foam is a particular subset of solid foam in which the matrix consists of metals or metal alloys. Typically, metal foam is characterized by the presence of a solid metal or alloy, often aluminum, with a substantial volume fraction of fine gas-filled pores, also referred to as cells. These cells fall into two categories:
(I). Open-cell foam, forming an interconnected network of voids.
(II). Closed-cell foam, featuring sealed voids.
The primary applications of metal foams and porous metals, along with the most highly cited advantages of metal foam in scientific literature, are highlighted in **Figures 1.8** and **1.9**.

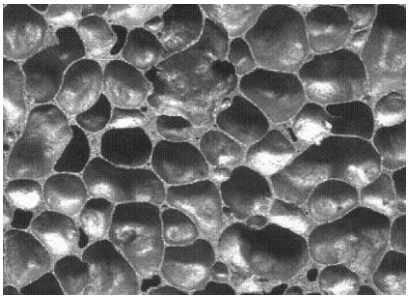

Fig 1.7a. Microstructure of Closed-cell aluminum foam. [47]

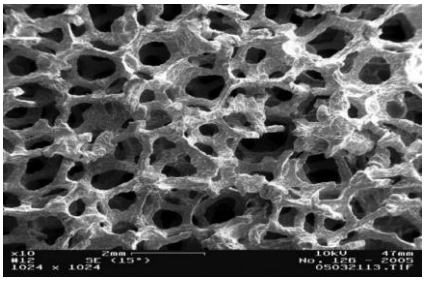

Fig 1.7b. Microstructure of Open-cell aluminum foam.[47]

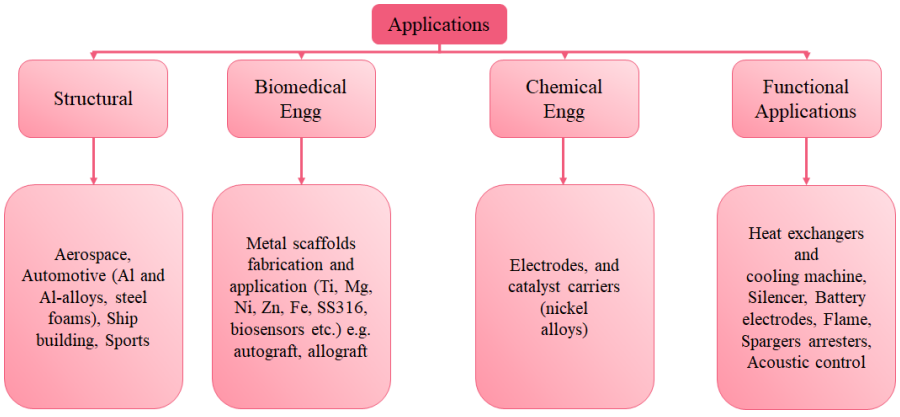

Fig. 1.8. Schematic of applications of metal foams [48,49]

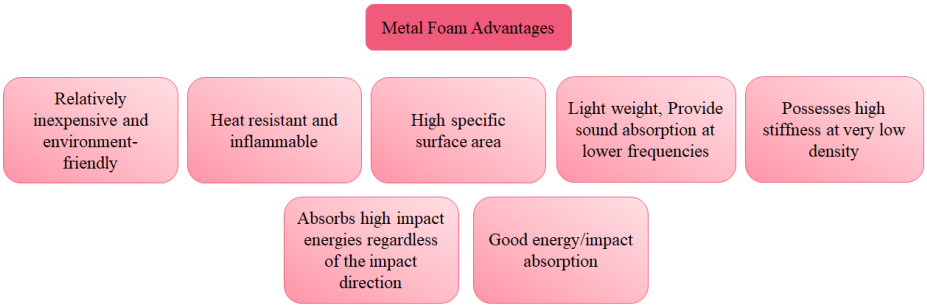

Fig. 1.9. The most highly cited metal foam advantages in scientific literature [49]

Metallic foams can be fabricated using a variety of methods tailored to achieve specific foam attributes. **Fig. 1.10** illustrates several techniques employed for crafting metal foams, while **Fig. 1.11** and **Fig. 1.12** outline the pros and cons associated with these materials. Metallic foams can be produced by pumping a compressed gas straight into a molten substance. The viscosity of the molten material is crucial in determining the outcome of the foaming process. The viscosity of the molten substance is often regulated by introducing ceramics such as SiC, Al_2O_3, MgO, and by adjusting the temperature of the molten substance. The process of foaming involves the injection of gases such as nitrogen, oxygen, or argon, which create tiny bubbles. These bubbles then cool down and form a foam-like structure. Gas injection is often unsuitable for materials that are prone to easy oxidation, such as magnesium (Mg) and titanium (Ti). Nevertheless, this method has been widely used for the production of aluminum alloy foam. Another technique for generating foam involves the liberation of gases from blowing agents. Typically, these substances consist of metal hydrides, carbonates, oxides, and similar compounds that produce gasses when heated. Blowing agents, such as TiH2 and ZrH2, are included into compositions at a weight percentage of 1 or less. These substances are incorporated into the liquid metal and agitated for an optimal duration. Occasionally, it might be challenging to extract blowing agents from the molten material when they get stuck inside a foam that has closed foam structures. Figure 5 depicts the manufacturing process of Alporas foam, in which TiH_2 is used as a blowing agent. Possible space fillers include hollow spheres, salt beads, ceramics, and polymers. The most prevalent gap filler is a salt that can be extracted after the molten metal has fully hardened. Woven wire mesh may serve as a spacer that creates linked porosity. The Lost precursor/wax method utilizes molten metal to generate metallic foam and has resemblance to the investment casting technique. The process involves four sequential

processes to generate metal foam: 1. Creating a mold pattern for a polymer, 2. Application of a polymeric/wax slurry coating onto the template, 3. Infiltration of molten metal into the template, 4. Extraction of the template after solidification occurs.

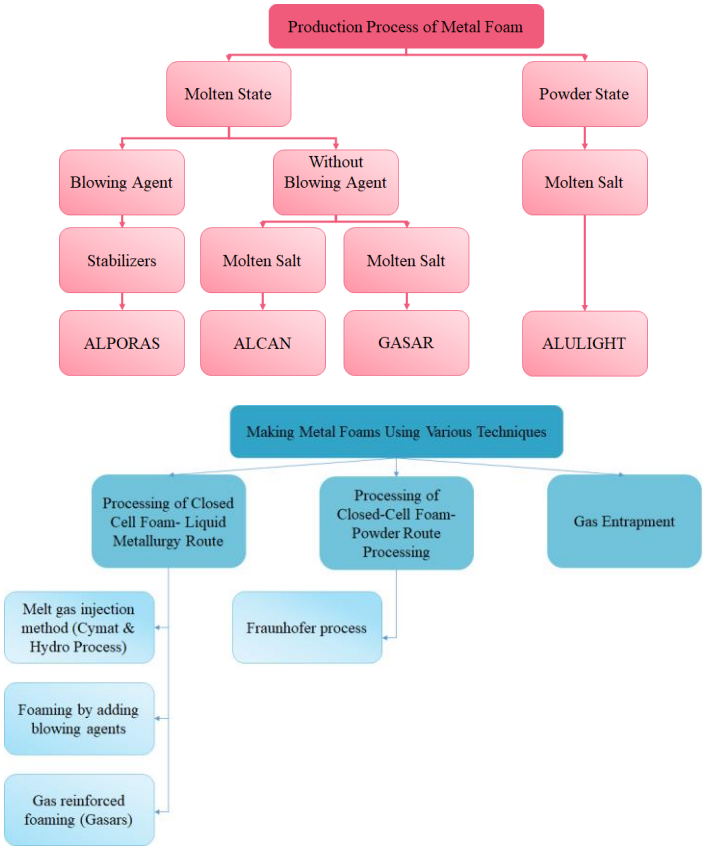

Fig. 1.10. Schematic of classification of metallic foams [50]

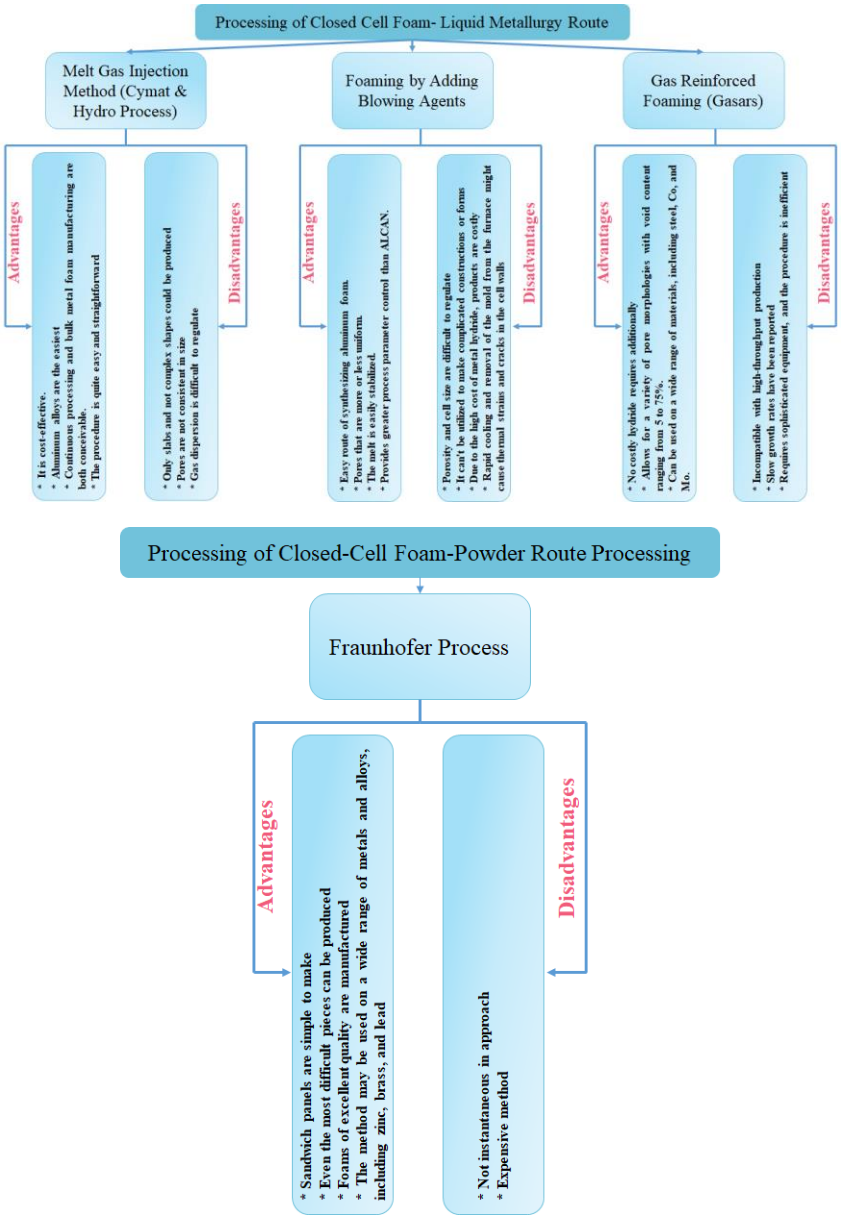

Fig. 1.11. Processing of Closed Cell Foam (top) Liquid monadology routes, (bottom) powder routes processing [50]

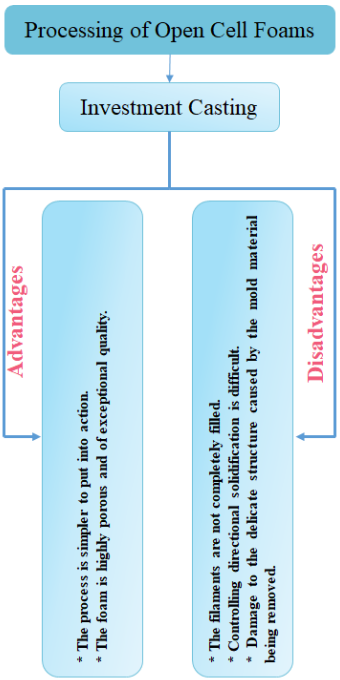

Fig. 1.12 Advantage and Disadvantage of processing open cell foam [50]

The market report on metal foam offers extensive insights into the industry, providing projected figures for both volume, measured in square footage, and revenue, in USD millions, spanning from 2018 to 2032, as depicted in **Figure 1.13**.

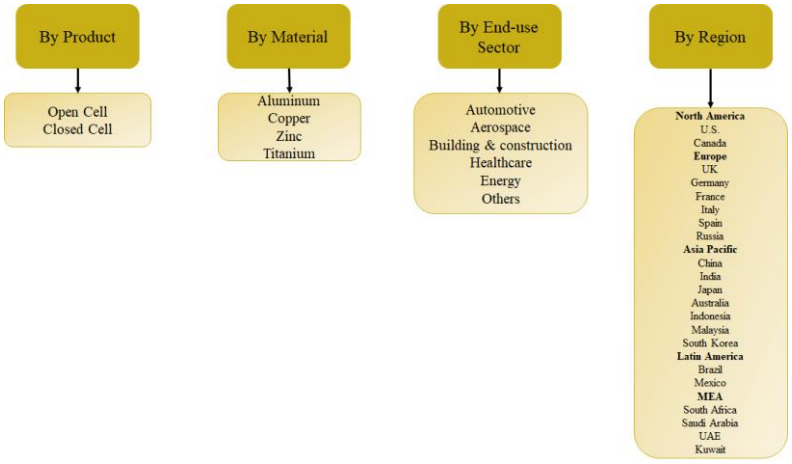

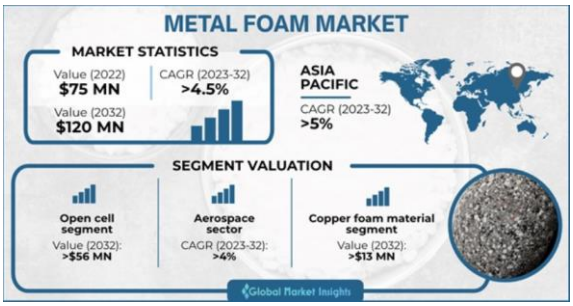

Fig. 1.13 metal foam market report [51]

Thanks to advancements in manufacturing technology, various techniques for creating metal foams have been introduced and refined in recent decades. To achieve specific pore structures in metal foams, different preparation methods are employed for open-cell and closed-cell variants. These manufacturing processes yield metal foams with varying characteristics, including porosity, Pores Per Inch (PPI), and permeability. In this section, we will elaborate on several prevalent techniques utilized for producing metal foams (refer to **Table 1.4** for details). Additionally, a summary of commonly available commercial metal foams can be found in **Table 1.5**.

Table 1.4 Summary of porous ss-PCMs and their properties in experimental studies on phase change heat transfer.

Authors/ Year	**Material**		**Operating conditions & Outcome**
	PCM	**Porous**	
2019 [52]	Paraffin	• **Aluminum Foam**	Porosity: 0.893–0.948; Pore size (mm): 0.635–5.08; Phase change point of PCM (◦C): 40; Thermocouple; Temperature variation of PCM; The time of melting/ solidification was shortened by more than 2 h; od: 62 mm, h: 800 mm; Phase change rate: 0.89ε > 0.93ε > 0.95ε.
2019 [53]	Paraffin		Porosity: 0.92–0.93; Pore size (mm): 0.635–5.08; Phase change point of PCM (◦C): 42–64; l: 20 mm, w: 100 mm, h: 100 mm, rectangular cavity.
2019 [54]	Coconut oil		Porosity: 0.88–0.96; Pore size (mm): 1.27–5.08; Phase change point of PCM (◦C): 24; Thermocouple, conventional camera; Phase interface of melting process, melting time; Thermal energy storage rate: 20PPI > 5PPI > 10PPI, 0.00%~0.12%wt nanoparticles; 5PPI > 20PPI > 10PPI, 0.3%wt nanoparticles.

2019 [55]	Coconut oil		Porosity: 0.88–0.96; Pore size (mm): 5.08; Phase change point of PCM (◦C): 24; Thermocouple, conventional camera; Phase interface of melting process, temperature variation of PCM at one position, phase change time, melting fraction by 41.2% at 1814W/m^2 and 2160s; Energy storage rate was increased by 28.81% at 2835W/m^2 and 2280s; l: 50 mm, w: 62 mm, h: 72 mm, rectangular cavity.
2019 [56]	PCM		Pore size (mm): 2.54; Phase change point of PCM (◦C): 15; Thermocouple; Temperature variation of PCM at the axis.
2017 [57]	Paraffin		Porosity: 0.859–0.958; Phase change point of PCM (◦C): 52–57; Thermocouple, conventional camera; Phase interface.
2016 [58]	Paraffin		Porosity: 0.77–0.95; Phase change point of PCM (◦C): 50–60; Thermocouple, conventional Camera; Average temperature variation, phase; interface of melting process; Rate of PCM temperature variation: 0.77ε > 0.95ε.
2015 [59]	Water		Porosity: 0.946; Pore size (mm): 0.64; Phase change point of PCM (◦C): 0; Thermocouple; Temperature variation at inlet/outlet; The overall heat transfer coefficient was increased 20% for solidification process and 100% for melting process; id: 177.8 cm, l: 508 cm 27 heat transfer tube: od: 0.64 mm, Tube-and-shell unit.
2015 [60]	Paraffin		Porosity: 0.7–0.9; Phase change point of PCM (◦C): 46–52; Thermocouple; Temperature variation of PCM at nine positions; The heat storage time was saved 26.4% and 25.6% in cases of heat flux = 7000 W/m^2 and 12000 W/m^2, respectively; l: 90 mm, w: 50 mm, h: 40 mm, rectangular cavity.
2015 [61]	n-octadecane		Porosity: 0.87–0.96; Pore size (mm): 0.635–5.08; Phase change point of PCM (◦C): 28; Thermocouple; Temperature variation at fifteen points;

			Phase change rate: 0.870ε > 0.912ε > 0.949ε; Solidification rate: 20PPI > 40PPI.
2014 [62]	Paraffin		Porosity: 0.9137; Pore size (mm): 2.82; Phase change point of PCM (◦C): 55–60; Infrared camera, microscope; Phase interface of melting process; temperature field of ss-PCM.
2018 [63]	Paraffin	• **Copper foam**	Porosity: 0.95–0.97; Pore size (mm): 0.73–1.69; Phase change point of PCM (◦C): 47–57; Thermocouple; Temperature variation of PCM at eight points and heater; Decrease in base temperature: 0.95εa > 0.97ε.
2019 [64]	Paraffin		Porosity: 0.968; Pore size (mm): 1.27; Phase change point of PCM (◦C): 48–50; Thermocouple, HD camera; Phase interface of melting process, temperature variation of PCM at fifteen position, phase change time, melting fraction; Melting time was shortened by 64%; od: 85 mm, id: 22mm, h: 300 mm, Tube-and-shell unit.
2019 [65]	Paraffin		Porosity: 0.97; Pore size (mm): 2.54; Phase change point of PCM (◦C): 68; Thermocouple; Temperature variation of PCM at six positions.
2018 [64]	Paraffin		Porosity: 0.974; Pore size (mm): 2.54; Phase change point of PCM (◦C): 26; Thermocouple, HD camera, infrared camera. ; Temperature variation of PCM at five positions. ; Melting rate was improved by 2 times; l: 50 mm, w: 5 mm, h: 7 mm, rectangular cavity.
2018 [67]	Paraffin		Porosity: 0.95; Pore size (mm): 5.08; Phase change point of PCM (◦C): 48.4–63.6; Thermocouple, HD camera; Temperature variation of PCM at three positions; The total melting time was shortened 20.5%; The biggest temperature difference was reduced from 57 ◦C to 23 ◦C. l: 100 mm, w: 30 mm, h: 100 mm, rectangular cavity.

2018 [68]	Water		Porosity: 0.93–0.97; Pore size (mm): 0.85–3.18; Phase change point of PCM (◦C): 0; Total solidification time was saved 87.5% and 76.7% for metal foam with porosity of 0.93 and 0.97, respectively; l: 28 mm, w: 68 mm, h: 68 mm, rectangular cavity; Solidification rate: 0.93ε > 0.97ε.
2017 [69]	Paraffin		Porosity: 0.97; Pore size (mm): 1.02; Phase change point of PCM (◦C): 54.43–64.11; Thermocouple, infrared camera, conventional camera Temperature of both PCM and skeleton at centre position, phase interface, temperature field of ss-PCM, phase change time.
2017 [70]	Paraffin		Porosity: 0.98; Pore size (mm): 1.69; Phase change point of PCM (◦C): 52–54.
2017 [71]	Paraffin		Porosity: 0.949–0.961; Pore size (mm): 0.51–1.69; Phase change point of PCM (◦C): 46.4; Infrared camera; Thermocouple; Melting rate: 30PPI > 50PPI, 30 ◦C wall superheat; 30PPI = 50PPI, 20 ◦C wall superheat.
2016 [72]	Paraffin		Porosity: 0.92 Pore size (mm): 1.27 Phase change point of PCM (◦C): 48–50 Thermocouple, HD camera Melting time was shortened byover 1/3. l: 120 mm, w: 60 mm, h: 240 mm, id: 20 mm Tube-and-shell unit
2015 [73]	Paraffin		Porosity: 0.95; Pore size (mm): 0.635–5.08; Phase change point of PCM (◦C): 52–60; Thermocouple, conventional camera; Temperature variation of PCM at five positions.
2013 [74]	N-eicosane		Porosity: 0.86 ; Pore size (mm): 2.54; Phase change point of PCM (◦C): 36.5; Thermocouple ; Temperature variation of PCM at four points and heater.

2012 [75]	Paraffin		Porosity: 0.96 Pore size (mm): 1.27 Heat transfer rate was increased by 36%. od: 126 mm, id: 25mm, h: 325 mm, tube-and-shell unit		
2012 [76]	Paraffin		Porosity: 0.90–0.98 ; Pore size (mm): 0.64–2.54; Phase change point of PCM (◦C): 46.48–60.39; Thermocouple; Temperature variation of PCM at five positions; Temperature distribution uniformity: 0.90ε > 0.95ε; 10PPI > 40PPI.		
2010 [77]	Paraffin		Porosity: 0.90–0.95; Pore size (mm): 0.85–2.54; Phase change point of PCM (◦C): 58; Temperature difference between PCM and support: 0.85ε < 0.95ε; 30PPI < 10PPI.		
2008 [78]	Eicosane		Porosity: 0.95; Pore size (mm): 0.127–2.54; Phase change point of PCM (◦C): 36.5; Phase interface of melting/solidification process, temperature variation of PCM at one position; The effective thermal conductivity was increased from 0.423 W/(m·K) to 3.06 W/(m·K); Consuming time was reduced from 375min to 85min for solidification process, and from 500min to 250min for melting process; id: 155.5 mm, h:304.8 mm, tube		
2016 [79]	Paraffin	• Copper fiber sintered felt	Porosity: 0.75–0.95; Pore size (mm): 0.15; Phase change point of PCM (◦C): 48.6; Thermocouple; Temperature variation of PCM at three positions;		
2018 [80]	Paraffin PT37 Paraffin	• Aluminium foam • Aluminium foam /graphite foam	Porosity: Pore size (mm): Phase change point of PCM (◦C):	0.905–0.912 0.905–0.912 – 0.635–2.54 0.635–2.54 – 55.2 37 55.2	Thermocouple; Temperature variation of PCM at two points and heater; Melting rate: 40PPI > 20PPI > 10PPI;
2015 [81]	* PureTem	•Aluminum foam	Porosity: Phase change	*0.921–0.933 *0.947	Thermocouple;

	p® 25			*0.811	Temperature variation of PCM at four positions;
		• Copper foam	Pore size (mm):	*1.27–5.08 *1.27 *0.42	
		• Graphite foam	point of PCM (◦C):	*24.1–26.3 *NA *NA	
2015 [82]	Paraffin	• Expanded graphite	Phase change point of PCM (°C): 61.33–61.62 Temperature variation of PCM at fifteen positions		
2015 [83]	NaNO3 and KNO3 KNO3	•copper NaNO3 and •nickel foam	Porosity: Pore size (mm): Phase change point of PCM (◦C):	0.965 0.975 2.54 2.54 218–228 218–228	Solidification time was decreased by 28.8% and 19.3% in cases of copper foam and nickel foam, respectively.
2013 [84]	Paraffin	/stainless-steel fiber felt	Porosity: 0.8–0.9; Pore size (mm): 0.1–0.2; Phase change point of PCM (◦C): 47.38; Thermocouple, conventional camera Phase interface of melting process, variation of surface temperature, phase change time.		
2011 [85]	Paraffin	• Copper foam CaCl2·6H20/ copper foam • Expanded graphite	Porosity: Pore size (mm): Phase change point of PCM (◦C):	0.815 0.815 - 0.847 0.847 - 25-28 29 25–28	Temperature variation of PCM at three points and heater; Thermocouple Effective thermal Conductivities were improved by 1 and 2 times for paraffin and calcium chloride hexahydrate, respectively; 80 mm × 50 mm × 30 mm, rectangular cavity
2003 [86]	Paraffin	/carbon-fiber brushes	Porosity: 0.992–0.9932; Phase change point of PCM (◦C): 40–53; Thermocouple; Temperature variation of PCM at three positions.		
1988 [87]	Gallium	Glass beads	Porosity: 0.385; Phase change point of PCM (◦C): 29.78; Thermocouple; Temperature variation of PCM at thirty-three positions.		

			Thermocouple; Temperature variation of PCM at four positions;
1986 [88]	Water	Glass beads	Porosity: 0.36–0.38; Phase change point of PCM (◦C): 0; Conventional camera.
1986 [89]	Water	Aluminum beads	Porosity: 0.39; Phase change point of PCM (◦C):0; Thermocouple; Temperature variation of PCM at three positions.

Table 1.5. Table of summary of commonly available commercial metal foams [90]

Closed Cell Aluminum Foam Panel	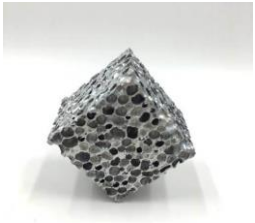	Aluminum foam products are known for their exceptional qualities, including their lightweight nature, strong sound absorption capabilities, excellent shock absorption, efficient energy impact absorption, outstanding electromagnetic shielding performance, remarkable heat insulation, high-temperature endurance, fire resistance, and distinctive environmental sustainability.
Closed Cell Aluminum Foam Panel with AL Sheet		This material finds application in various locations to reduce and suppress sound and noise, such as in pipeline sound dampeners, protective headgear, ventilation systems, cleaning facilities, food production facilities, pharmaceutical manufacturing plants, precision instrument workshops, research laboratories, medical wards and operating theaters, dining areas, watercraft and passenger sections, enclosed cabins, and air conditioning and ventilation systems.
Closed-Cell Aluminum Foam With Punched Holes		To achieve optimal sound absorption performance in outdoor environments like highways and railways, a specialized treated AFP (Aluminum Foam Panel) has been innovatively designed. This involves the systematic perforation of the AFP at a rate of 3%. This unique AFP variant significantly enhances its sound absorption capabilities.

Open Cell Aluminum Foam Panel		The manufacturing method for open-cell aluminum foam entails the melting of aluminum, aluminum-silicon, or aluminum-magnesium alloys, followed by shaping through die-casting. Open-cell AFP possesses qualities such as sound absorption, ventilation, fire resistance, extreme lightweight properties, complete environmental friendliness, and recyclability.
Sandwich Panel Aluminum Foam		Aluminum foam panels offer exceptional qualities, including soundproofing, fire resistance, waterproofing, and an incredibly low weight. When combined with aluminum sheets, these panels significantly enhance their sound insulation capabilities. These versatile panels find application in various areas, such as partition walls, enclosures, and more.
Composite Panel Aluminum Foam	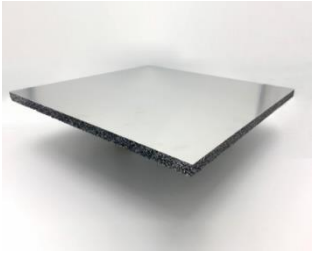	The Aluminum Foam and marble composite panel marries the elegance of natural, heavy stone, sliced into 3mm-thin layers, with the ultralight properties of foamed aluminum. This unique combination not only preserves the panel's structural integrity but also reduces the weight of the stone to an ultralight level. As a result, this versatile material can be effortlessly employed in diverse settings, including interior and exterior applications, container interiors (such as trains), yacht and cruise ship cabins, elevator components, furniture, and renovation materials for older buildings.
Copper Foam		Copper foam finds extensive application as a key component for various purposes, such as serving as the foundational material for the negative electrode in batteries, acting as a substrate for lithium-ion battery electrodes, playing a role as a carrier for catalysts in fuel cells, and serving as a material for electromagnetic shielding. Notably, copper foam stands out as the fundamental material for battery electrodes, offering distinct advantages in this context.

Nickel Foam		Porous metallic foam represents an emerging category of metal materials featuring a defined quantity and size of pores, along with a specific porosity level. This material exhibits traits such as low overall density, a substantial specific surface area, effective energy absorption, elevated specific strength, and notable specific rigidity.

According to the literature analysis, it is clear that all the proposed strategies to improve heat transfer in latent heat storage systems show promise. However, past papers indicate that researchers primarily focused on reducing the time it takes to charge and discharge these systems. According to the authors, there have been no studies that have combined experimental and numerical methods to investigate the effects of different heat transfer enhancement solutions on the performance of a thermal energy storage (TES) system. This study aims to determine if and to what extent the performance of the TES system for domestic and industrial application can be improved by combining these solutions, particularly when considering a complete heat storage and release cycle.

As previously mentioned, this chapter serves as a comprehensive exploration of latent heat thermal energy storage, addressing key facets including introduction, application, limitations, and methodologies. Following an exhaustive literature review, our rigorous analysis led to the discerning identification and selection of optimal methods distinguished for their superior performance in diverse settings, ranging from domestic to industrial applications. The judicious evaluation of data presented in Chapter One culminated in a strategic decision to incorporate these meticulously chosen methods and materials in our investigation of latent heat thermal energy storage—a demonstration of which will be expounded upon in the forthcoming Chapter 2. Moreover, Chapter 2 extends its purview by offering an encompassing overview of the practical applications of PCMs, metal foams, and nanoparticles in the realm of thermal energy storage in heat exchangers and thermal management. By elucidating their roles in various contexts, the chapter aims to provide a nuanced perspective on the potential advancements and innovations that can be derived from the integration of PCM, metal foams, and nanoparticles in the broader landscape of energy-related technologies.

References

[1] Wei G, Wang G, Xu C, Ju X, Xing L, Du X, Yang Y. Selection principles and thermophysical properties of high temperature phase change materials for thermal energy storage: A review. Renewable and Sustainable Energy Reviews. 2018 Jan 1;81:1771-86.

[2] Alva G, Lin Y, Fang G. An overview of thermal energy storage systems. Energy. 2018 Feb 1;144:341-78.

[3] Harikrishnan S, Imran Hussain S, Devaraju A, Sivasamy P, Kalaiselvam S. Improved performance of a newly prepared nano-enhanced phase change material for solar energy storage. Journal of Mechanical Science and Technology. 2017 Oct;31:4903-10.

[4] Keshteli AN, Sheikholeslami M. Nanoparticle enhanced PCM applications for intensification of thermal performance in building: a review. Journal of Molecular Liquids. 2019 Jan 15;274:516-33.

[5] Sheikholeslami M, Keshteli AN, Babazadeh H. Nanoparticles favorable effects on performance of thermal storage units. Journal of Molecular Liquids. 2020 Feb 15;300:112329.

[6] Oró E, Gil A, Miró L, Peiró G, Álvarez S, Cabeza LF. Thermal energy storage implementation using phase change materials for solar cooling and refrigeration applications. Energy Procedia. 2012 Jan 1;30:947-56.

[7] Chen D, Jiang J, Kim GH, Yang C, Pesaran A. Comparison of different cooling methods for lithium ion battery cells. Applied Thermal Engineering. 2016 Feb 5;94:846-54.

[8] Yoo DW, Joshi YK. Energy efficient thermal management of electronic components using solid-liquid phase change materials. IEEE Transactions on device and materials reliability. 2004 Dec;4(4):641-9.

[9] Moore D, Raghupathy A, Maltz W. Application of phase change materials in handheld computing devices. In2016 32nd Thermal Measurement, Modeling & Management Symposium (SEMI-THERM) 2016 Mar 14 (pp. 213-217). IEEE.

[10] Mongia R, Bhattacharya A, Pokharna H. Skin cooling and other challenges in future mobile form factor computing devices. Microelectronics Journal. 2008 Jul 1;39(7):992-1000.

[11] Browne MC, Norton B, McCormack SJ. Phase change materials for photovoltaic thermal management. Renewable and Sustainable Energy Reviews. 2015 Jul 1;47:762-82.

[12] Hawlader MN, Uddin MS, Khin MM. Microencapsulated PCM thermal-energy storage system. Applied energy. 2003 Jan 1;74(1-2):195-202.

[13] Amaral C, Vicente R, Marques PA, Barros-Timmons A. Phase change materials and carbon nanostructures for thermal energy storage: A literature review. Renewable and Sustainable Energy Reviews. 2017 Nov 1;79:1212-28.

[14] Hosseini MJ, Ranjbar AA, Rahimi M, Bahrampoury R. Experimental and numerical evaluation of longitudinally finned latent heat thermal storage systems. Energy and Buildings. 2015 Jul 15;99:263-72.

[15] Mondal S. Thermo-regulating textiles with phase-change materials. InFunctional textiles for improved performance, protection and health 2011 Jan 1 (pp. 163-183). Woodhead Publishing.

[16] Mondal S. Phase change materials for smart textiles–An overview. Applied thermal engineering. 2008 Aug 1;28(11-12):1536-50.

[17] Moreno P, Solé C, Castell A, Cabeza LF. The use of phase change materials in domestic heat pump and air-conditioning systems for short term storage: A review. Renewable and Sustainable Energy Reviews. 2014 Nov 1;39:1-3.

[18] Waqas A, Din ZU. Phase change material (PCM) storage for free cooling of buildings—A review. Renewable and sustainable energy reviews. 2013 Feb 1;18:607-25.

[19] Akeiber H, Nejat P, Majid MZ, Wahid MA, Jomehzadeh F, Famileh IZ, Calautit JK, Hughes BR, Zaki SA. A review on phase change material (PCM) for sustainable passive cooling in building envelopes. Renewable and Sustainable Energy Reviews. 2016 Jul 1;60:1470-97.

[20] Javadi FS, Metselaar HS, Ganesan P. Performance improvement of solar thermal systems integrated with phase change materials (PCM), a review. Solar Energy. 2020 Aug 1;206:330-52.

[21] Wheatley G, Rubel RI. Design improvement of a laboratory prototype for efficiency evaluation of solar thermal water heating system using phase change material (PCMs). Results in Engineering. 2021 Dec 1;12:100301.

[22] Waqas A, Kumar S. Phase change material (PCM)-based solar air heating system for residential space heating in winter. International journal of green energy. 2013 Apr 21;10(4):402-26.

[23] Keshteli AN, Sheikholeslami M. Nanoparticle enhanced PCM applications for intensification of thermal performance in building: a review. Journal of Molecular Liquids. 2019 Jan 15;274:516-33.

[24] Wang X, Li W, Luo Z, Wang K, Shah SP. A critical review on phase change materials (PCM) for sustainable and energy efficient building: Design, characteristic, performance and application. Energy and Buildings. 2022 Apr 1;260:111923.

[25] Islam MN, Ahmed DH. Delaying the temperature fluctuations through PCM integrated building walls—Room conditions, PCM placement, and temperature of the heat sources. Energy Storage. 2021 Oct;3(5):e245.

[26] Nagano K, Takeda S, Mochida T, Shimakura K, Nakamura T. Study of a floor supply air conditioning system using granular phase change material to augment building mass thermal storage—heat response in small scale experiments. Energy and buildings. 2006 May 1;38(5):436-46.

[27] Yanbing K, Yi J, Yinping Z. Modeling and experimental study on an innovative passive cooling system—NVP system. Energy and buildings. 2003 May 1;35(4):417-25.

[28] Takeda S, Nagano K, Mochida T, Shimakura K. Development of a ventilation system utilizing thermal energy storage for granules containing phase change material. Solar Energy. 2004 Sep 1;77(3):329-38.

[29] Belmonte JF, Izquierdo-Barrientos MA, Eguía P, Molina AE, Almendros-Ibáñez JA. PCM in the heat rejection loops of absorption chillers. A feasibility study for the residential sector in Spain. Energy and buildings. 2014 Sep 1;80:331-51.

[30] Sodhi GS, Muthukumar P. Compound charging and discharging enhancement in multi-PCM system using non-uniform fin distribution. Renewable Energy. 2021 Jun 1;171:299-314.

[31] Duan J, Xiong Y, Yang D. Study on the effect of multiple spiral fins for improved phase change process. Applied Thermal Engineering. 2020 Mar 25;169:114966.

[32] Mehta DS, Vaghela B, Rathod MK, Banerjee J. Thermal performance augmentation in latent heat storage unit using spiral fin: an experimental analysis. Journal of Energy Storage. 2020 Oct 1;31:101776.

[33] Modi N, Wang X, Negnevitsky M, Cao F. Melting characteristics of a longitudinally finned-tube horizontal latent heat thermal energy storage system. Solar Energy. 2021 Dec 1;230:333-44.

[34] Stritih U. Heat transfer enhancement in latent heat thermal storage system for buildings. Energy and buildings. 2003 Dec 1;35(11):1097-104.

[35] Alam M, Jamil H, Sanjayan J, Wilson J. Energy saving potential of phase change materials in major Australian cities. Energy and Buildings. 2014 Aug 1;78:192-201.

[36] Hasan MI, Basher HO, Shdhan AO. Experimental investigation of phase change materials for insulation of residential buildings. Sustainable cities and society. 2018 Jan 1;36:42-58.

[37] Ahangari M, Maerefat M. An innovative PCM system for thermal comfort improvement and energy demand reduction in building under different

climate conditions. Sustainable Cities and Society. 2019 Jan 1;44:120-9.

[38] Izquierdo-Barrientos MA, Belmonte JF, Rodríguez-Sánchez D, Molina AE, Almendros-Ibáñez JA. A numerical study of external building walls containing phase change materials (PCM). Applied Thermal Engineering. 2012 Dec 5;47:73-85.

[39] Alawadhi EM. Thermal analysis of a building brick containing phase change material. Energy and Buildings. 2008 Jan 1;40(3):351-7.

[40] Chen C, Guo H, Liu Y, Yue H, Wang C. A new kind of phase change material (PCM) for energy-storing wallboard. Energy and Buildings. 2008 Jan 1;40(5):882-90.

[41] Solgi E, Fayaz R, Kari BM. Cooling load reduction in office buildings of hot-arid climate, combining phase change materials and night purge ventilation. Renewable Energy. 2016 Jan 1;85:725-31.

[42] Zhou G, Yang Y, Xu H. Energy performance of a hybrid space-cooling system in an office building using SSPCM thermal storage and night ventilation. Solar Energy. 2011 Mar 1;85(3):477-85.

[43] Nagano K, Takeda S, Mochida T, Shimakura K, Nakamura T. Study of a floor supply air conditioning system using granular phase change material to augment building mass thermal storage—heat response in small scale experiments. Energy and buildings. 2006 May 1;38(5):436-46.

[44] Duraković B, Mešetović S. Thermal performances of glazed energy storage systems with various storage materials: An experimental study. Sustainable Cities and Society. 2019 Feb 1;45:422-30.

[45] Durakovic B, Torlak M. Experimental and numerical study of a PCM window model as a thermal energy storage unit. International Journal of Low-Carbon Technologies. 2017 Sep 1;12(3):272-80.

[46] Durakovic B, Torlak M. Simulation and experimental validation of phase change material and water used as heat storage medium in window applications. J. of Mater. and Environ. Sci. 2017;8(5):1837-46.

[47] Zhou, J., 2006. Advanced structural materials. Porous Metallic Materials, ed. e. Winston O. Soboyejo., CRC Press , Taylor & Francis Group. USA, 22.

[48] Lee JH, Kim HE, Shin KH, Koh YH. Improving the strength and biocompatibility of porous titanium scaffolds by creating elongated pores coated with a bioactive, nanoporous TiO2 layer. Materials Letters. 2010 Nov 30;64(22):2526-9.

[49] Bruder SP, Caplan AI. Bone regeneration through cellular engineering. Principles of tissue engineering. 2000 Jan 1;2:683-96.

[50] Kulshreshtha A, Dhakad SK. Preparation of metal foam by different methods: A review. Materials Today: Proceedings. 2020 Jan 1;26:1784-90.

[51] https://www.gminsights.com/industry-analysis/metal-foam-market

[52] Weaver JA, Viskanta R. Freezing of water saturated porous media in a rectangular cavity. International communications in heat and mass transfer. 1986 May 1;13(3):245-52.

[53] Diani A, Campanale M. Transient melting of paraffin waxes embedded in aluminum foams: Experimental results and modeling. International Journal of Thermal Sciences. 2019 Oct 1;144:119-28.

[54] Venkateshwar K, Ebadi S, Simha H, Mahmud S. Influence of pore density and porosity on the melting process of bio-based nano-phase change materials inside open-cell metal foam. Journal of Thermal Science and Engineering Applications. 2019 Aug 1;11(4).

[55] Al-Jethelah M, Ebadi S, Venkateshwar K, Tasnim SH, Mahmud S, Dutta A. Charging nanoparticle enhanced bio-based PCM in open cell metallic foams: An experimental investigation. Applied Thermal Engineering. 2019 Feb 5;148:1029-42.

[56] Caliano M, Bianco N, Graditi G, Mongibello L. Analysis of a phase change material-based unit and of an aluminum foam/phase change material composite-based unit for cold thermal energy storage by numerical simulation. Applied Energy. 2019 Dec 15;256:113921.

[57] Zhang Z, He X. Three-dimensional numerical study on solid-liquid phase change within open-celled aluminum foam with porosity gradient. Applied Thermal Engineering. 2017 Feb 25;113:298-308.

[58] Atal A, Wang Y, Harsha M, Sengupta S. Effect of porosity of conducting matrix on a phase change energy storage device. International Journal of Heat and Mass Transfer. 2016 Feb 1;93:9-16.

[59] Fleming E, Wen S, Shi L, da Silva AK. Experimental and theoretical analysis of an aluminum foam enhanced phase change thermal storage unit. International Journal of Heat and Mass Transfer. 2015 Mar 1;82:273-81.

[60] Wang Z, Zhang Z, Jia L, Yang L. Paraffin and paraffin/aluminum foam composite phase change material heat storage experimental study based on thermal management of Li-ion battery. Applied Thermal Engineering. 2015 Mar 5;78:428-36.

[61] Allen MJ, Bergman TL, Faghri A, Sharifi N. Robust heat transfer enhancement during melting and solidification of a phase change material using a combined heat pipe-metal foam or foil configuration. Journal of Heat Transfer. 2015 Oct 1;137(10).

[62] Chen Z, Gao D, Shi J. Experimental and numerical study on melting of phase change materials in metal foams at pore scale. International Journal of Heat and Mass Transfer. 2014 May 1;72:646-55.

[63] Ali HM. Experimental investigation on paraffin wax integrated with copper foam based heat sinks for electronic components thermal cooling. International Communications in Heat and Mass Transfer. 2018 Nov 1;98:155-62.

[64] Yang X, Wei P, Cui X, Jin L, He YL. Thermal response of annuli filled with metal foam for thermal energy storage: an experimental study. Applied Energy. 2019 Sep 15;250:1457-67.

[65] Cozzolino R, Chiappini D, Bella G. Experimental characterisation of a novel thermal energy storage based on open-cell copper foams immersed in organic phase change material. Energy Conversion and Management. 2019 Nov 15;200:112101.

[66] Yao Y, Wu H, Gao Z, Liu Z. Pore-scale visualization and measurement of paraffin solidification in high porosity open-cell copper foam. International Journal of Thermal Sciences. 2019 Jan 1;135:94-103.

[67] Zheng H, Wang C, Liu Q, Tian Z, Fan X. Thermal performance of copper foam/paraffin composite phase change material. Energy conversion and management. 2018 Feb 1;157:372-81.

[68] Yang X, Bai Q, Zhang Q, Hu W, Jin L, Yan J. Thermal and economic analysis of charging and discharging characteristics of composite phase

change materials for cold storage. Applied Energy. 2018 Sep 1;225:585-99.

[69] Fan LW, Jin HQ. Local thermal nonequilibrium during melting of a paraffin filled in an open-cell copper foam: a visualized study at the pore-scale. Journal of Heat Transfer. 2017 Mar 1;139(3).

[70] Jin HQ, Fan LW, Liu MJ, Zhu ZQ, Yu ZT. A pore-scale visualized study of melting heat transfer of a paraffin wax saturated in a copper foam: effects of the pore size. International Journal of Heat and Mass Transfer. 2017 Sep 1;112:39-44.

[71] Yang J, Yang L, Xu C, Du X. Experimental study on enhancement of thermal energy storage with phase-change material. Applied Energy. 2016 May 1;169:164-76.

[72] Martinelli M, Bentivoglio F, Caron-Soupart A, Couturier R, Fourmigue JF, Marty P. Experimental study of a phase change thermal energy storage with copper foam. Applied thermal engineering. 2016 May 25;101:247-61.

[73] Mancin S, Diani A, Doretti L, Hooman K, Rossetto L. Experimental analysis of phase change phenomenon of paraffin waxes embedded in copper foams. International Journal of Thermal Sciences. 2015 Apr 1;90:79-89.

[74] Baby R, Balaji C. Experimental investigations on thermal performance enhancement and effect of orientation on porous matrix filled PCM based heat sink. International Communications in Heat and Mass Transfer. 2013 Aug 1;46:27-30.

[75] Cui HT. Experimental investigation on the heat charging process by paraffin filled with high porosity copper foam. Applied thermal engineering. 2012 Jun 1;39:26-8.

[76] Li WQ, Qu ZG, He YL, Tao WQ. Experimental and numerical studies on melting phase change heat transfer in open-cell metallic foams filled with paraffin. Applied Thermal Engineering. 2012 May 1;37:1-9.

[77] Zhao CY, Lu W, Tian Y. Heat transfer enhancement for thermal energy storage using metal foams embedded within phase change materials (PCMs). Solar energy. 2010 Aug 1;84(8):1402-12.

[78] Siahpush A, O'brien J, Crepeau J. Phase change heat transfer enhancement using copper porous foam.

[79] Wang H, Wang F, Li Z, Tang Y, Yu B, Yuan W. Experimental investigation on the thermal performance of a heat sink filled with porous metal fiber sintered felt/paraffin composite phase change material. Applied Energy. 2016 Aug 15;176:221-32.

[80] Mallow A, Abdelaziz O, Graham S. Thermal charging performance of enhanced phase change material composites for thermal battery design. International Journal of Thermal Sciences. 2018 May 1;127:19-28.

[81] Jackson GR, Fisher T. Response of porous foams filled with phase change material under transient heating. In45th AIAA Thermophysics Conference 2015 (p. 2811).

[82] Xiao X, Zhang P. Numerical and experimental study of heat transfer characteristics of a shell-tube latent heat storage system: Part I–Charging process. Energy. 2015 Jan 1;79:337-50.

[83] Zhang P, Xiao X, Meng ZN, Li M. Heat transfer characteristics of a molten-salt thermal energy storage unit with and without heat transfer enhancement. Applied Energy. 2015 Jan 1;137:758-72.

[84] Li WQ, Qu ZG, Zhang BL, Zhao K, Tao WQ. Thermal behavior of porous stainless-steel fiber felt saturated with phase change material. Energy. 2013 Jun 15;55:846-52.

[85] Zhou D, Zhao CY. Experimental investigations on heat transfer in phase change materials (PCMs) embedded in porous materials. Applied Thermal Engineering. 2011 Apr 1;31(5):970-7.

[86] Fukai J, Hamada Y, Morozumi Y, Miyatake O. Improvement of thermal characteristics of latent heat thermal energy storage units using carbon-fiber brushes: experiments and modeling. International Journal of Heat and Mass Transfer. 2003 Nov 1;46(23):4513-25.

[87] Beckermann C, Viskanta R. Natural convection solid/liquid phase change in porous media. International journal of heat and mass transfer. 1988 Jan 1;31(1):35-46.

[88] Weaver JA, Viskanta R. Freezing of water saturated porous media in a rectangular cavity. International communications in heat and mass transfer. 1986 May 1;13(3):245-52.

[89] Weaver JA, Viskanta R. Melting of frozen, porous media contained in a

horizontal or a vertical, cylindrical capsule. International journal of heat and mass transfer. 1986 Dec 1;29(12):1943-51.

[90] https://www.metalfoamweb.com/

Chapter 2.
ENHANCING PCMS THERMAL CONDUCTIVITY

2.1. Introduction

Thermal Energy Storage (TES), or the storage of energy in thermal form, is regarded as the best solution for a wide range of applications, like for instance from solar water heaters to building air conditioning systems. Latent Heat Storage (LHS) systems, among the several forms of TES, offer the most promise to provide a cost-effective solution to this issue. Due to relevant features such as high latent heat, appropriate phase change temperature, high energy density and modest volume fluctuation during phase change, some classes of materials named Phase Change Materials (PCMs) are used to control the heat in various thermal processes, in particular to store and release heat. However, a typical issue with PCMs is that they have a limited thermal conductivity, which severely restricts their melting and solidification capabilities and limits applications range of such materials. Nowadays, geometry optimization, or usage of thermal performances techniques like finned surface, nanoparticles or highly conductive porous materials like honeycombs or metallic foams are some solutions to improve PCMs performances. Besides, employing customized PCMs depending on the local temperature is also a promising solution as happens in LHTES-based Triplex Tube Heat Exchanger (TTHX), that consist in heat exchangers equipped with PCM layers with different melting points.

2.1.1 Thermal enhancement techniques

2.1.1.1 Finned surfaces

Finned surfaces are widely used to increase the heat exchange area in heat transfer devices. Because the fin configuration has a substantial impact on the heat transfer performance of a heat exchanger, multiple researchers have built and analyzed several fin designs also in the very recent years, including longitudinal, triangular, pin, circular/annular, tree-like and Y-shaped fins. Finned surfaces are seen to be an excellent solution for addressing the PCM's low thermal conductivity and improving overall heat transfer performance in the LHS. Yıldız et al. [1] studied the effect of tree-shaped fins dimensions and structure on the phase change rate, and they found that a rectangular shape has a stronger influence on the system. Yu et al. [2] studied the potential of the LHS with tree-shaped fins and discovered that employing such fins reduces melting time by 27% and enhances heat storage rate by 45% compared to conventional fins. When high conductivity fins were implanted in a small size TES, Pizzolato et al. [3] observed a 37% and 15% increase in melting and solidification rates, respectively. Abdulateef et al. [4] evaluate the fins' configuration, finding that

the rectangular fins provide a 15% improvement over the triangular fins. Mat et al. [5] used a longitudinal fin in a LHS and found that the phase change time was reduced by 58% at constant HTF velocity and 86% at constant HTF inlet temperature. The percentage of using various kinds of fins for augmenting the performance of TES has been investigated in [6]. The results showed that longitudinal fins were employed in 51.51% of the articles, indicating that this sort of fin geometry is quite common among researchers.

2.1.1.2 Nanoparticles

Recently, nanoparticles have been routinely employed to improve the thermal conductivity of fluids, and also in LHS systems to compensate PCMs' poor heat conductivity. On the other hand, it is important to also remark that the use of nanoparticles alters the characteristics of PCM. It slightly reduces the fusion latent heat as well as the PCM's specific heat transfer coefficient, lowering heat storage capacity and necessitating a larger quantity of PCM mass to maintain the same heat storage capacity. Khodadadi and Hosseinizadeh [7] were the first to suggest to use nanoparticles to improve the temperature responsiveness of PCMs. They found that the improved functionality of PCMs due to nanoparticle dispersion is promising for use in thermal energy storage applications. Simultaneous charging and discharging of multi-tube heat storage devices employing copper fins and Cu nanoparticles was investigated by Mahdavi et al. [8]. The steady-state liquid fraction fluctuates between 37% and 60 % depending on where the cold and hot tubes are placed, with the bottom half claiming the maximum 60%. Mehrali et al. [9] investigated the use of shape-stabilized salt hydrate phase change material for simultaneous solar-thermal energy harvesting and storage. Mol et al. [10] investigated the thermal storage performance of encapsulated PCM particles in an unstructured packed bed using numerical modeling. It is discovered that employing smaller particles results in a quicker bed charging and discharging. By converting half of the bed to particles with a diameter of half that of the original, a 26% reduction was obtained. Additionally, it is discovered that adding tiny particles downstream has a greater influence on charging speed than placing them upstream when the bed is completely charged. Finally, they showed that charge and discharge times were reduced by 20% and 13%, respectively. The NanoRound project concept evolved from many working groups on CFD (Computational Fluid Dynamics) applied to nanofluids and efforts to establish the optimum numerical representation of a nanofluid flow. As a consequence, the goals of this research are to do a round robin test on numerical methods to nanofluids and compare numerical and experimental findings. The findings suggest that a numerical

technique based on computational fluid dynamics is an excellent tool for predicting nanofluid behavior during heat transfer and convection efficiency. Furthermore, it was shown that gravity has an influence on the nanofluid flow [11]. Parsazadeh and Duan [12] used plate fins and Alumina nanoparticles to enhance the melting rate of Paraffin wax PCM inside vertical shell and tube heat exchangers. They numerically analyzed the effect of fin angle, fin pitch and nanoparticles concentrations on charging time. Their results showed that adding nanoparticles decreases the heat transfer rate due to a reduction of natural convection in the liquid PCM. Also, they found that clock-wise positive angles of fins accelerates the charging rate due to enhanced natural convection with local vorticities formed below the fins. Mahdi and Nsofor [13] investigated the performance of the PCM charging rate in a triplex tube system. Simultaneous charging and discharging from a finer triple-tube LHS system was investigated, utilizing Al_2O_3 to improve PCM thermal conductivity. They demonstrated that adding fins had a considerably greater impact on adjusting the system's performance than nanoparticles. Sushobhan and Kar [14] used n-Octadecene paraffin as the PCM to investigate the influence of CuO nanoparticles on the performance of the LHS system. Naghavi et al. [15] investigated charging and discharging thermal performances of a compact design heat pipe solar collector with latent heat storage. The thermal efficiency of the system ranges from 38% to 42% on bright days, but drops to 34% to 36% on cloudy-rainy days, indicating an 8 percent variability in varied situations. Mehrali et al. [16] studied a graphene-based nanofluid for heat transfer applications. A significant thermal conductivity improvement of 45.1% was discovered for a volume proportion of 4%. Furthermore, the convective heat transfer coefficient including nanofluids in a laminar flow regime with uniform wall heat flux was examined to determine its cooling capabilities. Mehrali et al. [17] investigated the influence of carbon nanospheres on phase change material form stability and thermal behavior for thermal energy storage. They concluded that the laser flash technique was used to measure the thermal conductivity of the SA/CNS composite. For the maximum loading of CNS, the thermal conductivity rose by nearly 105% at 35°C (50 weight in percent). As a result, the prepared paraffin/GO composite is an appropriate PCM for thermal energy storage applications because of their good thermal properties, thermal reliability, chemical stability, and thermal conductivity. They showed that melting time is reduced by employing nanoparticles in the reduction of melting time, which is more effective by increasing the volume fraction of nanoparticles.

2.1.1.3 Metal foam

Metal foams have been shown to be promising for thermal conductivity enhancement in PCMs. Thermal performance study of PCMs embedded in gradient porous metal foams was performed by Ghahremannezhad et al. [18]. Findings demonstrate that when the enclosure size varies in different directions, the improvement is more pronounced depending on the position of the heat source and the direction of the gradient foam with regards to gravity. When the height of the enclosure is increased, a positive foam gradient in the left-heated layouts enhances melting, and similarly, a positive foam gradient in the bottom-heated layouts also improves melting. In a review study, Kuruneru et al. [19] investigated the use of porous metal foam heat exchangers and the consequences of particulate fouling for energy-intensive sectors. Ferfera et al. [20] conducted a pore-scale investigation using a body-centered cubic geometrical model, demonstrating that decreased porosity results in increased thermal conductivity with a uniform melting front and temperature within the composite. Zhang et al. [21] investigated the effects of centrifugal accelerations on paraffin melting in high porosity copper foam. The results of the experiments revealed that centrifugal acceleration had a significant impact on the phase transition process of PCM. Zhao et al. [22] investigated the use of foams and fins inside an annulus with constant temperature boundary conditions for inner and outer tubes. Carbon fiber fins and three different kinds of foam, including nickel, aluminum, and copper, were tested. Their findings showed that fins, if properly built, may be as productive as composite metal foams. The impact of metal foam and nanoparticles on the PCM in a triplex tube heat exchanger was investigated by Li et al. [23]. The key finding of their research was that increasing nanoparticles loading, or reducing the porosity of the porous medium, increases the PCM phase transition rate. In [24], the authors proposed that heat conduction occurs through a high conductivity porous foam rather than PCM in the composite porous/PCM, which improves the rate of thermal diffusion. It is shown that the influence of conduction heat transfer via porous foam has a substantial impact on the charging/discharging process performance. Yang et al. [25] used a 2D axisymmetric model to investigate the impact of porous medium addition in both PCM and HTF domains. They demonstrated that using metal foam in all domains decreases the melting time by about 88.5% and results in a more uniform temperature within the PCM when compared to the non-porous scenario. In [26] it has been experimentally showed that employing metal foam within the PCM domain reduced the melting time by 64%. It has been also showed that in the presence of a porous medium, the

inclination angle of the energy storage unit has no impact owing to the porous media overwhelming influence on conduction heat transfer. The phase change of a PCM embedded with metallic foam within a rectangular enclosure was studied experimentally and numerically by Zheng et al. [27]. The authors performed a 2D numerical simulation using the equilibrium thermal state by replacing the thermal conductivity of pure PCM with an effective thermal conductivity in the energy equation. According to their findings, the melting time of composite PCM/metallic foam was 20% faster than that of pure PCM. In addition, the temperature distribution in PCM/metallic foam composites became more uniform. By comparing experimental and computational data, Zhang et al. [28] discovered that non-equilibrium thermal conditions are more trustworthy for predicting the melting process of PCM/metal foam composite. They used two-temperature energy equations to get excellent agreement between experimental and numerical data. Their projected findings revealed a significant temperature difference between paraffin and copper foam ligament temperatures. Xu et al. [29] investigated a horizontal double-pipe thermal energy system in conjunction with a porous medium, and optimized the location of the porous media into the system. They discovered that a system with a partially-filled foam at the base portion had the same impact as a system with a completely-filled foam at the base part, with a melting rate increase of 80%. Kuruneru et al. [30] studied metal foam in heat exchangers, analysis of particle-laden fluid flows, tortuosity, and particle-fluid behavior. The streamline angle ratio and meandering of fluid flow channels are demonstrated to fluctuate with increasing porosity and tortuosity. Additionally, the Reynolds number and particle density have a significant effect on the resistance to fluid flow and permeability, which are connected to tortuosity and flow behavior variation. Li et al. [31] investigated microencapsulated phase change materials in metal foams by altering angles to evaluate natural convection effects. According to the authors, metal foam may decrease surface temperature by roughly 47%, with lower porosity configurations providing the highest thermal performance. Atal et al. [32] investigated the effect of foam porosity on a latent heat thermal energy storage system device and discovered that lower porosities might decrease the melting–freezing cycle. Martinelli et al. [33] examined the performance of vertical and horizontal designs, as well as bottom and top injections, using a TES system with a copper foam insert in the PCM. Yang et al. [34] studied the shell-and-tube TES unit experimentally and demonstrated that a full metal foam/PCM composite melt takes almost 1/3 less time than pure paraffin. Along with experimental research, numerical simulations are used to investigate the parameters and optimize the performance of a PCM-based heat

exchanger. For the PCM/foam zone, the volume-averaged theory is heavily used for predictions. Additionally, past research has largely simplified the physical issue by focusing only on the cross-section of the TES unit in a two-dimensional computational domain. Chen et al. [35] explored analysis and characterization of double-pipe metal foam-filled heat exchangers. There is good concordance between the current findings and previously published analytical data. The given study demonstrates how to optimize the operation of metal foam-filled double-pipe heat exchangers. Hossain et al. [36] have endorsed the idea of mixing nanoparticles with porous matrices to operate as a compound heat transfer enhancement approach. Mancin et al. [37] mixed copper metallic foam into a range of PCMs with different melting points (53, 57, and 59 °C). The experimental findings suggested that depending on the metal foam features, heat transfer may be increased by a factor of 4–8. Alshaer et al. [38] developed a model for simulating the phase transition of a metal foam/PCM composite using the Volume Averaging Technique (VAT) for governing equations. They employed NEPCM inside a metal foam module to cool the surface. Their findings indicated that the addition of multi-wall carbon nanotubes to a metallic foam matrix with a porosity of less than 0.75 resulted in an 11.5% reduction in the surface temperature of the module. Tasnim et al. [39] investigated a similar issue by considering heating at the side boundary and convection effects. Their research demonstrated that the inclusion of nanoparticles inhibits both conduction and convection heat transfer, hence prolonging the PCM melting process. Nithyanandam and Pitchumani [40] investigated the influence of metal foam on the performance of a latent heat system based on heat pipes. They discovered that reducing the pore size increases the rate of heat transfer. Li et al. [41] presented experimental and numerical analyses of a copper foam filled with paraffin in a vertical orientation and heated from a vertical plate. An excellent agreement between measurements and predictions is shown, demonstrating that more uniform temperatures may be attained by decreasing porosity to promote conduction or by decreasing pore density to increase natural convection. Additionally, the authors discovered that reduced porosities result in quicker solid/liquid interface movement.

2.1.2. Multiple-PCM

Multiple-PCM are employed to maximize heat transfer based on PCMs placed depending on local temperatures. Li et al. [42] examined the charging process for a thermal energy storage unit equipped with single and multiple PCMs for use in conventional air-conditioning systems. The findings suggested that using numerous PCMs in the thermal energy storage unit considerably

enhance the charging process as compared to using a single PCM. The overall energy charging capacity of the multiple-PCM unit increased by about 32% as compared to the single-PCM unit. Mahdi and Nsofor [43] investigated a two-dimensional double-tube LHS system made of multi-segment metal foam with varying porosity. They demonstrated that using foam with variable porosities in separate segments improves heat storage and recovery rates as compared to using a single porosity. Hu et al. [44] increased the performance of a frustum-shaped PCM unit by replacing a single PCM with numerous PCMs. As a five-PCM arrangement is used in the frustum-shaped unit or the typical shell-and-tube unit, the charging time is reduced by 21% and 47%, respectively, when compared to operating with a single PCM. Al-Abidi et al. [45] examined the influence of longitudinal fin layout on the charging time reduction in a triple-tube cylindrical LHS system. They conducted an experiment with internal-external fins and numerical simulations using a variety of fin configurations, including internal, external, and internal-external fins, as well as fin length and thickness. They demonstrated that a 34.7% decrease in melting time in the best case scenario. Adine and ElQarnia [46] evaluated the storage performance of the multi-PCM model with the single PCM model using numerical simulations and found that the multi-PCM model is more efficient and economical for low mass flow rates and low HTF inlet temperatures. The results indicated that by including numerous PCMs with varying melting temperatures into the slabs, the phase-change rates could be greatly increased compared to when a single PCM was used.

2.1.3. Aim and novelty of the present work

According to the above comprehensive review of the current state-of-art, there is a lack of studies regarding an exhaustive comparison of nanoparticles, metal foam and finned surfaces applications in PCM thermal energy storage systems, in particular with references to a triplex-tube heat exchanger that intensifies the PCM charging process. Besides, no studies considered a combination of the aforementioned thermal conductivity enhancement techniques. Based on the literature review, this study aims to compare, and also combine, porous metal foams, nanoparticles, and finned surface in a PCM-based Triplex Tube Heat Exchanger (TTHX)-LHS system. This paper aims to figure out which would be the best option by making references to either a single-PCM and multilayer-PCM, which has not been done so far according to the current literature. In the first part of the manuscript, geometries investigated are introduced, then lately the whole set of governing equations for each case, together with closure coefficients, boundary conditions, numerical methods and

validation, are presented. Geometries investigated are referred to TTHX that considers also finned surfaces in some cases. The PCM is located in the middle tube, while water passes in inner and outer tubes as the heat transfer fluid. Results will be shown and compared in terms of liquid fractions, temperature achieved and stored energy. The findings of this study will serve as a guide to appreciate the preferential option to enhance thermal conductivity in latent heat storage units, that could be applied to a wide variety of PCM-based applications, including for instance TES for solar energy systems, energy-efficient buildings, and electronic thermal management.

2.2. Physical model and mathematical formulation

2.2.1 Model geometry

The schematic of a domestic and industrial application with a TTHX with PCM has been presented in **Figure 2.1a** in order to understand where the mathematical CFD model that will be shown later comes from. Throughout the day the charging process takes place and at night the discharge process is done. Charging of the TES is done during the daytime when solar radiation is present in the following system, as shown in **Fig. 2.1a**. Valve 1 is maintained open throughout the charging period or during the day, whereas valve 2 is kept closed. The solar collector collects the cold water. Water absorbs heat from the sun, and part of the hot water flows through the heat storage unit in order to charge the PCM, while the remaining water is pumped straight to the water storage tank. Valve 1 must be closed during discharge at night, or when there is no solar radiation, since it is not essential to flow water through the collector. On the other hand valve 2 must be opened to pass water straight through the TES unit for releasing heat to water. Simultaneously, the PCM begins to solidify, and once this completely solidified, the PCM could be once again employed for charging. This technique is repeated through time until the PCM thermal cycle is completed. The choice of a PCM for a solar domestic hot water system should be chosen carefully to ensure that hot water is produced at an appropriate temperature range and that safety problems are minimized. Firstly, the phase change temperature of the material is a crucial factor depending on the application [47, 48, 49]. For domestic hot water applications, if one assumed that hot water comes in the thermal energy storage system at 60 °C, one could employ PCMs that present temperatures below the incoming hot water. Therefore, as occur in this study, one could employ PCMs with solidus temperatures, *i. e.* the temperature that might correspond to a unitary liquid fraction, of 33 °C (RT31), 36 °C (RT35), or 42 °C (RT42), if one assumes

uniform initial temperatures smaller than the ones from these PCMs. Since the HTF temperature is greater than the PCM melting temperature, heat will start penetrating through both inner and outer surfaces to initiate melting in form of a melt layer adjacent to each surface. The selection of such charging temperatures was based on a typical minimum operation temperature, say 60 °C, to power for instance some industrial and domestic hot water applications, like for example solar air conditioning systems. For times $t \geq 0$, both inner and outer surfaces of the annulus are suddenly exposed to the HTF throughout the whole charging (melting) process. 3D configuration of the studied physical models is exhibited in **Fig. 2.1b**. The geometry discussed in this study has been extrapolated from a typical application example previously described. The geometry of the TTHX together with the employed to describe the multilayer-PCM and Triplex-Tube/Fin geometry here used is seen in cross-section in **Figure 2.1b**. Because of the angular symmetry, only the left half of the physical domain was taken into account in the computations. The Triplex Tube Heat Exchanger (TTHX) unit is assumed to be 2 meters long and the diameters of the tubes are shown for all the cases in the figure. The longitudinal fin tubes (with a total of 8 fins) are produced by the high-frequency resistance welding method so any contact resistance is here neglected. Each of the three cases will be labelled lately as Case A (Simple-TTHX), Case B (Multilayer-TTHX) and Case C (Longitudinal fin-TTHX).

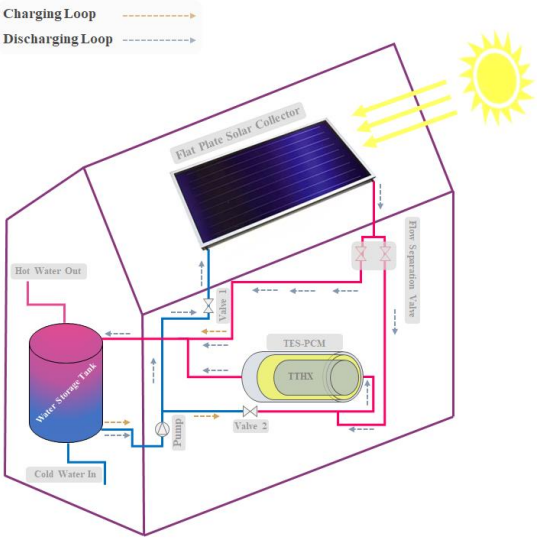

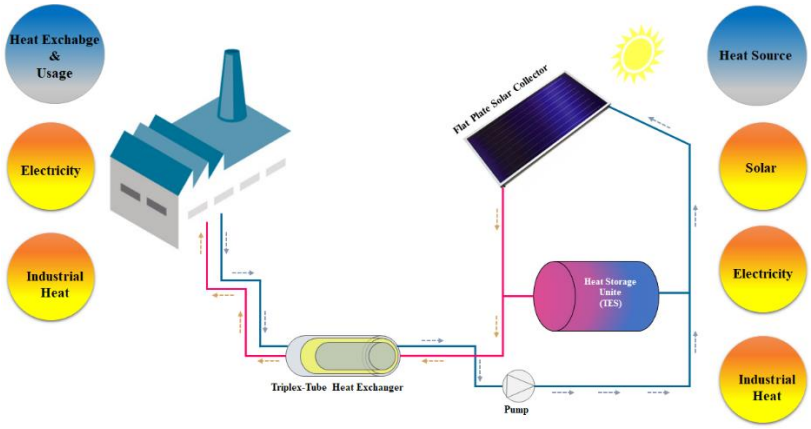

Fig. 2.1a The schematic of a domestic and industrial application with a TTHX with PCM

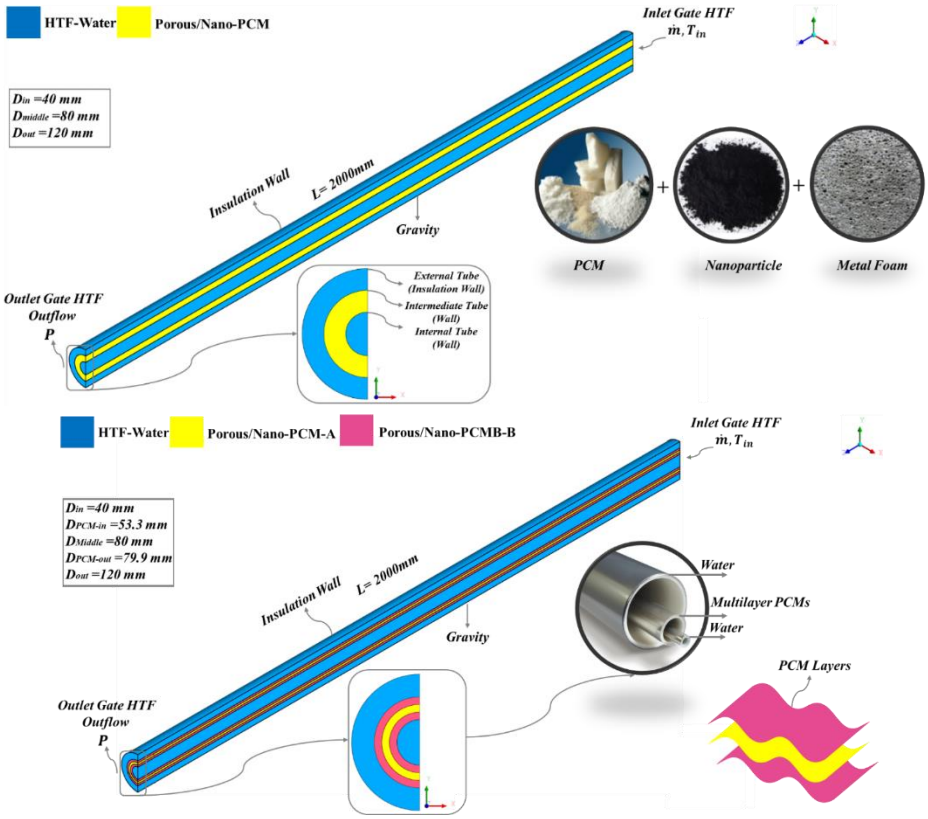

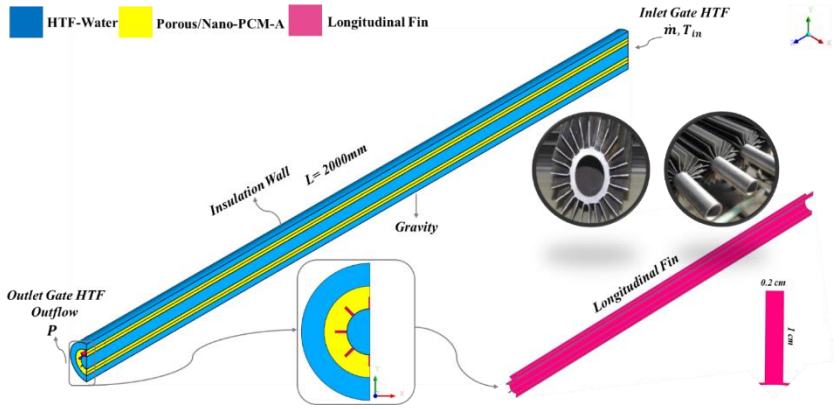

Fig. 2.1b. Schematic of a TTHX with PCM technologies: Case A (Top), Case B (middle), and Case C (Bottom)

2.2.2 Governing equations

The assumptions for the present study are listed as follows:

- Water fluid flow is 3D, steady, Newtonian, laminar, and incompressible,
- Volume expansion of phase change materials and thermal resistances in the tube metal thickness are negligible,
- Thermophysical properties for PCM too are assumed to be constant in the buoyancy force except for density,
- The outer shell is insulated, then heat transfer with the environment is not considered,
- Boussinesq approximation is used for natural convection in the liquid PCM,
- The nanoparticle distribution is homogeneous,
- Structure of porous medium is presumed to be homogeneous, isotropic and open-celled between porous medium and PCM,
- The PCM and the nanoparticles are in thermal equilibrium and there is no slip between them,
- No heat loss or gain from the surroundings,
- No thermal equilibrium exists between nanoPCM and porous metal foam, i.e. $T_f \neq T_s$,
- Thermal dispersion in the porous foam can be neglected [50],
- Time scales are as small as to consider constant boundary conditions.

The effective particle volume fraction, the range of shear rate, the viscosity of the base liquid influence the non-Newtonian shear thinning behavior of

nanofluids, and the characteristic shear rate, may be used to characterize a nanofluid [51]. However, according to the above assumptions, liquid Nano-PCM is Newtonian and incompressible, and their flows are assumed to be laminar. Mass flow rate here employed presents values with which a laminar flow assumption can be done. Based on these assumptions, continuity, momentum, and energy equations are stated as follows [22, 23]:

Continuity:

$$\nabla \cdot \vec{V} = 0 \tag{1}$$

Momentum in *x*-direction:

$$\frac{\bar{\rho}}{\varepsilon^2}\left(\varepsilon\frac{\partial u}{\partial t}+u\frac{\partial u}{\partial x}+v\frac{\partial u}{\partial y}+w\frac{\partial u}{\partial z}\right)=-\frac{\partial p}{\partial x}+\frac{\bar{\mu}}{\varepsilon}\nabla^2 u+A_m u\frac{(1-\lambda)^2}{\lambda^3+\delta}-\left(\frac{\bar{\mu}}{K}-\frac{\bar{\rho}C_f|u|}{\sqrt{K}}\right)u \tag{2}$$

Momentum in *y*-direction:

$$\frac{\bar{\rho}}{\varepsilon^2}\left(\varepsilon\frac{\partial v}{\partial t}+u\frac{\partial v}{\partial x}+v\frac{\partial v}{\partial y}+w\frac{\partial v}{\partial z}\right)=-\frac{\partial p}{\partial y}+\frac{\bar{\mu}}{\varepsilon}\nabla^2 v+\left(\overline{\rho\beta}\right)g\left(T-T_{int}\right)+A_m v\frac{(1-\lambda)^2}{\lambda^3+\delta}-\left(\frac{\bar{\mu}}{K}-\frac{\bar{\rho}C_f|v|}{\sqrt{K}}\right)v \tag{3}$$

Momentum in *z*-direction:

$$\frac{\bar{\rho}}{\varepsilon^2}\left(\varepsilon\frac{\partial w}{\partial t}+u\frac{\partial w}{\partial x}+v\frac{\partial w}{\partial y}+w\frac{\partial w}{\partial z}\right)=-\frac{\partial p}{\partial z}+\frac{\bar{\mu}}{\varepsilon}\nabla^2 w+A_m w\frac{(1-\lambda)^2}{\lambda^3+\delta}-\left(\frac{\bar{\mu}}{K}-\frac{\bar{\rho}C_f|w|}{\sqrt{K}}\right)w \tag{4}$$

Energy-Liquid NanoPCM:

$$\overline{\rho C}\left(\varepsilon\frac{\partial T}{\partial t}+V\cdot\nabla T\right)=k_{fe}\nabla^2 T_f+h_{sf}A_{sf}\left(T_s-T_f\right)-\varepsilon\overline{\rho L}_f\frac{\partial\lambda}{\partial t} \tag{5}$$

Energy-Porous medium (foam):

$$(1-\varepsilon)(\rho C)_s\frac{\partial T_s}{\partial t}=k_{se}\nabla^2 T_s-h_{sf}A_{sf}\left(T_s-T_f\right) \tag{6}$$

The Eq. 5 can be applied for the single-phase HTF too when permeability K is infinite and porosity ε is unitary. Subscripts f and s refer to liquid NanoPCM and porous medium (foam), respectively, T is the temperature, p is the effective pressure, μ is the dynamic viscosity, C is specific heat capacity, L_f is latent heat, is the porosity of Al6061 aluminum alloy, δ in Carman-Kozeny damping term is a tiny number (0.001) to avoid division by zero [52] and A_m is a mushy zone constant. The mushy zone constant has been set equal to 10^6 here since a value between 10^4 and 10^7 is typically suggested [53].

The function λ is the liquid fraction and it describes the distribution of PCM solid and liquid phases. Its value varies between 0 and 1 and is defined as:

$$\begin{aligned} &\lambda = 0 && if \;\; T \le T_s \\ &\lambda = \left(\frac{T - T_s}{T_l - T_s}\right) && if \;\; T_s < T < T_l \\ &\lambda = 1 && if \;\; T \ge T_l \end{aligned} \tag{7}$$

The parameters in Eqs. (1) – (7) needing definitions to close the problem are the permeability *K*, the inertial coefficient C_f: the fluid effective thermal conductivity k_{fe}, the solid effective thermal conductivity k_{se}: the interfacial heat transfer coefficient between nanoPCM and porous foam h_{sf}: and the specific surface area A_{sf}.

2.2.3. Permeability and inertial coefficient

Porosity ε, pore density ω also labelled as pores per inch (PPIs), and ligament diameter d_l are the basic parameters used to describe the structural characteristics of the metal foam. The ligament diameter could be estimated based on pore size d_p by the following relation:

$$\frac{d_l}{d_p} = 1.18\sqrt{\frac{1-\varepsilon}{3\pi}}\left(\frac{1}{1-e^{-(1-\varepsilon)/0.04}}\right), where \left(d_p = 0.0254/\omega\right) \tag{8}$$

Where 0.0254 is the conversion rate between inches and meters. This formula is a simplified form to correlate d_p with PPIs and often referred to the nominal pore diameter from the manufacturer, that generally is an expression of a rough average that considers both cell and pore sizes. The permeability, *K*, and inertial coefficient, C_f, required in Eq. (2), Eq. (3), and Eq. (4)), of copper foam are calculated using the models presented in [54] as follows:

$$\frac{K}{d^2_p} = 0.00073(1-\varepsilon)^{-0.224}\left(\frac{d_l}{d_p}\right)^{-1.11} \tag{9}$$

$$C_f = 0.00212(1-\varepsilon)^{-0.132}\left(\frac{d_l}{d_p}\right)^{-1.63} \tag{10}$$

We also mention here that often the inertial coefficient is negligible in such applications because of the low velocities achieved by the liquid PCM.

2.2.4. Effective thermal conductivity and interfacial heat transfer coefficient

The effective thermal conductivity in metal foam is a quantitative measure of the material's capacity to transmit heat in the presence of both solid and fluid phases within its structure. Metal foam is a permeable substance composed of a compact metal structure with empty areas that are occupied by air or another fluid. The effective thermal conductivity considers heat transport via both the solid and fluid phases. In Eqs. (3) and (4), the effective thermal conductivity of liquid nanoPCM, k_{fe}, and the effective thermal conductivity of the porous medium, k_{se}, were obtained from using the model proposed by Boomsma and Poulikakos [55] where it is possible to distinguish between k_{fe} and k_{se} starting from the overall effective thermal conductivity by assuming either $k_s = 0$ or $k_f = 0$. By employing this model, one can define each phase effective thermal conductivity by assuming a zero-thermal conductivity for the other phases:

$$k_{fe} = \frac{\sqrt{2}}{2\left(M_A + M_B + M_C + M_D\right)}\Big|_{k_s=0} \tag{11}$$

$$k_{se} = \frac{\sqrt{2}}{2\left(M_A + M_B + M_C + M_D\right)}\Big|_{k_f=0} \tag{12}$$

where

$$M_A = \frac{4\sigma}{\left(2e^2 + \pi\sigma(1-e)\right)k_s + \left(4 - 2e^2 + \pi\sigma(1-e)\right)k_f} \tag{13}$$

$$M_B = \frac{(e-2\sigma)^2}{\left(e-2\sigma\right)e^2 k_s + \left(2e - 4\sigma - (e-2\sigma)e^2\right)k_f} \tag{14}$$

$$M_C = \frac{(\sqrt{2}-2e)^2}{2\pi\sigma^2(1-2e\sqrt{2})k_s + 2\left(\sqrt{2} - 2e - \pi\sigma^2(1-2e\sqrt{2}))\right)k_f} \tag{15}$$

$$M_D = \frac{2e}{e^2 k_s + \left(4 - e^2\right)k_f} \tag{16}$$

$$\sigma = \sqrt{\frac{\sqrt{2}(2 - 5/8e^3\sqrt{2} - 2\varepsilon)}{\pi(3 - 4e\sqrt{2} - e)}},\ and\ e = 0.339 \tag{17}$$

Furthermore, A_{sf} and h_{sf} in Eqs. (5) and (6) indicate the metal foams specific surface area and interfacial heat transfer coefficient. Correlations to be used for the interfacial heat transfer coefficient is still an open question [50], and different adapted correlations based on tube banks natural convection [56, 57], or on low-velocity tube banks cross-flow [58,28, 59] or PCM/foam pore-scale analysis [60] have been proposed. In the present work we used low-velocity tube banks cross-flow correlations, that have been also employed in similar studies [28, 59]. Reynolds number is computed in Eq. 19 by using the ligament diameter d_l as the characteristic length. The Reynolds number is here 2000 because the inlet mass flow rate is equal to 0.021kg/s.

$$A_{sf} = \frac{3\pi d_l (1 - e^{-(1-\varepsilon)/0.04})}{(0.59 d_p)^2} \tag{18}$$

$$h_{sf} = \begin{cases} 0.76\, Re_d^{0.4}\, Pr_{PCM}^{0.37} \left(\frac{k_f}{d_f}\right), 1 \le Re_d \le 40 \\ 0.52\, Re_d^{0.5}\, Pr_{PCM}^{0.37} \left(\frac{k_f}{d_f}\right), 40 \le Re_d \le 1000 \\ 0.26\, Re_d^{0.6}\, Pr_{PCM}^{0.37} \left(\frac{k_f}{d_f}\right), 1000 \le Re_d \le 2\times 10^5 \end{cases} \tag{19}$$

2.2.5. Thermo-physical properties

In this subsection, thermophysical properties for nanofluid and PCM are reported. Nano-fluid density is expressed as follow by considering that this is embedded in a metal foam:

$$\begin{aligned} &NanoPCM: \rho_{np} = (1-\varphi)\rho_{pcm} + \varphi\rho_n \\ &Foam/NanoPCM: \bar{\rho} = \rho_{np} \end{aligned} \tag{20}$$

Specific heat, latent heat, and thermal expansion coefficient are expressed as:

$$\begin{aligned} &NanoPCM: (\rho C)_{np} = (1-\varphi)(\rho C)_{pcm} + \varphi(\rho C)_n \\ &Foam/NanoPCM: \overline{\rho C} = (\rho C)_{np} \end{aligned} \tag{21}$$

$$NanoPCM: \left(\rho L\right)_{np} = (1-\varphi)\left(\rho L\right)_{pcm}$$
$$Foam / NanoPCM: \overline{\rho L} = \left(\rho L\right)_{np} \tag{22}$$

$$NanoPCM: \left(\rho\beta\right)_{np} = (1-\varphi)\left(\rho\beta\right)_{pcm} + \varphi\left(\rho\beta\right)_{n}$$
$$Foam / NanoPCM: \overline{\rho\beta} = \left(\rho\beta\right)_{np} \tag{23}$$

In the equations listed above, φ is the volume fraction of nanoparticles and subscripts n, np,and pcm refer to particles of solid, nanofluid, and base fluid, respectively. In the following, for nanofluids the effective dynamic viscosity is expressed as [7]:

$$NanoPCM: \mu_{np} = \frac{\mu_{pcm}}{(1-\varphi)^{2.5}}$$
$$Foam / NanoPCM: \overline{\mu} = \mu_{np} \tag{24}$$

The nanoPCM thermal conductivity was written using the model developed Maxwell equation [61]. The effective thermal conductivity is expressed as:

$$\frac{k_{np}}{k_{pcm}} = \frac{k_{CuO} + 2k_{pcm} - 2\phi(k_{pcm} - k_{CuO})}{k_{CuO} + 2k_{pcm} - \phi(k_{pcm} - k_{CuO})} \tag{25}$$

The following generic formula is used to calculate the heat transfer rate of melting p_L; the average heat rate is an expression of a mean melting velocity, defined as the stored/released thermal energy over the melting/solidification time as [46]:

$$p_L = \frac{Q}{t_m} = \frac{m_{pcm}\left(\int_{T_i}^{T_s} C\ dT + L_f + \int_{T_l}^{T_e} C\ dT\right)}{t_m} = \frac{m_{pcm}\left[C\left(T_s - T_i\right) + L_f + C\left(T_e - T_l\right)\right]}{t_m} \tag{26}$$

Where t_m is the amount of time required to complete the melting process. The numerator Q is also the stored energy used later for computations. It is worth noting that the simulations in this work end once the liquid percentage in the whole domain hits 1.0 during the melting process, *i. e.* complete melting. When the simulation is finished, Eq. (26) is used to calculate the total energy and PCM temperature. Subscripts in Eq. 26 stands for endpoint (end of the simulation), initial (beginning of the simulation), liquidus and solidus, respectively. Finally, materials chosen here are listed in the following. Because of the melting temperature range here chosen, Rubitherm organic materials (RT31, RT35 and RT42, where the numbers refer to their melting temperatures)

have been chosen as the PCM material. Foam bulk material is Al6061, because of its very high thermal conductivity. CuO nanoparticles have been used here as nanoparticles as widely done. In addition, the tubes were chosen to be made of copper (Cu). Thermo-physical properties of PCMs, water, nanoparticle, and metal foam are listed in **Table 2.1**, and **2.2**. In **Table 2.1**, solidus and liquidus temperatures are reported, where the melting temperature can be computed as $T_m = \left(T_s + T_l\right)/2$. Finally, a table that resumes group of cases here investigated (Case A, B and C), which will be simulated by considering PCM, NEPCM, metal foam, multilayer-PCM, and/or longitudinal fins, is reported as **Table. 2.3**.

Table 2.1. Thermophysical properties of the PCM [62]

Property	**RT31**	**RT35**	**RT42**
T_s/T_l	27/33	29/36	38/42
ρ_s/ρ_l *(kg /m^3)*	860/770	850/780	850/780
C *(J /kg K)*	2000	2000	2000
k *(W/m K)*	0.2	0.2	0.2
μ *(kg/m s)*	0.0035	0.023	0.02351
β *(1/K)*	0.0006	0.0006	0.0005
λ *(kJ/kg)*	165	170	165

Table 2.2. Thermophysical properties of the CuO (nanoparticles), Al6061 (foam bulk), Cu (metal), and water [63, 64, 65]

Property	**CuO**	**Al6061**	**Cu**	**Water at 60 °C**
ρ *(kg/m^3)*	6510	140	8920	983.20
μ *(kg/m s)*	5.12×10^{-6}	-	-	3.544×10^{-4}
C *(J/kg K)*	540	0.869	380	4184.3
k *(W/m K)*	18	167	400	0.654

Table 2.3. A resume of regrouped cases here investigated

Cases	**Number of PCM**	**Description**
Case A	RT35	Single PCM-TTHX
Case B	RT42-RT31-RT35	Multilayer PCM-TTHX
Case C	RT35	Single PCM-TTHX-Fin

2.3. Boundary and initial condition and numerical procedure

At the initial time for the melting process, *i. e.* PCM charging process, the initial temperatures of PCM (*i. e.* RT35), initial temperatures of HTF system, and HTF (water) were 29 °C, 25 °C and 60 °C, respectively. As previously mentioned, these temperatures have been established based on a typical

minimum operation temperature of 60 °C for typical industrial and domestic hot water applications. The outer tube of the TTHX is assumed to be insulated. Extremities of the PCM system domain at the same axial location of HTF inlet and outlet sections are assumed to be no-slip and adiabatic, while temperature and heat flux continuity are invoked at every adjacent boundary. High foam porosities with porosities typically higher than 92% and quite-low nanoparticle volume fractions ($\phi = 5\%$) [14,66] were selected, noting that if foam porosity decreases and/or the volume percentage of nanoparticles increases, there is less volume for the PCM. Besides, with higher nanoparticle concentrations, segregation (*i. e.*, separation of nanoparticles from PCM) could happen, which is something to avoid. Besides, nanoparticles raises the viscosity of the PCM-melt. At the HTF inlet and outlet sections, we assumed incoming mass flow rate and pressure outflow, while no-slip conditions for velocities are invoked at the boundaries. A uniform entrance temperature of 60 °C is assumed with an outflow condition for the temperature at the exit section. Furthermore, it has been widely shown that porosity has a greater impact on PCM thermal conductivity than PPI [57, 67-72].

After generating the 3D structure, the commercial finite volume code ANSYS is used to solve governing equations. The pressure correction equation is solved using the Staggering Pressure Option (PRESTO) scheme. The pressure-velocity coupling is solved using the well-known Semi-Implicit Pressure-Linked Equation (SIMPLE) algorithm. To solve the momentum and energy equations, a Quadratic Upwind Differencing (QUICK) scheme is used. Energy, continuity, and momentum equations all have a convergence criterion of 10^{-6}, 10^{-5}, and 10^{-5}, respectively, that guarantees invariance of the solution.

The grid distribution of various perspectives of the produced mesh for Triplex-Tube Heat Exchangers is shown in **Fig. 2.2.a**. Different grid sizes and time steps for case A (PCM and no metal foam or nanoparticles) liquid fraction reduction over time were examined. Grids with 634000, 880000, 1060000, and 1280000 cells were studied, and in the end, it was found that 1060000 grids would be appropriate for this study since no relevant changes in liquid fraction have been found. The structured mesh was employed in the fluid zone, and wavy wall, and the more acceptable cell was applied near the border of the wavy wall tube. The reason for selecting such finer mesh is these regions have a more significant gradient of scalars. Furthermore, different time steps have been analyzed to verify its independence. It has been found that findings in terms of liquid fraction obtained for Δt = 1.0, 0.5, and 0.1 seconds are negligible, thus a time step of Δt = 0.5 s (the total charging time will be always far from the time

step employed) is a reasonable choice. A resume of these findings is shown in **Fig. 2.2b**.

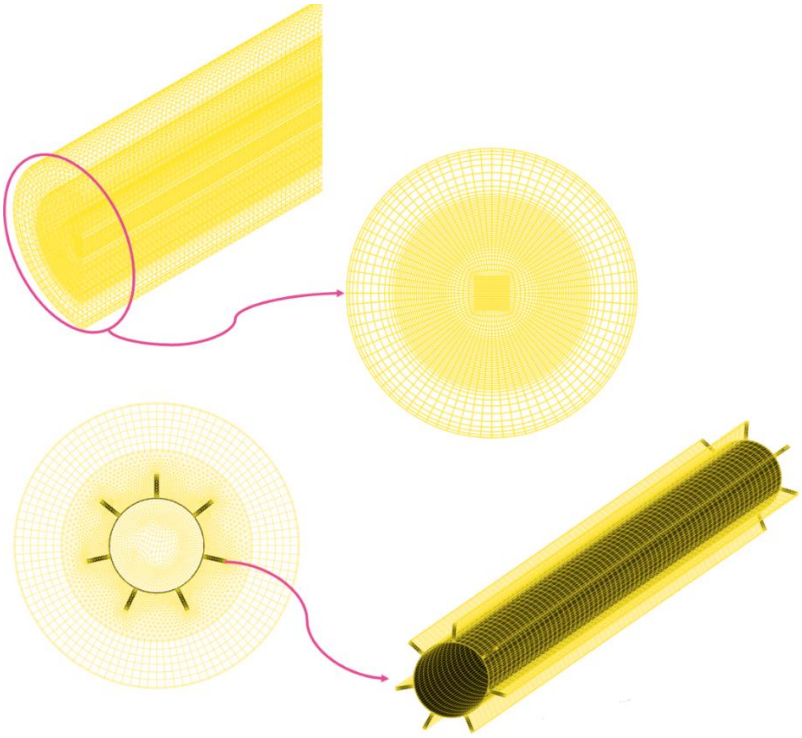

Fig. 2.2a. Different views of the generated mesh for Triplex-Tube Heat Exchangers

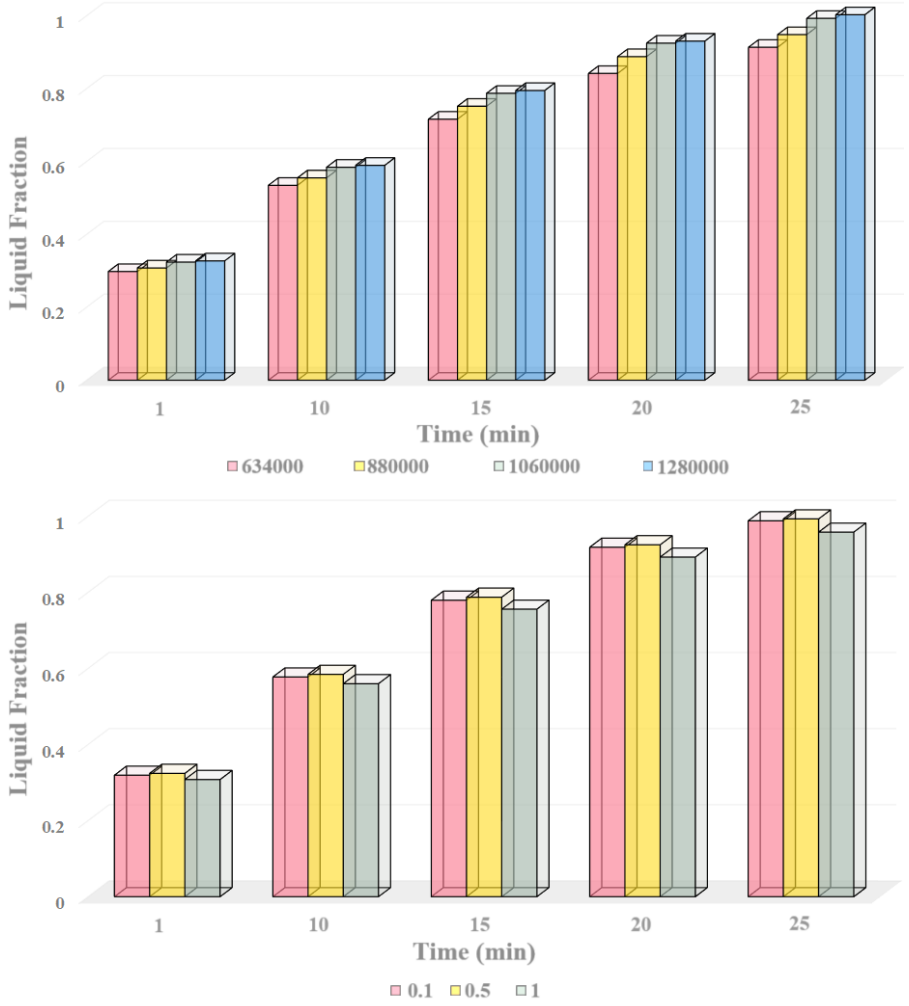

Fig. 2.2b. Grid (top) and time step (bottom) independence check performed on liquid fraction of whole TTHX during the charging process for pure PCM

4. Validation

Comparison with experimental and numerical results from Al-Abidi et al. [45] on RT82 melting in a triplex-tube heat exchanger with charging from both the inner and outside tubes are here presented in order to validate the code. The average temperature profile during melting for the two experiments is shown in **Fig. 2.3a**. Comparisons with a porous foam NEPCM system from Mahdi and Nsofor [13] are reported too in **Fig. 2.3b** in terms of liquid fraction evolution for two different porosities to perform comparisons for the code when nanoPCM is considered. The graphs behavior and melting durations present a very good agreement. It is also underlined that Mahdi and Nsofor [13] validated

their model with experiments from the literature. The same initial conditions, boundary conditions, and thermal physical properties in the studies were adopted in the current study to validate the code. Rounding-off and discretization in the numerical solution may account for the minor discrepancy between these answers. However, the graphs' behavior and melting durations are nearly identical, concluding that the code here shown is considered to be validated.

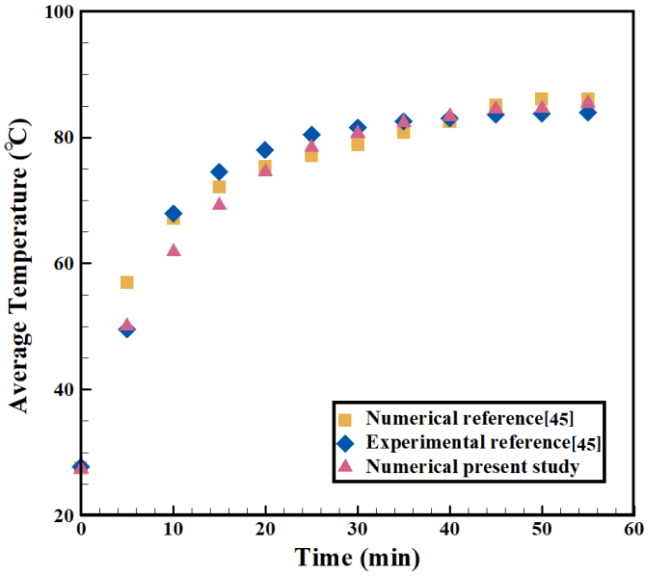

Fig. 2.3a. Comparisons with experiments and numerical from Al-Abidi et al. [45] in terms of average temperature

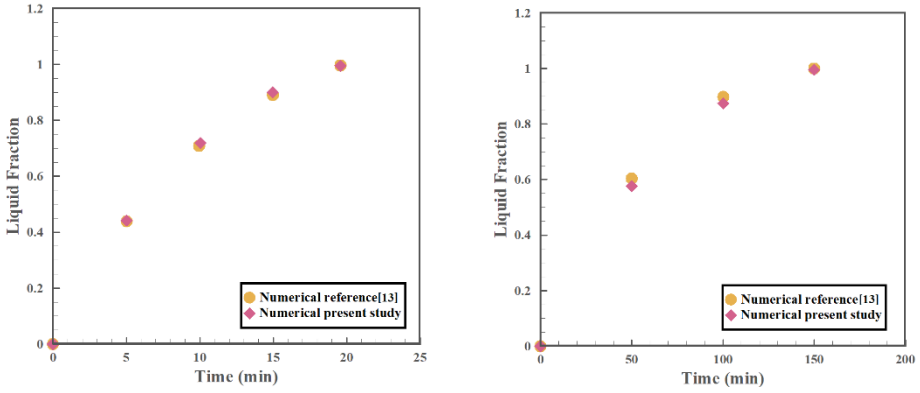

Fig. 2.3b. Comparisons with [13] in terms of liquid fraction evolution: (left) ε = 0.95 and (right): ε = 0.98

2.5. Results and discussion

2.5.1. Case A-Single PCM

2.5.1.1. Case A-Pure PCM

In this paper, numerical simulations for Single PCM (Case A-Single PCM), Multilayer PCM (MP) (Case B-Multi PCM), Single PCM with fins (Case C-Single PCM), and for all the cases their combination with porous metal foam and/or nanoparticles, were investigated. Temperatures employed on HTF side cause the PCM to melt since these are higher than PCM initial temperature. The heat exchanger (Case A-Pure PCM), that is a basic TTHX without Nanoparticles (NPs), Metal Foam (MF), multilayer, or fins, was researched and assessed first as the baseline case to perform comparisons later. **Fig. 2.4** illustrates liquid fraction, PCM-average temperature, and stored energy for the Case A with pure PCM (Case A-Pure PCM). It is shown that both liquid fraction and energy stored curves decrease with time, reaching a plateau when they reach complete melting; on the other hand, for the PCM-average temperature profile it is shown that the slope changes at about 10 minutes. This happens because PCM-average temperature has a distribution in the PCM that of course affects temperature evolution even during melting. In other words, since the simulation stops when all the PCM is melted, after a certain time most of the PCM is melted through the domain, and temperature would rise up a lot since there is a very large amount of sensible heat. This happens also for all the other cases, making in most of the cases PCM-average temperatures far larger than melting temperatures. From all the figures, it is shown that they reach complete melting at 27.72 minutes.

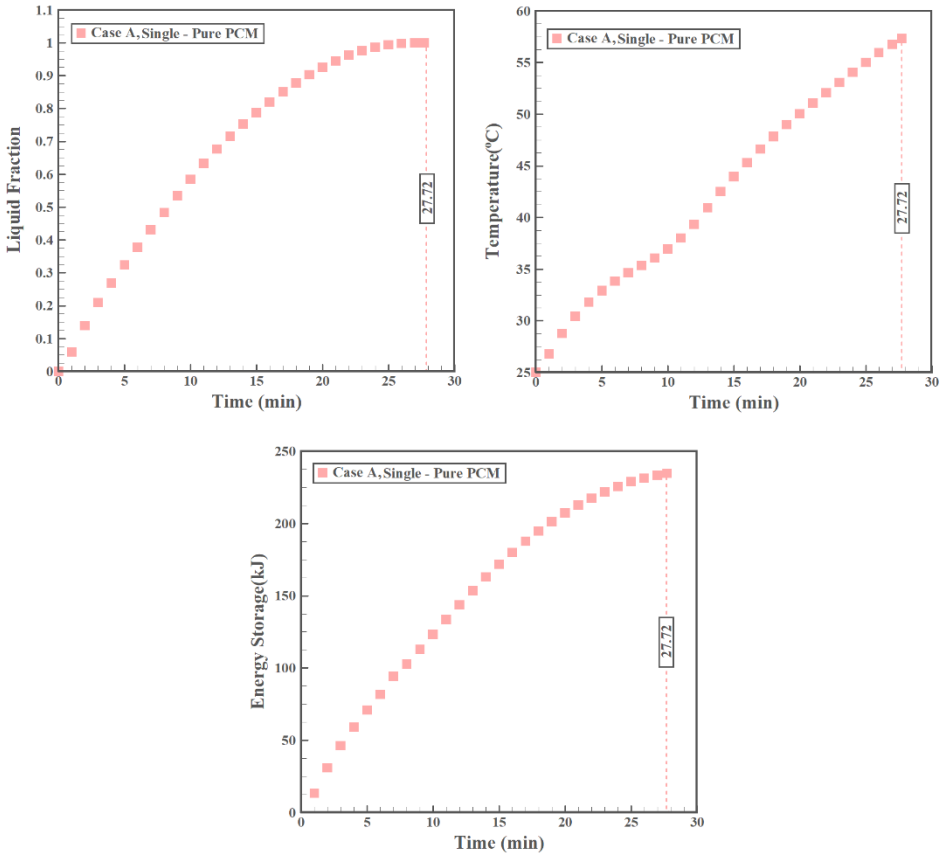

Fig. 2.4. Case A-Pure PCM during melting (charging) process: liquid fraction (top-left), PCM-averaged temperature (top-right) and energy stored (bottom)

During the melting process, there are solid and liquid regions, and their proportions vary according to the liquid fraction evolution shown in **Fig. 2.4**. Also, the heat transfer mechanism in each region is different. In a solid region, there is only conduction heat transfer where the temperature of PCM increases by conduction heat transfer from its initial temperature to the melting point of PCM. The temperature then stabilizes because most of the PCM faces phase change. In the liquid phase, natural convection heat transfer becomes more important as the process progresses, and temperatures increase mostly everywhere if most of the PCM is melted. This effect is enhanced with the expansion of the melting zone, natural convection becomes more intense. Liquid fraction and temperature contours for Case A-Pure PCM-Single PCM at shown at 5, 15 and 25 minutes in **Fig. 2.5** and **Fig. 2.6**. The represented cross-sections are chosen at distances 0.0, 0.5, 1.0, 1.5 and 2.0 m from the HTF entrance section, that is located at the right-top of the channel (see **Fig. 2.1b**). It

is shown that the PCM around HTF internal and external boundaries along the flow direction melts uniformly along the periphery because of its direct contact with the HTF. With conduction heat transfer, the liquid PCM around the heat transfer fluid and the top surface is impacted by HTF too. Buoyancy effects are becoming more important as the melting process advances as happens at 15 minutes and 25 minutes, making both liquid fraction and temperature distributions to be less homogeneous. This process is performed at a higher speed in the upper zone. When the heat reaches the pipe, the phase changing in the unit continues from the bottom area. With references to various sections represented, it is clear that higher temperatures and melting fraction are achieved at the entrance section (see **Fig. 2.1b**) because the inlet HTF temperature is assumed to be constant and equal to 60 °C.

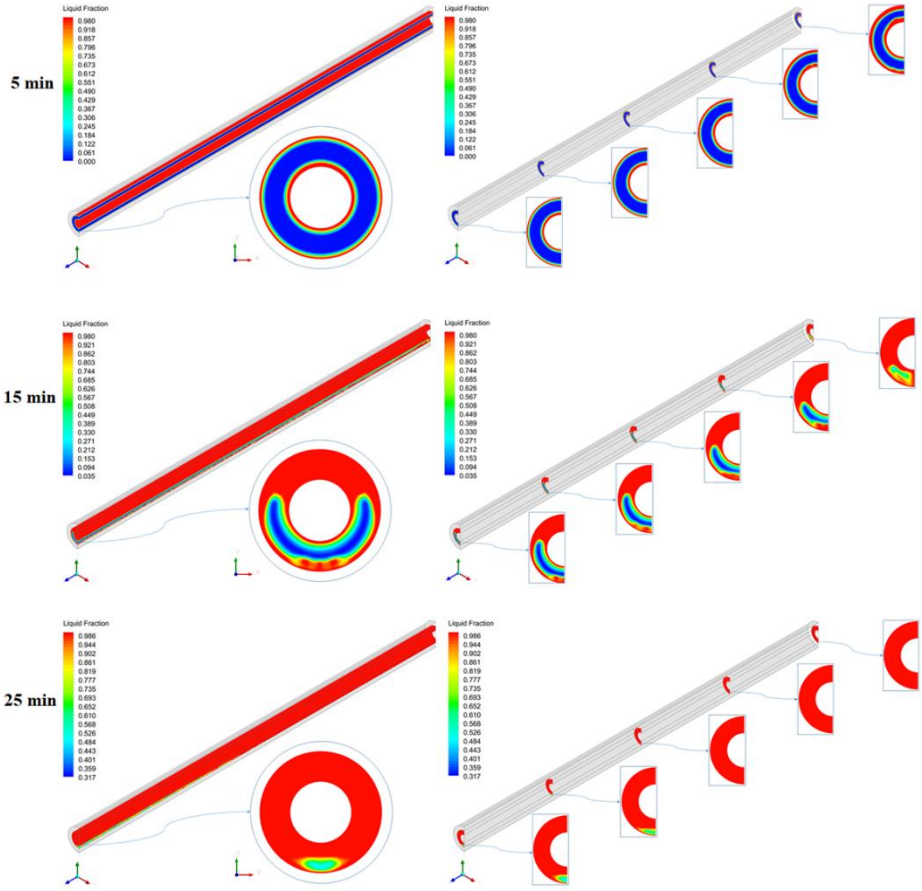

Fig. 2.5. Liquid Fraction fields for Case A-Pure PCM-Single PCM at different times: 5 minutes (top), 15 minutes (middle) and 25 minutes (bottom)

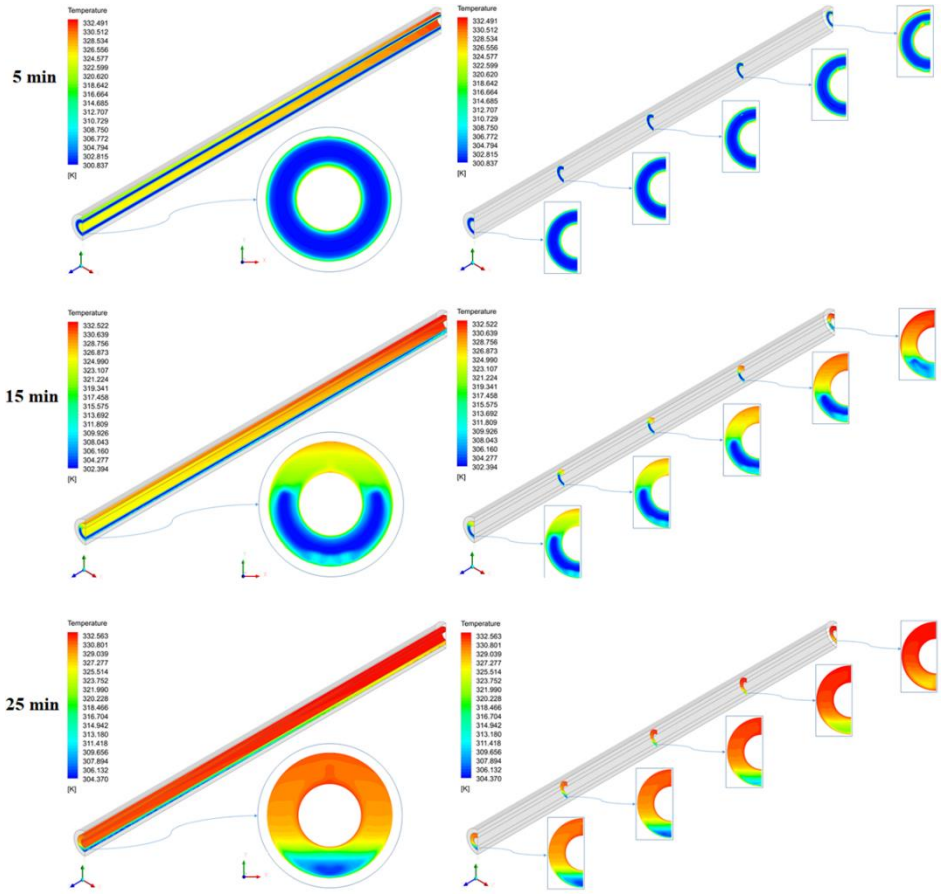

Fig. 2.6. Temperature fields for Case A-Pure PCM-Single PCM at different times: 5 minutes (top), 15 minutes (middle) and 25 minutes (bottom)

2.5.1.2 Case A-NEPCM

Comparisons between liquid fraction, PCM-averaged temperature, and energy stored between Case A-Pure PCM and Case A-NEPCM is shown in **Fig. 2.7**, where volume percentage for the NEPCM is assumed to be 5%. Temperature graphs show that NEPCM configuration here provides similar temperatures with a slight reduction in terms of melting time, say 3.35%. However, from the figures it is shown that even if the melting time is slightly smaller, the amount of stored heat in the PCM without nanoparticles is higher but later it will be shown that the velocity at which heat is stored has an opposite trend, making NEPCM performing better than pure PCM. The amount of the stored energy during the melting process can be defined by calculating

the energy transferred from the hot lateral walls to the cold phase change material during the heating process, as previously shown in Eq. 26. The total energy stored increases during the period of time, and also the total energy stored decreases up to the 0.0–0.5% nanoparticles variation in the mass fraction in RT35. This may happen due to the less temperature difference in radial and axial direction during the charging process, and to the requirement of less charging time in the case of 0.5% CuO nanoparticles based NEPCM.

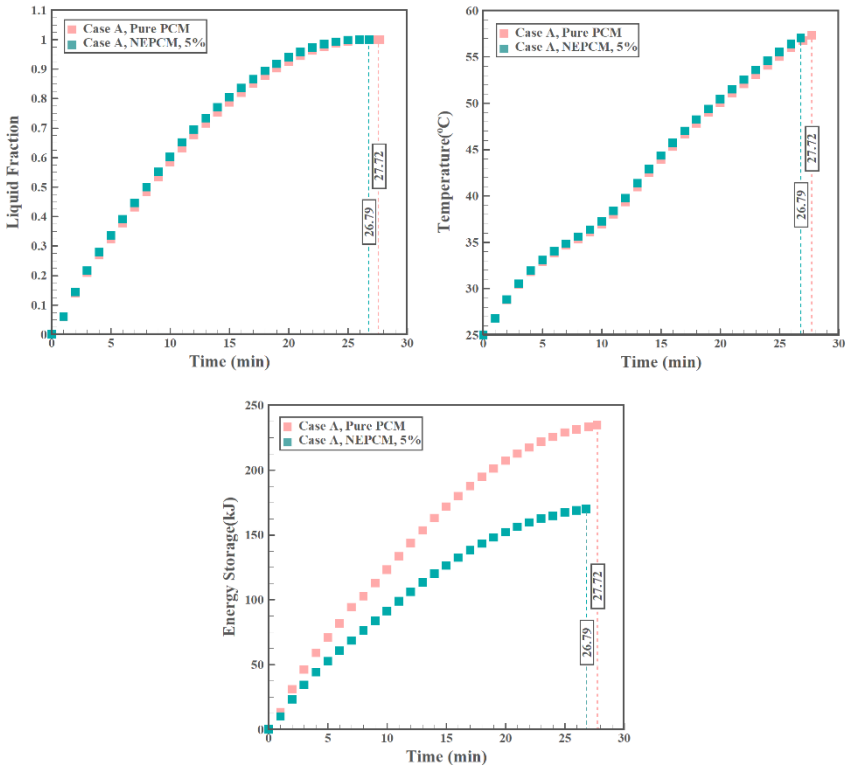

Fig. 2.7. Case A-Pure PCM vs Case A-NEPCM during melting (charging) process: liquid fraction (top-left), PCM-averaged temperature (top-right) and energy stored (bottom)

2.5.1.3 Case A-PCM/Metal Foam (Aluminum foam)

The effects of employing metal foams for case A are here presented. Here, three distinct porosities of $\varepsilon = 0.98$, $\varepsilon = 0.95$, and $\varepsilon = 0.92$ are employed at equal PPIs (say, 10) because it has been shown through the years that porosity has a higher effect than PPIs [57, 73]. **Fig. 2.8** (top) illustrates comparison in terms of liquid fraction evolution between Case A-Pure PCM and Case A-PCM/Metal Foam with different porosities. It is shown that melting time changes

remarkably with porosity (**Fig. 2.8**, bottom) mainly because less porosity means more metal to enhance overall thermal conduction. Full melting time of metal foam/PCM with ε = 0.98 and ε = 0.95, and ε = 0.92 is 2.59%, 39% and 43%, respectively less than that of Case A-Pure PCM. The reason why this enhancement is not linear is that overall conduction increase with lower porosity is not linear, as shown in [13].

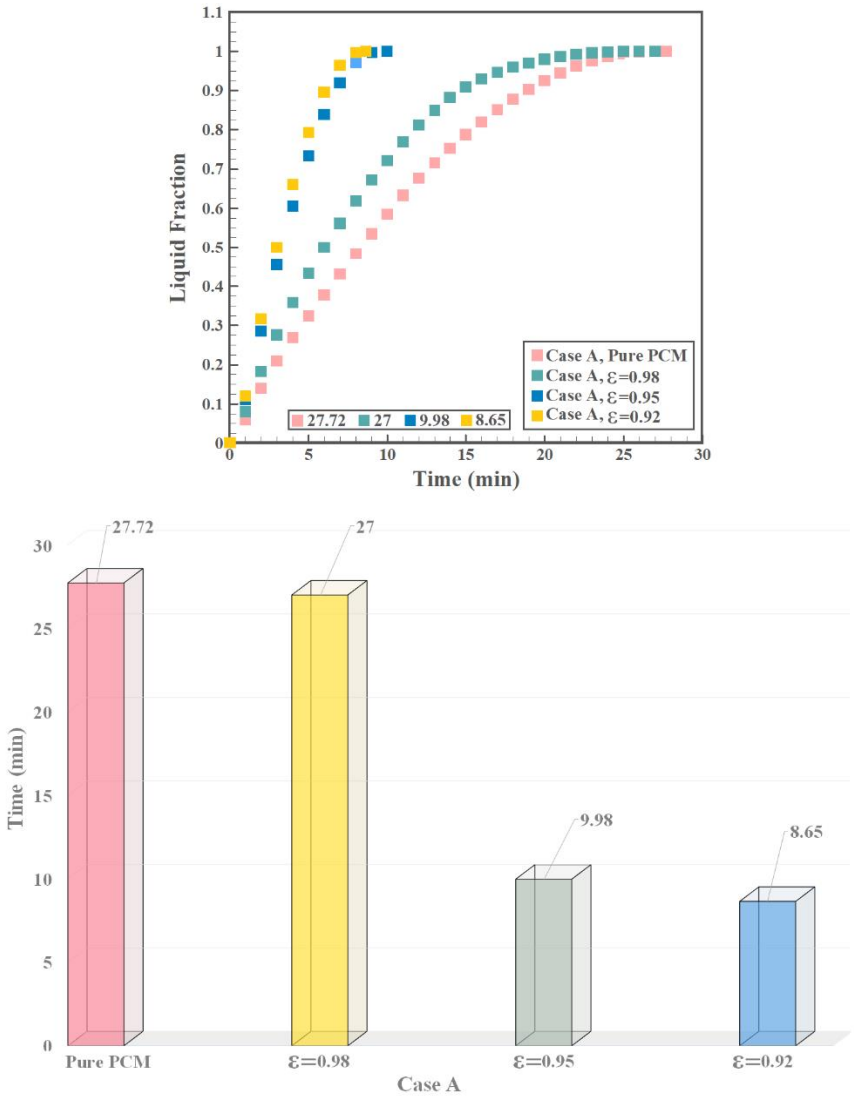

Fig. 2.8. Effects of porosity on instantaneous liquid fraction Case A-Pure PCM and Case A-PCM/Metal Foam

Comparisons between Case A-Pure PCM and Case A-PCM/Metal Foam are shown in **Figs. 2.9** and **Fig. 2.10** in terms of liquid fraction and temperature fields after 5 min. With references to the melting fraction at t = 5 min, one can notice that results are similar between pure PCM and ε = 0.98; on the other hand, ε = 0.95 and ε = 0.92 present similar distributions, in particular showing lower melting fractions compared to the previous two ones. This because lower porosities promote melting fraction due to the increased conduction as already mentioned before for **Fig. 2.8**. Because of the overall increased thermal conductivity, compared to paraffin without aluminum foams, temperature distributions in paraffin with aluminum foams are more homogenous, especially for lower porosity. This is similar to what has been shown in Mancin et al. [37], who showed a drastic reduction in the wall temperature when foams are employed. As a result, using aluminum foam flavored with paraffin facilitates heat transfer and increases the melting point of paraffin. **Fig. 2.10** demonstrates temperature contours for pure PCM and metal foam/PCM composite melting with porosities of 0.98, 0.95, and 0.92 computed at the outlet cross-section after 5 min. It can be understood that the temperature of metal foam/PCM composite is higher than that of pure PCM. Also, it shows that inserting copper foam in the base PCM diminishes the thermal stratification and creates uniform temperature distribution in metal foam/PCM. Finally, as shown in **Fig. 2.6**, sections closer to the HTF entrance (**Fig. 2.1b**) present higher temperatures and higher melting fraction because HTF inlet temperature is constant and higher to 60 °C. This aspect is recurrent in all the cases that we have represented in the present manuscript.

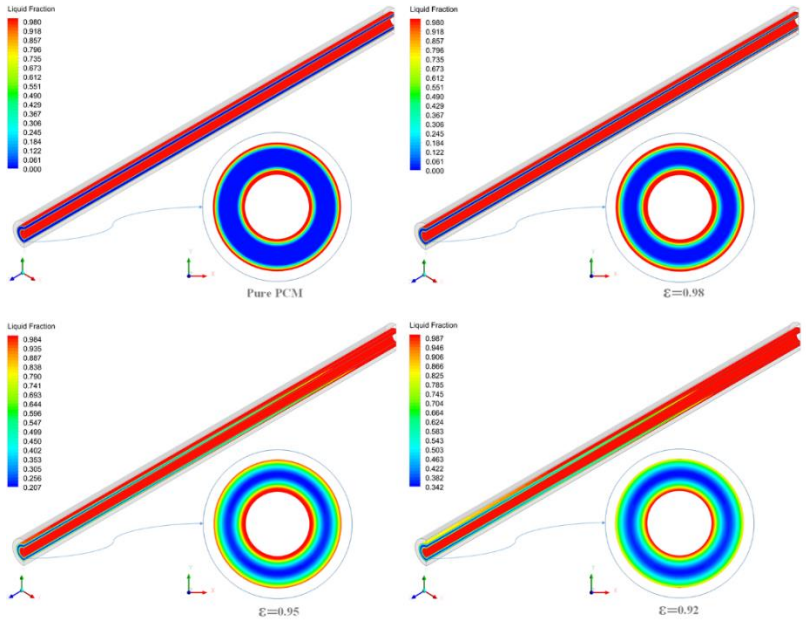

Fig. 2.9 Liquid fraction fields for Case A-Pure PCM and Case A-PCM/Metal Foam for different porosities after 5 minutes

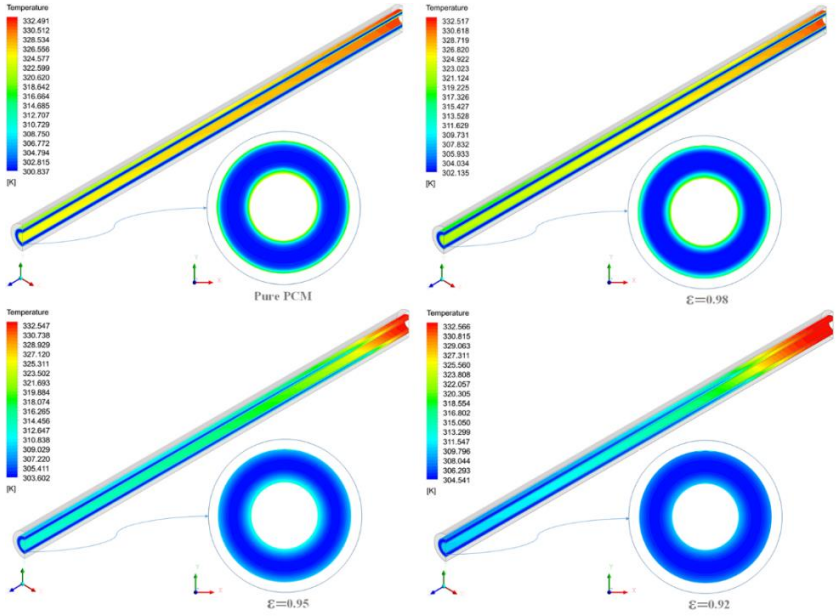

Fig. 2.10 Temperature fields for Case A-Pure PCM and Case A-PCM/Metal Foam for different porosities after 5 minutes

2.5.1.4. Case A-NEPCM/Metal Foam

Melting time and stored energy for case A referred to pure PCM and various configurations that include NEPCM, PCM/Metal Foam and NEPCM/Metal Foam within a TTHX, where volume fraction of NEPCM is 5%, are shown in **Fig. 2.11**. Stored energy is here computed after 5 minutes for the sake of comparison. The bar chart shows that the insertion of NEPCM-Metal Foam causes a remarkable enhancement of the melting (charging) rate with references to required time. With references to the stored energy, it is shown that in general the pure PCM configurations provide the lowest values, together with cases with $\varepsilon = 0.98$. When comparing PCM/foam with NEPCM at $\varepsilon = 0.95$ and $\varepsilon = 0.92$, the figure shows that the highest amount of energy is stored for the PCM system, while the lowest occurs if NEPCM is employed. This happens because NEPCM has a lower energy storage capacity due to its thermophysical properties. On the other hand, we have also to consider that we are constraining here the stored energy time in the figure (say, 5 minutes), at which some solutions are prone to reach complete melting, while other ones are just at the beginning of the melting process. When compared to the same PCM volume, the nano-PCM has a lesser energy released capacity but takes less time to deliver the highest demand thermal energy released. At the specific time ($t = 5$ min), as indicated in **Fig. 2.11**, the liquid fraction values for nano-PCM were lower than those for pure PCM.

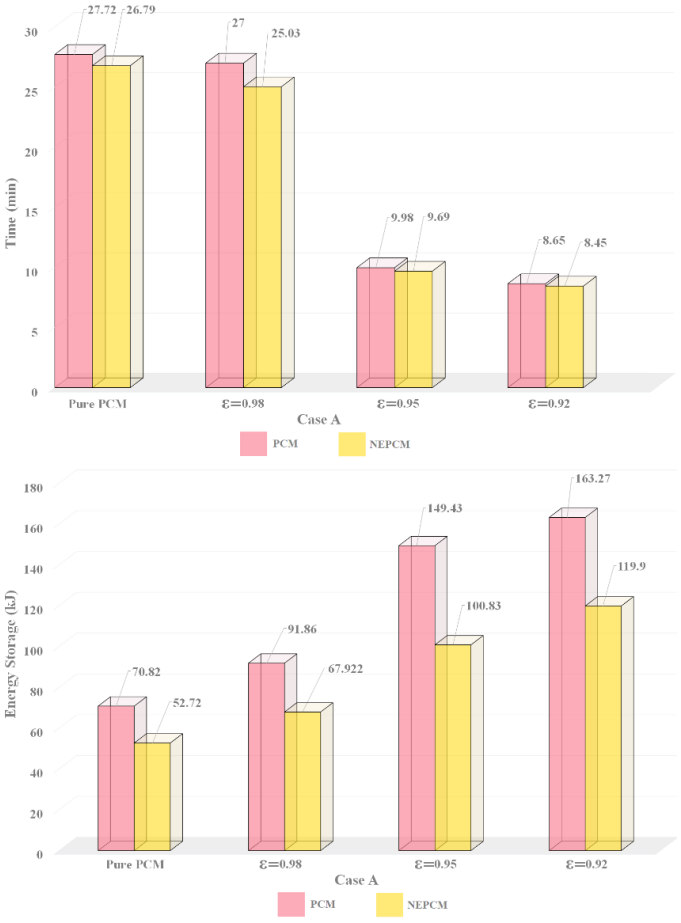

Fig. 2.11. A comparison between various solutions (Case A) that consider pure PCM or NEPCM, or foams with different porosities ε, in terms of liquid fraction (top) and stored energy (after 5 minutes) Pure PCM, NEPCM, PCM/Metal Foam, and NEPCM/Metal Foam

A resume of melting time, time-saving compared with reference pure PCM case, and heat storage rate p_L computed via Eq. 26, is shown in **Table 2.4**. Note that here the average storage heat rate is always computed from the stored energy previously shown in **Fig. 2.11**, where time at the denominator is the melting time that depends on the single computed case. The heat storage rate is significantly higher for the PCM/foam cases compared with the pure PCM case, especially for lower porosities. The average storage heat rate for ε = 0.92 is almost 2.4% and 12.9% higher than ε = 0.95 and 0.98, respectively. Finally, we saw that the heat storage rate for the NEPCM is slightly higher than that of

PCM. This means that foams are the primary reason of thermal behavior improvement, but NEPCM could give a boost too.

Table. 2.4. A resume of melting time and average storage heat rate for PCM and NEPCM by including Metal Foams (MF) too

	PCM			**NEPCM**		
	Melting Time	**% Time Saving Compared with Pure PCM**	**Heat storage rate (p_L), Eq. 26**	**Melting Time**	**% Time Saving Compared with Pure PCM**	**Heat storage rate (p_L), Eq. 26**
Case A-Without MF	1663 s	0	419.9	1607 s	-3.35	434.5
Case A-With MF ($\varepsilon = 0.98$)	1580 s	-4.97	431.1	1503 s	-9.63	465.1
Case A-With MF ($\varepsilon = 0.95$)	599 s	-63.99	1166	581.5 s	-65.04	1201
Case A-With MF ($\varepsilon = 0.92$)	519 s	-68.80	1346	507 s	-69.512	1377

2.5.2. Case B-Multi-layer PCM

2.5.2.1. Case B-Pure PCM

In this subsection, Case B will be investigated. We consider the effects of employing a multilayer PCM, *i. e.* PCMs with different melting points. A comparison between pure PCM (Case A-Pure PCM with results from here Case B-Pure PCM, denoted also as RT42/RT31/RT42 to denote different melting points for the PCMs) is reported in **Fig. 2.12** in terms of liquid fraction evolution, PCM-averaged temperature and liquid fraction achieved when one of the layers reach melting in the multilayer configuration. We underline here that PCM employed as the pure PCM is RT35 that present a temperature that is the average of melting temperatures of the multilayer cases, say 31 °C and 42 °C. From the figures, it is shown that liquid fraction evolution is slower for the multilayer because local temperature are less prone to the HTF temperatures, while they approach to the same time value, *i. e.* melting time, at the end. This happens by maintaining lower temperatures for the multilayer (see **Fig. 2.12**

top). From **Fig. 2.12** at the bottom, is shown that when the middle layer is completely melted (liquid fraction equal to 100%), inner and outer layers are 84.2% and 90.6% melted, respectively.

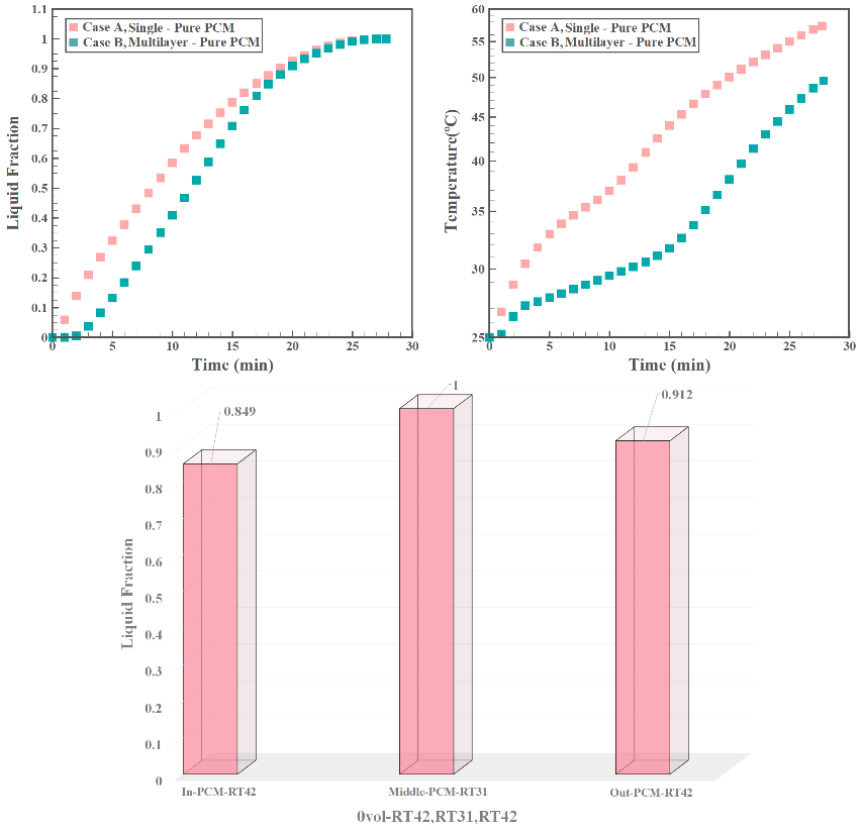

Fig. 2.12. Comparison between Case A-Pure PCM and Case B-Pure PCM in terms of liquid fraction (top-left), PCM-averaged temperature (top-right) and liquid fraction for multilayer at melting time (bottom)

Liquid fraction and temperature fields at 15 minutes are shown for Case B-Pure PCM in **Fig. 2.13**. Cross-sections are presented distanced each other of 0.5 m. Due to the buoyancy effects, some natural convection occurred in the PCM domain after the first sections, especially in the middle top of the domain and close to the entrance section (see **Fig. 2.1b**) because of the larger temperature gradients. Therefore, in addition to the melting in the near-wall region, natural convection helps PCM melting by circulating the liquid PCM. As shown in the temperatures fields plots on the right figure, the dominating natural convection shows a higher temperature at a fixed point on the top portion, while poor conduction causes a weak temperature increase at a point in the bottom portion,

that is the symmetric of the highest temperature point, when heated from the side.

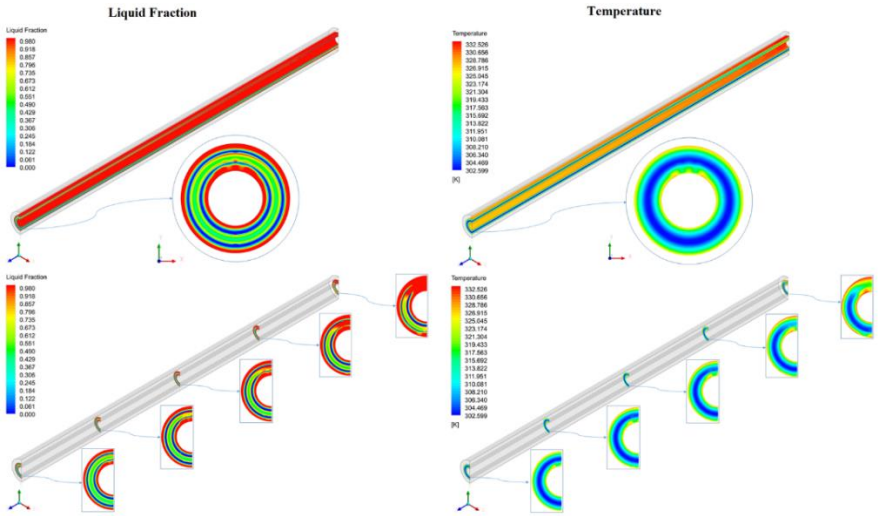

Fig. 2.13. Liquid fraction (left) and temperature fields (right) for Case B-Pure PCM at 15 minutes

Comparisons in terms of liquid fraction and temperature profiles between pure PCM (Case A-Pure PCM) and multilayer PCM (Case B-Pure PCM) are respectively presented in **Figures 2.14a** and **2.14b**, respectively obtained after 5 and 15 minutes. For t = 5 min, the heat transfer from the hot fluid HTF to both sides of the PCM results in melting from the inside and the outside. As a result, it moves like a ring with uniform melting on both sides. This doesn't happen at all in the Case B because of the different melting temperatures of the PCM investigated. After 15 minutes, as this process continues, the effect of heat transfer to the middle parts of the PCM will decrease while natural convection in the molten areas will increase. Then, as the upper PCM melts, gravity gradually dominates and the lower PCM becomes liquid, making natural convection effects relevant too. As shown in the figure, in the melting process of the PCM, due to heat transfer from both sides, the middle part of the PCM is the last place to be melted. Multilayer PCM concept is based on this, since two PCM concentric layers along with keeping mean melting properties the same were replaced to be tested due to the lower melting temperature in the middle and the expectation of faster melting. Despite the strengthening of the middle part melting, in the end, the melting time could not be less than a Case A with a single PCM layer, as previously shown in **Fig. 2.12**. According to the results, this is due to the presence of multilayer PCM walls. These walls provide more

or less the same melting time (see **Fig. 2.12**) by preventing uniform heat transfer and reducing the effect of liquid PCM free movement, which has the greatest effect on the melting process. That is, a triplex-tube heat exchanger with three layers of PCM has a similar performance at fixed melting time but the advantages of more uniform melting and reduced achieved temperatures too, as previously reported in **Fig. 2.12**.

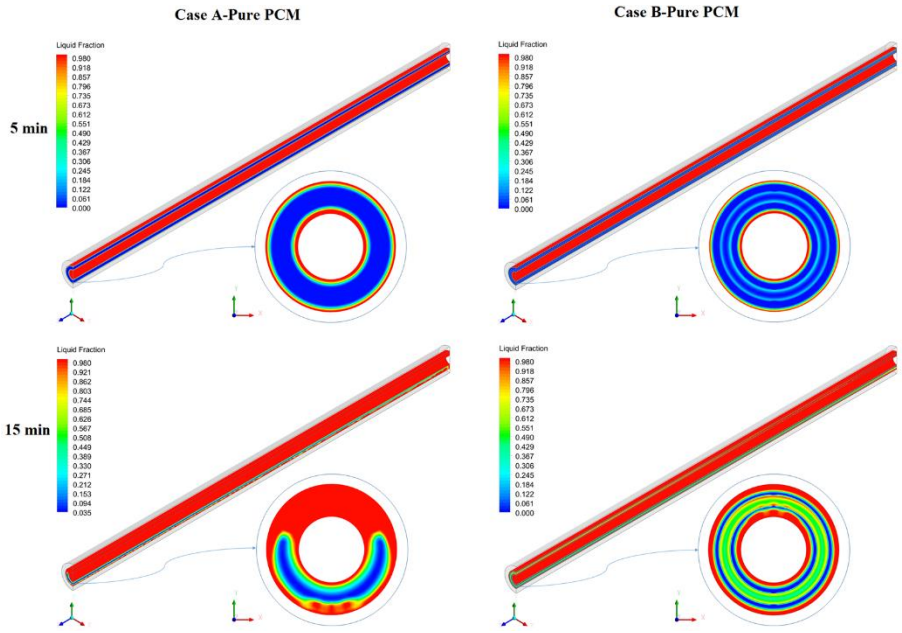

Fig. 2.14.a Liquid fraction fields at 5 (top) and 15 (bottom) minutes for Case A-Pure PCM (left) and Case B-Pure PCM (right)

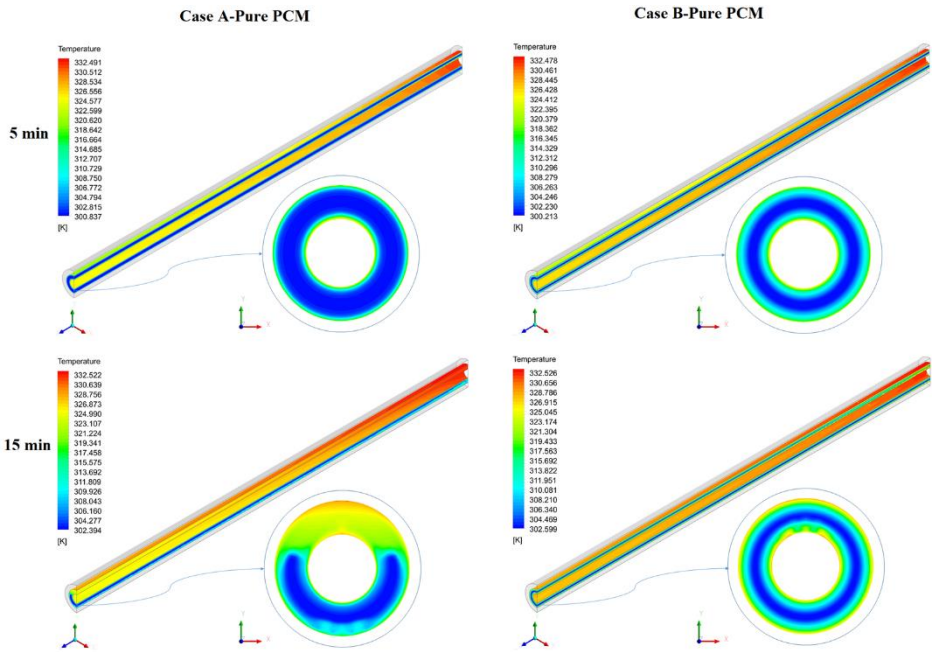

Fig. 2.14.b Temperature fields at 5 (top) and 15 (bottom) minutes for Case A-Pure PCM (left) and Case B-Pure PCM (right)

2.5.2.2. Case B-NEPCM

Comparisons between Case A-NEPCM and Case B-NEPCM are presented in terms of melting time in Figure **2.15**. In the same figure, cases without NEPCM are shown too for the sake of comparison. In the figure, it is shown that Case B present slightly lower melting time, especially when NEPCM is used. In particular, melting time passes from 26.72 to 25.96 minutes.

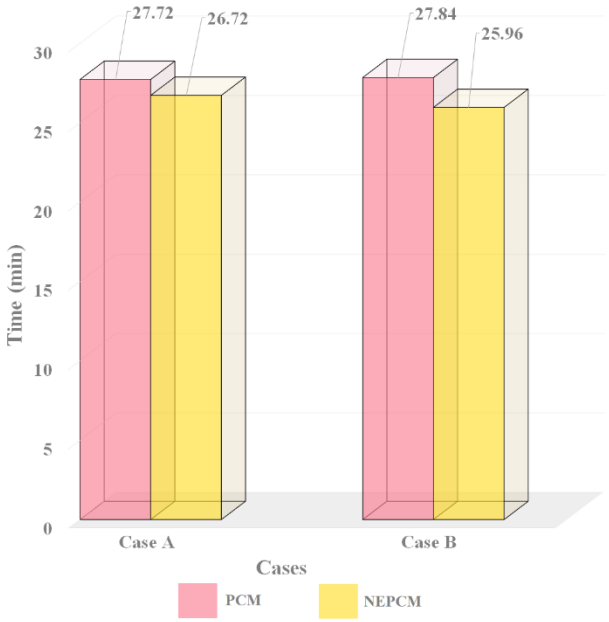

Fig. 2.15. Comparison in terms of melting time between Case A and Case B with references to pure PCM and NEPCM

2.5.2.3. Case B-PCM/Metal Foam

In this subsection, comparisons between Case A and Case B by considering metallic foam for the case B are presented. When a metal foam is employed in the multilayer system, it is also considered here that foam layers could have different porosities too. Since the core of the middle-PCM is far from the heat that comes from the inner and outer boundary surfaces, we employ here for this case a lower porosity foam in the core of the multi-layer PCM to promote conduction where this is weaker. Liquid fraction and temperature after 5 minutes for Case B-Pure PCM and Case B-PCM/Metal foam are shown in **Figure 2.16**. Foam layers are assumed to respectively have porosities of 0.98, 0.92, and 0.98 from the inner to the outer boundary surfaces. Due to the higher rate of heat transfer in the PCM/ Metal foam case, PCM melts more quickly and melting fraction looks generally higher. Even if the porosity is smaller in the core, melting should also start in the core region even if liquid fraction values are higher than that of pure PCM. For example, after 5 min, the liquid fraction of the PCM at the center of the unit is almost 0.30, while it is 0.00, say solid phase, for the pure PCM case, which means that the heat is not transferred to the center of the domain. For both systems, the temperature is almost uniform because of the multi-layer configuration.

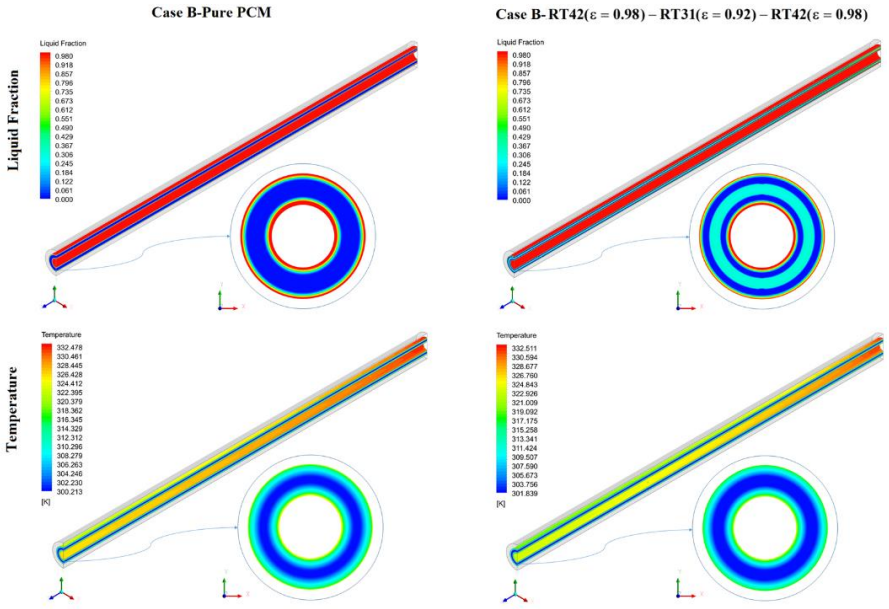

Fig. 2.16. Liquid fraction (top) and temperature (bottom) fields after 5 minutes for Case B-Pure PCM (left) and Case B-PCM/Metal Foam (right)

2.5.2.4. Case B-NEPCM/Metal Foam

Finally, the Case B-NEPCM/Metal Foam is modeled by considering NEPCM together with Metal Foam. Again, NEPCM is assumed to have a 5% volume fraction as always done here, while metal foam presents 0.98, 0.92 and 0.98 porosity samples for each layer like as done in the previous subsection. A comparison in terms of melting time for various configurations, say all the Case B configurations here shown until now, is presented in **Fig. 2.17**. In the same figure, liquid fraction when the middle layer reaches melting is shown.

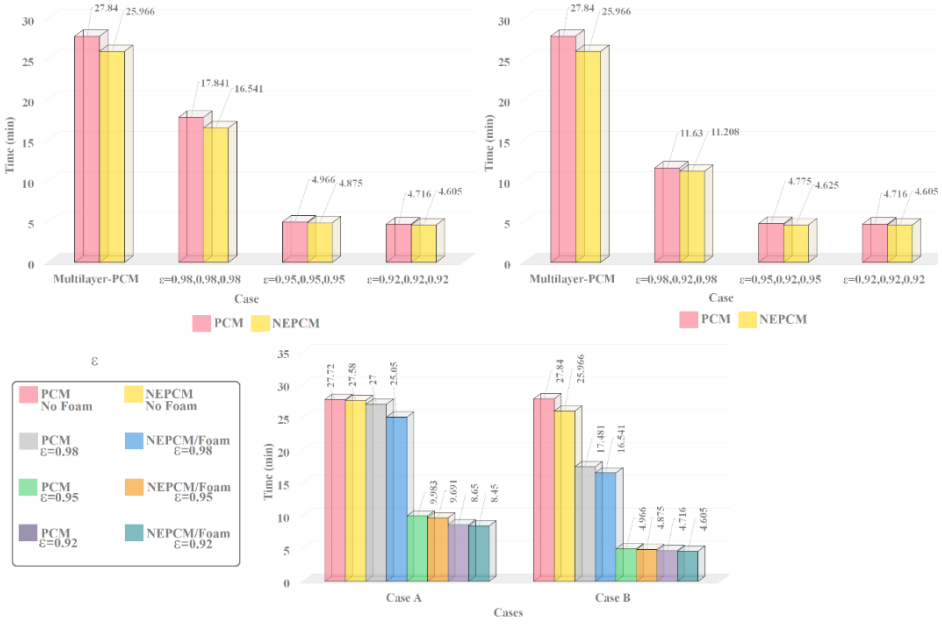

Fig. 2.17. The comparison of the melting time bar chart for the Case A and Case B TTHX with nanoparticle and metal foam with various porosities

Even if configurations with different foam layers have been previously presented by assuming the smallest porosities in the foam core, computations by moving such foam layers in different positions have been presented too here. Therefore, based on these simulations and on the simulations before presented for Case B, **Table 2.5**, and **Table 2.6**, summarizes melting times, percentage of time-saving compared to the pure PCM unit, and the amount of stored energy on the PCM in the melting process. Multi-layer PCM is also labelled here as RT42/RT31/RT42 to underline melting temperatures employed for each PCM layer. The rate of heat storage is significantly higher for the PCM/Metal Foam cases compared with the pure PCM unit with no foam. Furthermore, reducing the porosity results in an increase of heat transfer rate and therefore higher heat storage rate is achieved. It should be noted that, by reducing the porosity and the existence of more metals in the domain, a higher rate of heat transfer occurs which also results in a shorter melting time. On the other hand, by reducing porosity and therefore reducing the available PCM volume, the dimensions of the unit should be increased to have a similar PCM mass in different cases for the meaningful comparison which results in a higher melting time. However, due to the significant advantages of high conductivity metal foams rather than a small enhancement in the storage size, by reducing the porosity, the melting time should always decrease as widely known. When comparing different

porosities, one can see that lowering the porosity leads to a greater heat transfer rate, which results in a shorter melting time and hence a higher heat storage rate. These findings demonstrate the extraordinary impact of employing metal foam during PCM melting, which considerably improves efficiency depending on the application.

Table. 2.5. Melting time for different configurations investigated for the Case B, where porosity values for each layer are shown starting from the inner surface of the tube

Middle PCM	**PCM**		**NEPCM**	
	Melting Time	**Time Saving Compared with Pure PCM**	**Melting Time**	**Time Saving Compared with Pure PCM**
Multi-Layer/No Foam	1671 s	0	1558 s	-6.74 %
Multi-Layer/0.98/0.92/0.98	698 s	-58.22 %	672 s	-59.74 %
Multi-Layer/0.95/0.92/0.95	287 s	-82.85 %	278 s	-83.39 %
Multi-Layer/0.92/0.92/0.92	283 s	-83.06 %	276 s	-83.46 %
Multi-Layer/0.98/0.98/0.98	1070 s	-35.92 %	992 s	-40.59 %
Multi-Layer/0.95/0.95/0.95	298 s	-82.16 %	293 s	-82.49 %

Table. 2.6. Stored energy after 5 minutes for different configurations investigated for the Case B, where porosity values for each layer are shown starting from the inner surface of the tube

	PCM	**NEPCM**
	Stored Energy (kJ) at 5 minutes	**Stored Energy (kJ) at 5 minutes**
Multi-Layer/No Foam	27.25	21.05
Multi-Layer/0.98/0.92/0.98	74.15	46.74
Multi-Layer/0.95/0.92/0.95	194.37	139.57
Multi-Layer/0.92/0.92/0.92	197.23	146.57
Multi-Layer/0.98/0.98/0.98	51.31	46.059
Multi-Layer/0.95/0.95/0.95	193.69	138.51

2.5.3. Case C-Single PCM

2.5.3.1. Case C-Pure PCM

Case C, that is the case in which fins are included to enhance thermal conduction in the PCM-TTHX system, is presented here and compared too with Cases A and B. Liquid fraction and PCM-averaged temperature evolution for Case C-Pure PCM are presented together with the results previously achieved for Case A and Case B in **Figure 2.18**. The results show that when fins are added to the TTHX has happen in Case C, the unit efficiency improves in terms of liquid fraction at equal time, reaching also slightly higher temperatures because a larger amount of PCM is melted. Similar observations about higher temperatures achieved due to PCM melt have been discussed previously for Case A. As it can be observed in **Figure 2.18**, after installing fins in the TTHX, melting time decreases by 18.10% compared to case A. Case C presents higher temperatures because there is liquid PCM in the domain that cause temperatures increase.

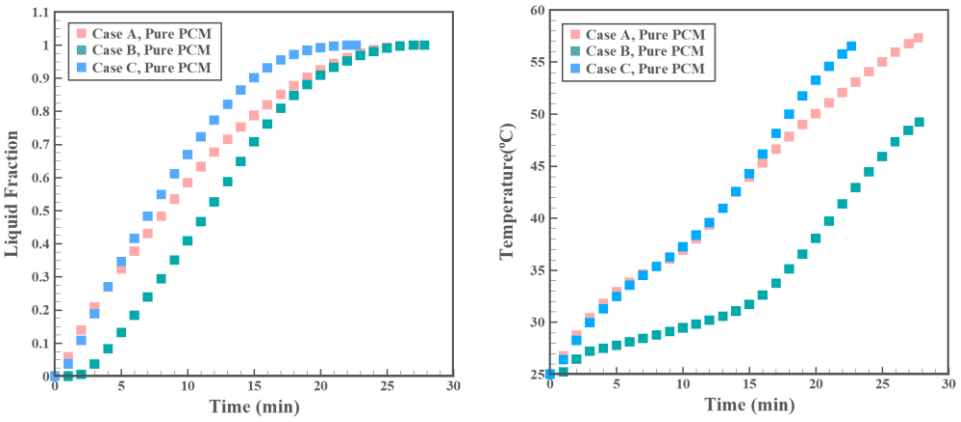

Fig. 2.18. Liquid fraction (left) and PCM-averaged temperature evolution (right) for Cases A, B and C with pure PCM

Case C liquid fraction and temperature fields at different sections, say each computed with a distance of 0.5 m from the previous one, are presented in **Figure 2.19** after 5 (top) and 15 minutes (bottom). As can be noticed in **Figure 2.19**, the thermal conduction in the proximity of the HTF tubes makes the PCM melting uniformly, especially at 5 minutes. As time passes, say after 15 minutes, the effect of fins increases and the uniformity which existed in the initial minutes of the process disappears, while the melting is faster in the top section of the triplex pipe. After the PCM in the top half of the HX melted, the

melting continues at the bottom half of the TTHX. With references to different sections along the HTF direction, it is noticed that the last sections referred to the HTF exit (see **Fig. 2.1b**) generally present lower temperatures because they are influenced by the HTF distribution, that presents lower temperatures at the end of the channel (bottom part of each channel represented) since we assumed that HTF inlet temperature is 60 °C. Similar qualitative observations can be done for the melting fraction presented at the top of **Figure 2.19**.

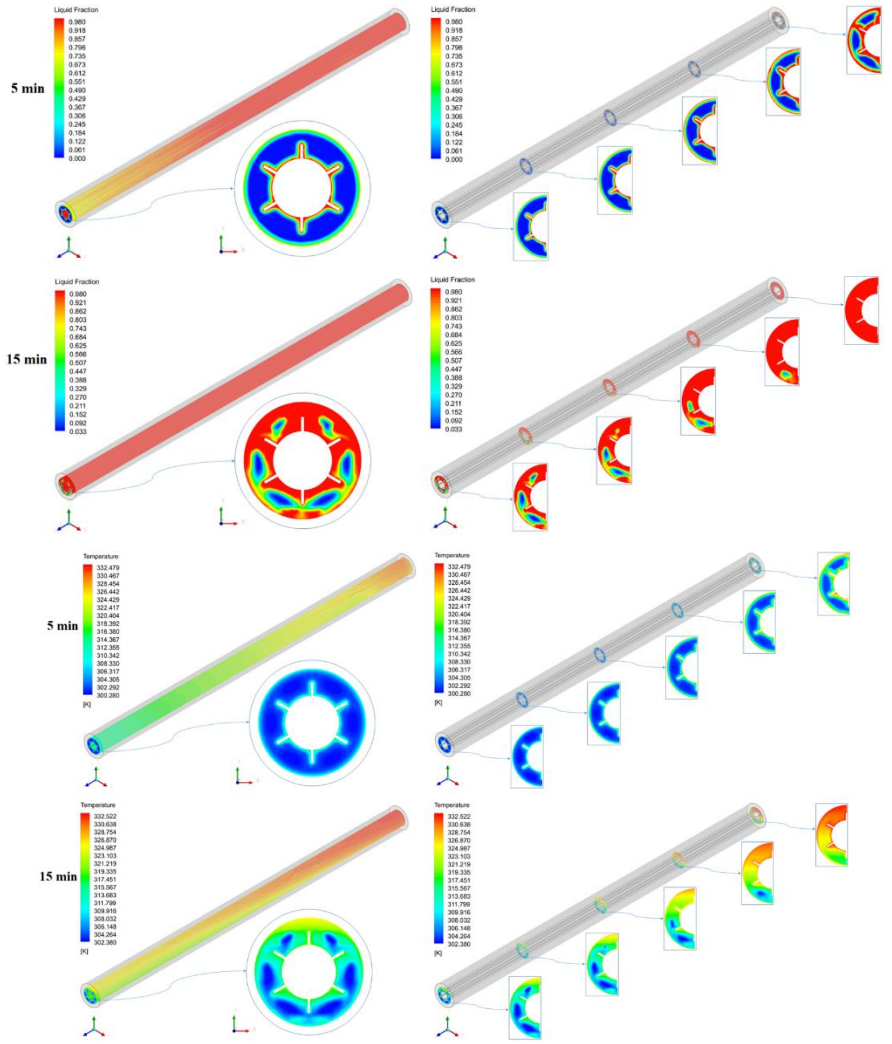

Fig. 2.19. Liquid fraction (top figures) and temperature (bottom figures) at 5 minutes and 15 minutes for Case C-Pure PCM

2.5.3.2. Case C-Pure PCM/NEPCM/PCM-Foam/NEPCM

All the other cases that include PCM, NEPCM and Metal Foam, together with the combination between NEPCM and metal foam, are shown in this subsection. Melting time and stored energy for Case C, together with Case A and Case B, are presented for various configurations here investigated. With references to Case B, cases with porosities layers of ε = 0.95, 0.95 and 0.95, are presented in **Fig. 2.20**. It is generally shown that melting time is smaller for PCM/Metal Foam and NEPCM/Foam, making metal foams very useful to increase PCM thermal performances. With references to Case C, generally higher times have been found. This because when fins are employed the heat transfer enhancing effect caused by foams is not so relevant. Energy stored is presented too in the same figure. It is shown that Case C presents slightly higher stored energy when compared to Cases A and B pure PCM and multilayer PCM. On the other hand, Case C has smaller stored energy if we compare PCM/Metal Foam and NEPCM/Metal Foam systems with Cases A and B. This is also consistent with melting times previously shown since stored energy is computed at equal times (say, after 5 minutes).

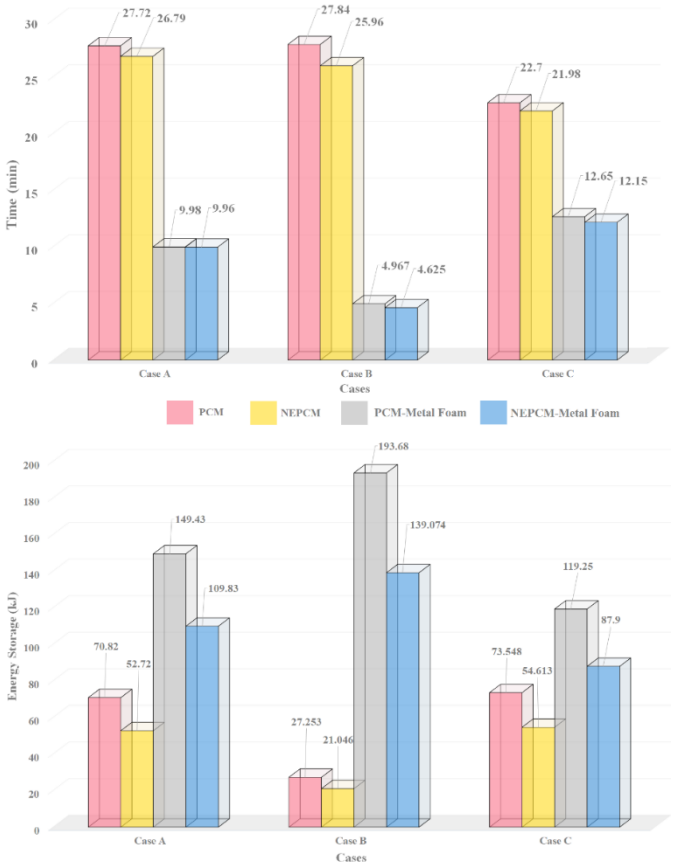

Fig. 2.20. Melting time (top) and energy stored (bottom) for Cases A, B and C including various solutions with PCM, NEPCM, PCM/Metal Foam (0.95), and NEPCM/Metal Foam (0.95)

Liquid fraction and temperature contours, after 5 and 15 minutes, are presented for Cases A, B, and C in **Figure 2.21** with pure PCM for the sake of comparison in order to appreciate what happens in cross-sections (HTF entrance section shown in **Fig. 2.1b**) for pure PCM cases. These plots show that the PCM generally melts uniformly when in contact with the HTF tubes. It can be found that the performance of the finned model (Case C) is slightly better than Case A and Case B because, with the addition of a finned surface, the contact surface with the PCM increases in both top and bottom sections of the TTHX, achieving a better temperature distribution in the TTHX. It was observed that the charging process in the top region of the system, is faster than that in the bottom part of the TTHX. This is due to the fins that cause faster melting in the top part of the TTHX by including some natural convection effects too. Considering the temperature contours in **Figure 2.21**, at first, the temperature

rise can be observed in all cases, but the temperature rise in the top half of the finned TTHX (Case C) is higher compared to the finless TTHX (Case A). The reason for such difference is the higher heat conduction because of the fins. After 15 minutes from the beginning of the melting process, a considerable portion of the PCM is melted and the temperature of the top half is still rising. In other words, in the top half of the TTHX, the heat is consumed for increasing the temperature, *i. e.* latent heat, while in the lower region it is used for melting the PCM, *i. e.* sensible heat.

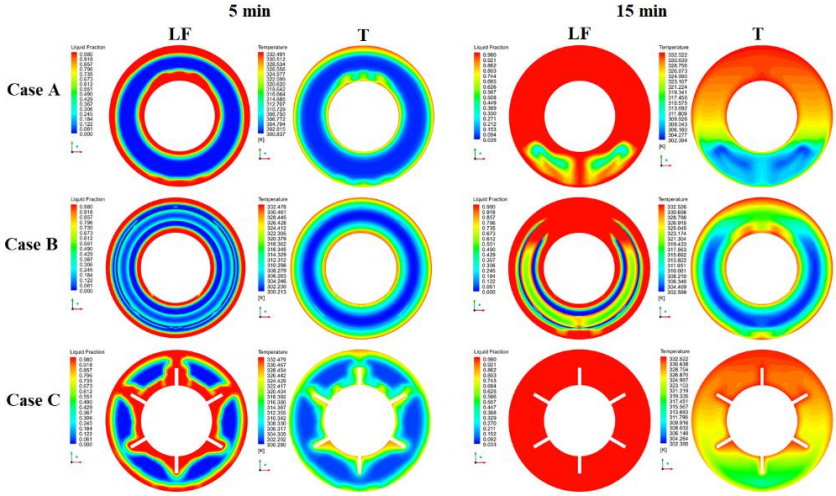

Fig. 2.21. Comparison among cases investigated in terms of Liquid Fraction (LF) and Temperature (T) at 5 and 15 minutes computed at the HTF entrance section depicted in **Fig. 2.1b**

Finally, in **Figure 2.22** a resume of all melting times reached in the present study under different configurations is presented. From this figure, we notice that the Case B shows lower melting temperatures when metal foams are employed. In particular, the shortest time is achieved with NEPCM/Metal foams if ε = 0.92 is employed (say, 276 seconds, i. e. 83.39% reduction compared to pure PCM for Case A). This means that employing a multilayer PCM is very important to optimize heat transfer here, and foams with NEPCM are very helpful too. With references to all the other single cases, it is shown that foams are in general the first cause of heat transfer enhancement, but NEPCM would be very helpful since they provide a further slight reduction in terms of melting time. For instance, if a 83.39% reduction is assumed for the NEPCM/Metal Foam Case B with ε = 0.92, then without nanoparticles the reduction would still be 82.99%. This happens also for other cases; for instance, if we consider Case B at ε = 0.98, then with nanoparticles reduction is 40.35%,

while without nanoparticles this become 35.66%. This means that using nanoparticles is very helpful to further increase PCM/Metal Foam devices in this context. With references to finned surfaces (Case C), it is shown that pure PCM has better times, but on the other hand using metal foams and NEPCM would not have the same impact as for Cases A and B. From our results, which show that case B with both nanoparticles and foam provides the minimum melting time, say 276.3 s, we found a smaller melting time compared to similar studies on this topic from the literature like [5]. Mat et al. [5] investigated the melting process in a triplex tube heat exchanger with PCM with internal-external fins, where they found that the minimum melting time has been found to be about 50 minutes. This value is far larger than the minimum melting time found in this work by combining different solutions.

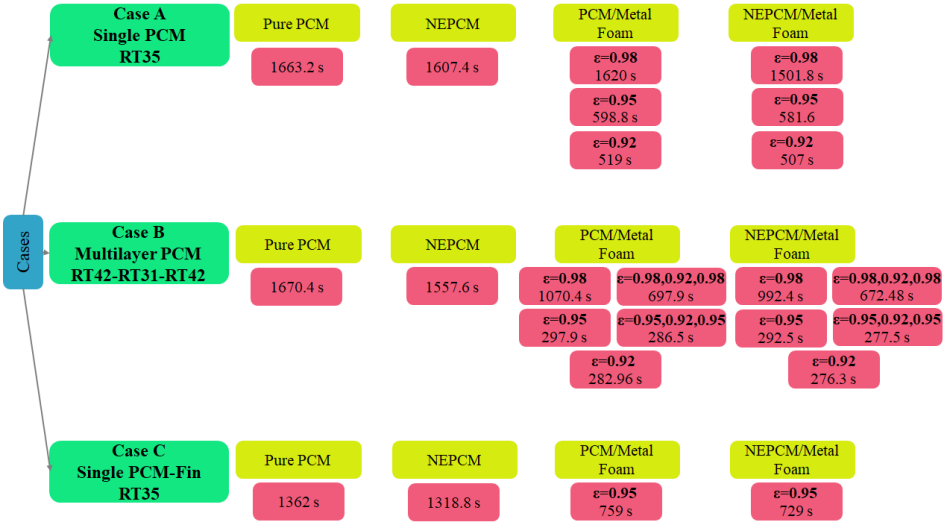

Fig. 2.22. Melting time for all cases

2.6. Conclusions

Thermal energy storage systems based on PCMs has a pivotal role in the domestic, household, and industrial sectors for water heating systems, and increasing their thermal performances with TTHX, metal foams, nanoparticles and finned surfaces is a very challenging task nowadays. In this work, a throughout numerical comparison of various thermal performances increase solutions for a TTHX for thermal energy storage has been presented, and also these solutions have been considered together to appreciate how this solution would increase thermal performances of these devices. To predict temperature, liquid fraction and stored energy, a 3D Local Thermal Non-Equilibrium

(LTNE) porous-media volume-averaged model is employed by considering nanoparticles together with the PCM in a single-phase equivalent medium, while water is considered as the working HTF. The model has been exhaustively validated with experimental data from literature under various conditions. PCM layers with different melting points have been proposed for the TTHX, together with aluminum foams with various porosities ranging from 92% and 98% and CuO nanoparticles with a fixed 5% volume percentage. Case A with pure PCM, Case B with Multi-layer PCMs and Case C with finned surfaces have been investigated by considering pure PCM with either metal foam or nanoparticles, and also pure PCM with a combination of metal foams and nanoparticles. The following findings were made from the results here derived:

- With the addition of nanoparticles with volume fraction of 5%, for Case A, Case B and Case C melting time is reduced of a 3.35%, 6.75%, and 3.17%, respectively, when compared to the TTHX pure PCM without nanoparticles and Metal Foam, since thermal conductivity in the PCM will be enhanced by adding nanoparticles.
- The addition of both nanoparticles and metal foam with porosities of 0.98, 0.95, and 0.92 in the Case A reduces the melting time of 9.70%, 65.04%, and 69.52%, respectively, when compared to the Case A with only pure PCM. The reason for this is that the use of nanoparticles and metal foam improves thermal conductivity in the PCM.
- The addition of nanoparticles to a multilayer-PCM has an effect on melting time. When nanoparticles were added to the TTHX (Case B), the melting times were cut by 6.3% compared to the TTHX (Case A) without them.
- Adding a Multilayer-PCM with the addition of nanoparticles and metal foam with a 0.92 porosity has a significant impact on reducing melting time. For example, in the TTHX (Case B), the inclusion of nanoparticles and metal foam reduced the melting durations by 83.39% compared to the TTHX (Case A) without NEPCM/Metal Foam.
- The installation of fins makes heat transfer easier. Adding a finned surface has a significant impact on reducing melting time. For example, in the TTHX (Case C) with pure PCM, adding a finned reduced the melting durations by 18.11% compared to the TTHX (Case A) with Pure PCM.
- Adding a finned surface together with the addition of nanoparticles and foam has a significant impact on reducing melting time. For example, in the TTHX (Case C), the inclusion of NPs with foam reduced the melting durations by 53.17% compared to the TTHX (Case A) without NEPCM. On

the other hand, melting time is reduced by 20.70% if we compared the TTHX (Case A) without NEPCM.

- All proposed methods to increase heat transfer have dramatically increased the rate of energy storage with significant reduction on the melting time. When compared to all cases where foam is the primary source of heat transfer enhancement, NEPCM/Metal Foam has a higher heat storage rate.

In conclusion, we can state that NEPCMs have a lower thermal energy storage capacity, but they take less time to eventually supply the peak thermal energy demand when compared to PCMs of the same volume because they present a larger heat storage rate. In addition, Multi-layer PCMs that considers nanoparticles and foam too, *i. e.* a NEPCM/Metal Foam, has a larger heat storage rate compared with all Cases, where foam is the first cause of heat transfer enhancement.

In the upcoming Chapter 3, the application of these methods will be intricately woven into the integration of solar systems, with a dedicated emphasis on optimizing latent heat energy storage capabilities throughout the diurnal cycle, encompassing both day and night periods. The overarching aim of this endeavor is to significantly augment the efficiency of the melting and solidification processes inherent in a PCM-based flat plate solar collector. This enhancement will be achieved through the strategic incorporation of advanced elements, including but not limited to metal foams, nanoparticles, and a distinctive wavy wall-Y shaped surface configuration. Moreover, as one of our principal objectives, we aspire to transcend the confines of singular applications. The intention is to establish a versatile framework, allowing the implementation of these refined methods across a spectrum of diverse applications. This holistic approach is geared towards addressing the evolving demands of various sectors, ranging from residential and industrial settings to broader energy storage and utilization initiatives, thereby contributing to the broader landscape of sustainable and efficient energy solutions.

References

[1] Yıldız Ç, Arıcı M, Nižetić S, Shahsavar A. Numerical investigation of natural convection behavior of molten PCM in an enclosure having rectangular and tree-like branching fins. Energy. 2020 Sep 15;207:118223.

[2] Yu C, Wu S, Huang Y, Yao F, Liu X. Charging performance optimization of a latent heat storage unit with fractal tree-like fins. Journal of Energy Storage. 2020 Aug 1;30:101498.

[3] Pizzolato A, Sharma A, Maute K, Sciacovelli A, Verda V. Design of effective fins for fast PCM melting and solidification in shell-and-tube latent heat thermal energy storage through topology optimization. Applied Energy. 2017 Dec 15;208:210-27.

[4] Abdulateef AM, Mat S, Sopian K, Abdulateef J, Gitan AA. Experimental and computational study of melting phase-change material in a triplex tube heat exchanger with longitudinal/triangular fins. Solar Energy. 2017 Oct 1;155:142-53.

[5] Mat S, Al-Abidi AA, Sopian K, Sulaiman MY, Mohammad AT. Enhance heat transfer for PCM melting in triplex tube with internal–external fins. Energy conversion and management. 2013 Oct 1;74:223-36.

[6] Sheikholeslami M, Keshteli AN, Babazadeh H. Nanoparticles favorable effects on performance of thermal storage units. Journal of Molecular Liquids. 2020 Feb 15;300:112329.

[7] Khodadadi JM, Hosseinizadeh SF. Nanoparticle-enhanced phase change materials (NEPCM) with great potential for improved thermal energy storage. International communications in heat and mass transfer. 2007 May 1;34(5):534-43.

[8] Mahdavi A, Moghaddam MA, Mahmoudi A. Simultaneous charging and discharging of multi-tube heat storage systems using copper fins and Cu nanoparticles. Case Studies in Thermal Engineering. 2021 Oct 1;27:101343.

[9] Mehrali M, Johan E, Shahi M, Mahmoudi A. Simultaneous solar-thermal energy harvesting and storage via shape stabilized salt hydrate phase change material. Chemical Engineering Journal. 2021 Feb 1;405:126624.

[10] Mol J, Shahi M, Mahmoudi A. Numerical Modeling of Thermal Storage Performance of Encapsulated PCM Particles in an Unstructured Packed Bed. Energies. 2020 Jan;13(23):6413.

[11] Minea AA, Buonomo B, Burggraf J, Ercole D, Karpaiya KR, Di Pasqua A, Sekrani G, Steffens J, Tibaut J, Wichmann N, Farber P. NanoRound: A benchmark study on the

numerical approach in nanofluids' simulation. International Communications in Heat and Mass Transfer. 2019 Nov 1;108:104292.

[12] Parsazadeh M, Duan X. Numerical study on the effects of fins and nanoparticles in a shell and tube phase change thermal energy storage unit. Applied energy. 2018 Apr 15;216:142-56.

[13] Mahdi JM, Nsofor EC. Melting enhancement in triplex-tube latent heat energy storage system using nanoparticles-metal foam combination. Applied energy. 2017 Apr 1;191:22-34.

[14] Sushobhan BR, Kar SP. Thermal modeling of melting of nano based phase change material for improvement of thermal energy storage. Energy Procedia. 2017 Mar 1;109:385-92.

[15] Naghavi MS, Ong KS, Badruddin IA, Mehrali M, Metselaar HS. Thermal performance of a compact design heat pipe solar collector with latent heat storage in charging/discharging modes. Energy. 2017 May 15;127:101-15.

[16] Mehrali M, Sadeghinezhad E, Akhiani AR, Latibari ST, Talebian S, Dolatshahi-Pirouz A, Metselaar HS, Mehrali M. An ecofriendly graphene-based nanofluid for heat transfer applications. Journal of cleaner production. 2016 Nov 20;137:555-66.

[17] Mehrali M, Latibari ST, Mehrali M, Metselaar HS, Silakhori M. Shape-stabilized phase change materials with high thermal conductivity based on paraffin/graphene oxide composite. Energy conversion and management. 2013 Mar 1;67:275-82.

[18] Ghahremannezhad A, Xu H, Salimpour MR, Wang P, Vafai K. Thermal performance analysis of phase change materials (PCMs) embedded in gradient porous metal foams. Applied Thermal Engineering. 2020 Oct 1;179:115731.

[19] Kuruneru ST, Vafai K, Sauret E, Gu Y. Application of porous metal foam heat exchangers and the implications of particulate fouling for energy-intensive industries. Chemical Engineering Science. 2020 Jul 17:115968.

[20] R.S. Ferfera, B. Madani, R. Serhane, Investigation of heat transfer improvement at idealized microcellular scale for metal foam incorporated with paraffin, Int. J. Therm. Sci. 156 (2020) 106444.

[21] Zhang H, Li X, Liu L, Ma T, Wang Q, Liu J. Experimental investigation on paraffin melting in high porosity copper foam under centrifugal accelerations. Applied Thermal Engineering. 2020 Sep 1;178:115504.

[22] Zhao C, Opolot M, Liu M, Bruno F, Mancin S, Hooman K. Numerical study of melting performance enhancement for PCM in an annular enclosure with internal-external fins and metal foams. International Journal of Heat and Mass Transfer. 2020 Apr 1;150:119348.

[23] Li Z, Shahsavar A, Al-Rashed AA, Talebizadehsardari P. Effect of porous medium and nanoparticles presences in a counter-current triple-tube composite porous/nano-PCM system. Applied Thermal Engineering. 2020 Feb 25;167:114777.

[24] Sardari PT, Grant D, Giddings D, Walker GS, Gillott M. Composite metal foam/PCM energy store design for dwelling space air heating. Energy Conversion and Management. 2019 Dec 1;201:112151.

[25] Yang X, Yu J, Guo Z, Jin L, He YL. Role of porous metal foam on the heat transfer enhancement for a thermal energy storage tube. Applied Energy. 2019 Apr 1;239:142-56.

[26] Yang X, Wei P, Cui X, Jin L, He YL. Thermal response of annuli filled with metal foam for thermal energy storage: an experimental study. Applied Energy. 2019 Sep 15;250:1457-67.

[27] Zheng H, Wang C, Liu Q, Tian Z, Fan X. Thermal performance of copper foam/paraffin composite phase change material. Energy conversion and management. 2018 Feb 1;157:372-81.

[28] Zhang P, Meng ZN, Zhu H, Wang YL, Peng SP. Melting heat transfer characteristics of a composite phase change material fabricated by paraffin and metal foam. Applied Energy. 2017 Jan 1;185:1971-83.

[29] Xu Y, Ren Q, Zheng ZJ, He YL. Evaluation and optimization of melting performance for a latent heat thermal energy storage unit partially filled with porous media. Applied energy. 2017 May 1;193:84-95.

[30] Kuruneru ST, Sauret E, Vafai K, Saha SC, Gu Y. Analysis of particle-laden fluid flows, tortuosity and particle-fluid behaviour in metal foam heat exchangers. Chemical Engineering Science. 2017 Nov 23;172:677-87.

[31] Li W, Wan H, Lou H, Fu Y, Qin F, He G. Enhanced thermal management with microencapsulated phase change material particles infiltrated in cellular metal foam. Energy. 2017 May 15;127:671-9.

[32] Atal A, Wang Y, Harsha M, Sengupta S. Effect of porosity of conducting matrix on a phase change energy storage device. International Journal of Heat and Mass Transfer. 2016 Feb 1;93:9-16.

[33] Martinelli M, Bentivoglio F, Caron-Soupart A, Couturier R, Fourmigue JF, Marty P. Experimental study of a phase change thermal energy storage with copper foam. Applied thermal engineering. 2016 May 25;101:247-61.

[34] Yang J, Yang L, Xu C, Du X. Experimental study on enhancement of thermal energy storage with phase-change material. Applied Energy. 2016 May 1;169:164-76.

[35] Chen X, Tavakkoli F, Vafai K. Analysis and characterization of metal foam-filled double-pipe heat exchangers. Numerical Heat Transfer, Part A: Applications. 2015 Nov 17;68(10):1031-49.

[36] Hossain R, Mahmud S, Dutta A, Pop I. Energy storage system based on nanoparticle-enhanced phase change material inside porous medium. International Journal of Thermal Sciences. 2015 May 1;91:49-58.

[37] Mancin S, Diani A, Doretti L, Hooman K, Rossetto L. Experimental analysis of phase change phenomenon of paraffin waxes embedded in copper foams. International Journal of Thermal Sciences. 2015 Apr 1;90:79-89.

[38] Alshaer WG, Nada SA, Rady MA, Le Bot C, Del Barrio EP. Numerical investigations of using carbon foam/PCM/Nano carbon tubes composites in thermal management of electronic equipment. Energy Conversion and Management. 2015 Jan 1;89:873-84.

[39] Tasnim SH, Hossain R, Mahmud S, Dutta A. Convection effect on the melting process of nano-PCM inside porous enclosure. International Journal of Heat and Mass Transfer. 2015 Jun 1;85:206-20.

[40] Nithyanandam K, Pitchumani R. Computational studies on metal foam and heat pipe enhanced latent thermal energy storage. Journal of heat transfer. 2014 May 1;136(5).

[41] W.Q. Li, Z.G. Qu, Y.L. He, W.Q. Tao, Experimental and numerical studies on melting phase change heat transfer in open-cell metallic foams filled with paraffin, Appl. Therm. Eng. 37 (2012) 1–9.

[42] Li XY, Yang L, Wang XL, Miao XY, Yao Y, Qiang QQ. Investigation on the charging process of a multi-PCM latent heat thermal energy storage unit for use in conventional air-conditioning systems. Energy. 2018 May 1;150:591-600.

[43] Mahdi JM, Nsofor EC. Multiple-segment metal foam application in the shell-and-tube PCM thermal energy storage system. Journal of Energy Storage. 2018 Dec 1;20:529-41.

[44] Hu Z, Li A, Gao R, Yin H. Enhanced heat transfer for PCM melting in the frustum-shaped unit with multiple PCMs. Journal of Thermal Analysis and Calorimetry. 2015 May;120(2):1407-16.

[45] Al-Abidi AA, Mat S, Sopian K, Sulaiman MY, Mohammad AT. Internal and external fin heat transfer enhancement technique for latent heat thermal energy storage in triplex tube heat exchangers. Applied thermal engineering. 2013 Apr 29;53(1):147-56.

[46] Adine HA, El Qarnia H. Numerical analysis of the thermal behaviour of a shell-and-tube heat storage unit using phase change materials. Applied mathematical modelling. 2009 Apr 1;33(4):2132-44.

[47] Navarro L, Barreneche C, Castell A, Redpath DA, Griffiths PW, Cabeza LF. High density polyethylene spheres with PCM for domestic hot water applications: Water tank and laboratory scale study. Journal of Energy Storage. 2017 Oct 1;13:262-7.

[48] Freeman J, Guarracino I, Kalogirou SA, Markides CN. A small-scale solar organic Rankine cycle combined heat and power system with integrated thermal energy storage. Applied thermal engineering. 2017 Dec 25;127:1543-54.

[49] Mahfuz MH, Anisur MR, Kibria MA, Saidur R, Metselaar IH. Performance investigation of thermal energy storage system with Phase Change Material (PCM) for solar water heating application. International Communications in Heat and Mass Transfer. 2014 Oct 1;57:132-9.

[50] Yao Y, Wu H. Macroscale Modeling of Solid–Liquid Phase Change in Metal Foam/Paraffin Composite: Effects of Paraffin Density Treatment, Thermal Dispersion, and Interstitial Heat Transfer. Journal of Thermal Science and Engineering Applications. 2021 Aug 1;13(4):041024.

[51] Yapici K, Osturk O, Uludag Y. Dependency of nanofluid rheology on particle size and concentration of various metal oxide nanoparticles. Brazilian Journal of Chemical Engineering. 2018 Apr;35:575-86.

[52] Arasu AV, Mujumdar AS. Numerical study on melting of paraffin wax with Al2O3 in a square enclosure. International Communications in Heat and Mass Transfer. 2012 Jan 1;39(1):8-16.

[53] Brent, A. D., Voller, V. R., & Reid, K. T. J. (1988). Enthalpy-porosity technique for modeling convection-diffusion phase change: application to the melting of a pure metal. Numerical Heat Transfer, Part A Applications, 13(3), 297-318.

[54] Calmidi VV. Transport phenomena in high porosity fibrous metal foams. University of Colorado at Boulder; 1998.

[55] Boomsma K, Poulikakos D. On the effective thermal conductivity of a three-dimensionally structured fluid-saturated metal foam. International Journal of Heat and Mass Transfer. 2001 Feb 1;44(4):827-36.

[56] Churchill SW, Chu HH. Correlating equations for laminar and turbulent free convection from a horizontal cylinder. International journal of heat and mass transfer. 1975 Sep 1;18(9):1049-53.

[57] Iasiello M, Mameli M, Filippeschi S, Bianco N. Metal foam/PCM melting evolution analysis: Orientation and morphology effects. Applied Thermal Engineering. 2021 Mar 25;187:116572.

[58] Žkauskas A. Heat transfer from tubes in crossflow. InAdvances in heat transfer 1987 Jan 1 (Vol. 18, pp. 87-159). Elsevier.

[59] Li WQ, Qu ZG, He YL, Tao WQ. Experimental and numerical studies on melting phase change heat transfer in open-cell metallic foams filled with paraffin. Applied Thermal Engineering. 2012 May 1;37:1-9.

[60] Yao Y, Wu H, Liu Z. Direct simulation of interstitial heat transfer coefficient between paraffin and high porosity open-cell metal foam. Journal of Heat Transfer. 2018 Mar 1;140(3).

[61] Maxwell JC. A Treatise on Electricity and Magnetism (Clarendon, Oxford).1879.

[62] Rubitherm Technologies GmbH. RT data sheet

[63] Kant K, Shukla A, Sharma A, Biwole PH. Heat transfer studies of photovoltaic panel coupled with phase change material. Solar Energy. 2016 Dec 15;140:151-61.

[64] Arıcı M, Tütüncü E, Yıldız Ç, Li D. Enhancement of PCM melting rate via internal fin and nanoparticles. International Journal of Heat and Mass Transfer. 2020 Aug 1;156:119845.

[65] Engineers Edge - Engineering Reference Data and Tools | GD&T ASME Training | DFM DFA Training

(https://www.engineersedge.com/physics/water__density_viscosity_specific_weight_13146.htm)

[66] Jesumathy S, Udayakumar M, Suresh S. Experimental study of enhanced heat transfer by addition of CuO nanoparticle. Heat and Mass Transfer. 2012 Jun;48(6):965-78.

[67] Madruga S. Modeling of enhanced micro-energy harvesting of thermal ambient fluctuations with metallic foams embedded in Phase Change Materials. Renewable Energy. 2021 May 1;168:424-37.

[68] Carmona M, Rincón A, Gulfo L. Energy and exergy model with parametric study of a hot water storage tank with PCM for domestic applications and experimental validation for multiple operational scenarios. Energy Conversion and Management. 2020 Oct 15; 222:113189.

[69] Dardir M, Roccamena L, El Mankibi M, Haghighat F. Performance analysis of an improved PCM-to-air heat exchanger for building envelope applications–An experimental study. Solar Energy. 2020 Mar 15;199:704-20.

[70] Mallow A, Abdelaziz O, Graham S. Thermal charging performance of enhanced phase change material composites for thermal battery design. International Journal of Thermal Sciences. 2018 May 1;127:19-28.

[71] Diani A, Rossetto L. Melting of PCMs Embedded in Copper Foams: An Experimental Study. Materials. 2021 Jan;14(5):1195.

[72] Lafdi K, Mesalhy O, Shaikh S. Experimental study on the influence of foam porosity and pore size on the melting of phase change materials. Journal of Applied Physics. 2007 Oct 15;102(8):083549.

[73] Liu Z, Yao Y, Wu H. Numerical modeling for solid–liquid phase change phenomena in porous media: Shell-and-tube type latent heat thermal energy storage. Applied energy. 2013 Dec 1;112:1222-32.

Chapter 3.
INCREASING MELTING AND SOLIDIFICATION PERFORMANCES OF A PHASE CHANGE MATERIAL-BASED FLAT PLATE SOLAR COLLECTOR

3.1. Introduction

Solar-thermal power systems produce clean energy in the form of electricity as well as usable heat for domestic hot water and/or space heating on a large scale and in a variety of applications. In solar household hot water systems, TES is essential, as it helps to compensate for the temporal mismatch between supply of solar radiation and demand for hot water. They can be designed as Latent Energy Storage (LES) systems equipped with PCMs to store/release energy in the form of latent heat of fusion, providing a greater energy storage density. Sari and Karaipekli [1] tested a variety of fatty acids and discovered favorable qualities such as stability across thousands of melting and solidification cycles. Since they have good phase-change stability, they may be used as a component in solar household systems. Nowadays, PCM thermal characteristics, as well as low thermal conductivity and specific heat capacity while working at low temperatures (<100 °C), still remain primary challenges [2]. So, it is crucial to establish the thermal performance standards, as well as heat transfer properties of a PCM, before employing it for an energy storage application [3]. Due to this limitation, the heat transfer rate to the PCMs is slowed, limiting the storage capacity of the system if a given charging and discharging duration is prescribed together with the energy to be stored and released. Thermal conductivity enhancers such as porous metal foams, nanoparticles, or extended surfaces, have been extensively used to improve such thermal performances. Metal foams are excellent candidates for the improvement of the efficiency of thermal systems and PCMs due to their high thermal conductivity and wide surface area per unit volume, as well as the fact that they have no relevant influence on the heat storage capacity of PCMs. Other potential promising candidates to increase thermal performances are dispersed nanoparticles and extended surfaces to replace straight walls, such as fin and wavy walls. All of these methods for boosting thermal conductivity help the PCM to complete a full charge or discharge in less time, which is critical to balance a time-variable energy source, allowing to a reduction in terms of Energy Storage System (ESS) size too.

3.1.1. Flat plate solar collectors

Combining PCMs with Flat Plate Solar Collectors (FPSCs) helps to guarantee a certain thermal performance for an energy system even if there is no sunlight available. Eames and Griffiths [4] analyzed TES using PCM slurry in a FPSCs. If there is sunlight for about 10 hours, the PCM slurry systems equipped

with either 10 or 30% concentrations, showed better performances in heat absorption than water-filled storage. Chen et al. [5] examined the energy storage process of an FPSC with an integrated aluminum foam porous structure filled with PCM. The findings indicated that the use of aluminum foams in paraffin has a significant impact on heat transmission and paraffin melting rate. Haillot et al. [6] utilized a combination of Compressed Expanded Natural Graphite (CENG) and PCM as the storage medium. They found that the collector performance can be improved during summer seasons by using both PCM and graphite. However, the efficiency of the collector decreased in winter climates. In their study, Haillot et al. [7] examined the effectiveness of a solar domestic hot water system that incorporated a PCM. They substituted the conventional copper-based solar absorber with a combination of CENG and PCM in a flat plate solar collector. Their results indicated that the CENG/RT65 paraffin (RUBITHERM) and CENG/pentaglycerin composites exhibited the most potential for use in the solar collector. Lin et al. [8] studied three alternative inclination angles for FPSC with a PCM, namely 10, 20, and 30 degrees. They kept delivering hot water for another three hours until PCM and water temperatures approach thermal equilibrium. They discovered that a 10° collector tilt with a 0.5 kg/min water flow rate were the greatest settings for maximum output. A numerical optimization of a FPSC contain a PCM layer under the plate was done by Allouhi et al. [9]. The liquid fraction (LF) was investigated under PCM layer thicknesses and different mass flow conditions. Teamah et al. [10] examined a typical Solar Domestic Hot Water heating (SDHW) system that employs a hybrid PCM/water thermal storage. The PCMs were placed in the water tank as vertical cylindrical modules, and the flowing water along the length of the tank was used as the heat transfer fluid. Their results revealed that incorporating PCMs in the storage tank could decrease the storage tank volume necessary to achieve the same peak solar fraction. Cascaded PCMs were implemented by Teamah et al. [11] to heat hot water in a solar domestic water system for multiple households. Using the cascaded PCM modules in the TES system shows a 50% reduction for the storage volume needed to have the same amount of hot water. Khan et al. [12] investigated existing FPSC design and analysis methodologies using PCMs. Shirinbakhsh et al. [13] examined solar heater arrangement, PCM integration and supply demand on an FPSC all at the same time. An FPSC prototype with integrated PCM thermal model was experimentally validated by Carmona and Palacio [14]. Under various operating circumstances, the model was utilized to estimate the thermal performance of the collector using PCM. Thermal performance of

shape stabilized PCM in a solar collector was examined by Yeh et al. [15] using both experimental and numerical analysis. When compared to a situation in which the water is still, the circulation plays a significant role in both the acceleration of the charging rate and the regulation of the temperature at the tube's surface. Although, no significant variation in charging rate was discovered among the four water-circulated designs. In an attempt to decrease the building energy request, de Araujo Passos et al. [16] developed a model for a Heating, Ventilation, and Air Conditioning (HVAC) system, that consists of components like sunshade, skylight, and heat pump. They employed nonlinear optimization techniques to determine the most efficient operational parameters for the system.

3.1.2. Nanoparticles

Yousefi et al. [17] studied the thermal performance of FPSC using Multi-Walled Carbon Nanotubes (MWCNT)-water nanofluid, discovering that nanofluids considerably enhanced the thermal efficiency of FPSCs. Saw et al. [18] revealed the results of an experimental evaluation of a 1.44 m^2 flat plate solar collector with nano-composite PCM for home water heating. In the experimental run, FPSC performance was increased by 6.9% and 8.4% if integrated PCM and nano-composite PCM are employed. A prototype of an FPSC with an integrated nano-PCM storage unit was tested at different inclination angles by Al-Kayiem and Lin [19]. Metal fins included into the nano-PCM unit were used to improve the contact area between the accumulation system and the absorber plate. When compared to a pure PCM matrix, the finned storage system had a 24% greater heat conductivity. Experimental outdoor assessment of a FPSC with an integrated nanocomposite PCM was reported by Owolabi et al. [20]. To improve thermal characteristics of the paraffin-based PCM, various nano powder of aluminum, zinc, iron, and copper, were used, reaching a 58.5% increase in terms of thermal efficiency. After that, Lin and Al-Kayiem [21] investigated the effect of copper nanoparticles in paraffin wax. When 0.5%, 1.0%, 1.5%, and 2.0% weight of copper nano powder were added to PCM, thermal conductivity increases by 14.0%, 23.9%, 42.5%, and 46.3%, respectively. A flat plate solar collector incorporating 1.0% copper nano-composite PCM demonstrated a 1.7% efficiency boost in performance when compared to a pure PCM-based solar collector. Furthermore, Verma et al. [22] extended their study by investigating the efficiency performance of FPSC utilizing a variety of nanofluids, including Copper Oxide (CuO), titanium dioxide (TiO_2), MWCNT, and graphene/water

nanofluids. They discovered that the MWCNT nanofluid exhibits the greatest increase in FPSC efficiency. Mehrali et al. [23] investigated shape-stabilized salt hydrate PCM for solar thermal energy harvesting and storage. The photo-thermal efficiency of these innovative shape stabilized PCMs (SSPCMs) is 92.6%, indicating exceptional thermal cycle dependability. Kalbande et al. [24] conducted a study to evaluate the effect of utilizing Hybrid Nano-Enhanced Phase Change Material (HNEPCM) in reducing energy consumption. They discovered that the inclusion of MWCNT-CuO nanoparticles led to a 66.6% reduction in melting time. A novel system that integrates a solar collector with a PCM layer was developed by Sharma et al. [25] to leverage the advantages of solar radiation. Through an experimental setup, they demonstrated that using nanoparticles can increase the rate of both charging and discharging by approximately 24% and 28%, respectively. For energy-saving goals, Lu et al. [26] created the novel composite using iron oxide nanoparticles. They statistically assessed the performance throughout the course of the whole cycle while optimizing the NEPCM preparation procedure. A metal-foam based improvement technique developed by Moghaddam et al. [27] resulted in a 52% increase in the rate at which PCM melted in a TTHX.

3.1.3. Porous metal foams

As previously mentioned, metal foams have also been utilized to improve PCMs thermal conductivity. A copper foam has been added by Zhao et al. [28] to improve the paraffin RT58, a PCM material, thermal efficiency. Findings revealed that greater phase-change rate might be achieved based on the type of metal foam structure plus substrate. Cui [29] developed and constructed an experimental apparatus using the paraffin PS58 as PCM and copper metal foam as the porous material. The findings reveal that the foam material not only results in a better temperature distribution inside the TES unit, but also significantly reduces the charging time. According to experimental and computational study by Li et al. [30], temperature uniformity within paraffin soaked in copper foams can be strengthened by reducing pore density to accelerate natural convection or decreasing porosity to increase effective thermal conductivity. Hirasawa et al. [31] examined the influence of porous metal foam in reducing heat losses in an experimental setting. They used a high-porosity foam atop the collection plate and found that natural convection heat losses were decreased by up to 7%. Experiments were performed by Mancin et al. [32] on copper foams implanted in various melting point paraffin waxes. The foam skeleton embedded within the PCM acts as a heat spreader, therefore the

temperature distribution looks to be more uniform, and phase change becomes faster. The performance of a solar collector filled with metal foam was studied by Saedodin et al. [33]. Because of the porous media aided by metal foam, experimental data supported by numerical modeling demonstrate a 18.5% increase in thermal efficiency, and a 82% increase in Nusselt number. Zhu et al. [34] performed some studies about a heat sink that is filled with PCM and a copper foam. They used a PCM with a melting temperature of 46 °C and two copper foams with a porosity of 96%. Joshi and Rathod [35] conducted a numerical analysis to investigate how foam porosity and filling ratio affect the phase change. Thermal efficiency is improved especially when a 0.25 filling ratio, that is the lowest, is employed. Increasing the filling ratio from 0.75 to 1 times the height of the foam requires about the same amount of melting time, while the overall melting rate decreased as both filling ratio and porosity decrease. Carmona et al. [36] examined the use of a PCM to store latent heat in home hot water systems; on the other hand, Dardir et al. [37] developed a novel PCM-to-air heat exchanger design that allows to improve charging capacity of the cooling system. Yang et al. [38] examined heat transfer during solidification of a PCM implanted in a metal foam using pin fins. Experiments shown that inserting pin fins into the pore considerably enhances the solidification process, independently from the pore size parameter gradient. A solidification rate enhancement can be found if more effort is done on porosity gradient instead of bulk material. Finally, a hybrid pin fin-metal foam matrix with a gradient in metal foam porosity was proposed as the optimal structure. Marri and Balaji [39] used both experimental and computational methods to analyze PCM-metal foam heat sink with a cylindrical form. They looked at aluminum foams with varying PPIs, varied porosities, and encapsulated with n-eicosane as the PCM. The findings revealed that reducing the porosity or raising the PPI from the bottom to the top enhanced the heat sink thermal efficiency when comparisons are done to the case with uniform porosity and PPI. Diani et al. [40] investigated melting of several PCMs at various melting temperatures, say 42, 55, and 64 °C. Copper foam with a porosity of 90.5% performed slightly better than copper foam with a porosity of 93.3%, according to the results. Similarly, the PCM melting temperature is determined by how much time is required from the passive cooling system. Iasiello et al. [41] studied PCMs implanted in aluminum foams under varied orientations, PPIs, heat fluxes, and porosities. Such analysis has been done with both experimental and numerical approaches. It has been concluded that the smaller the porosity, the larger the melting percentage, and that PPIs and orientation have no influence on melting time. An

infrared camera was used to monitor the evolution of the melting front and record the temperature distribution, demonstrating the potential of this technology for understanding melting front dynamics. Li et al. [42] employed a composite material consisting of metal foam and PCM to enhance the effectiveness of an integrated system for energy storage, release, and harvesting. Their research determined that a foam/PCM composite with a lower porosity was able to store the greatest amount of thermoelectric energy and enable superior temperature control. According to Teamah and Teamah [43], the increased conductivity provided by nanometals helps speeding up charging and discharging, boosting the solar system efficiency by 7% when compared to the basic PCM case, and of a 16% when compared to the no PCM scenario. Lei et al. [44] investigated the effects of porosity in copper foams in terms of heat transfer. They discovered that incorporating copper foam considerably enhanced the heat storage capability. When compared to a fixed porosity, the total time taken for complete melting, and the average heat flux for the variable porosity case, decreased by 6.8% and increased by 4.3%, respectively. The thermal performance of LHTES unit with a shell-and-tube shape was examined by Buonomo et al. [45] in relation to the application of a metal foam layer on the tube. The findings demonstrated that increasing the thickness of the foam layer altered the heat transfer, reducing the melting time.

3.1.4. Extended surfaces

Finned surfaces are viewed as a great approach to enhance the overall heat transfer performance in LHS systems, aiming to figure out the PCM poor thermal conductivity issue. Abdulateef et al. [46] examined fin design, finding that rectangular fins outperform triangular fins by 15%. Shahsavar et al. [47] studies melting and solidification within a double-pipe LHTES, that considers sine-shaped wavy channels coupled with a porous media. Reduction of melting and solidification times reached up to 91.4% and 96.7%, respectively, if comparison is done with a pure PCM system coupled with a smooth channel; however, the heat transfer rate for the wavy channel composite PCM is 10.4 and 18.9 times, respectively and in terms of an average, larger than that of the straight channel pure PCM. Li et al. [48] simulates a sine-shape enclosure that includes nanoparticles to improve PCM thermophysical properties. The so-called adiabatic wall form factor, as well as the amplitude, were explored. If this amplitude A is 0.1, utilizing Platelet powder instead of sphere speeds up the method by 8.34%. If the shape factor m is 3, and the value of A rises, an increase of 44.99% has been observed for the freezing time. Keshteli and

Sheikholeslami [49] studied a TTHX equipped with wavy walls and fins that are Y-shaped. This heat exchanger is equipped with PCM and Aluminum Oxide (Al_2O_3) nanoparticle dispersion. Results revealed that adding fins or nanoparticles considerably enhanced the solidification rate. Yldz et al. [50] investigated the impact of tree-shaped fin size and structure on phase change rate, and they reported that a rectangular form had a stronger influence on the system. Hosseinzadeh et al. [51] use the Galerkin-based Finite Element Method (FEM) to solve the influence of Hybrid Nanoparticles (HNP) and fins on the solidification process of the LHTES system. They discovered that using HNPs and fins boosted the solidification rate by 14%. Hosseinzadeh et al. [52] use hybrid NEPCM in their numerical analysis, together with rectangular fins, and showed that using these promoters simultaneously enhance solidification time by up to 12%. Guo et al. [53] conducted four different tests to demonstrate the impact of fins and foam on the enhancement of phase change heat transfer. They suggested that the addition of fins or metal foam could accelerate the PCM melting, but the best results were obtained when both fin sets and metal foam were combined. The experimental findings indicate that the fin-foam hybrid configuration surpasses the alternative structures, exhibiting a substantial 83.35% decrease in the duration required for complete melting when compared with the bare tube. Hosseinzadeh et al. [54] used FlexPDE software to investigate the effect of two distinct fins (longitudinal-tree-like) and hybrid nano-particles (Molybdenum disulfide (MoS_2)-TiO_2) on the solidification process in a TTHX. The results showed that combining tree-like fins and nanoparticles lowered solidification time by 78% when compared to bare tube and tree-like fins.

3.1.5. Innovation and purpose of the present study

Based on the literature survey, it is evident that all the solutions to enhance heat transfer in latent heat storage systems are promising; on the other hand, charging and discharging time reduction was considered as main target of researchers according to previous articles. As per the authors' knowledge, no studies simultaneously applied different heat transfer enhancement solutions, which allows to understand if and how much the TES system performances can be maximized by mixing together these solutions, especially if a whole heat storage and release cycle is considered. In this contribution, a numerical investigation of different heat transfer enhancement techniques for a PCM-based TES system coupled with a FPSC, which are nanoparticles, and metal foams to be considered simultaneously or not, is here presented. Specifically, a

new design of the FPSC thermal storage system has been proposed here, which involves a new shape of the extended surface, such as a wavy wall coupled with a Y-shaped fin. This innovative design allows for an increased heat transfer area, better sunlight penetration, and consequently improved phase change and fluid flow characteristics, which can lead to higher thermal efficiency and better thermal performances. The utilization of a Y-shaped fin design in a heat exchanger with PCM offers various advantages. These include enhanced heat transfer, improved dispersion of PCM, reduced thermal resistance, optimized fluid flow, and compactness. These favorable aspects substantiate the choice to augment the efficiency and performance of the PCM-based heat exchanger through the implementation of a Y-shaped fin configuration. The main objective of this work is to appreciate which solution maximizes relevant heat transfer aspects like charging and discharging process (melting and solidification), say phase change times, and stored/released energy. Based on temperatures usually achieved in these applications, a paraffin wax with the commercial name RT82, whose melting point is around 81 °C, is here employed. On the other hand, aluminum foams with 10 PPIs, and 0.92, and 0.95 porosity, as well as nanoparticles with a 5% volume fraction made up by Al_2O_3, Silicon Dioxide (SiO_2), Zinc Oxide (ZnO), and Copper Oxide (CuO), are here employed. A thorough comparison of these solutions, by considering geometries like straight, wavy walls, or wavy walls with fin, are here analyzed in order to appreciate which configuration allows to maximize heat transfer performances in terms of liquid fraction and stored/recovered energy. The present research offers valuable insights into the effects of different operating parameters on the heat transfer and thermal storage capacity of these materials, which can help in the design of efficient TES systems. In detail, a 3D domain was developed for numerical modeling purposes using enthalpy-porosity, LTNE, and homogeneous mixture models, which allowed for an accurate representation of the physical processes involved in the heat transfer and thermal storage phenomena. The novel approach of combining these models enabled a comprehensive investigation of the effects of various parameters on the performance of the TES system, such as the effects of porosity, particles type, and geometry, on PCM melting and solidification. Moreover, the results of this study were thoroughly validated with both experimental and numerical outcomes from the literature. The accomplishments of this research were then illustrated and explained by showing liquid fraction, temperature, heat transfer rates, as well as PCM dimensionless parameters, for different cases investigated.

3.2. Methods

This section provides a comprehensive overview of the investigated Flat Plate Solar Collectors Thermal Energy Storage (FPSC-TES) system. First of all, a general description of the system investigated is presented to appreciate the role of the storage system. After this, it will be shown how to pass from the storage system concept up to the geometry to be investigated here via numerical analysis. After showing governing equations, together with the appropriate assumptions, boundary conditions will be defined, together with the thermophysical properties. Particular attention will be given to both heat storage medium and typical temperature and flow conditions to be simulated; these variables have to be typical of flat plate solar collector applications. Finally, methods to solve the mathematical model are introduced, while a throughout code validation will be done to appreciate the reliability of the present computations.

3.2.1. System description

A schematic diagram of the studied FPSC-TES system is shown in **Figure 3.1**. Because the primary aim here is to perform comparisons among various heat transfer enhancement solutions by considering a whole melting and solidification cycle, one can develop a CFD model for just a zone of the collector; from the results achieved, conventional energy balances as black-box models, as well as typical heat transfer correlations, can be used to extend the present analysis. The geometry of the flat-plate solar collector TES system used in this application is also shown in cross-section in **Figure 3.1** for three cases: straight wall (Case A), wavy wall (Case B), and wavy wall with a Y-shaped fin (Case C), along with the function used to characterize wavy wall and Y-shaped fin geometries.

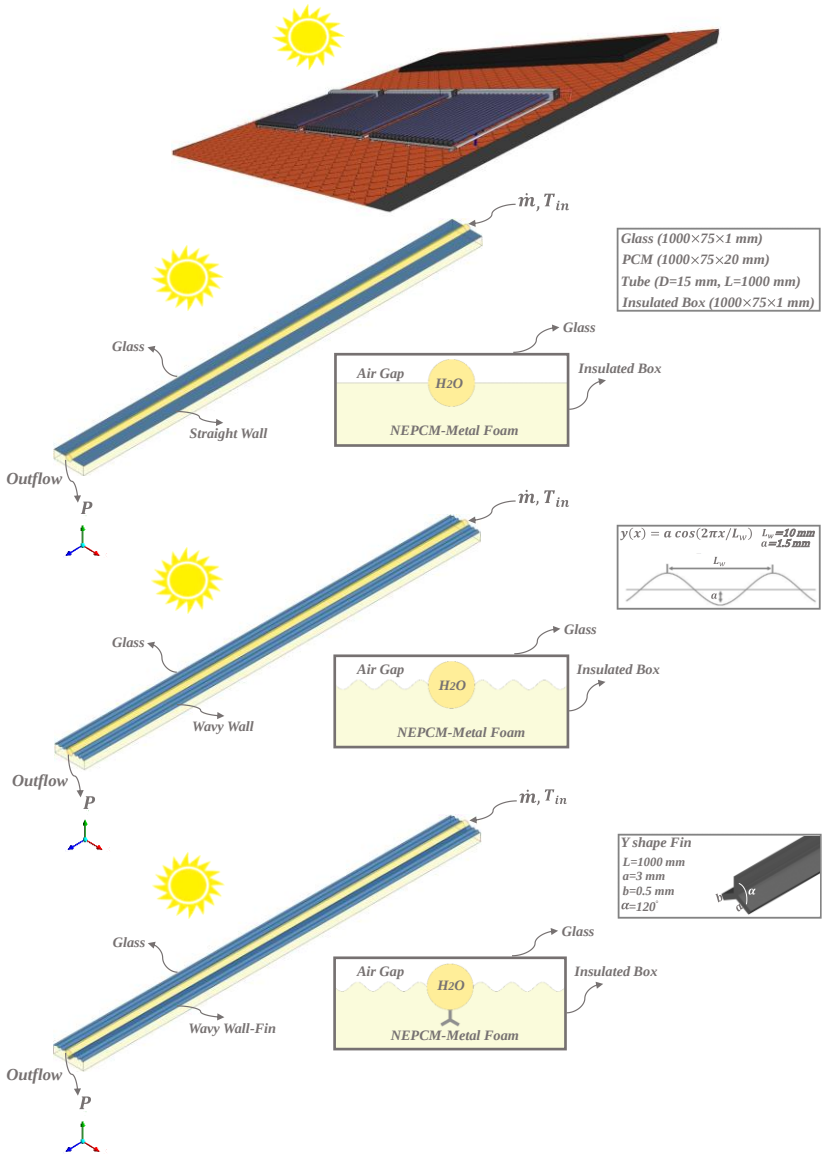

Fig. 3.1. A sketch of the FPSC with PCM enhancement technologies: Case A (top), Case B (middle), and Case C (bottom)

3.2.2. Assumptions and governing equations

A resume of the mathematical model assumption here employed is reported in the following. When the metal foam is included in the device analyzed, governing equations are written for a representative elementary volume accounting for two distinguished phases, says PCM or NEPCM and foam. On

the other hand, when nanoparticles are considered (NEPCM), the homogeneous single-phase approach is used; in particular, one assumes that governing equations for the PCM are averaged by accounting for nanoparticles dispersion. Therefore, model assumptions, followed by governing equations written in a generic form and referred to both HTF and PCM-related regions, are:

- Fluid flow is generally 3D, unsteady, laminar, and incompressible when invoked by governing equations,
- Air gap, thermal conduction from the glass, thermal dispersion, and micro-inertial effects are neglected,
- The Boussinesq approximation is employed to model natural convection within the liquid PCM,
- Volume change during phase transition is negligible, and PCM density is always computed as an average of the solid and liquid densities, say $\rho_m = (\rho_s + \rho_l)/2$,
- Thermophysical properties are assumed to be constant and uniform,
- Nanoparticle distribution is homogeneous,
- PCM and nanoparticles are in local thermal equilibrium with no relative motion between them,
- The porous metal foam is open-celled, homogeneous, and isotropic,
- NEPCM or PCM and porous foam are in a local thermal non-equilibrium condition.

Continuity:

$$\nabla \cdot \vec{V} = 0 \tag{1}$$

x-Momentum equation:

$$\frac{\bar{\rho}}{\varepsilon^2}\left(\varepsilon\frac{\partial u}{\partial t} + V.\nabla u\right) = -\frac{\partial p}{\partial x} + \frac{\bar{\mu}}{\varepsilon}\nabla^2 u + \left(\frac{A_m(1-\lambda)^2}{\lambda^3 + 0.001} - \frac{\bar{\mu}}{K}\right)u \tag{2}$$

y-Momentum equation:

$$\frac{\bar{\rho}}{\varepsilon^2}\left(\varepsilon\frac{\partial v}{\partial t} + V.\nabla v\right) = -\frac{\partial p}{\partial y} + \frac{\bar{\mu}}{\varepsilon}\nabla^2 v + \left(\overline{\rho\beta}\right)g\left(T - T_{ini}\right) + \left(\frac{A_m(1-\lambda)^2}{\lambda^3 + 0.001} - \frac{\bar{\mu}}{K}\right)v \tag{3}$$

z-Momentum equation:

$$\frac{\bar{\rho}}{\varepsilon^2}\left(\varepsilon\frac{\partial w}{\partial t} + V.\nabla w\right) = -\frac{\partial p}{\partial z} + \frac{\bar{\mu}}{\varepsilon}\nabla^2 w + \left(\frac{A_m(1-\lambda)^2}{\lambda^3 + 0.001} - \frac{\bar{\mu}}{K}\right)w \tag{4}$$

NanoPCM energy equation:

$$\overline{\rho C}\left(\varepsilon\frac{\partial T}{\partial t}\right)+\varepsilon\overline{\rho L_f}\frac{\partial \lambda}{\partial t}+\overline{\rho C}\left(V\cdot\nabla T\right)=k_{fe}\nabla^2 T+h_{sf}A_{sf}\left(T_f-T_s\right) \tag{5}$$

Solid foam energy equation:

$$(1-\varepsilon)(\rho C)_s\frac{\partial T_s}{\partial t}=k_{se}\nabla^2 T_s-h_{sf}A_{sf}\left(T_s-T_f\right) \tag{6}$$

The following equation is used to calculate the liquid fraction λ at each cell:

$$\begin{aligned}&\lambda=0 && if\quad T\le T_{solidus}\\ &\lambda=(T-T_{solidus}/T_{liquidus}-T_{solidus}) && if\quad T_{solidus}<T<T_{liquidus}\\ &\lambda=1 && if\quad T\ge T_{liquidus}\end{aligned} \tag{7}$$

3.2.2.1 Correlations for metal foam parameters

When metal foam is included, it is necessary to have the porous medium closure coefficients to close governing equations. Subscripts f and s refer to liquid NanoPCM and porous medium (foam), respectively, T is the temperature, p is the effective pressure, μ is the dynamic viscosity, C is specific heat capacity, Lf is latent heat, is the porosity of Al6061 aluminum alloy, □ in Carman-Kozeny damping term is a tiny number (0.001) to avoid division by zero and A_m is a mushy zone constant. A summary of the correlations that were employed in this study can be seen in **Table 3.1**. The equations shown before (Eqs. 1-6) represent a generic form that can be employed for the HTF region if one define porosity $\varepsilon = 1$ and infinite permeability K. The mushy zone constant term, A_m, in Carman-Kozeny damping term is 10^6, and tiny number, δ, is 0.001 to prevent division by zero [55], [56]. Using the models described in [57], the permeability, K, required in Eqs. (2), (3), and (4), are calculated. Boomsma and Poulikakos [58] proposed heat transfer correlations to be used here to compute the effective thermal conductivity of PCM or NEPCM, (k_{fe}), and the effective thermal conductivity of the porous medium, k_{se}. Correlations to be used for the interfacial heat transfer coefficient in phase change material is still an open question because of the complexity of the problem [59], and different correlations have been proposed in the past [30], [41], [60], [61], [62], [63]. Low-velocity tube bank cross-flow correlations, which have been utilized in similar studies [62], [30], were utilized in the current study here by assuming that the metal foam structure is very similar to tube banks.

Table 3.1. The employed correlations of metallic foam parameters for Eqs. (2-6)

Parameter	Correlation	Reference
Permeability, $\boldsymbol{K}$	$\frac{K}{d^2_p} = 0.00073(1-\varepsilon)^{-0.224}\left(\frac{d_l}{d_p}\right)^{-1.11}$ $\frac{d_l}{d_p} = 1.18\sqrt{\frac{1-\varepsilon}{3\pi}}\left(\frac{1}{1-e^{-(1-\varepsilon)/0.04}}\right)$ $where\ \left(d_p = 0.0254(m)/\omega(PPI)\right)$	[57]
Effective thermal conductivity of PCM or nanoPCM, $\boldsymbol{k_{fe}}$ Effective thermal conductivity of the porous medium, $\boldsymbol{k_{se}}$	$k_{fe} = \frac{\sqrt{2}}{2\left(M_A + M_B + M_C + M_D\right)}\Big\vert_{k_s=0}$ $k_{se} = \frac{\sqrt{2}}{2\left(M_A + M_B + M_C + M_D\right)}\Big\vert_{k_f=0}$ $M_A = \frac{4\sigma}{\left(2e^2 + \pi\sigma(1-e)\right)k_s + \left(4 - 2e^2 + \pi\sigma(1-e)\right)k_f}$ $M_B = \frac{(e-2\sigma)^2}{\left(e-2\sigma\right)e^2k_s + \left(2e - 4\sigma - (e-2\sigma)e^2\right)k_f}$ $M_C = \frac{(\sqrt{2}-2e)^2}{2\pi\sigma^2(1-2e\sqrt{2})k_s + 2\left(\sqrt{2}-2e-\pi\sigma^2(1-2e\sqrt{2})\right)k_f}$ $M_D = \frac{2e}{e^2k_s + \left(4-e^2\right)k_f}$ $\sigma = \sqrt{\frac{\sqrt{2}(2-6/8e^3\sqrt{2}-2\varepsilon)}{\pi(3-4e\sqrt{2}-e)}},\ and\ e = 0.339$	[58]
Specific surface area, $\boldsymbol{A_{sf}}$ Interfacial heat transfer coefficient, $\boldsymbol{h_{sf}}$	$A_{sf} = \frac{3\pi d_l(1-e^{-(1-\varepsilon)/0.04})}{(0.59d_p)^2}$ $h_{sf} = \begin{cases} (0.76\,Re_d^{0.4}\,Pr_{PCM}^{0.37}\left(\frac{k_f}{d_f}\right), 1 \le Re_d \le 40 \\ (0.52\,Re_d^{0.5}\,Pr_{PCM}^{0.37}\left(\frac{k_f}{d_f}\right), 40 \le Re_d \le 1000 \\ (0.26\,Re_d^{0.6}\,Pr_{PCM}^{0.37}\left(\frac{k_f}{d_f}\right), 1000 \le Re_d \le 2\times10^5 \end{cases}$	[30], [41], [60], [61], [62], [63]

3.2.2.2 Thermo-physical properties

Thermophysical characteristics of both nanofluid and PCM are given in this subsection. Properties listed in the following are also applied to the nanoPCM without foam; this can be done by assuming a unitary porosity in governing Eqs. 1-6.

Properties of NEPCM material are shown in **Figure 3.2**. The thermal conductivity of the NEPCM was written according to Maxwell model [64]. This value would close previously introduced by determining the value of k_f, that is the thermal conductivity of the PCM with either nanoparticles or not.

To calculate the TES performance of the LHTES unit, the melting $p_{L,m}$ heat transfer rate is employed and determined using Eq (8). The thermal energy release and storage rates $p_{L,s}$ and $p_{L,m}$ represent the thermal energy release and storage capacity per unit solidification and melting time, which is an average heat rate as a representation of the mean melting velocity and is defined as the stored thermal energy throughout the melting/solidification time as [65], [66]. Subscripts *m* and *s* refer to melting and solidification, respectively. This value can be determined as follows:

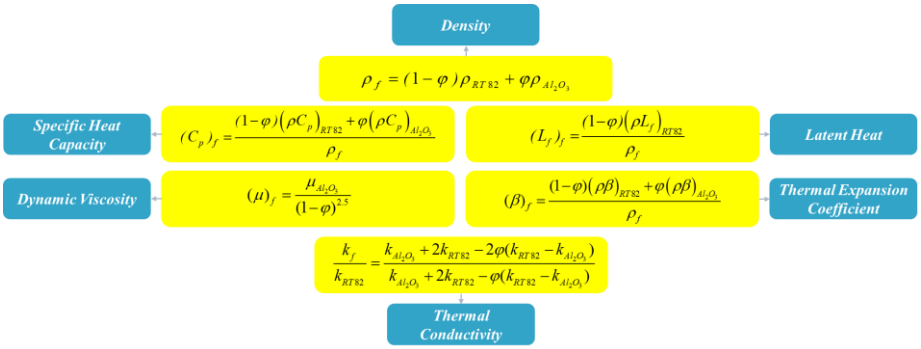

Fig. 3.2. Formulations of thermophysical features of nano-enhanced PCM material.

$$p_{L,m} = \frac{Q}{t_m} = \frac{m_{pcm}\left(\int_{T_{ini}}^{T_{solidus}} c\,dT + L_f + \int_{T_{liquidus}}^{T_e} c\,dT\right)}{t_m} = \frac{m_{pcm}\left[c\left(T_{solidus} - T_{ini}\right) + L_f + c\left(T_e - T_{liquidus}\right)\right]}{t_m}$$
$$p_{L,s} = \frac{Q}{t_s} = \frac{m_{pcm}\left(\int_{T_{liquidus}}^{T_{ini}} c\,dT + L_f + \int_{T_e}^{T_{solidus}} c\,dT\right)}{t_s} = \frac{m_{pcm}\left[c\left(T_{ini} - T_{liquidus}\right) + L_f + c\left(T_{solidus} - T_e\right)\right]}{t_s} \quad (8)$$

Times required to complete the melting and solidification processes are represented by t_m and t_s, respectively. Finally, a list of the materials that were selected, as well as a resume of thermophysical properties here employed, are

depicted in **Table 3.2**. Because of typical operation temperature here investigated, the RT82 PCM, that melts in between 77 and 85 °C with a mean T_m of 81 °C, has been chosen as the PCM here.

Table 3.2. Properties of RT82, Al_2O_3, Al6061, and Cu

Property	**RT82**	**Al_2O_3**	**Al6061**	**Cu**
$T_{solidus}/T_{liquidus}$ *(°C)*	77/85	-	-	-
ρ_s/ρ_l *(kg /m^3)*	950/770	3600	140	8920
C (J /kg K)	2000	765	869	380
k (W/m K)	0.2	36	167	400
β *(1/K)*	0.001	-	-	-
μ *(kg/m s)*	0.03499	-	-	-
L_f *(kJ/kg)*	176	-	-	-

3.2.3. Initial and boundary conditions

The temperature of the whole domain is 70 °C at the beginning of all the simulations. In this contribution, a single melting cycle will be analyzed to underline the role of different heat transfer enhancement techniques when charging the PCM; furthermore, a whole continuous melting/solidification cycle is analyzed to consider what happens if the energy absorbed from the PCM is directly reused. For all the cases, once the transient starts, say $t > 0$, a 90 °C inlet temperature is assumed for the water (HTF) that comes in the domain to let the PCM melting. This reproduces the case in which there is enough energy to charge the PCM. From the top of the domain, as shown in **Fig. 3.1**, an incoming solar heat flux comes with 900 W/m^2 which is a consistent value if one considers the middle of a day. This value can be assumed to be constant and uniform because of the small time and space scales here investigated in these simulations during the melting phase. When reference is done to the solidification, say discharging, case, it is assumed that it starts immediately after the melting process is completed in the whole PCM at $t = t_m$. The solidification process starts since the HTF now comes in at 70 °C for $t \geq t_m$. This case represents a situation where it is necessary to reuse the heat from the PCM to reheat again the HTF, in order to maintain its temperature at the highest possible for usage. A typical reuse application might be PCM-based solar collectors with HVAC systems that can offer a more sustainable and efficient solution for heating and cooling in commercial buildings. This might be advantageous since HVAC systems are known to be significant energy consumers. For instance, it

could be assumed that there is a cloudy weather after complete melting, so the incoming heat flux from the sun suddenly becomes zero; on the other hand, it can also be generally assumed that the objective is to efficiently reuse heat immediately after its storage. Another situation that might occur instead of cloudy weather is the reduction of incoming solar heat flux that also happens in sunny days during afternoon and night. With references to the fluid flow problem, an inlet mass flow rate of 0.028 kg/s is assumed to constantly go inside the domain with its own temperature. In this study, foams with relatively high porosities, says 0.92 and 0.95, as well as nanoparticles with relatively low nanoparticle volume fractions ($\phi = 5\%$), are employed. This because it has been shown that higher porosities are helpful to let the nanoparticles flowing in the domain once the PCM is liquid, even if it must be underlined that smaller porosities allow to faster melting fraction [41]. Other boundary conditions to close the problem are reported in the following. For the outlet section of the HTF, atmospheric pressure and temperature outflow were assumed. At the other domain boundaries, no-slip and thermal insulation boundary conditions are here employed. Finally, in all the adjacent domains, temperature and heat flux continuity conditions are invoked. Boundary conditions applied for different surfaces of the domain have been reported in **Table 3.3**.

Table 3.3. Boundary conditions for different surfaces of the domain shown in Fig. 1 (the upper collecting plate heat transfer is neglected, together with the air within the cavity); PCM includes also cases with foam and/or nanoparticles

Location	**Boundary conditions**
Top of tube/ PCM	900 W/m^2; no-slip
Fins/PCM interface	Thermally-coupled boundaries; no-slip
Tube/PCM interface	Thermally-coupled boundaries; no-slip
Bottom and lateral walls	Adiabaticity; no-slip
Tube inlet	90 °C; $\dot{m}$ = 0.028 kg/s
Tube outlet	p_{out} = 1 atm
Everywhere (initial condition)	T = 70 °C; u = v = w = 0

3.2.4. Numerical methods and validation

After generating the 3D structure, governing equations with appropriate boundary conditions are solved using the commercial finite volume code ANSYS software (see **Fig. 3.3**). The pressure correction equation has been discretized using the well-known PRESTO scheme, while the coupling of pressure and velocity was discretized using the SIMPLE algorithm. Furthermore, to solve the momentum and energy equations, the QUICK approach was employed. The convergence criterion for the continuity, momentum, and energy equations were set at 10^{-5}, 10^{-5}, and 10^{-6}, respectively, ensuring the guaranteeing the invariance of the solution. The under relaxation factors were chosen to be 0.9 for the liquid fraction, 1.0 for energy, 0.7 for velocity, and 0.3 for pressure. In addition, the QUICK approach is used to solve the momentum and energy equations. Furthermore, the PRESTO scheme strategy is used to solve the pressure correction equation. Convergence criterion for continuity, momentum, and energy equations, present a convergence criterion of 10^{-5}, 10^{-5}, and 10^{-6} guaranteeing the invariance of the solution.
Space and time grid independence referred to Case A with no PCM is resumed in **Fig. 3.3** in terms of Liquid Fraction (LF). Because using a smaller grid had no discernible impact on the curves, the final grid that was chosen contains 1152333 elements. With references to the time step analyzed, say Δt = 1, 0.5, and 0.1 seconds, no relevant deviations have been found. Therefore, by accounting for computational times too, a time step of 0.5 seconds is here assumed by also considering that this time is far smaller than typical transient times here simulated.

To test the model, four different literature sources were employed: 1) Melting PCM, 2) Melting Nano-enchantment PCM with metal foam, 3) Photovoltaic thermal (PVT), 4) Solidification PCM, and 5) FPSC with fin.

First, a comparison of both experimental and numerical results on the average PCM temperature, T_{avg}, profile of melting of RT82 in a TTHX with both inner and outer tubes is performed between the present modeling and the work from Al-Abidi et al. [67]. It can be seen from **Fig. 3.4** that the present result has a reasonable agreement with that of the study from Al-Abidi et al. [67]. A second comparison test is performed against the numerical work of Mahdi et al. [68] for the melting process inside TTHX containing a NEPCM-metal foam (see **Fig. 3.5**). The LFs show good agreement for two different porosities with results from Mahdi et al. [68]. It is also emphasized that Mahdi et al. [68] validated their model using published experiments. As a third

validation to verify the accuracy of this model in modeling PVT systems, a numerical analysis by Khanjari et al. [69] was used (see **Fig. 3.6**). Khanjari et al. [69] examined the effectiveness of a PVT collector using 5% nanoparticles as the working fluid and 800 W/m^2 of solar energy as heat source. The profiles of both the average T_{out} and $T_{absorber}$ illustrate good agreement between the validation of the present study and the study of Khanjari et al. [69]. Finally, comparisons with Al-Abidi et al. [70] (see **Fig. 3.7**) are here shown for the solidification process of RT82 when a TTHX is considered. The aforementioned interpretation is convincing evidence of the correctness of the current approach and dependability in replicating the melting and solidification process. In **Figure 3.8**, the liquid fraction of PCM during a summer day is compared with numerical results from Badiei et al. [71]; In that study, the authors utilized a 3D transient CFD model to examine an FPSC integrated with a layer of PCM for accurate modeling of the flat plate solar collector. The model employed in this work was adapted to facilitate comparison with the results presented in [71]. This comparison demonstrates acceptable agreement with their numerical data, and it is noted that Badiei et al. [71] validated their model with experimental data [72], [73]. **Tables 3.4** display average and maximum deviations between simulations and various literature sources, covering a comprehensive dataset for the purpose of comparison. The small deviations observed in both the average and maximum differences indicate that there is an excellent agreement, supporting the validity of the current modeling approach.

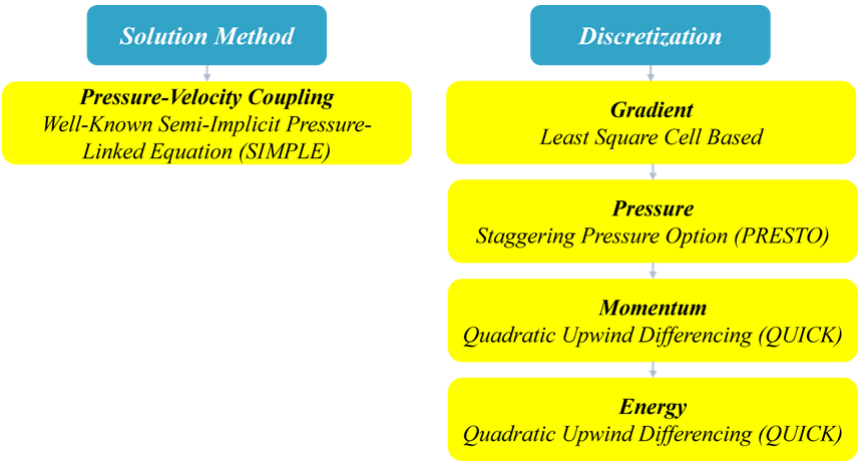

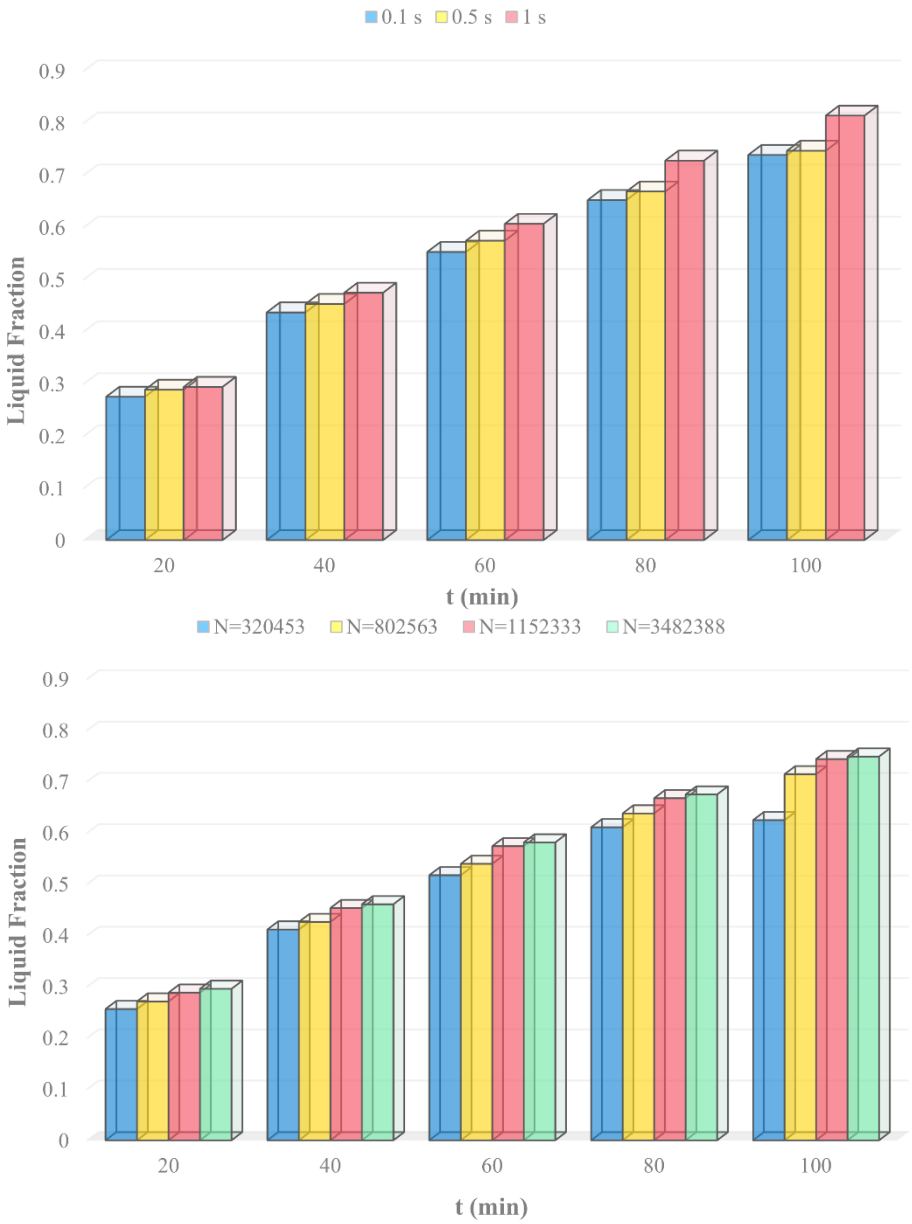

Fig. 3.3 Numerical solution: Fluent workflow (top), and LF of whole FPSCs during the melting process (pure PCM): (middle) the impact of Δt on the LF and (bottom) the impact of grid elements number N on the LF

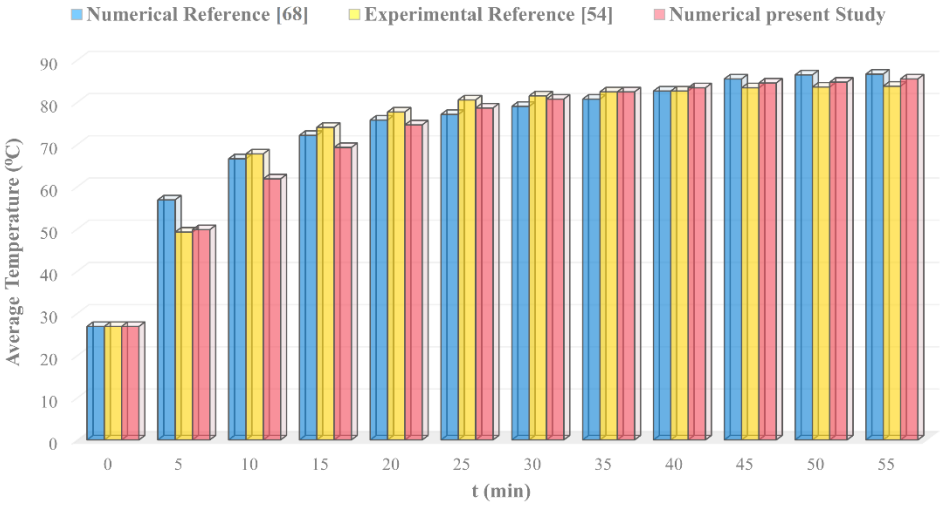

Fig. 3.4. PCM Average temperature vs time: comparisons with both simulations and experiments from Al-Abidi et al. [67]

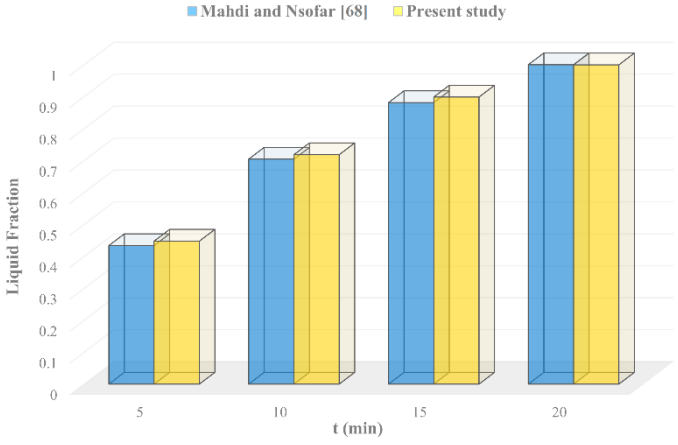

$$\varepsilon = 0.95$$

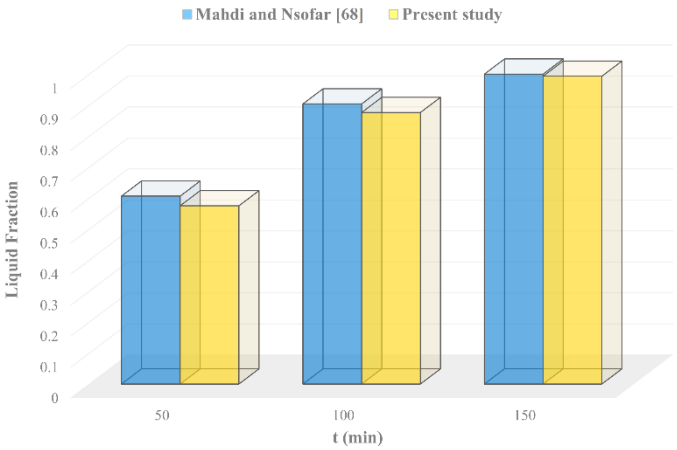

$$\varepsilon = 0.98$$

Fig. 3.5. LF evolution vs time for ε = 0.95 and ε = 0.98 compared with [68]

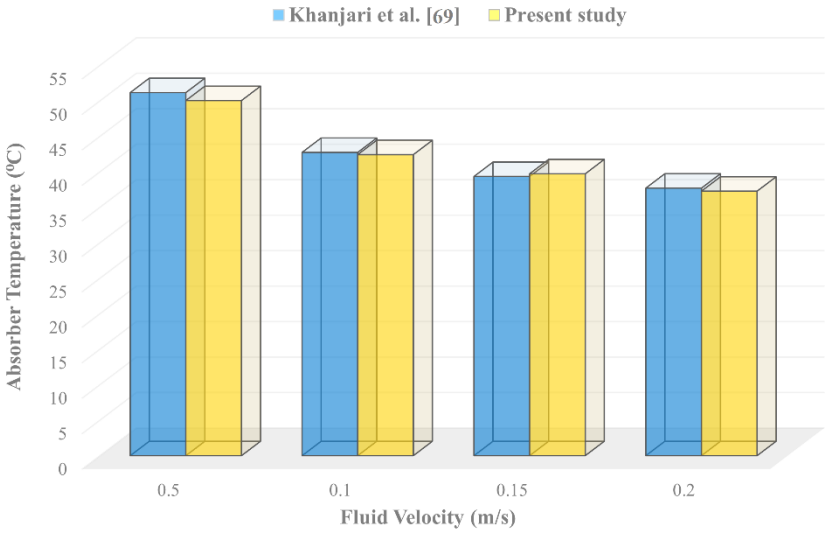

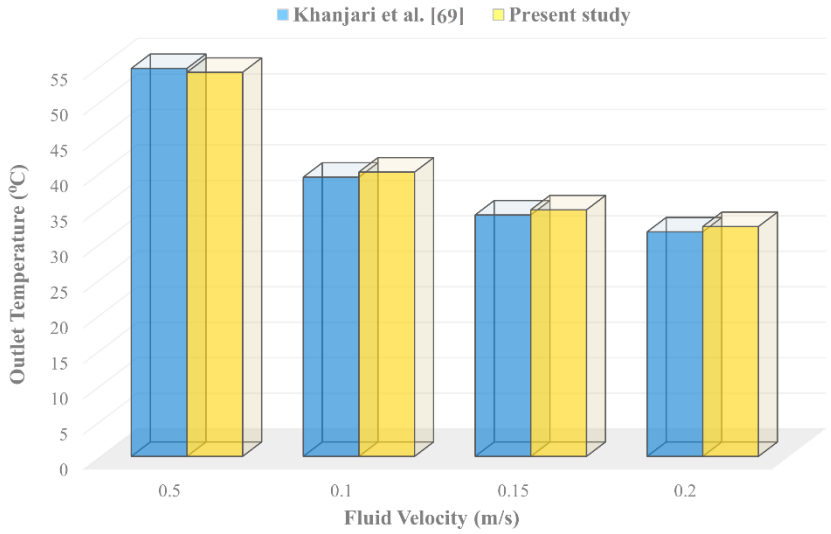

Fig. 3.6. Absorber (top) and outlet (bottom) temperature vs. HTF inlet velocity: comparisons with [69]

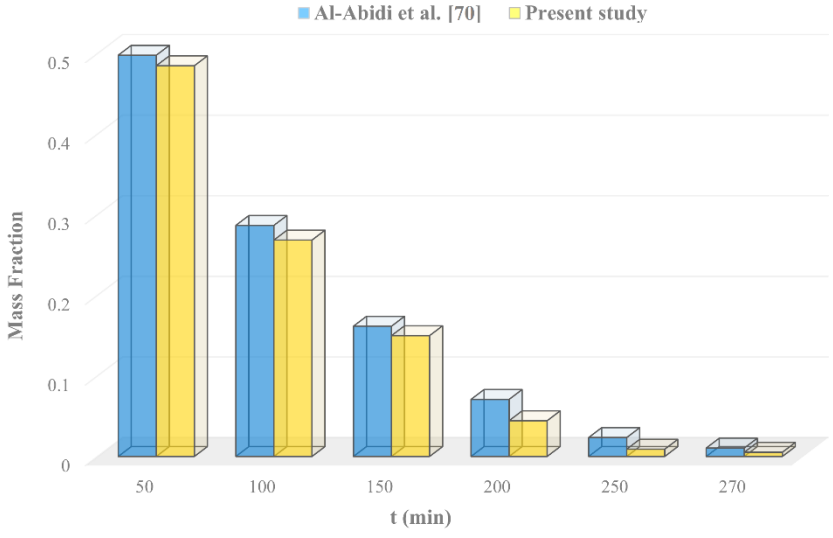

Fig. 3.7. Comparison between present work and Al-Abidi et al. [70]

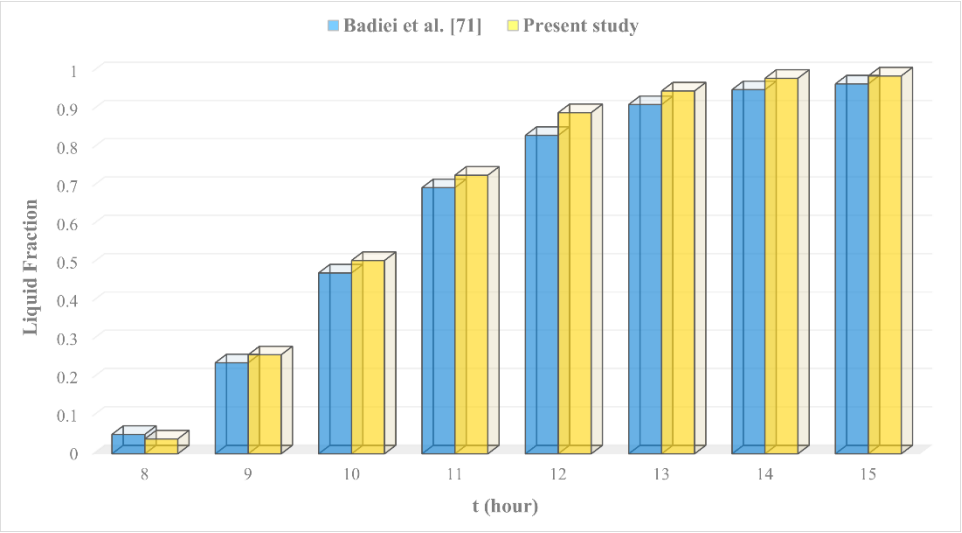

Fig. 3.8 Liquid fraction of PCM in FPSC during the summer day: comparisons with [71]

Table 3.4. Deviations between liquid fraction, and average temperature obtained by here and data provided by [67], [68], [69], [70] and [71]

	Average difference (LF or °C)	**Maximum difference (LF or °C)**
Experimental [67]	**(°C):** 0.9231	**(°C):** 5.92
Numerical [67]	**(°C):** 1.16	**(°C):** 7.06
Numerical- ε = 0.95 [68]	**(LF):** 0.00745	**(LF):** 0.02
Numerical- ε = 0.98 [68]	**(LF):** 0.017	**(LF):** 0.031
Absorber Temperature [69]	**(°C):** 0.40	**(°C):** 1.315
Outlet Temperature [69]	**(°C):** 0.38	**(°C):** 0.76
Numerical [70]	**(LF):** 0.00745	**(LF):** 0.02
Liquid fraction [71]	**(LF):** 0.023	**(LF):** 0.057

3.3. Results and discussion

When LHTES systems are designed, monitoring the liquid fraction evolution (Eq. 7) is fundamental since it establishes how fast are charging and discharging process to store as much heat as possible when temperature gradients are not relevant. If phase change time is not so high, then one could take advantage of fast transient induced by short charging and discharging windows. Besides,

improving the liquid fraction evolution aspects would be also helpful in order to reduce the storage system size.

3.3.1. Melting process: Effects of geometrical design

A comparison in terms of bar chart with respect to geometries investigated (Case A, Case B, and Case C) referred to pure PCM, in order to appreciate the melting time at total simulation time, is depicted in **Fig. 3.9 (a)** Comparisons between Cases A, B, and C, that respectively refer to a straight collector, wavy wall, and wavy wall-Y shaped fin (**Fig. 3.1**), have been performed by constraining the heat exchanger area, allowing to have a fixed quantity of PCM with respect to all the cases here considered. In this study, the analysis is based on assuming that the HTF and PCM containers have the same volume in all cases. Results show that the LFs for the FPSC with wavy wall-Y shaped fin (Case C) with pure PCM are higher than other Cases, which means that employing wavy wall and fin allows to melt more PCM. Both wavy wall and fin system is proposed to extend the heat transfer area. **Fig. 3.9 (b)** and **Fig. 3.9 (c)** present LFs and PCM-temperature average, T_{avg}, evolution overtime for all cases with pure PCM. It is shown that the melting fraction rapidly increases at the beginning; on the other hand, this increase becomes smaller, approaching to a unitary value once melting is completed. After some time, the temperature would not increase as at the beginning of transient, because there is more PCM melted that generally reduces temperature gradients within the domain. Once the transient approaches to an end, it seems that temperature increases faster again. This because there is a larger amount of PCM fully melted. Results here achieved showed that Case C with pure PCM allows to a reduction in terms of complete melting of a 25.66% if compared to Case A; on the other hand, this value is 21.96% when Case C is compared to Case B. This means that, compared with Case A, strong advantages can be found for Case C instead of Case B.

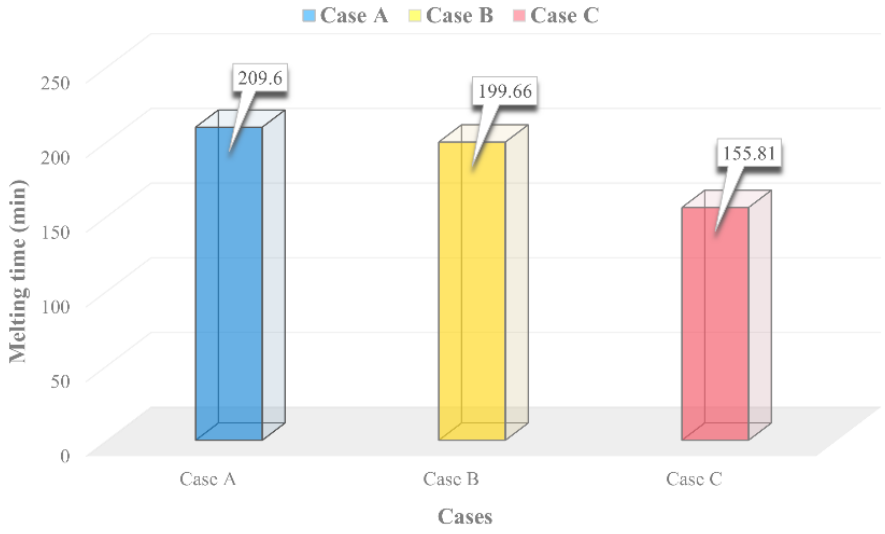
Case A
Case B
Case C
209.6
199.66
155.81
250
200
150
100
50
0
Melting time (min)
Case A
Case B
Case C
Cases

(a)

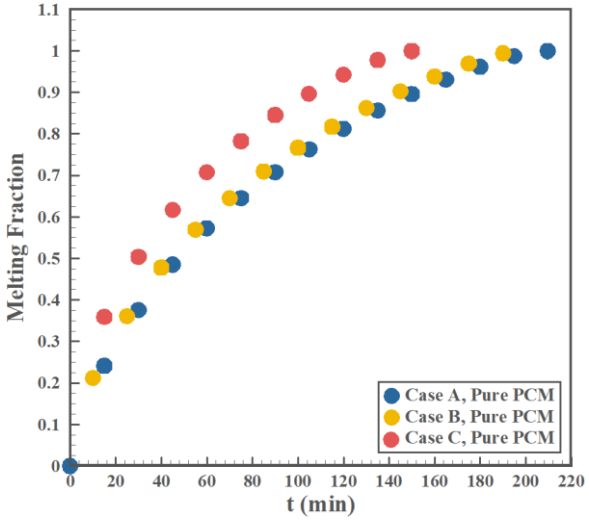
1.1
1
0.9
0.8
0.7
0.6
0.5
0.4
0.3
0.2
0.1
0
Melting Fraction
0
20
40
60
80
100
120
140
160
180
200
220
t (min)
Case A, Pure PCM
Case B, Pure PCM
Case C, Pure PCM

(b)

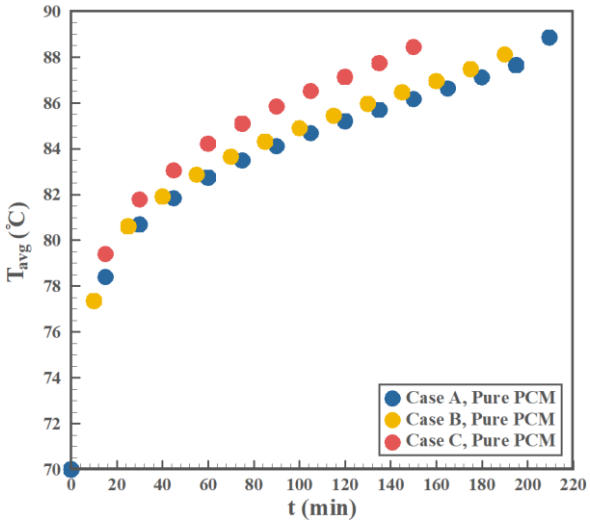

(c)

Fig. 3.9. (a) Melting time, (b) LF, and (c) T_{avg} for all integrated pure PCM cases

3.3.2. Melting process: Effects of nanoPCM-Metal Foam

In **Fig. 3.10**, melting times referred to cases here investigated with pure PCM or NEPCM, are compared. It is shown that wavy wall-Y shaped fin (Case C) presents faster melting among all cases. With references to Case A with just pure PCM, including wavy wall (Case B) and wavy wall-Y shaped fin (Case C) together with NEPCM, causes a melting time reduction of 18.15% and 40.17%, respectively.

In **Figure 3.11**, melting time and time-saving percentage are presented for different geometries of investigated solutions referred to pure PCM, NEPCM, PCM-metal foam, and NEPCM-metal foam. Percentages are referred to (Case A-pure PCM). In all the cases, with the addition of nanoparticles, the melting time is drastically reduced. Also, a faster melting compared with other cases is shown if wavy wall together with the Y-shaped fin (Case C) is considered. On the other hand, it is remarked that foams have more effect than nanoparticles on melting time; combining this allows to a slight additional improvement. From **Fig. 3.11**, it is shown that the best solution, which is Case C that considers nanoparticles and foam together, allow to reduce melting time of a 87.21% compared to Case A with pure PCM.

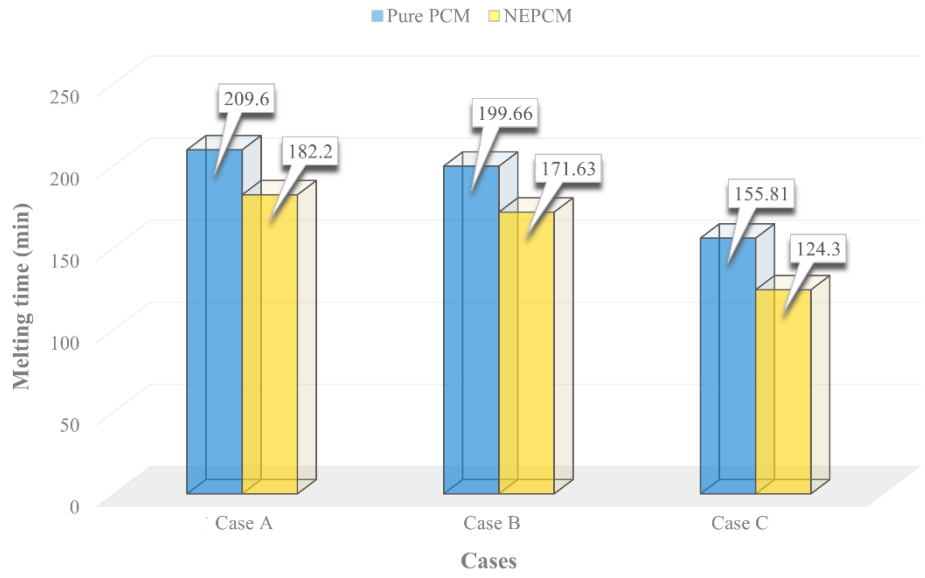

Fig. 3.10. Bar chart for the melting time for different cases with 0 or 5% of nanoparticles

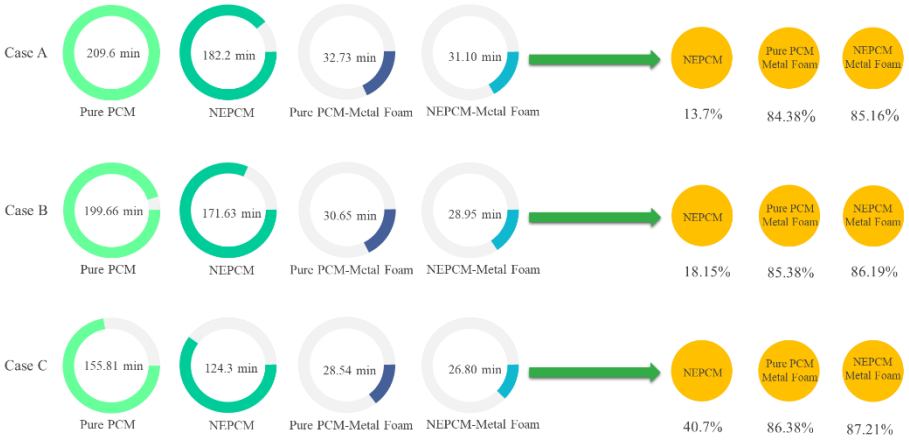

Fig. 3.11. Time-saving in the melting process for all cases with different configurations compared to Case A-pure PCM

Heat storage rates $p_{L,m}$ here obtained using Eq. 8 are presented in **Fig. 3.12**. With this term one would appreciate how fast melting is when compared to the stored energy. The latent heat of fusion, and liquid sensitive heat of PCM, as well as the solid sensitive heat of the additions, are all covered by the thermal

storage capacity. In actuality, the latent heat of fusion is the most important metric in determining the TES capacity, and the sensitive heat can be neglected since it is much less if the storage system is well-designed. The amount of energy stored depends on the specific heat, the temperature change, the amount of material melting and phase change time. The shorter the melting period (i.e., the quicker it melts), the higher the rate of energy storage. It is here observed that the average storage heat rate is always obtained starting from the stored energy, where the time at the denominator corresponds to the melting time that depend on the single case. When compared with pure PCMs, by employing nanoparticles, one obtains slightly higher heat storage rates $p_{L,m}$; on the other hand, employing metal foams drastically improves $p_{L,m}$. This means that combined solutions allow to have a strong increase in terms of stored energy velocity, especially due to the inclusion of metal foam.

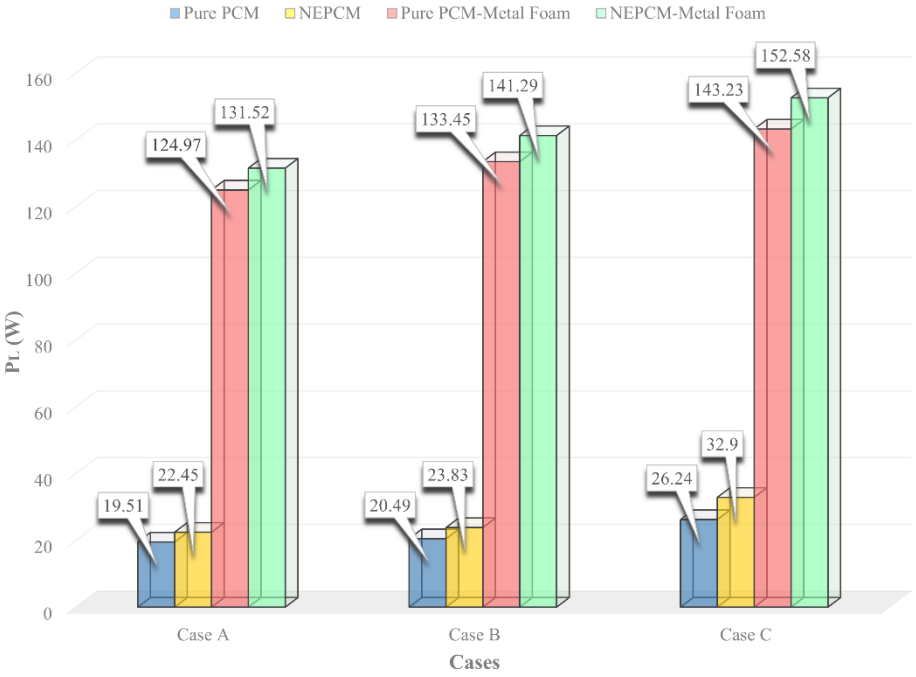

Fig. 3.12. A resume of average storage heat rate for different configurations

A comparison among all cases, namely cases A, B, and C with pure PCM and NEPCM-Metal Foam, is presented in **Figs. 3.13** and **Fig. 3.14**, in terms of LF and T_{avg} evolution after 20 minutes. From the figures it is shown that when the wavy wall system coupled with the Y-shaped fin is used, most of the PCM

is fully melted. This effect is attributed to the because the irregular shape due to wavy wall and Y shaped fin, that promotes heat transfer in the domain, especially in the PCM core region. In addition, Y-shaped fins have the capacity to create vortices in the fluid PCM can be generated close to the fin, around them, which improves heat transfer by encouraging turbulence and fluid mixing. This effect is especially helpful in low-speed flow situations when laminar flow may restrict the rate of heat transfer, and might be similarly applied for PCMs since these present some liquid in which there is some natural convection. In **Fig. 3.14**, temperature fields are shown too. From this figure, it is evident that there is also more penetration from the radiative heat flux due to the extended surfaces, making generally temperatures higher.

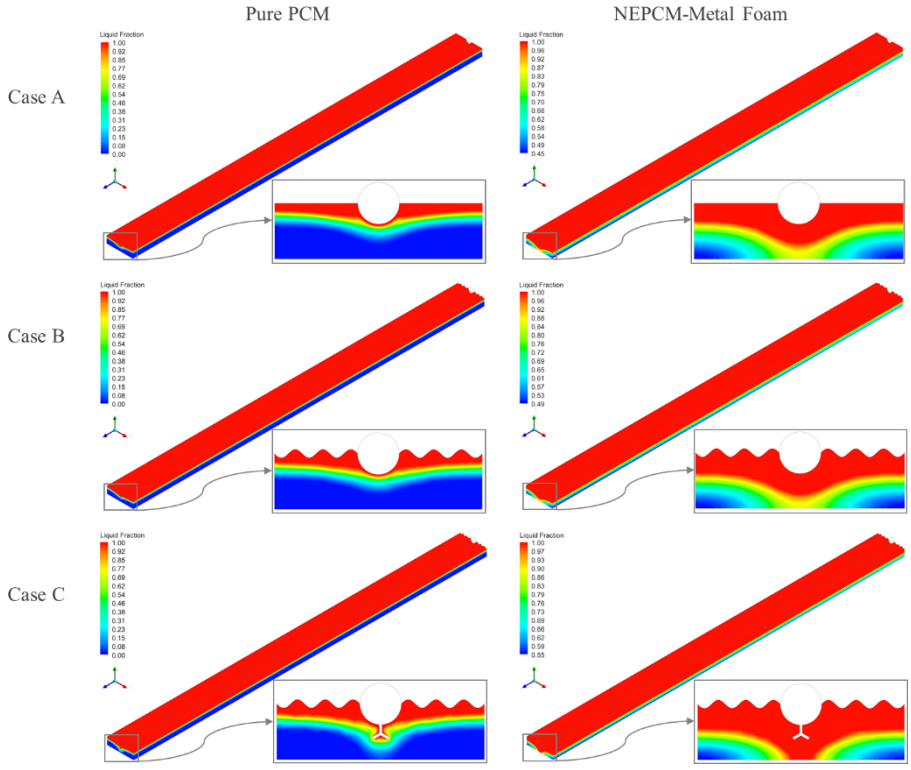

Fig. 3.13. LF field all Cases with pure PCM and NEPCM-Metal Foam after 20 minutes

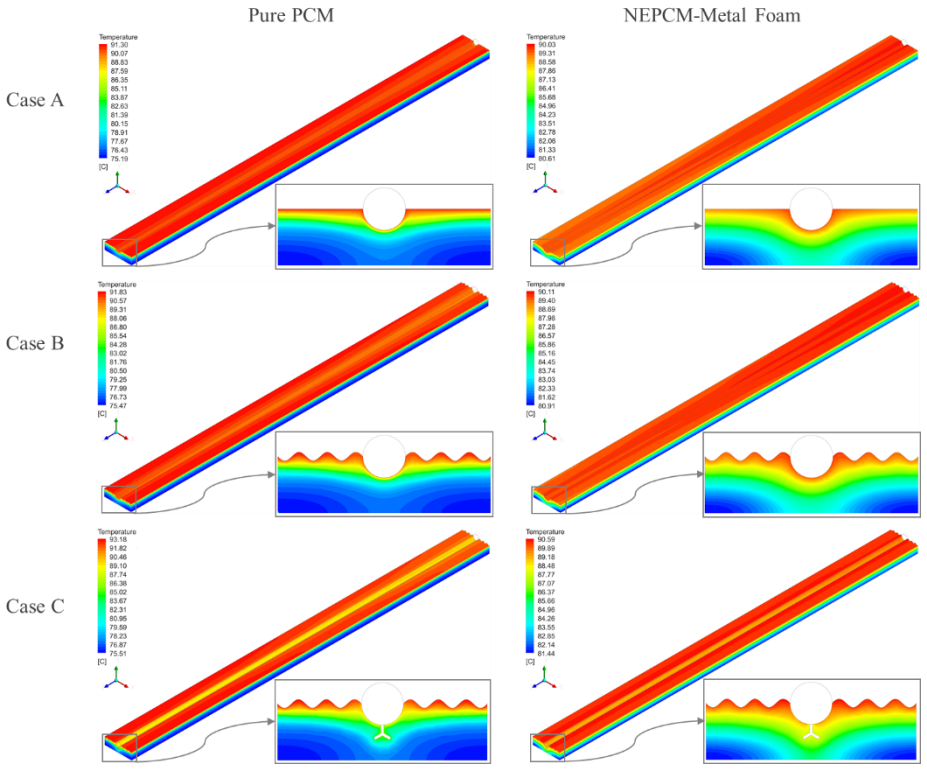

Fig. 3.14. T_{avg} field all Cases with pure PCM and NEPCM-Metal Foam after 20 minutes

3.3.3. Solidification process: Effects of nanoPCM-Metal Foam

Comparisons in this section are primarily focused on the two optimal geometry scenarios, namely the pure PCM case without the addition of nanoparticles or foam (referred to as Case B), and the comprehensive case that involves NEPCM-Metal foam (referred to as Case C). As mentioned in the boundary conditions description section, during solidification, it is assumed that during solidification there is no sun radiation to simulate sudden cloudy weather, or in general references is here done to applications that involve energy reuse during afternoon or night. It can be seen that the gradient in the LF is greater at the beginning of the discharging process and that the discharging rate of the phase change material steadily diminishes with time. Additionally, the discharging process rate is increased during the first discharge phases due to the lower heat resistance. Result shows that both melting and solidification lasts each for about 3 hours.

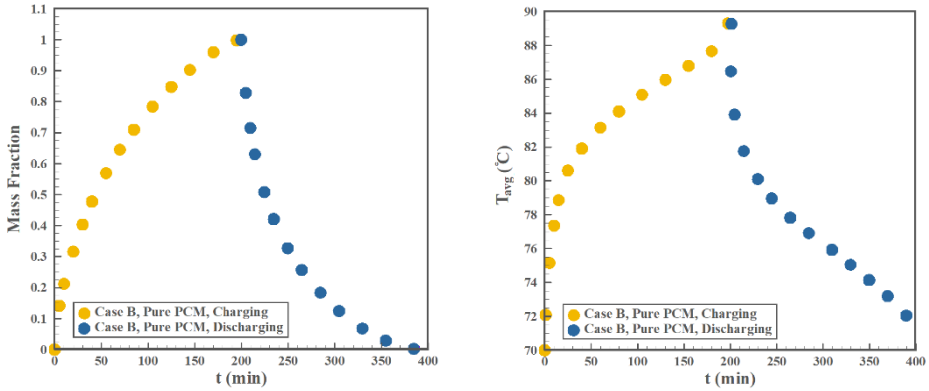

Fig. 3.15. LF and T_{avg} changes during a successive charging and discharging process for Case B-pure PCM

Bar chart comparisons in terms of solidification time and heat storage rate computed via Eq. 8 are shown in **Fig. 3.16**. Each case reported has his own melting time. Heat transfer performances in terms of both solidification time and heat storage rate look to be far better if nanoparticles are employed, which means far more PCM is freezed at equal time by adding nanoparticles and metal foam. When comparing Case C-NEPCM-Metal Foam to Case B-pure PCM, a reduction of a 84.49% in terms of melting time has been found. The average storage heat rate is always computed from the stored energy, while the time at the denominator corresponds to the melting time that depends on the single case. The $p_{L,s}$, for NEPCM-Metal Foam, is drastically higher than for pure PCM. This makes freezing velocity to be much higher if combined solutions are considered.

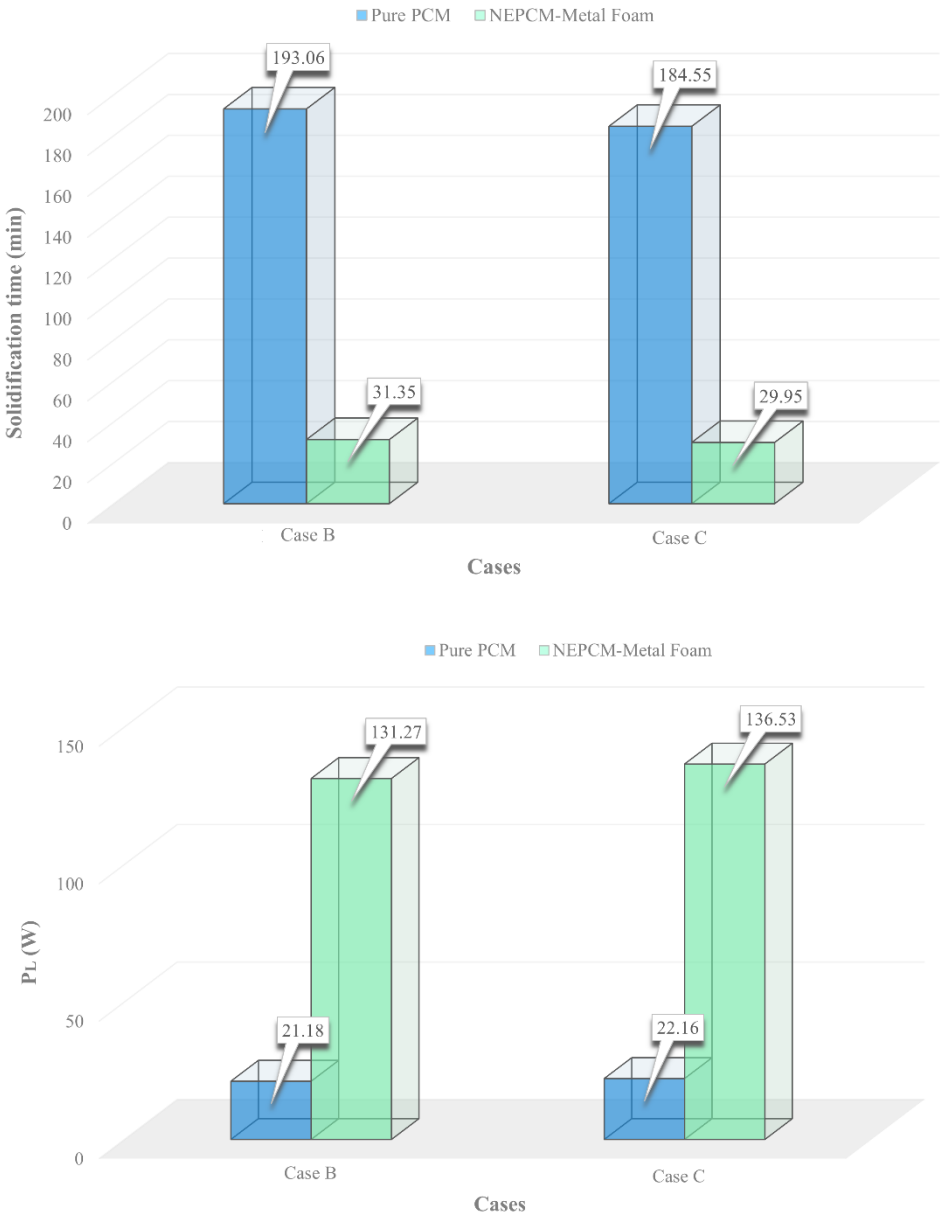

Fig. 3.16. Solidification time (upper) for different cases with 0% or 5% of nanoparticles and rate of heat storage (lower) for different cases with pure PCM and NEPCM-Metal Foam

Comparisons in terms of LF and T_{avg} after 20 minutes is shown in **Figs. 3.17** and **18**. Initially the whole PCM is assumed to be in liquid state with a uniform temperature of 93°C. Also, it is reminded that the surface of the inner tube is exposed to a temperature, T_{HTF}, which is lower than the lowest solidification temperature of the PCMs in order to have the phase change. This causes solidification to begin at the surface of the outer tube, generating a thin solidified layer next to the surface of the outer tube. As will be demonstrated later in this section, the addition of nanoparticles or porous foam significantly accelerates the PCM solidification. The evolution of solidification was evaluated at a constrained time (20 min) in terms of temperature and LF fields. As for melting, natural convection might have a role here in solidification too. Especially for pure PCM cases, it can be seen some unregular temperature variations that can be attributed to unstable natural convection. Qualitatively similar temperature fields have been observed for PCM with foams heated from below [41], [74]. The solid region moves from the top surface, as shown by the outlines. As previously noted, free convection is beneficial during the first phases of the freezing process; but, as the process progresses, the natural convection impact tends to reduce. Result indicates that when comparing NEPCM-Metal foam with pure PCM, it is clear that there is more solid PCM after 20 minutes. Also, for NEPCM-Metal Foam, it seems that there is less convection at this time. This because foam generally acts as something that makes an obstruction to natural convection movement if compared to pure PCM. Furthermore, if wavy wall together with Y-shaped fin is employed, there is more melted PCM. This happens because the temperature of heat transfer fluid absorbed from Y-shape fin; furthermore, there is radiative heat flux penetration within the domain due to the wavy wall irregular shape. All this is something that helps heat transfer especially in the PCM core. Consequently, for all the cases, when comparing Cases B and C, it is shown that the fin (Case C) would promote local solidification because of the extended area. Similar conclusions can be done by considering temperature fields (**Fig. 3.18**).

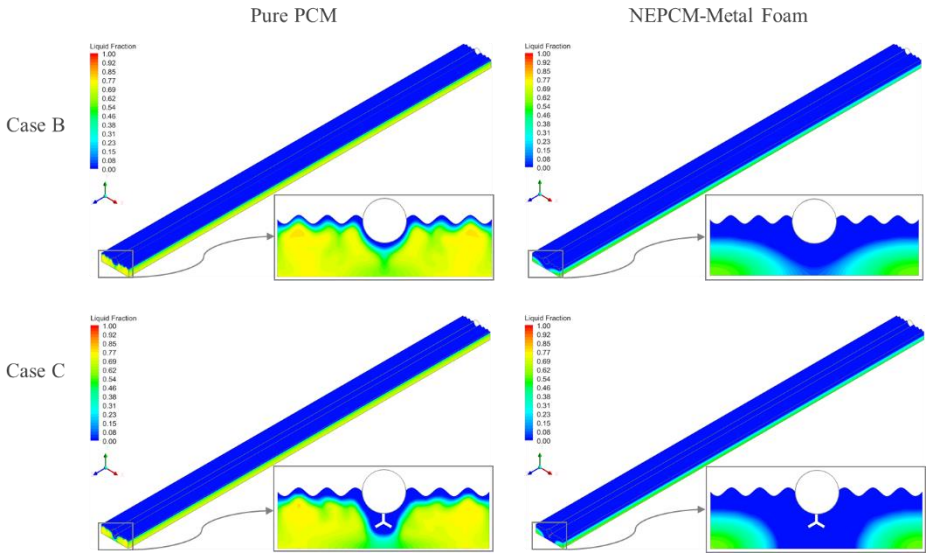

Fig. 3.17 LF field all Cases with pure PCM and NEPCM-Metal Foam at 20 minutes

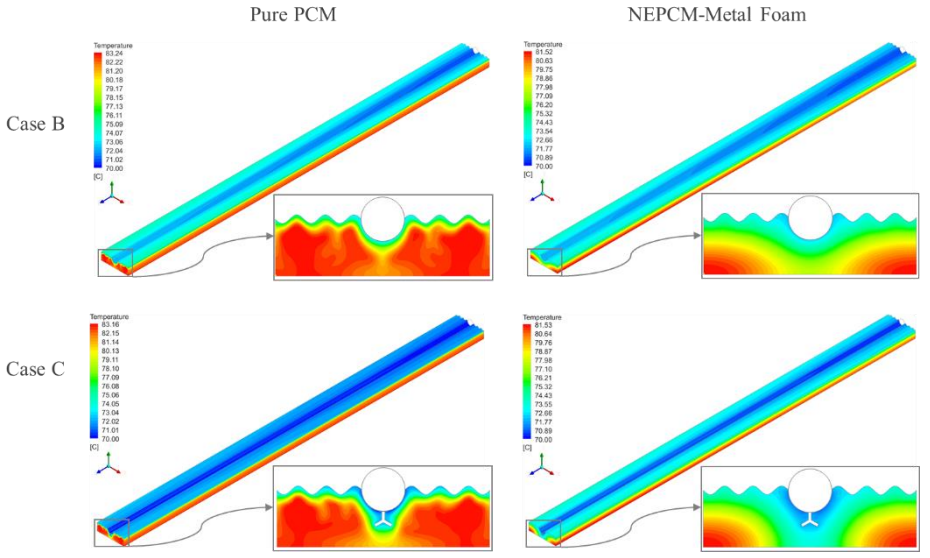

Fig. 3.18. T_{avg} field all Cases with pure PCM and NEPCM-Metal Foam at 20 minutes

3.3.4. Solidification process: Effects of various nanoparticles

The influence of various type of nanoparticles on the solidification time of PCMs is shown in **Figure 3.19** to highlight the melting fraction if one constraints the simulation time to be equal to the NEPCM-Metal Foam case, say 10 minutes. A resume of thermophysical properties of various type of nanoparticles is depicted in **Table 3.5**. The findings obtained from the figure reveal that in Case C-NEPCM, adding Al_2O_3 nanoparticles to PCM had the biggest impact on the solidification process. This might be attributed to the fact that such nanoparticles present the highest thermal diffusivity (see **Table 3.5**).
A bar chart comparison is shown in **Fig. 3.20** for the different volume fractions of the nanofluid for best case type of investigated solution (Case C-NEPCM-Metal Foam); as before, comparisons are done at equal simulation time, *i. e.* 10 minutes. The nanofluid employed in this analysis is Al_2O_3. The findings obtained from the figure reveal that in Case C-NEPCM-Metal Foam with nanoparticles (5%) to water had the biggest impact on the solidification process. This because the higher the percentage, the higher is the effect of nanoparticles on the overall heat transfer. However, one should also underline that increasing the volume fraction allow to other issues like for instance sedimentation.

Table 3.5. Thermophysical properties of different types of nanoparticles

Property	**Al_2O_3**	**SiO_2**	**ZnO**	**CuO**
ρ (kg /m^3)	3600	2200	5600	6500
c (J /kg K)	765	703	495.2	535.6
k (W/m K)	36	1.2	13	20
β (1/K)	5.8	5.5	4.3	4.3
α (mm^2/s)	13.228	0.7759	4.688	5.745

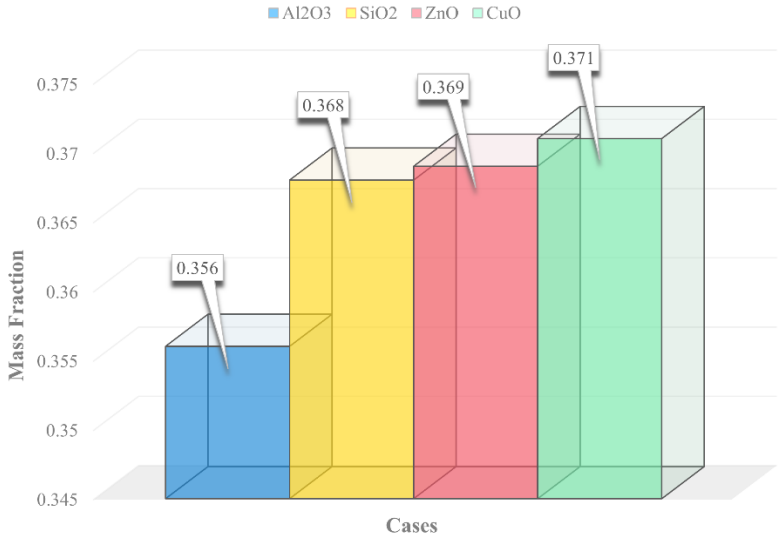

Fig. 3.19. Bar chart for the LFs at t = 10 min for Case C-NEPCM-Metal Foam for different nanoparticles

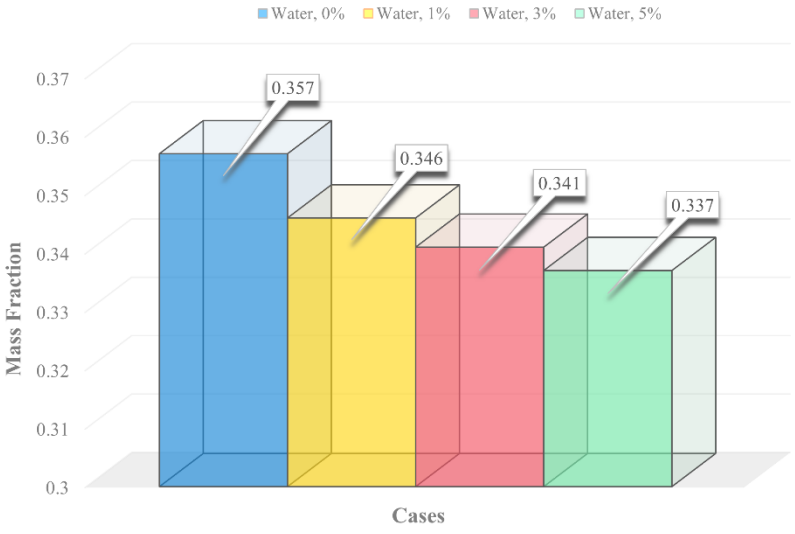

Fig. 3.20. Bar chart for the LFs at t = 10 min for Case C-NEPCM-Metal Foam for different nanofluids volume fractions

3.3.5. Solidification process: Effects of different Stefan numbers

Comparisons for different Stefan number for best case type of investigated solution (NEPCM-Metal Foam) referred to Case C, in order to show the fraction at a fixed simulation time, say 5 minutes because this is the melting time of the

NEPCM-Metal Foam case, are represented in **Fig. 3.21**. In this sub-sub-section, the effects of inlet water (HTF) temperature are considered too. In particular, values of 70 °C, 65 °C, 60 °C and 55 °C are analyzed and included in the analysis shown in **Fig. 3.21** by means of different modified Stefan number, Ste:

$$Ste = \frac{c_p(T_m - T_{HTF})}{L} \tag{9}$$

Herein, Stefan numbers of 0.125, 0.189, 0.239 and 0.295, respectively, are employed. This means that for these three configurations the latent heat contribution should increase when HTF inlet temperature increases. **Figure 3.21** shows the impact of Stefan number on LF at an equal time (t =5 min). As time increase the difference of various cases becomes more observable, the case with Ste = 0.295 has the lowest fraction.

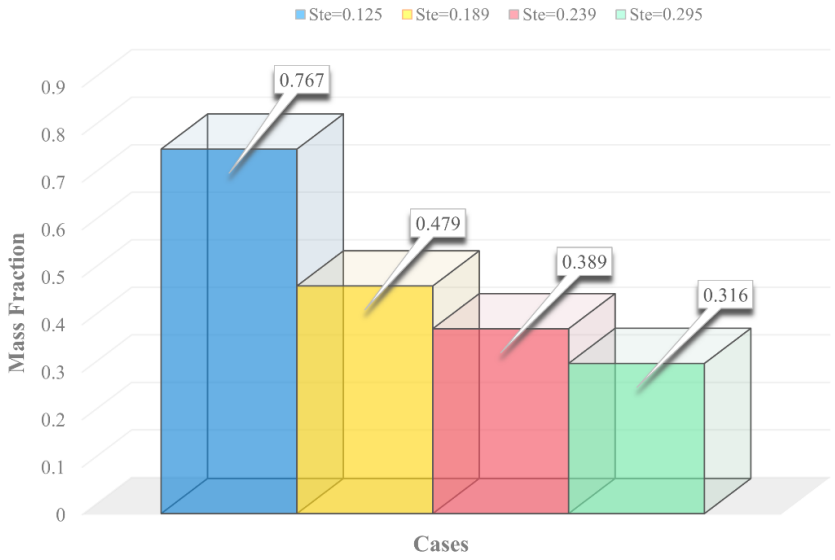

Fig. 3.21. Bar chart for the LFs at t = 5 min for Case C-NEPCM-Metal Foam for different Stefan number

3.3.6. Solidification process: Effect of various metal foam porosities

Summary of solidification time, as well as Case C time saved, and heat storage rate $p_{L,s}$ (Eq. 8), is shown in **Fig. 3.22** to underline how relevant is porosity on the thermal performances of the device proposed as Case C. Here, two distinct porosities (say, 0.95 and 0.92) are employed at equal PPIs (say, 10) since it has been shown that porosity has a greater impact than PPIs throughout the period of the research [37], [41], [75], [76]. The time saving and rate of

energy released for the porosity of 92% is almost higher than all the other cases. In comparison with the pure PCM system, the effect of porous foam and nanoparticles is significant on system, where foams show to have a primary role in these thermal performances enhancement. Also, lowering porosity would reduce solidification time, as it has been widely observed over the years [28],[47].

Fig. 3.23 shows the LFs distribution throughout the solidification process for the Case C-NEPCM-Metal Foam with porosities of 95%, 92%, compared with the pure PCM system in the solidification process for the sake of comparison. It is clear that including both metal foam and nanoparticles always makes the solidification process faster, as also observed before in **Fig. 3.23**. It is shown here that decreasing porosity has a significant effect on the solidification process, even if this might suppress natural convection [77] For this case, one can observe that solidification is more or less reached for a 92% porosity.

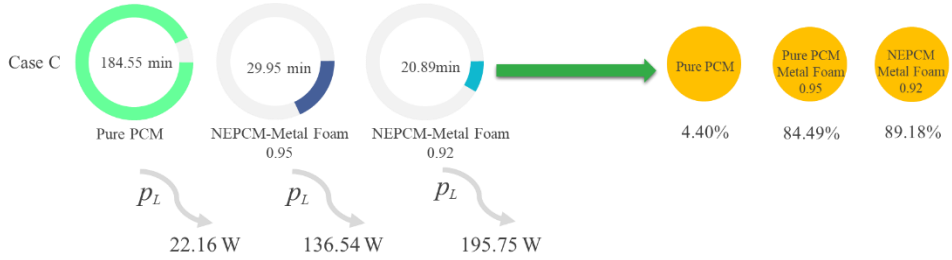

Fig. 3.22. Time-saving in the melting process for Case C with different porosity compared to Case B-pure PCM

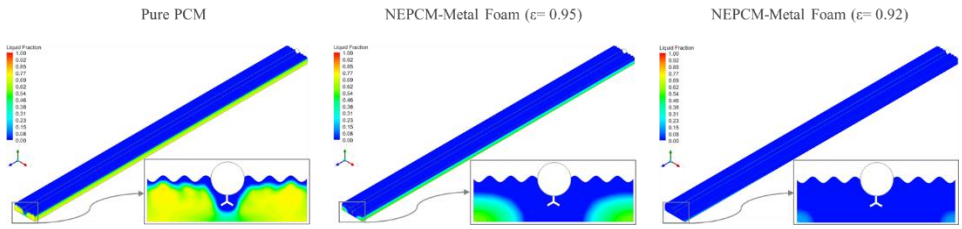

Fig. 3.23. LF field for Case C with different porosity at 20 minutes

Despite the relatively high cost associated with implementing PCM, metal foam, and nanoparticles in solar collectors, the utilization of these specialized materials can significantly enhance the thermal performance of the system. This enhancement results in a higher conversion efficiency of solar energy into heat,

leading to potential cost savings and reduced energy consumption for commercial enterprises relying on solar energy for hot water or heating. Additionally, incorporating PCM with metal foam and nanoparticles can mitigate the environmental impact of solar energy systems, reducing energy consumption and the overall carbon footprint. As a result, these advanced solar collectors offer a more eco-friendly and sustainable option for energy production, while also potentially minimizing sizing requirements.

3.4. Conclusions

Nowadays, thermal energy storage systems based on phase change materials are crucial in order to store and release heat that comes from solar energy-based intermittent sources like flat plate solar collectors for solar energy. Improving their thermal performances is therefore fundamental to improve characteristics like stored or released energy at equal time or size. When considering practical implementation, the primary hurdle is enhancing the heat transfer performances of PCM while it undergoes the melting and solidification phase. To accomplish this task, additives like aluminium oxide (Al_2O_3), silicon dioxide (SiO_2), zinc oxide (ZnO), and copper oxide (CuO) nanoparticles, aluminum foams, or extended surfaces like wavy walls and Y-shaped fin, have been simulated in this work; based on the conditions of the flat plate solar collector system to be analyzed, the RT82 (RUBITHERM) phase change material has been used. Simulations have been run by considering different combinations of the aforementioned solutions, as well as a whole melting/solidification cycle to consider a practical situation in which for instance the sun source is reduced due to cloudy weather or similar conditions. LHTES unit was modeled by employing the enthalpy-porosity method. Governing equations have been written by employing the porous media approach under the LTNE assumption when foam is included; on the other hand, nanoparticles are considered by assuming that the PCM acts as a unique equivalent homogeneous material with intermediate properties. The heat transfer fluid – say, water – is modeled too with Navier-Stokes equations. For the boundary conditions, during melting a constant incoming solar flux is assumed because of the relatively short transient time, while water velocity, as well as temperatures, are chosen to be consistent with typical industrial and domestic applications. During the solidification, there is no incoming solar flux, to replace situations like cloudy weather or in general with no sunlight available. Case A (straight wall), Case B (wavy wall), and Case C (wavy wall plus Y-shaped fin have been analyzed for all the heat enhancement techniques considered. The aim of this study is to appreciate

which is the best solution among the ones considered with references to a flat plate solar collector and a whole charging/discharging cycle, and to understand which solution is the most impactful. The code has been extensively validated with results from the open literature, and the main outcomes from the present work are resumed in the following:

- With references to Case A (straight wall) and compared with pure PCM, adding both nanoparticles and metal foam makes melting time reduced by 85.16%; this reduction becomes 84.38% if one considers just metal foams. This means that most of the time reduction is attributed to metal foam, even if they slightly reduce the volume available to store energy;

- If one just employed geometrical changes to the structure (Cases B and C vs. case A), say wavy walls (Case B) and wavy wall with Y-shaped fin (Case C), reductions in terms of melting time reach up to a 4.74% and 25.66% when compared to pure PCM, respectively; therefore, using a Y-shaped fin is really helpful since it penetrates far inside the PCM domain;

- A combination of all the solutions investigated (Case C), which means metal foam, nanoparticles, wavy wall, and Y-shaped fin, makes melting time smaller than a 87.21% compared to the Case A with pure PCM;

- Adding nanoparticles and foam, combined with a Y-shaped fin, significantly shorten the solidification time. For example, in Case C, the inclusion of nanoparticles with foam 0.95 and 0.92 reduced the solidification time durations by 84.49% and 89.18% compared to the Case B (wavy wall) with just pure PCM;

This research gives insight for the design of charging and discharging cycles within LHS systems by modifying their functional design, including some enhancing methods too. From all the observations and arguments, it can be realized that the best configuration of FPSC occurs when nanoparticles and metals foam with wavy wall and Y-shaped fin are used, with foams that have the main role in this performances improvement. These thermal enhancement techniques would be really helpful to reduce sizes of these thermal energy storage devices, as well as to improve their capability or absorbing/releasing it from/to the working fluid, and potential benefits due to aspects like system cost reduction would allow to also apply this technology to high-capacity storage systems.

In the forthcoming Chapter 4 of this thesis, a comprehensive unveiling of strategic enhancements awaits exploration, particularly in the context of LHTES-Heat Exchangers systems. This chapter takes a deliberate and nuanced approach, honing in on the intricacies of optimizing the geometry associated with both the charging and discharging processes within these innovative systems. The optimization strategies discussed in Chapter 4 strive to propel the LHTES-DPHX systems to new heights of performance, fostering a future where these technologies play a pivotal role in the broader landscape of efficient and eco-friendly energy storage and utilization.

References

[1] Sarı A, Karaipekli A. Preparation, thermal properties and thermal reliability of palmitic acid/expanded graphite composite as form-stable PCM for thermal energy storage. Solar Energy Materials and Solar Cells. 2009 May 1;93(5):571-6.

[2] Sarı A, Kaygusuz K. Some fatty acids used for latent heat storage: thermal stability and corrosion of metals with respect to thermal cycling. Renewable Energy. 2003 May 1;28(6):939-48.

[3] Sarı A, Kaygusuz K. Thermal and heat transfer characteristics in a latent heat storage system using lauric acid. Energy Conversion and Management. 2002 Dec 1;43(18):2493-507.

[4] Eames PC, Griffiths PW. Thermal behaviour of integrated solar collector/storage unit with 65 C phase change material. Energy conversion and management. 2006 Dec 1;47(20):3611-8

[5] Chen Z, Gu M, Peng D. Heat transfer performance analysis of a solar flat-plate collector with an integrated metal foam porous structure filled with paraffin. Applied thermal engineering. 2010 Oct 1;30(14-15):1967-73.

[6] Haillot D, Nepveu F, Goetz V, Py X, Benabdelkarim M. High performance storage composite for the enhancement of solar domestic hot water systems: Part 2: Numerical system analysis. Solar energy. 2012 Jan 1;86(1):64-77.

[7] Haillot D, Goetz V, Py X, Benabdelkarim M. High performance storage composite for the enhancement of solar domestic hot water systems: Part 1: Storage material investigation. Solar energy. 2011 May 1;85(5):1021-7.

[8] Lin SC, Al-Kayiem HH, Aris MS. Experimental investigation on the performance enhancement of integrated PCM-flat plate solar collector. Journal of Applied Sciences. 2012 Dec 1;12(9):2390-6.

[9] Allouhi A, Msaad AA, Amine MB, Saidur R, Mahdaoui M, Kousksou T, Pandey AK, Jamil A, Moujibi N, Benbassou A. Optimization of melting and solidification processes of PCM: Application to integrated collector storage solar water heaters (ICSSWH). Solar Energy. 2018 Sep 1;171:562-70.

[10] Teamah HM, Lightstone MF, Cotton JS. An alternative approach for assessing the benefit of phase change materials in solar domestic hot water systems. Solar Energy. 2017 Dec 1;158:875-88.

[11] Teamah HM, Lightstone MF, Cotton JS. Potential of cascaded phase change materials in enhancing the performance of solar domestic hot water systems. Solar Energy. 2018 Jan 1;159:519-30.

[12] Khan MM, Ibrahim NI, Mahbubul IM, Ali HM, Saidur R, Al-Sulaiman FA. Evaluation of solar collector designs with integrated latent heat thermal energy storage: a review. Solar Energy. 2018 May 15;166:334-50.

[13] Shirinbakhsh M, Mirkhani N, Sajadi B. A comprehensive study on the effect of hot water demand and PCM integration on the performance of SDHW system. Solar Energy. 2018 Jan 1;159:405-14.

[14] Carmona M, Palacio M. Thermal modelling of a flat plate solar collector with latent heat storage validated with experimental data in outdoor conditions. Solar Energy. 2019 Jan 1;177:620-33.

[15] Yeh CY, Boonk KJ, Gholamabbas S, Mehrali M, Shahi M, Brem G, Mahmoudi A. Experimental and numerical analysis of thermal performance of shape stabilized PCM in a solar thermal collector. Case Studies in Thermal Engineering. 2021 Dec 16:101706.

[16] de Araujo Passos LA, van den Engel P, Baldi S, De Schutter B. Dynamic optimization for minimal HVAC demand with latent heat storage, heat recovery, natural ventilation, and solar shadings. Energy Conversion and Management. 2023 Jan 15;276:116573.

[17] Yousefi T, Shojaeizadeh E, Veysi F, Zinadini S. An experimental investigation on the effect of pH variation of MWCNT–H2O nanofluid on the efficiency of a flat-plate solar collector. Solar Energy. 2012 Feb 1;86(2):771-9.

[18] Saw CL, Al-Kayiem HH, Owolabi AL. Experimental investigation on the effect of PCM and nano-enhanced PCM of integrated solar collector performance. WIT Transactions on Ecology and the Environment. 2013 Dec 3;179:899-909.

[19] Al-Kayiem HH, Lin SC. Performance evaluation of a solar water heater integrated with a PCM nanocomposite TES at various inclinations. Solar Energy. 2014 Nov 1;109:82-92.

[20] Owolabi AL, Al-Kayiem HH, Baheta AT. Nanoadditives induced enhancement of the thermal properties of paraffin-based nanocomposites for thermal energy storage. Solar Energy. 2016 Oct 1;135:644-53.

[21] Lin SC, Al-Kayiem HH. Evaluation of copper nanoparticles–Paraffin wax compositions for solar thermal energy storage. Solar Energy. 2016 Jul 1;132:267-78.

[22] Verma SK, Tiwari AK, Chauhan DS. Experimental evaluation of flat plate solar collector using nanofluids. Energy conversion and Management. 2017 Feb 15;134:103-15.

[23] Mehrali M, Johan E, Shahi M, Mahmoudi A. Simultaneous solar-thermal energy harvesting and storage via shape stabilized salt hydrate phase change material. Chemical Engineering Journal. 2021 Feb 1;405:126624.

[24] Kalbande VP, Fating G, Mohan M, Rambhad K, Sinha AK. Experimental and theoretical study for suitability of hybrid nano enhanced phase change material for thermal energy storage applications. Journal of Energy Storage. 2022 Jul 1;51:104431.

[25] Sharma HK, Kumar S, Kumar S, Verma SK. Performance investigation of flat plate solar collector with nanoparticle enhanced integrated thermal energy storage system. Journal of Energy Storage. 2022 Nov 25;55:105681.

[26] Lu B, Zhang Y, Zhang J, Zhu J, Zhao H, Wang Z. Preparation, optimization and thermal characterization of paraffin/nano-Fe3O4 composite phase change material for solar thermal energy storage. Journal of Energy Storage. 2022 Feb 1;46:103928.

[27] Moghaddam ME, Abandani MH, Hosseinzadeh K, Shafii MB, Ganji DD. Metal foam and fin implementation into a triple concentric tube heat exchanger over melting evolution. Theoretical and Applied Mechanics Letters. 2022 Feb 1;12(2):100332.

[28] Zhao CY, Lu W, Tian Y. Heat transfer enhancement for thermal energy storage using metal foams embedded within phase change materials (PCMs). Solar energy. 2010 Aug 1;84(8):1402-12.

[29] Cui HT. Experimental investigation on the heat charging process by paraffin filled with high porosity copper foam. Applied thermal engineering. 2012 Jun 1;39:26-8.

[30] Li WQ, Qu ZG, He YL, Tao WQ. Experimental and numerical studies on melting phase change heat transfer in open-cell metallic foams filled with paraffin. Applied Thermal Engineering. 2012 May 1;37:1-9.

[31] Hirasawa S, Tsubota R, Kawanami T, Shirai K. Reduction of heat loss from solar thermal collector by diminishing natural convection with high-porosity porous medium. Solar Energy. 2013 Nov 1;97:305-13.

[32] Mancin S, Diani A, Doretti L, Hooman K, Rossetto L. Experimental analysis of phase change phenomenon of paraffin waxes embedded in copper foams. International Journal of Thermal Sciences. 2015 Apr 1;90:79-89.

[33] Saedodin SA, Zamzamian SA, Nimvari ME, Wongwises S, Jouybari HJ. Performance evaluation of a flat-plate solar collector filled with porous metal foam: Experimental and numerical analysis. Energy Conversion and Management. 2017 Dec 1;153:278-87.

[34] Zhu ZQ, Huang YK, Hu N, Zeng Y, Fan LW. Transient performance of a PCM-based heat sink with a partially filled metal foam: Effects of the filling height ratio. Applied Thermal Engineering. 2018 Jan 5;128:966-72.

[35] Joshi V, Rathod MK. Thermal performance augmentation of metal foam infused phase change material using a partial filling strategy: An evaluation for fill height ratio and porosity. Applied Energy. 2019 Nov 1;253:113621.

[36] Carmona M, Rincón A, Gulfo L. Energy and exergy model with parametric study of a hot water storage tank with PCM for domestic applications and experimental validation for multiple operational scenarios. Energy Conversion and Management. 2020 Oct 15; 222:113189.

[37] Dardir M, Roccamena L, El Mankibi M, Haghighat F. Performance analysis of an improved PCM-to-air heat exchanger for building envelope applications–An experimental study. Solar Energy. 2020 Mar 15;199:704-20.

[38] Yang X, Wei P, Liu G, Bai Q, He YL. Performance evaluation on the gradient design of pore parameters for metal foam and pin fin-metal foam hybrid structure. Applied Thermal Engineering. 2020 Jul 5;175:115416.

[39] Marri GK, Balaji C. Experimental and numerical investigations on the effect of porosity and PPI gradients of metal foams on the thermal performance of a composite phase change material heat sink. International Journal of Heat and Mass Transfer. 2021 Jan;164:120454.

[40] Diani A, Rossetto L. Melting of PCMs Embedded in Copper Foams: An Experimental Study. Materials. 2021 Jan;14(5):1195.

[41] Iasiello M, Mameli M, Filippeschi S, Bianco N. Metal foam/PCM melting evolution analysis: Orientation and morphology effects. Applied Thermal Engineering. 2021 Mar 25;187:116572.

[42] Li WQ, Zhang TY, Li BB, Cui FQ, Liu LL. Experimental investigation on combined thermal energy storage and thermoelectric system by using foam/PCM composite. Energy Conversion and Management. 2021 Sep 1;243:114429.

[43] Teamah HM, Teamah M. Integration of phase change material in flat plate solar water collector: A state of the art, opportunities, and challenges. Journal of Energy Storage. 2022 Oct 1;54:105357.

[44] Lei J, Tian Y, Zhou D, Ye W, Huang Y, Zhang Y. Heat transfer enhancement in latent heat thermal energy storage using copper foams with varying porosity. Solar Energy. 2021 Jun 1;221:75-86.

[45] Buonomo B, Manca O, Nardini S, Plomitallo RE. Numerical study on latent heat thermal energy storage system with PCM partially filled with aluminum foam in local thermal equilibrium. Renewable Energy. 2022 Aug 1;195:1368-80.

[46] Abdulateef AM, Mat S, Sopian K, Abdulateef J, Gitan AA. Experimental and computational study of melting phase-change material in a triplex tube heat exchanger with longitudinal/triangular fins. Solar Energy. 2017 Oct 1;155:142-53.

[47] Shahsavar A, Al-Rashed AA, Entezari S, Sardari PT. Melting and solidification characteristics of a double-pipe latent heat storage system with sinusoidal wavy channels embedded in a porous medium. Energy. 2019 Mar 15;171:751-69.

[48] Li Z, Ibrahim TK, Selim MM, Issakhov A, Albadarin AB. Simulation of sinusoidal enclosure filled with nanoparticles enhanced PCM. Journal of Molecular Liquids. 2021 Sep 1;337:116388.

[49] Keshteli AN, Sheikholeslami M. Effects of wavy wall and Y-shaped fins on solidification of PCM with dispersion of Al 2 O 3 nanoparticle. Journal of Thermal Analysis and Calorimetry. 2020 Apr;140(1):381-96.

[50] Yıldız Ç, Arıcı M, Nižetić S, Shahsavar A. Numerical investigation of natural convection behavior of molten PCM in an enclosure having rectangular and tree-like branching fins. Energy. 2020 Sep 15;207:118223.

[51] Hosseinzadeh K, Moghaddam ME, Asadi A, Mogharrebi AR, Ganji DD. Effect of internal fins along with hybrid nano-particles on solid process in star shape triplex latent heat thermal energy storage system by numerical simulation. Renewable Energy. 2020 Jul 1;154:497-507.

[52] Hosseinzadeh K, Mogharrebi AR, Asadi A, Paikar M, Ganji DD. Effect of fin and hybrid nano-particles on solid process in hexagonal triplex latent heat thermal energy storage system. Journal of Molecular Liquids. 2020 Feb 15;300:112347.

[53] Guo J, Liu Z, Du Z, Yu J, Yang X, Yan J. Effect of fin-metal foam structure on thermal energy storage: An experimental study. Renewable energy. 2021 Jul 1;172:57-70.

[54] Hosseinzadeh K, Moghaddam ME, Asadi A, Mogharrebi AR, Jafari B, Hasani MR, Ganji DD. Effect of two different fins (longitudinal-tree like) and hybrid nano-particles (MoS2-TiO2) on solidification process in triplex latent heat thermal energy storage system. Alexandria Engineering Journal. 2021 Feb 1;60(1):1967-79.

[55] Brent, A. D., Voller, V. R., & Reid, K. T. J. (1988). Enthalpy-porosity technique for modeling convection-diffusion phase change: application to the melting of a pure metal. Numerical Heat Transfer, Part A Applications, 13(3), 297-318.

[56] Arasu AV, Mujumdar AS. Numerical study on melting of paraffin wax with Al2O3 in a square enclosure. International Communications in Heat and Mass Transfer. 2012 Jan 1;39(1):8-16.

[57] Calmidi VV. Transport phenomena in high porosity fibrous metal foams. University of Colorado at Boulder; 1998.

[58] Boomsma K, Poulikakos D. On the effective thermal conductivity of a three-dimensionally structured fluid-saturated metal foam. International Journal of Heat and Mass Transfer. 2001 Feb 1;44(4):827-36.

[59] Yao Y, Wu H. Macroscale Modeling of Solid–Liquid Phase Change in Metal Foam/Paraffin Composite: Effects of Paraffin Density Treatment, Thermal Dispersion, and Interstitial Heat Transfer. Journal of Thermal Science and Engineering Applications. 2021 Aug 1;13(4):041024.

[60] Churchill SW, Chu HH. Correlating equations for laminar and turbulent free convection from a horizontal cylinder. International journal of heat and mass transfer. 1975 Sep 1;18(9):1049-53.

[61] Žkauskas A. Heat transfer from tubes in crossflow. InAdvances in heat transfer 1987 Jan 1 (Vol. 18, pp. 87-159). Elsevier.

[62] Zhang P, Meng ZN, Zhu H, Wang YL, Peng SP. Melting heat transfer characteristics of a composite phase change material fabricated by paraffin and metal foam. Applied Energy. 2017 Jan 1;185:1971-83.

[63] Yao Y, Wu H, Liu Z. Direct simulation of interstitial heat transfer coefficient between paraffin and high porosity open-cell metal foam. Journal of Heat Transfer. 2018 Mar 1;140(3).

[64] Maxwell JC. A Treatise on Electricity and Magnetism (Clarendon, Oxford).1879.

[65] Xu Y, Ren Q, Zheng ZJ, He YL. Evaluation and optimization of melting performance for a latent heat thermal energy storage unit partially filled with porous media. Applied energy. 2017 May 1;193:84-95.

[66] Adine HA, El Qarnia H. Numerical analysis of the thermal behaviour of a shell-and-tube heat storage unit using phase change materials. Applied mathematical modelling. 2009 Apr 1;33(4):2132-44.

[67] Al-Abidi AA, Mat S, Sopian K, Sulaiman MY, Mohammad AT. Internal and external fin heat transfer enhancement technique for latent heat thermal energy storage in triplex tube heat exchangers. Applied thermal engineering. 2013 Apr 29;53(1):147-56.

[68] Mahdi JM, Nsofor EC. Melting enhancement in triplex-tube latent heat energy storage system using nanoparticles-metal foam combination. Applied Energy. 2017 Apr 1;191:22-34.

[69] Khanjari Y, Pourfayaz F, Kasaeian AB. Numerical investigation on using of nanofluid in a water-cooled photovoltaic thermal system. Energy Conversion and Management. 2016 Aug 15;122:263-78.

[70] Al-Abidi AA, Mat S, Sopian K, Sulaiman MY, Mohammad AT. Numerical study of PCM solidification in a triplex tube heat exchanger with internal and external fins. International Journal of Heat and Mass Transfer. 2013 Jun 1;61:684-95.

[71] Badiei Z, Eslami M, Jafarpur K. Performance improvements in solar flat plate collectors by integrating with phase change materials and fins: A CFD modeling. Energy. 2020 Feb 1;192:116719.

[72] Selmi M, Al-Khawaja MJ, Marafia A. Validation of CFD simulation for flat plate solar energy collector. Renewable energy. 2008 Mar 1;33(3):383-7.

[73] Muhammad MD, Badr O, Yeung H. Validation of a CFD melting and solidification model for phase change in vertical cylinders. Numerical Heat Transfer, Part A: Applications. 2015 Sep 2;68(5):501-11.

[74] Ghahremannezhad A, Xu H, Salimpour MR, Wang P, Vafai K. Thermal performance analysis of phase change materials (PCMs) embedded in gradient porous metal foams. Applied Thermal Engineering. 2020 Oct 1;179:115731.

[75] Madruga S. Modeling of enhanced micro-energy harvesting of thermal ambient fluctuations with metallic foams embedded in Phase Change Materials. Renewable Energy. 2021 May 1;168:424-37.

[76] Lafdi K, Mesalhy O, Shaikh S. Experimental study on the influence of foam porosity and pore size on the melting of phase change materials. Journal of Applied Physics. 2007 Oct 15;102(8):083549.

[77] Tao YB, Liu YK, He YL. Effects of PCM arrangement and natural convection on charging and discharging performance of shell-and-tube LHS unit. International Journal of Heat and Mass Transfer. 2017 Dec 1;115:99-107.

Chapter 4.
THERMAL ENHANCEMENT TECHNIQUES FOR A LOBED-DOUBLE PIPE PCM THERMAL STORAGE SYSTEM

4.1. Introduction

All global energy forecasts account for the role that renewable energy sources, like for instance solar energy, will have to address growing global energy demand. More than 30% of overall energy usage is referred to buildings, and household water heating has been identified as the primary application of solar energy [1]. For renewable technology to be widely adopted, it is widely known that an appropriate energy storage system is relevant to guarantee more continuous working. For solar-based energy systems that involve significant heat transfer, LTES based on PCMs is a realistic and cost-effective solution. While the temperature remains constant, such materials may store or release large amounts of energy; as a result, the capacity to preserve thermal energy is the most important property of PCMs. Such compounds' excellent storing capacity is triggered when their phase changes and the disadvantage of such materials is that they require a long period of charging due to their low conductivity. PCMs, despite their numerous advantages, have a poor conductive heat transfer coefficient. Numerous research has been done recently on the use of NP, HNF, Porous Metal Foams, and altered tube geometry to enhance PCMs' heat responsiveness.

Based on the literature, integration of solar collectors and PCM not only saves space but also results in lower heat losses and improved solar thermal system performance [2], that are common components in household SDHW. Features of PCM and its application sector must be considered while designing PCM energy storage devices. In a study by Alomar et al. [3], the performance of a single-pass solar air heater thermal collector was analyzed with the incorporation of porous media and finned plate. The findings revealed that Model-2 exhibited the highest efficiency of 67% and Model-1 achieved 60% efficiency at a mass flow rate of 0.02 kg/s. Alomar et al. [4] investigated the efficiency improvement of a Solar Air Heater (SAH) by utilizing an absorber plate with v-corrugated geometry and impinging jet flow. Their study was conducted through experimental means. Salih et al. [5] conducted an experiment to compare the performance of two types of solar air collectors: a Double-Pass Solar Air Heater (DPSAH) with and without a porous medium. The study showed that the DPSAH with porous medium achieved maximum efficiencies of 87% and 81% for natural and forced convection, respectively. On the other hand, the DPSAH without porous medium reached maximum efficiencies of 82% and 67% for natural and forced convection, respectively. Abd et al. [6] evaluated the performance of a Compound Parabolic Concentrator (CPC)

integrated with a flat plate receiver during winter. Their study revealed that an increase in water mass flow rate inside the receiver resulted in a higher collector efficiency. However, this also led to a decrease in the water temperature at the receiver outlet. Therefore, a trade-off between the collector efficiency and the desired outlet water temperature must be carefully considered. Yassien et al. [7] conducted an experimental investigation of two Triple-Pass Solar Air Heater (TPSAH) collectors. The study aimed to compare the performance of TPSAH-1 and TPSAH-2, where a net of tubes was added below the absorber surface and double glass cover was applied to one of the collectors. The results showed that TPSAH-2 outperformed TPSAH-1, with a maximum efficiency of 80.2% and 73.4%, respectively, for high air mass flow rates. Salih et al. [8] evaluated the performance of a DPSAH with a finned absorber plate under natural and forced circulation processes. The study showed that natural circulation flow led to a higher efficiency of 73.5% and a significant temperature difference. Additionally, the addition of fins to the absorber increased the thermal performance of the SAH under both natural and forced circulation processes. Lamrani et al. [9] investigated the thermal efficiency of a linked solar parabolic trough collector and PCM for SWHS in big buildings. At the ion of the charging process, the maximum quantity of latent heat stored in PCM is 2.24 times more than the amount stored in sensible form. Gorzin et al. [10] examined PCM charging for home hot water system energy savings. The results demonstrate that by arranging the PCM mass in a certain configuration in which 40% of the PCM mass is in the inner tube, the melting time is reduced by 52%. The PCM uses on the SWHS were reviewed by Wang et al. [11]. Discussions covered the system design with the solar collector and the examination of the weather conditions. It was noted that the choice of material has an impact on the effectiveness of solar energy gathering. The type of material chosen affected both the storage size and the optimal working temperature. Nkwetta et al. [12] investigated design tools and experimental research including PCMs in HWT applications and central thermal storage. The influence of using water and air in HTF as well as the inherent barrier of the PCM low heat conductivity were investigated. Jian [13] investigated heat transfer in a triple tube with PCM for TES using numerical and experimental methods. In that test, the PCM was put in the central tube, and hot (inner tube) and cold (outer tube) fluids flowed. The results demonstrated that greater melting temperatures and lower solidification temperatures produce the best outcomes. Experimental research on PCM in a Double-Pipe Heat Exchanger (DPHX) was done by Baran and Sari [14]. The findings showed that while increasing Reynolds (Re) and Stefan (Ste) numbers

can enhance melting, they had no effect on solidification. Another finding was that temperature changes have a significant impact on the charging and recharging conditions.

In addition to PCM-based heat transfer improvement techniques, numerous other heat transfer enhancement techniques concentrated on improving heat exchanger geometry. To overcome the common problem in all PCMs, the contact surface between the working fluid and PCM can be improved, thereby increasing the heat exchange rate by working fluid convection. Stritih [15] experimented with a latent-heat storage unit featuring fins to compare its solidification and melting processes with a plain-surfaced unit. The results indicate improved heat transfer during solidification with fins, as seen in the increasing fin effectiveness value up to 3.06 followed by a decrease, and a 40% reduction in solidification time. Joybari et al. [16] investigated the enhancement of heat transfer in PCMs by fins during simultaneous charging and discharging. They found that the use of three hot tube fins and one cold tube fin yields the best performance under simultaneous charging and discharging conditions due to natural convection. Rennie and Raghavan [17] analyzed the impact of fluid thermal properties on heat transfer characteristics in a double-pipe helical heat exchanger. Their findings indicate that counterflow exhibits superior heat transfer rates to parallel flow, but the ratio of the differences remains consistent between thermally dependent and independent properties. Ahmadi et al. [18] conducted numerical simulations on a spiral coil tube in a shell and tube heat storage unit. They found that increasing the spiral coil diameter from 50 mm to 70 mm reduces total melting time by up to 71.4%, while tube diameter has little effect on the melting process. Najafabadi [19] investigated a novel heat storage method for solar collectors using PCM in a twisted DPHX with a lobed pipe. They proved that the three-lobed DPHX has the maximum heat transfer surface and melts 6% faster than the five-lobed DPHX. Mahdi et al. [20] investigated a multi-PHX incorporating PCM. Their investigation revealed that using six pipes with equal cross-sections instead of one increases the melting rate by 85%. In another study, a conical tube HX was employed by Mahdi et al. [21] as an energy storage device. They reported that using a conical tube considerably decreases the PCM melting time. Suresh [22] investigated the storage unit containing latent and sensible energy, and this approach was found to be helpful in terms of cost reduction and maintaining a stable energy supply. Dhaidan [23] investigated a HX with an elliptic shape surface in both horizontal and vertical directions with heat flux on the outside wall. Based on the results, using an elliptical cross-section instead of a circular shape increase the melting rate.

Additionally, the horizontal elliptical surface increases melting time by 7.71% as compared to the vertical surface. Anish [24] conducted an experimental investigation of the double-spiral coil TES-PCM charging and discharging behavior. The charging rate increased by increasing the HTF intake temperature and mass flow rate. On the other hand, the flow rate has minimal influence on the discharge rate. Kabbara et al. [25] investigated a tank holding a PCM as a TES system with a curved inner tube conveying working fluid as a TES system. The findings indicate that this form drastically reduces melting time and increases conduction heat transfer.

In recent years, NP have been used often to increase the thermal conductivity of fluids and to make up for the weak heat conductivity of PCMs in LTES systems. On the other hand, it's crucial to note that the usage of NP modifies the properties of the PCM. Khedher et al. [26] performed both experimental and numerical investigations to evaluate the effectiveness of using fins and NEPCMs in LHTES systems. Their results showed a significant decrease in both charging and discharging times, with reductions of 62% and 71%, respectively. A CFD analysis was studied on heat storage using phase-change materials and dimple-shaped fins by Khedher et al. [27]. The findings suggest that incorporating a greater number of dimple fins (ranging from 8 to 32) can lead to heat storage rates that are up to 8.7% faster than those without dimple fins. Furthermore, the study reveals that the heat storage rate can improve by nearly 12% in the best-case scenario compared to that of the no-fin case. Elarem et al. [28] calculated the hot HTF outlet temperature in an Evacuated Tube Collector (ETC) under various conditions, including the addition of copper NP to the PCM, the geometry of fins, and the Re number. To speed up heat transfer and provide a consistent PCM temperature distribution, thin and closely spaced fins are advised. Mehrali et al. [27] investigated the use of salt hydrate as a PCM for simultaneous solar thermal energy harvesting/storage. Zhang et al. [29] used PEG composite PCM assisted by Silver-GNS to improve solar thermal energy conversion. By Abdulateef et al. [30], longitudinal fins were installed through a triplex tube, and paraffin (RT82) and alumina NP were used to improve conduction. They provided data that the period has been cut by around 17% with the use of these two strategies. Li and Zhai [31] investigated a solar unit with a moderate temperature and used paraffin to improve the efficiency. The authors attempted to achieve a performance of 40.17% by dispersing graphite NP. Sushobhan and Kar [32] investigated the effect of CuO as NP on the performance of the n-Octadecene-based LTES system. Arici et al. [33] examined the phase change of PCM (Paraffin) containing NP (Al_2O_3) as in

a tank and discovered that the heat saved by PCM can be increased by adjusting the tilted walls. Naghavi et al. [34] examined the thermal capacity of a small-design heat pipe solar collector in the LTES system for thermal charging/discharging. The thermal efficiency of the system varies between 38% and 42% on sunny days but reduces to 34% to 36% on overcast or wet days, showing an 8% range of fluctuation. Mehrali et al. [35] studied a graphene-nanofluid for applications involving heat transfer. For a volume percentage of 4%, a substantial improvement in thermal conductivity of 45.1% was found.

MF has been demonstrated to be promising for improving thermal conductivity in PCMs. In a study on improving PCMs thermal conductivity in TTHX, NematpourKeshteli et al. [36] compared porous MF, NP, and finned surfaces. They reported that the addition of NP/ MF in Case B (Multilayer PCM-TTHX) decreased the melting times by 83.48% when compared to Case A (Single Pure PCM-TTHX). Li et al. [37] investigated the effect of MF/NP PCM on TTHX. The researchers found that the PCM phase transition rate is accelerated by either increasing the NP and reducing the porosity of the MF. The use of MF within the PCM domain was experimentally demonstrated in [38] to result in a 64% reduction in melting time. MF was used by Yang et al. [39] to increase TES. A suggested unit was modeled using imposing MF. They also investigated the effect of MF porosity. They also demonstrated the charging treatment of PCM embedded in foam and pure PCM [40]. For their testing, they took into account inclination angles of 0°, 30°, 60°, and 90°. According to their findings, the charging time decreased by 34.21%, 22.81%, and 12.28% at 60°, 30°, and 0°, respectively, as compared to the case at 90°. Kuruneru et al. [41] investigated the behavior of particle-fluid systems, tortuosity, and MF in HX. Although there was no direct correlation between metal foam porosity and improved heat transmission, it did have some effect on melting heat transfer. Analysis of double-pipe MF-filled HX were investigated by Chen et al. [42]. The latest findings and the analytical data that was previously disclosed are in good agreement. The presented study shows how to enhance the performance of DPHX packed with MF.

4.1.2 Aim and novelty of the present work

The studies presented here revealed that there are several strategies for upgrading LHTES- DPHX systems. However, further study on this topic is needed, particularly in systems that combine PCM with NP, HNF, and MF of solar concentrating units with the thermal storage systems, in order to improve the overall system efficiency. Previous studies recommend more research into

the pairing of a solar concentrating unit with heat storage. In this study, MF with high porosities ranging from 0.88 to 0.95 and 20 PPI were proposed, along with NP suspensions with low NP volume fractions of approximately 0.04%. Moreover, in accordance with the detailed analysis of the state-of-the-art presented above, there is a few studies have been done comparing NP, MF, and optimizing the contact surface between the working hot fluid and PCM domain, particularly with references to a DPHX that intensifies both charging and discharging process. To preserve solar radiation, a double-lobed pipe system with PCM in the inner area has been proposed in this study. Since the fluid in the outer pipe is discharged from a concentrating solar panel, a high-temperature range has been involved as the boundary condition for the inner surface. The goal of this research is to establish the variables that have the highest effect on the collector thermal performance and to suggest a novel design for the system framework. Four strategies for accelerating melting and solidification have been employed in the current solar concentrating unit with a thermal storage/harvesting system to reduce the time needed for charging/discharging and increase the rate of energy storage/harvesting:
1) Improving the heat exchanger geometry (lobed pipe); **2)** Dispersing Al_2O_3 nano-sized powders into paraffin (RT82); **3)** Dispersing Al_2O_3-MWCNT nano-sized powders into H_2O; **4)** Adding MF with different porosity (aluminum foam)

Innovation in this technology includes the development of new types of metal foam and PCM materials, as well as the integration of these materials into different types of heat exchangers with adding nanoparticles. For modeling purposes, a 3D domain has been presented, and the Finite Volume (FV) approach was used to solve the equations. Simulations based on the finite volume method were done for both zones, water, and PCM in the laminar regime. The incorporation of the HX and solar thermal collector description, material, assumption and mathematical formulation, and boundary conditions have been listed in section 2. Section 3 contains a numerical procedure, grid size and time step independence, and validation with available data. The main target and outputs of the present work have been resumed in the last section which contains the effect of inlet HTF temperature, the effect of geometry optimization, the effect of pure NP and HNF, and MF in both melting and solidification have been scrutinized in the rest of section 4. The present study will present and compare the results in terms of liquid fractions, average achieved temperature, dimensionless parameters, and stored energy, with the aim of understanding how much one could improve the performances of the

proposed engineering device, i. e. a tube-in-tube PCM thermal energy storage system with a concentrated solar power source. The findings of this research will provide insights into improving thermal performance in latent heat storage units, with potential applications in various PCM-based systems, such as TES for solar energy systems and energy-efficient buildings. The proposed engineering device can be applied in residential buildings for space heating and cooling by storing excess heat or coolness during the day and releasing it at night, or vice versa. Moreover, this technology can be employed in industries to facilitate the thermal management of electronic devices and equipment or in processes that necessitate heat storage and release. Additionally, it can be used in domestic and industrial hot water systems for energy efficiency improvement.

4.2. Thermal storage system equipped with lobed heat exchanger

4.2.1 Incorporation of the solar system with lobed heat exchanger

One of the most cost-effective methods to have a water heater is to use solar collectors. However, one should theoretically design an appropriate thermal energy storage system in order to guarantee that hot water is always available at all times by following continuous full charge/discharge cycles. In a parabolic trough system equipped with a heat exchanger and PCM, the parabolic mirrors focus the rays from the sun onto a receiver tube positioned at the focal line. The receiver tube absorbs the concentrated solar energy and supplies hot water, while a HTF such as water or oil flows through a parallel loop that runs alongside the receiver tube, carrying the absorbed heat to the heat exchanger. The PCM stores the excess heat from the HTF as latent heat through a phase change process. All the heat transfer mechanisms, except radiation, are here involved; natural convection within the PCM might arise too. Upon passing through the heat exchanger, the HTF returns to the parabolic troughs to be reheated, completing the cycle. The use of PCM allows for the storage of solar energy during periods of high insulation, which can be released during periods of low insulation, ensuring a more stable and consistent supply of energy to the heat exchanger. This might be the case of a cloudy day, or in general of days with no relevant incoming solar energy. In the current study, a novel design for a heat storage unit with a lobed shape has been provided as a solution to increase the TES system performances. A concentrating solar collector system together with the position of the relative TES system are depicted schematically in **Fig. 4.1**. A lobed DPHX included has been proposed to store/release heat, as

shown in **Fig. 4.1a**. The hot inlet HTF from the concentrating solar system flows within the outer tube, and the inner pipe with the PCM (RT82) is here employed by considering one up to six lobes. The average temperature of the inner surface is raised up to 360.15, 363.15, or 366.15 K by the flow of hot fluid within the inner tube. To minimize heat dissipation, the outer surface is thermally insulated. At the beginning of the simulation, the temperature of the system is initialized to 340 K. Overall length of the HX is 1000 mm and pipes are made of copper with a thickness of 1 mm. Paraffin volumes used in all six arrangements were assumed to be the same. Lobes here simulated, where the PCM is modeled by also considering the presence of thermal conduction enhancers such as metal foams or nanoparticles, are shown in **Fig. 4.1b** with references to each case label; on the other hand, geometrical characteristics of the various profiles are shown in **Table 4.1**. The lobes on the pipes create turbulence in the fluid flow, which enhances heat transfer by promoting better mixing of the fluids. This turbulent flow helps break down the boundary layer that forms on the surface of the pipes, allowing for more effective heat exchange. Lobed pipe heat exchangers are often used in contexts where optimal heat transmission is of utmost importance, such as in industrial processes, and diverse thermal management applications. The design and layout of lobed pipe heat exchangers might vary depending on the intended use and the fluids used in the heat exchange process. Each of the three cases will be labelled lately as Case A (Simple-DPHX), Case B (2-lobed -TTHX), Case C (3-lobed -TTHX), Case D (4-lobed -TTHX), Case E (5-lobed -TTHX), and Case F (6-lobed -TTHX).

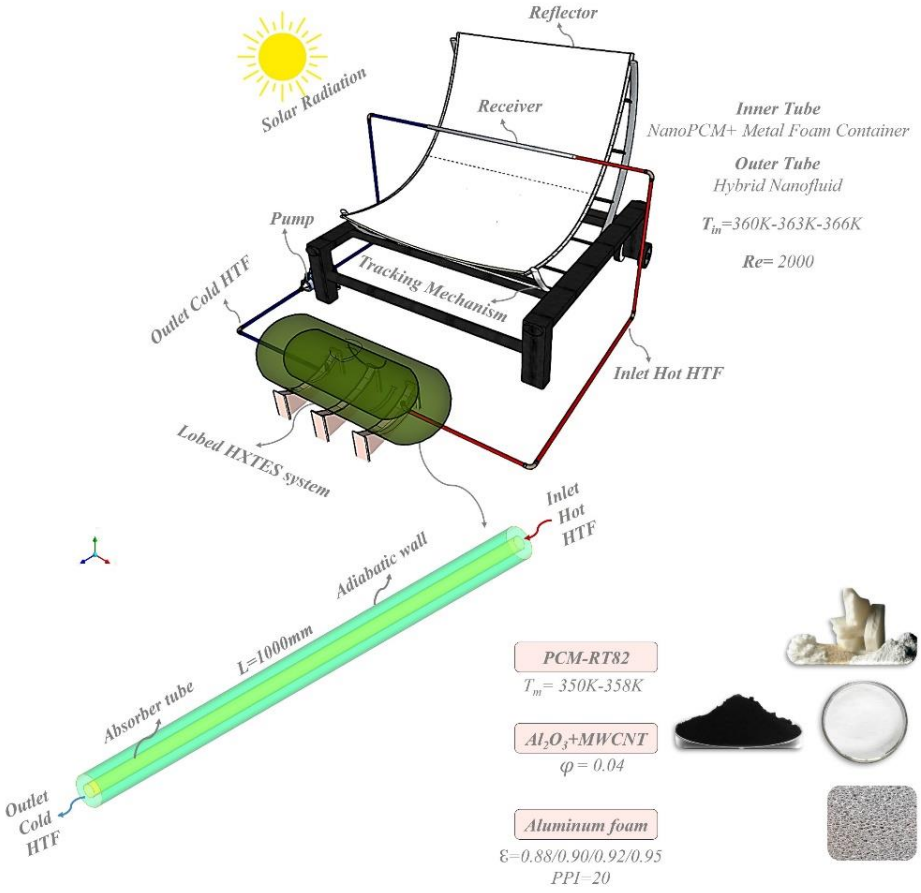
Reflector
Solar Radiation
Receiver
Inner Tube
NanoPCM+ Metal Foam Container
Outer Tube
Hybrid Nanofluid
T_{in}=360K-363K-366K
Re= 2000
Pump
Tracking Mechanism
Outlet Cold HTF
Inlet Hot HTF
Lobed HXTES system
Inlet Hot HTF
Adiabatic wall
L=1000mm
Absorber tube
Outlet Cold HTF
PCM-RT82
T_m= 350K-358K
Al_2O_3+MWCNT
φ = 0.04
Aluminum foam
ε=0.88/0.90/0.92/0.95
PPI=20

(a)

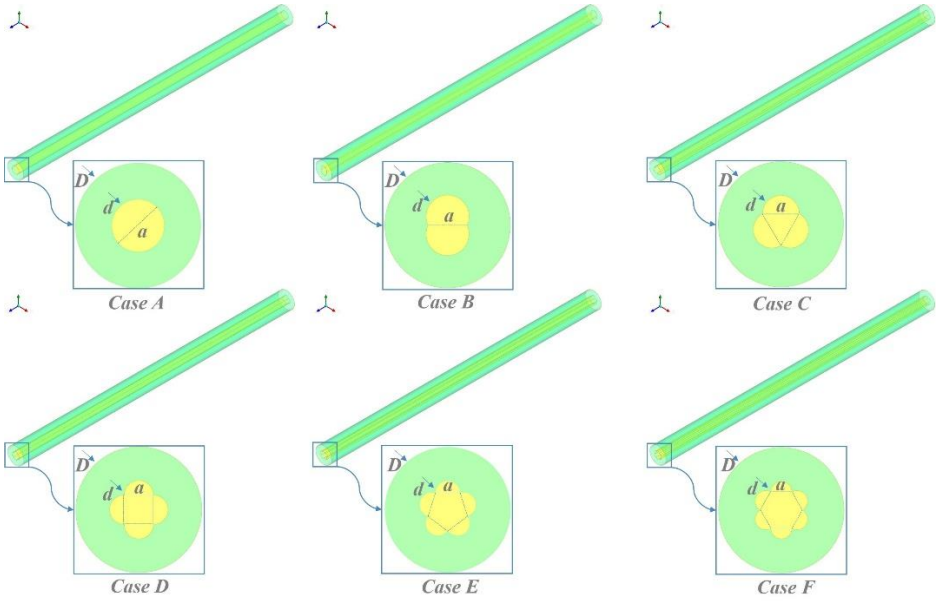

(b)

Fig. 4.1. (a) Configuration of heat storage and solar thermal collector, (b) Schematic figure of the different cases investigated for lobed DPHX, and geometrical parameters of a profile.

Table 4.1. Geometrical characteristics of the double lobed-pipe heat exchanger with S the heat transfer area

Cases	**S (mm^2)**	**D (mm)**	**d (mm)**	**a (mm)**
Case A/1-lobed	79894	60	25.116	25.116
Case B/2-lobed	82564	60	10.226	18.64
Case C/3-lobed	83627	60	17.536	17.536
Case D/4-lobed	88215	60	13.882	13.882
Case E/5-lobed	92071	60	11.597	11.597
Case F/6-lobed	95239	60	10	10

4.2.2. Materials and mathematical modeling

4.2.2.1 Materials

The inner zone has been filled with RT82 is an organic pure PCM (354K). More information on it can be obtained from Al-Abidi et al. [43] where the authors use the properties reported from the manufacturer (RUBITHERM GmbH-Germany). It is chemically inert, has an unlimited lifetime and provides a very effective means for storing heat and cold at nearly constant temperature. To improve its thermal performances, Al_2O_3 (volume fraction of 4%) nanoparticles, and aluminum foam, are embedded within the PCM. In order to improve the HTF performances too, Al_2O_3-Multi Walled Carbon Nanotube (MWCNT-volume proportion of 4%) hybrid nanofluid are dispersed within the water. **Table 4.2** contains a list of the bulk material properties used in the current paper [43-46].

Table 4.2. Properties of RT82, Al_2O_3, MWCNT, Foam, and Cu

Property	**RT82 [43]**	**Al_2O_3 [44]**	**MWCNT [45]**	**Foam [46]**	**Cu**
T_s/T_l (°C)	350/358	-	-	-	-
$\rho_s/\ \rho_l$ (kg /m^3)	950/770	3970	2100	2700	8920
c (J /kg K)	2000	765	711	900	380
k (W/m K)	0.2	25	2000	220	400
β (1/K)	0.001	-	-	-	-
μ (kg/m s)	0.03499	-	-	-	-
L_f (kJ/kg)	176	-	-	-	-

4.2.2.2 Assumption and mathematical formulation

A three-dimensional model was used to study RT82 melting and solidification, and all six combinations used the same amount of paraffin, *i. e.* the volume of the lobed heat exchangers is the same. The enthalpy-porosity technique was used to predict the transient process, with assumptions for the current investigation resumed in **Fig 4.2.** The conditions for laminar flow assumption are presented in **Figure 4.1**, and the governing equations for this study are summarized in **Table 4.3** [47-48], which includes the continuity, momentum, and energy equations based on the given assumptions. Equations here reported are a generic form, applied to both HTF and PCM domains; this

are applied to each case by doing some considerations for the different variables shown. The variables in this study are denoted by different subscripts, where the subscript *f* corresponds to liquid NanoPCM and the subscript *s* refers to the porous medium (foam). The temperature is denoted by *T*, the effective pressure by *p*, the dynamic viscosity by μ, the specific heat capacity by *c*, and the latent heat by L_f. The porosity of the Al6061 aluminum alloy is represented by ε, and a damping term δ is included in the Carman-Kozeny equation to prevent division by zero, where a small value of 0.001 is typically used. Furthermore, the mushy zone constant A_m is set to a value of 10^6, as values between 10^4 and 10^7 are commonly recommended [47-48]. The liquid fraction function λ is used to characterize the distribution of solid and liquid phases in the PCM, with a value range between 0 and 1. Its definition is provided in **Table 4.3**. Also, it is assumed that liquid Nano-PCM is incompressible and Newtonian, with laminar flows that can be assumed based on the mass flow rate values. For the HTF, one assumes porosity $\varepsilon = 1$ and $K = \infty$ for the momentum equations. Energy equations, with only references to the fluid-phase one, are written without the phase change term, and by considering HTF-equivalent properties to be defined in the following subsection. In the PCM region, with references to **Table 4.3**, we can distinguish among cases with pure PCM, metal foam, and/or nanoparticles.

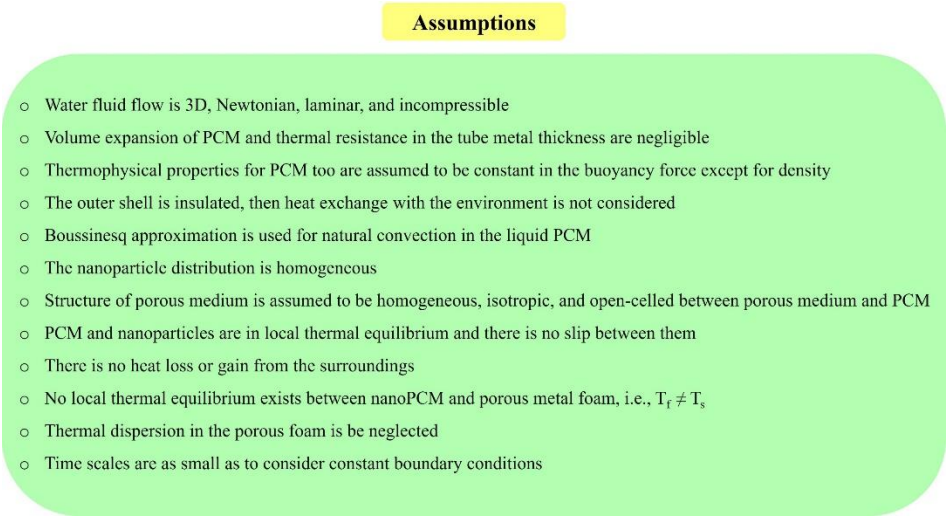

Fig. 4.2. Assumptions for the present study

Table 4.3. Continuity, momentum, and energy equations for a 3D rectangular coordinate system

Equation	**Equation**
Continuity:	$\nabla \cdot \vec{V} = 0$
x-Momentum equation	$\frac{\bar{\rho}}{\varepsilon^2}\left(\varepsilon\frac{\partial u}{\partial t}+u\frac{\partial u}{\partial x}+v\frac{\partial u}{\partial y}+w\frac{\partial u}{\partial z}\right)=-\frac{\partial p}{\partial x}+\frac{\bar{\mu}}{\varepsilon}\nabla^2 u+\left(\frac{A_m(1-\lambda)^2}{\lambda^3+\delta}-\frac{\bar{\mu}}{K}\right)u$
y-Momentum equation	$\frac{\bar{\rho}}{\varepsilon^2}\left(\varepsilon\frac{\partial v}{\partial t}+u\frac{\partial v}{\partial x}+v\frac{\partial v}{\partial y}+w\frac{\partial v}{\partial z}\right)=-\frac{\partial p}{\partial y}+\frac{\bar{\mu}}{\varepsilon}\nabla^2 v+\left(\overline{\rho\beta}\right)g\left(T-T_{ini}\right)+\left(\frac{A_m(1-\lambda)^2}{\lambda^3+\delta}-\frac{\bar{\mu}}{K}\right)v$
z-Momentum equation	$\frac{\bar{\rho}}{\varepsilon^2}\left(\varepsilon\frac{\partial w}{\partial t}+u\frac{\partial w}{\partial x}+v\frac{\partial w}{\partial y}+w\frac{\partial w}{\partial z}\right)=-\frac{\partial p}{\partial z}+\frac{\bar{\mu}}{\varepsilon}\nabla^2 w+\left(\frac{A_m(1-\lambda)^2}{\lambda^3+\delta}-\frac{\bar{\mu}}{K}\right)w$
Fluid-phase energy equation	$\overline{\rho C}\left(\varepsilon\frac{\partial T}{\partial t}+V\cdot\nabla T\right)=k_{fe}\nabla^2 T_f+h_{sf}A_{sf}\left(T_f-T_s\right)-\varepsilon\overline{\rho L_f}\frac{\partial\lambda}{\partial t}$
Solid-phase energy equation	$(1-\varepsilon)(\rho C)_s\frac{\partial T_s}{\partial t}=k_{se}\nabla^2 T_s-h_{sf}A_{sf}\left(T_s-T_f\right)$
Parameter	**Expression**
Carman-Kozeny damping term, A_m, δ [47-48]	$A_m=10^6, \delta=0.001$
Liquid fraction, λ	$\lambda=\begin{cases}0 & \rightarrow if\ \ T\le T_{solidus}\\ (T-T_s/T_l-T_s) & \rightarrow if\ \ T_{solidus}<T<T_{liquidus}\\ 1 & \rightarrow if\ \ T\ge T_{liquidus}\end{cases}$
Stefan number, Ste	$Ste=\frac{c_p(T_{in}-T_{PCM})}{L_f}, Ste=\begin{cases}0.113\rightarrow if\ \ T_{in}=360\\ 0.147\rightarrow if\ \ T_{in}=363\\ 0.181\rightarrow if\ \ T_{in}=366\end{cases}$

The characterization of governing equations for the other cases in which foams and/or nanoparticles are employed are reported in the following. When nanofluids are employed, momentum equations are considered with ε = 1 and $K=\infty$; for the energy equation, only the fluid phase energy equation is employed with thermophysical properties to be listed in the following subsection. The subscripts *f* and *s* denote the liquid NanoPCM and porous medium (foam) respectively. *T* represents temperature, *p* represents effective pressure, μ represents dynamic viscosity, C represents specific heat capacity, L_f represents latent heat, ε represents the porosity of Al6061 aluminum alloy, δ in the Carman-Kozeny damping term is a small value (0.001) used to prevent division

by zero, and A_m is a constant representing the mushy zone. When MF is included, equations are essentially used as they are by considering a zero volume fraction for the nanoparticles. Generally speaking, in order to close such equations, it is necessary to have the porous medium closure coefficients to characterize such variables. In particular, the following parameters from **Table 4.3** require clear definitions: K, which denotes the permeability of the system; k_{fe}, the effective thermal conductivity of the fluid; k_{se}, the effective thermal conductivity of the solid; h_{sf}, the coefficient governing interfacial heat transfer between the nanoPCM, or eventually pure PCM, and porous foam; and A_{sf}, the specific surface area. A summary of the correlations that were employed in this study can be seen in **Table 4.4** [46, 49-56]. With references to nanofluids, these are characterized by their volume fraction, range of shear rates, and base liquid viscosity, which influences the characteristic shear rate and non-Newtonian shear thinning behavior of nanofluids [57]. Their equivalent properties will be shown in the next subsection. The fundamental structural properties of metal foam are determined by several key parameters, including the level of porosity denoted by ε, the density of pores referred to as ω or PPIs (20), and the diameter of the ligaments d_l. The simplified parameter d_l provides a means to establish a correlation between d_p and PPIs and is typically associated with the nominal pore diameter specified by the manufacturer. This value is generally an approximation that takes into account both cell and pore sizes to provide a rough average. **Table 4.4** presents the values for the effective thermal conductivities of the liquid nanoPCM (k_{fe}) and the porous medium (k_{se}), which were obtained using the approach introduced by Boomsma and Poulikakos [50]. This model, derived starting from a unit cell geometrical model, calibrated by means of experimental runs, allows for the determination of k_{fe} and k_{se} by assuming either $k_s = 0$ or $k_f = 0$, based on the overall effective thermal conductivity. By utilizing this method, it is possible to calculate the effective thermal conductivity of each phase by assuming zero thermal conductivity for the other phases. Additionally, **Table 4.4** displays the specific surface area of the metal foam, A_{sf}, as well as the interfacial heat transfer coefficient, h_{sf}. The specific surface area is derived by means of a geometrical model [45,52-56]. The selection of an appropriate correlation for h_{sf} remains a subject of ongoing research, with various adapted correlations proposed based on tube banks natural convection or low-velocity tube banks crossflow, or on PCM/foam pore-scale analysis. In this study, we utilized correlations for low-velocity tube banks crossflow, which have been previously implemented in similar investigations. Another term that arises in Table 4 is the permeability, that is obtained by using

the empirical from [49] valid for open-cell metal foams. In this correlation, another input parameter is the ligament thickness d_l, that is linked to the pore size d_p and PPIs from the manufacturer. The Reynolds number is calculated in **Table 4.4** by taking the ligament diameter, d_l, as the characteristic length, and is determined to be 2000 as the inlet mass flow rate is 0.0945 kg/s.

Table 4.4. Employed correlations for metallic foam closure coefficients

Parameter	Correlation	Reference
Permeability ***(K)***	$K = d^2{}_p \left(0.00073(1-\varepsilon)^{-0.224} \left(\frac{d_l}{d_p} \right)^{-1.11} \right)$ $d_l = 1.18\sqrt{\frac{1-\varepsilon}{3\pi}} \left(\frac{1}{1-e^{-(1-\varepsilon)/0.04}} \right) d_p$ $where\ \ d_p = 0.0254(m)/\omega(PPI)$ $\varepsilon = 0.88, 0.90, 0.92, 0.95 \,/\, \omega(PPI) = 20$	[49]
Effective thermal conductivity of PCM or nanoPCM ***(k_{fe})*** Effective thermal conductivity of the porous medium ***(k_{se})***	$k_{fe} = \frac{\sqrt{2}}{2\left(M_A + M_B + M_C + M_D\right)}\Big\vert_{k_s=0}$ $k_{se} = \frac{\sqrt{2}}{2\left(M_A + M_B + M_C + M_D\right)}\Big\vert_{k_f=0}$ $M_A = \frac{4\sigma}{\left(2e^2 + \pi\sigma(1-e)\right)k_s + \left(4 - 2e^2 + \pi\sigma(1-e)\right)k_f}$ $M_B = \frac{(e-2\sigma)^2}{\left(e-2\sigma\right)e^2 k_s + \left(2e - 4\sigma - (e-2\sigma)e^2\right)k_f}$ $M_C = \frac{(\sqrt{2}-2e)^2}{2\pi\sigma^2(1-2e\sqrt{2})k_s + 2\left(\sqrt{2} - 2e - \pi\sigma^2(1-2e\sqrt{2}))\right)k_f}$ $M_D = \frac{2e}{e^2 k_s + \left(4-e^2\right)k_f}$ $\sigma = \sqrt{\frac{\sqrt{2}(2 - 6/8e^3\sqrt{2} - 2\varepsilon)}{\pi(3 - 4e\sqrt{2} - e)}},\ and\ \ e = 0.339$	[50-51]

Interfacial heat transfer coefficient, (h_{sf})	$h_{sf} = \begin{cases} (0.76\, Re_d^{0.4}\, Pr_{PCM}^{0.37}\left(\frac{k_f}{d_f}\right), 1 \le Re_d \le 40 \\ (0.52\, Re_d^{0.5}\, Pr_{PCM}^{0.37}\left(\frac{k_f}{d_f}\right), 40 \le Re_d \le 1000 \\ (0.26\, Re_d^{0.6}\, Pr_{PCM}^{0.37}\left(\frac{k_f}{d_f}\right), 1000 \le Re_d \le 2\times10^5 \end{cases}$ $Re_d = \sqrt{u^2+v^2+w^2}\,\frac{d_l}{\varepsilon\mu}$ $A_{sf} = \frac{3\pi d_l (1-e^{-(1-\varepsilon)/0.04})}{(0.59 d_p)^2}$	[45,52-56]

4.2.2.3 Thermo-physical properties

Thermophysical properties and characteristics of PCM-nanoparticles here employed, as well as hybrid nanofluids used for the working fluid, are given in this subsection. Particles of Al_2O_3 and Al_2O_3+MWCNT were mixed with base paraffin and H_2O, respectively, for either PCM or HTF; for simulation purposes, single phase equivalent formulations have been utilized in all the cases. Given that it has been assumed that nanomaterial concentrations are lower than 0.04, the homogeneous mixture proposition was proposed to compute properties; to improve thermal performance, the base working fluid was combined with a total concentration of 0.04 HNF alumina-MWCNT (see **Fig. 4.3**) [58]. Nano-fluid density, specific heat, thermal expansion coefficient, latent heat, effective dynamic viscosity, and thermal conductivity are expressed in **Fig. 4.3**. The nanoPCM thermal conductivity was written using the model developed by Maxwell equation [59]. In this study, parameters to appreciate how fast melting and solidification are, say melting ($P_{L,m}$) and solidification ($P_{L,s}$) heat transfer rate, are resumed in **Table 4.5**. These parameters are the thermal energy stored/released capacity per unit charging and discharging time, representing the average heat rate as the mean melting/solidification velocity [60, 61]. Such parameters are also presented in a scaled form here via $P_{L,m}^*$ and $P_{L,s}^*$; their physical meaning is presented in **Table 4.5** too.

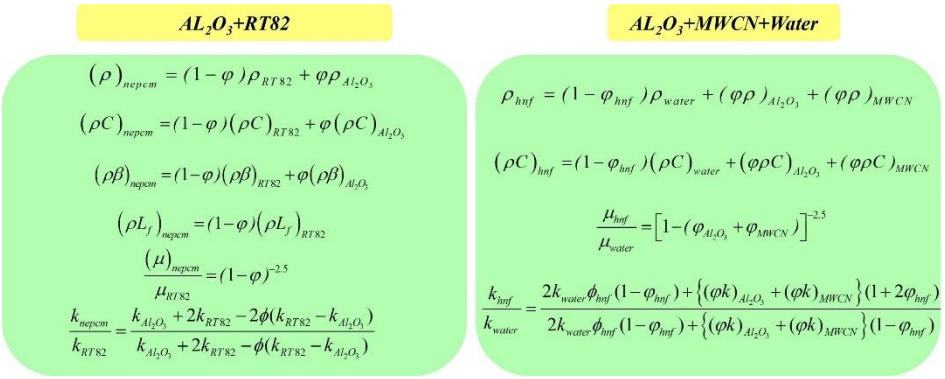

Fig. 4.3. NEPCM (Al_2O_3+RT82) and hybrid nano-fluid (Al_2O_3+MWCNT+H_2O) thermophysical equivalent properties [58, 59]

Table 4.5. Melting and solidification heat transfer rates equations as the ratios between stored/released thermal energy and charging/discharging time [60,61]

Processes	Equations
Melting	$p_{L,m} = \frac{Q}{t_m} = \frac{m_{pcm}\left(\int_{T_{initial}}^{T_{solidus}} c\,dT + L_f + \int_{T_{liquidus}}^{T_{inlet}} c\,dT\right)}{t_m} = \frac{m_{pcm}\left[c\left(T_{solidus} - T_{initial}\right) + L_f + c\left(T_{inlet} - T_{liquidus}\right)\right]}{t_m}$ c_{pcm}=2000 *J /kg K*, $T_{solidus}$=350 *K*, $T_{initial}$=*340 K*, L_f=*176 kJ/kg*, T_{inlet}=*360, 363, 366 K*, $T_{liquidus}$=358 *K*
	$p_{L,m}^{*} = \frac{p_{L,m}}{\dot{m}c\left(T_{inlet} - T_{melting}\right)} = \frac{\text{Average heat rate}}{\text{Sensible enthalpy variation rate}}$ $\dot{m}$= 0.0945 *kg/s*, c_{water}=4182 *J /kg K*, T_{inlet}=*360, 363, 366 K*, $T_{melting}$=*354 K*
Solidification	$p_{L,s} = \frac{Q}{t_s} = \frac{m_{pcm}\left(\int_{T_{liquidus}}^{T_{initial}} c\,dT + L_f + \int_{T_{inlet}}^{T_{solidus}} c\,dT\right)}{t_s} = \frac{m_{pcm}\left[c\left(T_{initial} - T_{liquidus}\right) + L_f + c\left(T_{solidus} - T_{inlet}\right)\right]}{t_s}$ c_{pcm}=2000 *J /kg K*, $T_{solidus}$=350 *K*, $T_{initial}$=*366 K*, L_f=*176 kJ/kg*, T_{inlet}=*340 K*, $T_{liquidus}$=358 *K*
	$p_{L,s}^{*} = \frac{p_{L,s}}{\dot{m}c\left(T_{melting} - T_{inlet}\right)} = \frac{\text{Average heat rate}}{\text{Sensible enthalpy variation rate}}$ $\dot{m}$= 0.0945 *kg/s*, c_{water}=4182 *J /kg K*, T_{inlet}=*340 K*, $T_{melting}$=*354 K*

4.2.2.4 Boundary conditions

In this study, we investigate both single melting and solidification cycles to highlight the function of various heat transfer enhancement strategies; solidification cycle is modeled to account for what would happen if one considers also the reusage of the stored energy after some time, and also to see

the behavior under different operating conditions. For the melting scenario cases, once the transient process begins, let's say at t> 0, hot fluid flows inside the outer tube. It is assumed here that the HTF flows at a uniform inlet temperatures of 360.15, 363.15, or 366.15 K, in order to account for different PCM charging conditions. As a result, in the current study, a PCM with a melting temperature below these inlet temperatures is used. The charging temperatures were chosen based on a normal typical minimum working temperature, say 333.15 K, typical of various typical industrial and home hot water applications, such as solar air and water conditioning system. In all cases, melting temperatures of PCM (i. e. RT82), as well as the overall system initial temperature (t=0 s), are chosen at 358.15 and 340.15 K, respectively. For the HTF, at the inlet section and for both melting and solidification cases, we assumed a uniform mass flow rate; on the other hand, for the outlet section, we assumed atmospheric pressure and temperature outflow. The inlet mass flow rate of all HTF system was assumed to be 0.0945 kg/s that refer to Re = 2000, and at the exterior surface insulation to help with heat loss reduction is assumed. With references to the solidification scenario, it is assumed that the PCM is at 366.15 K for t = 0, then water sudden comes in at 340.15 K for t > 0. A boundary conditions resume for both charging and discharging scenario is shown in **Table 4.6**. Foams with relatively high porosities, say from 0.88 to 0.95, and 20 PPIs, as well as NP with relatively low NP volume fractions, say 0.04%, are used in this work. The reason why these values has been chosen here is shown in the following. For the foams, it has been established that porosity affects PCM thermal conductivity more so than PPI [46, 62-66]. For the nanoparticles, higher concentrations can result in segregation from PCM, which should be avoided; besides, along with a rise in heat conductivity, a considerable increase in melt viscosity is noticed, resulting in alterations in the hydrodynamics of the melt flow.

4.3. Numerical solution

4.3.1. Numerical approach and validation

The unsteady equations stated above have been solved using a finite volume code. Following the creation of the 3D structure, the ANSYS FLUENT software commercial finite volume code is utilized to solve the governing equations [67]. A resume of the code input parameters is shown in **Figure 4.4** together with coupling, discretization, and convergence criterion employed.

Table 4.6. Boundary conditions for scenarios of melting and solidification

Boundary condition	Charging	Discharging
System temperature, T_{PCM}, T_{HTF} (t = 0 s)	340.15 K	366.15 K
HTF inlet temperature, T_i	360.15, 363.15, 366.15 K	340.15 K
Concentrating solar system	During day	During night

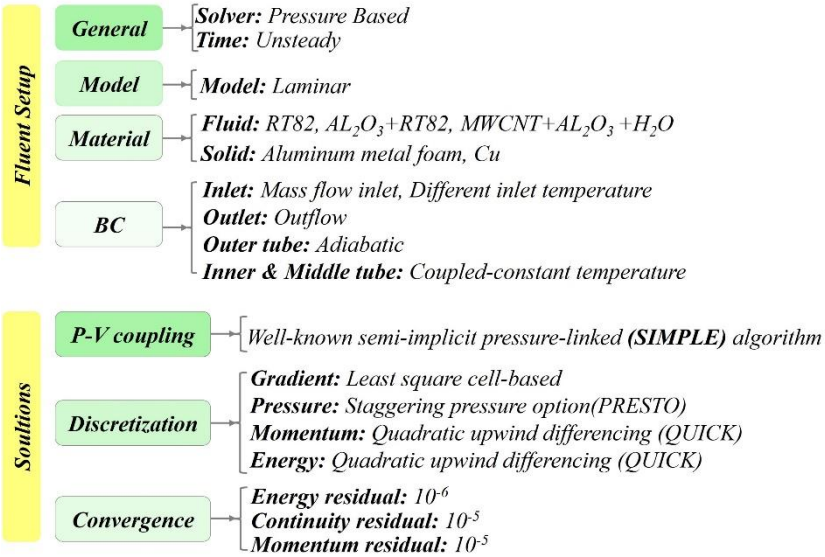

Fig. 4.4. Summary of the selected setup and solution techniques in simulations; BC stands for boundary conditions and P-V for pressure-velocity

In this study, code validation is done with two literature data to be sure that the output result is valid. Studies from Al-Abidi et al. [43], Liu et al. [68], and Mahdi and Nsofor [69], were employed to validate the current investigation. Because, as per the authors' knowledge, similar lobes-configuration experimental outcomes are not available from the literature, comparisons are done with very similar engineering devices. In order to make the melting of PCM(RT82) faster, Al-Abidi et al. [43] explored how to increase heat transport for a TTHX numerically and experimentally. **Figure 4.5** depicts the average PCM temperature evolution of the PCM during the melting phase, as well as the average and maximum differences between the current study to be adapted in terms of boundary conditions by following [43] and the experimental and numerical data from Al-Abidi [43]. Comparisons with numerical results from Liu et al. [69], which simulated the melting process inside a circular annulus

filled with RT58 and copper foam, are here presented too. The liquid fractions obtained from the simulations (**Fig. 4.6.a**) show good agreement with the previous study for both thermal equilibrium and non-equilibrium conditions. **Fig. 4.6.b** presents the average and maximum deviations between the simulations of Liu et al. [68] and the results of the present numerical approach for the entire melting process, indicating very small deviations for both average and maximum values. As can be seen, temperature results present good accuracy in comparison to the current study. In **Fig. 4.7**, comparisons with predictions from [69], in which a NP/MF (RT82-Al_2O_3) system is TTHX, are shown in terms of LF evolution concerning the time, for two different porosities. A very good agreement for the average liquid fraction is exhibited, and also the maximum differences observed look very small. It should be noted that Mahdi and Nsofor [69] used experiments study from the literature to validate their model [70, 71].

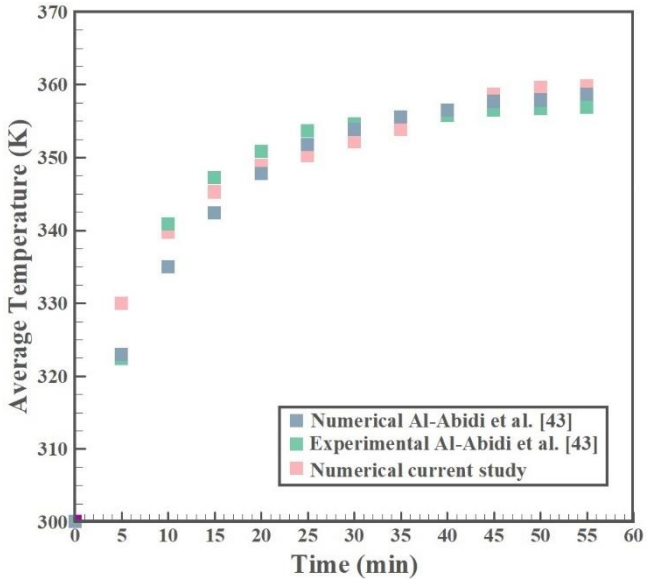

(a)

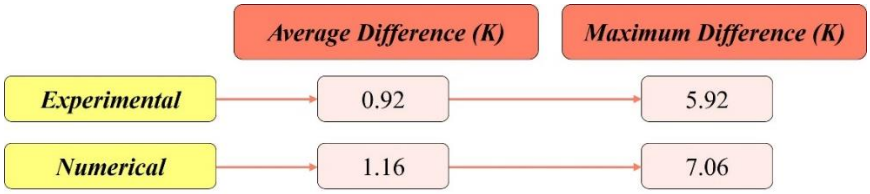

(b)

Fig. 4.5. (a) PCM-averaged temperature vs time: comparisons with experiments and simulations from Al-Abidi et al. [43] (b) Deviations between the average temperature obtained here and experimental/numerical data provided by Al-Abidi et al. [43]

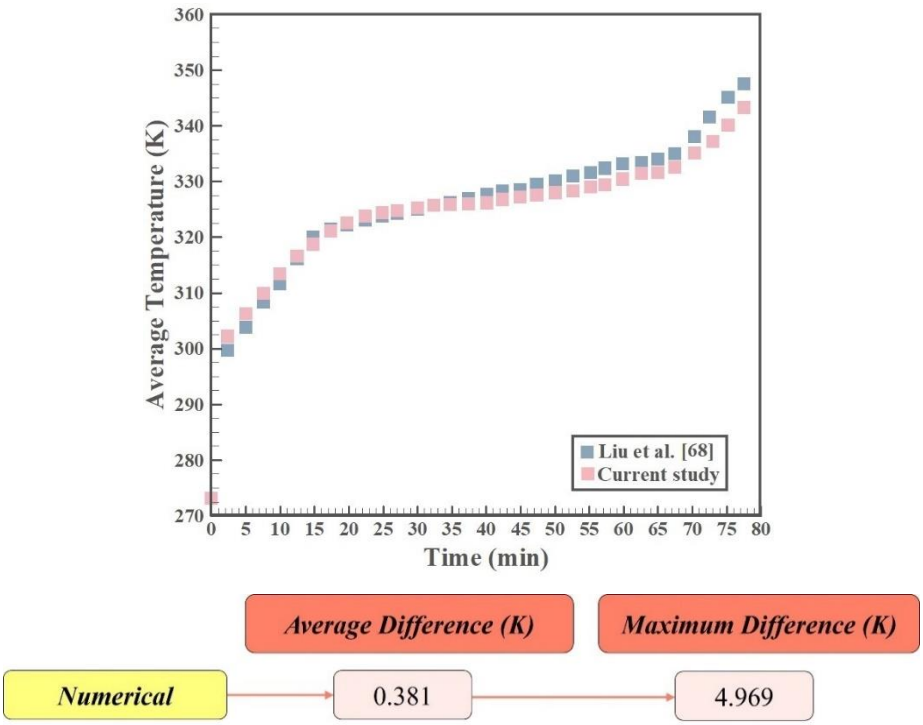

Fig. 4.6. (a) Comparison of instantaneous liquid fraction between present work of Liu et al. [68] for metal foam/PCM composite.

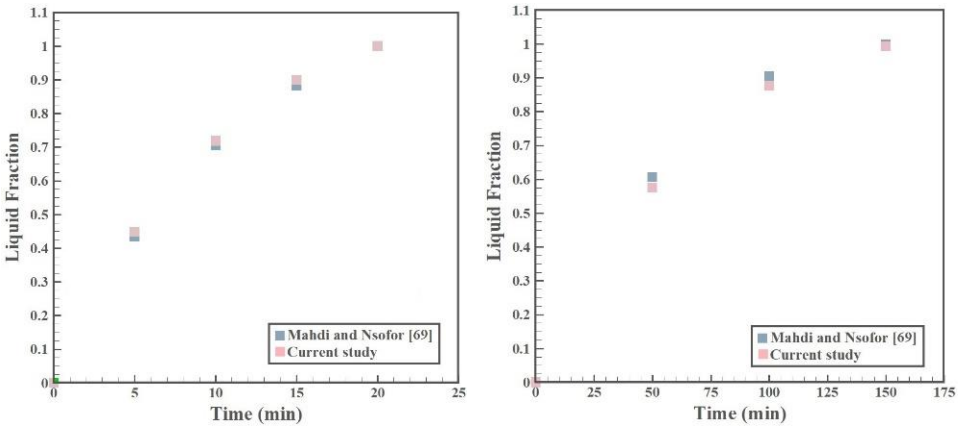

(a)

	Average difference (LF)	Maximum Difference (LF)
Numerical, 0.95	0.00745	0.02
Numerical, 0.98	0.017	0.031

(b)

Fig. 4.7. (a) Liquid fraction evolution vs time for ε = 0.95 (left) and ε = 0.98 (right) compared with [69], (b) Deviation between liquid fraction obtained by here and data provided by Mahdi and Nsofar [69]

4.3.2 Grid and time step independence

In order to reduce the computational expenses for each configuration, it is important to carefully choose the appropriate element size during grid generation as well as an optimal value for the time step. The generated grid geometry, as well as the employed grid size and time steps for case A (one-lobed DPHX) are shown in **Fig. 4.8**. Prior to modeling, several grids have to be evaluated to determine how responsive the findings are to different grid sizes. If the grid size is less than a specific number of elements, mesh resolution cannot alter the values of scalars. Such a number ought to be picked as the grid's optimal size in each situation. As shown in **Fig. 4.8 (b)**, four alternative grid-size cells were investigated in order to examine the impact of grid size on the numerical solution. Finally, the 2864133 cell-produced grid was chosen as the ideal grid for the simulations. Also, due to the presence of the gravity effect, the

small values for time steps should be considered. The difference between the data acquired with Δt of 0.1 s and 0.5 s was negligible, as shown in **Fig. 4.8 (c)**, hence a Δt of 0.5 s was chosen for the simulations.

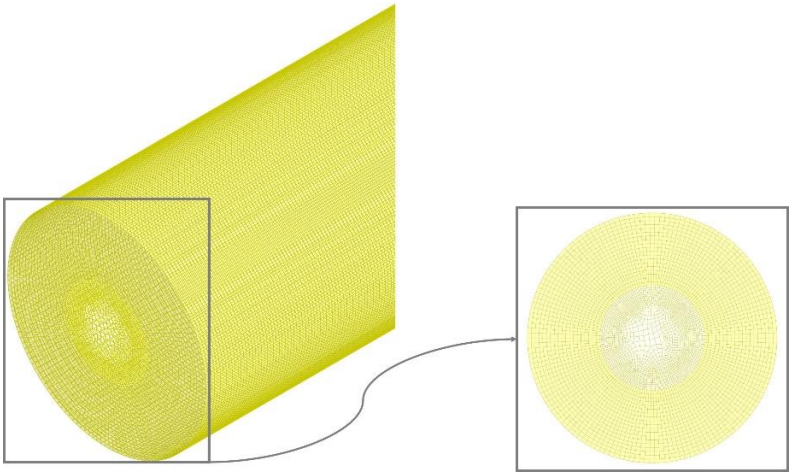

(a)

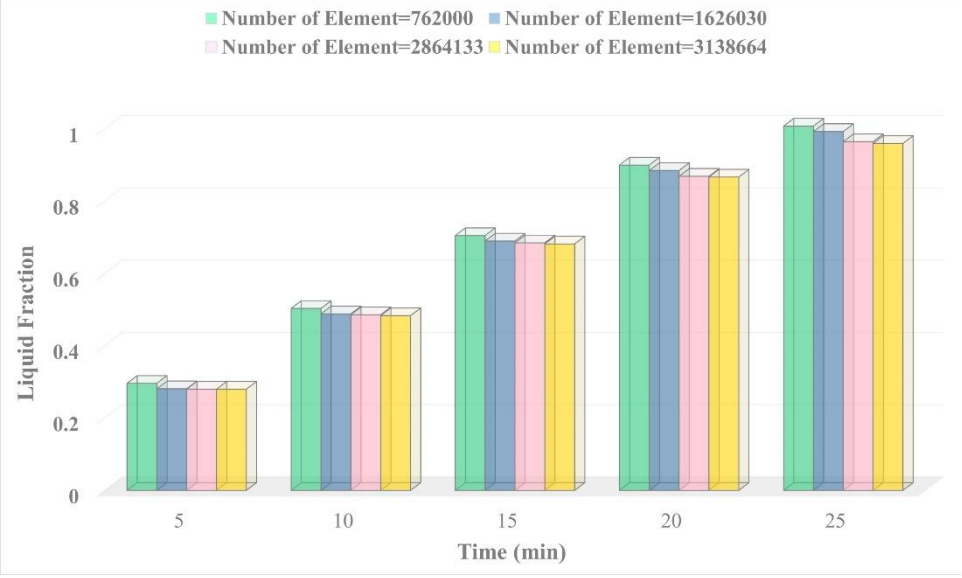

(b)

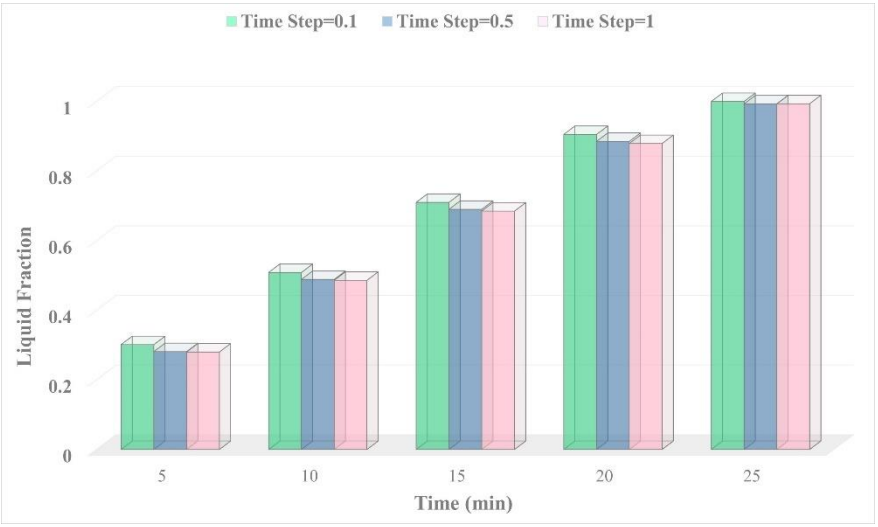

(c)

Fig. 4.8. (a) Different views of the generated mesh, (b) and (c) mesh and time step independence check performed on the liquid fraction of Case A with pure PCM

4.4. Results and discussion

In this contribution, dispersing Al_2O_3 nano-sized powders, Al_2O_3-MWCNT nano-sized powders into H_2O, and porous MF into the pure PCM (RT82), as well as different heat exchanger geometries (one to six lobed pipe), are here analyzed to improve both PCM melting and solidification. The goal of the computations was to apply some enhancing techniques to get better storage/harvesting energy rates while also achieving the quickest melting and solidification times needed by the PCM in an energy storage/harvesting unit. Seven distinct PCM compositions were used as the foundation for all of the numerical work done in this study:

- Pure PCM (PP)
- NanoPCM /Pure PCM (NP)
- Hybrid Nanofluid/Pure PCM (PP-HNF)
- Hybrid Nanofluid/ NanoPCM /Pure PCM (NP-HNF)
- Metal Foam/Pure PCM (PP-MF)
- Metal Foam / NanoPCM /Pure PCM (NP-MF)
- Metal Foam /Hybrid Nanofluid/ NanoPCM /Pure PCM (NP-HNF-MF)

Where each case, labeled by a letter, is referred to the number of lobes and already shown in **Fig. 4.1** before. For the aforementioned cases, HNF referred to

the cases in which the water (HTF) is mixed with the MWCNT powder; when there is no HNF then just water is employed as the HTF.

4.4.1 Melting scenario

4.4.1.1 Stefan Number: Effect of inlet HTF temperature

Figure 4.9 demonstrates the melting time (t_m), energy storage (E), time-saving (%), and heat transfer rates ($P_{L,m}$ and $P_{L,m}^{*}$), for three different HTF inlet temperatures of 360.15, 363.15, and 366.15 K, which respectively correspond to Ste numbers 0.113, 0.147, and 0.181. The Stefan number represents the ratio between sensible to latent heat. By assuming linear heat conduction, phase change at a fixed temperature, and negligible density differences between the phases, this number describes how sensitive is the thermal process compared to the reference latent heat. Thus, increasing Ste means that the relative weight of sensible heating compared to latent one is increased; this is obvious if one considers higher HTF inlet temperatures. It is important to note that the melting time, which depends on each simulated case, is used to calculate the average storage heat rate starting from the stored energy (see **Table 4.5**). According to **Fig. 4.9**, it is shown that the higher the Stefan numbers in Case A-PP, the higher is the ΔT between the HTF and t of PCM; therefore, energy storage and heat transfer rate increase, making PCM to melt in less time. All this is confirmed in **Figs. 4.9b** and **4.9c**, where it is shown that energy storage is generally higher for higher Ste; on the other hand, time saving for higher Ste reaches up to 52.53%. By using higher Ste HTFs, one could then store larger amounts of energy in less time and design thermal energy storage systems based on this outcome. An appropriate combination of dimensionless numbers from Fourier, Stefan, and Rayleigh is employed to correlate the liquid fractions in accordance with the dimensional analysis conducted by Ho and Viskanta [72], Shatikian et al. [73], and Kamkari et al. [74]. **Fig. 4.9d** depicts the liquid fraction versus a suitable combination of the Stefan ($\mathrm{Ste} = \frac{c(T_{in} - T_m)}{h_f}$), Fourier ($\mathrm{Fo} = \frac{\alpha t}{L^2}$) that α and t refer to the diffusivity and time respectively, and Rayleigh numbers ($\mathrm{Ra} = \frac{g\beta(T_{in} - T_m)L^3}{\nu\alpha}$), namely $\mathrm{Ste}^2\mathrm{FoRa}^{0.25}$, for Case A with pure PCM considered in the present study. $\mathrm{Ste}^2\mathrm{Fo}$, the product of the Fourier and Stefan numbers, is an independent dimensionless quantity that accounts for transient heat conduction and phase change. Convection in the liquid phase is another

physical phenomena that should be included in this research. So, for the influence of natural convection on the melting process, the Rayleigh number, $Ra^{0.25}$, is the suitable value. The amplification of convective flows is related to heat transfer augmentation and, as a result, melting time decrease in enclosures.

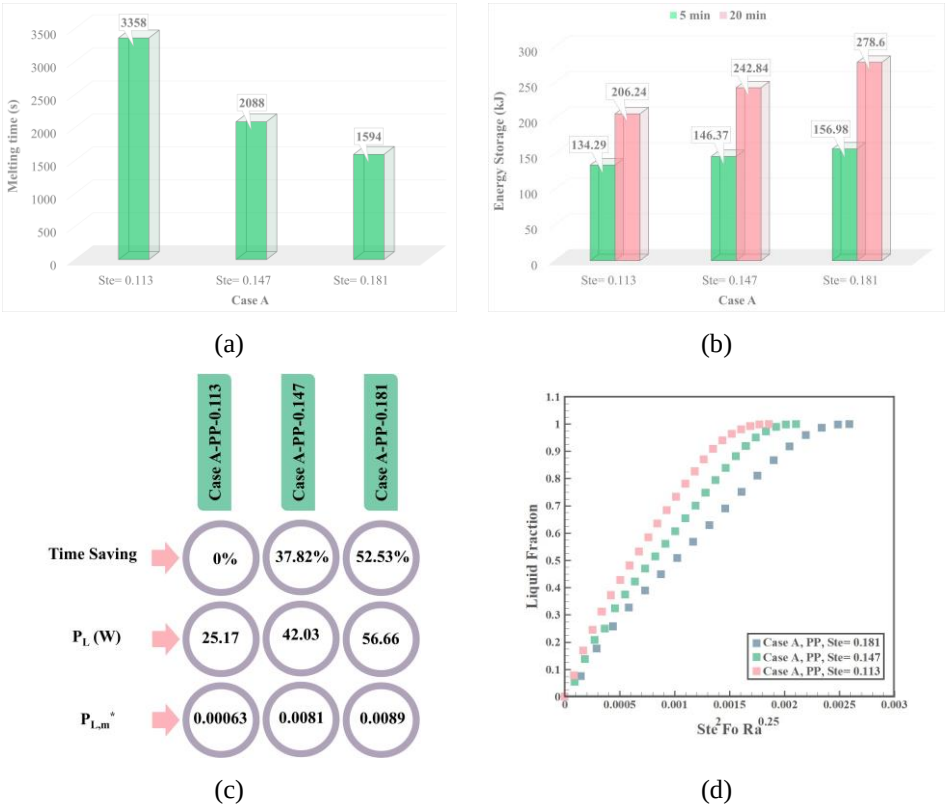

Fig. 4.9. A comparison between different inlet HTF temperature (Ste) on instantaneous (a) melting time, (b) stored energy (after 5 and 20min.), (c) time saving and heat transfer rates, and (d) liquid fractions versus $Ste^2FoRa^{0.25}$

Fig. 4.10 demonstrates the effect of different water inlet temperatures – *i. e.*, Ste numbers - on the charging process, including liquid fraction (LF) and average temperature (T) of PCM-PP for five different cross-sections after t=20 min. Heat will start to seep through the outer surfaces since the working hot fluid temperature is higher than the PCM melting point, which will start to melt in the form of a melt layer next to the inner surface. If one constraint the cross-section location (highlighted ones in **Fig. 4.10**), there is more amount of melted PCM if the inlet HTF temperature is higher.

In **Fig. 4.11**, results are presented for the $z = L/2$ section in terms of liquid fraction contours, thermal field, and liquid PCM streamlines, for two different times (t = 5, 20 min). First of all, it is noticed that there is more melted PCM after 20 minutes. The findings demonstrate that the liquid percentage operates similarly in each scenario of Ste value, appearing and growing from the outer tube toward the inner because the heat comes from the exterior (HTF) tube. Additionally, the thermal distribution follows the same trend as the liquid fraction, with the PCM temperature increasing as it moves from the outer tube to other parts of the container. The growth of the liquid-solid fraction and the location of the liquid-solid interface (mushy zone) are in agreement with the thermal fields. Streamlines are here presented to underline the role that natural convection has during melting. Due to its significant role in advanced stages, by observing the isothermal and mushy zone, it is clear that a core of unmelted PCM might remain in the core because the heat comes from the periphery. In particular, there is more liquid on top of the cross-section than at the bottom. Such recirculation areas are visible in the melted zones, generated owing to the action of buoyancy and gravity forces in the vertical direction. Because PCM liquid density is lower than that of the solid, the warm liquid travels upside in the annulus during the early phases of melting. These recirculation flows most likely formed as a result of low-density liquid upwelling from the heated inner tube. In addition, the pace of melting in the top part of the system is accelerated by these powerful buoyancy-driven motions. The movement in the liquid PCM governs heat transfer at advanced phases, as seen in **Fig. 4.11**, where the streamlines depict the flow of the molten PCM and demonstrate that the molten PCM has adopted a rolling form due to the buoyancy force in the liquid portion. The streamlines also illustrate behavior and intensity of the buoyancy force of natural convection, which are seen to develop similarly in Case A-PP-360.15 at early times (t = 5 min), then streamline get larger and denser especially with higher Stefan numbers, as seen at the advanced time (t = 20 min). In the situation of Ste = 0.181, it is seen that the liquid zone assumes a regular shape after t = 5 min that follows the shape of the inner tube (circular). It can be seen that for Ste = 0.113, Ste = 0.147, and Ste = 0.181, the developed liquid on the top always heightens with time. Additionally, the molten PCM moved parallel to the inner tube before turning round, giving the melt zone the irregular shape previously described and shown in **Fig. 4.11**.

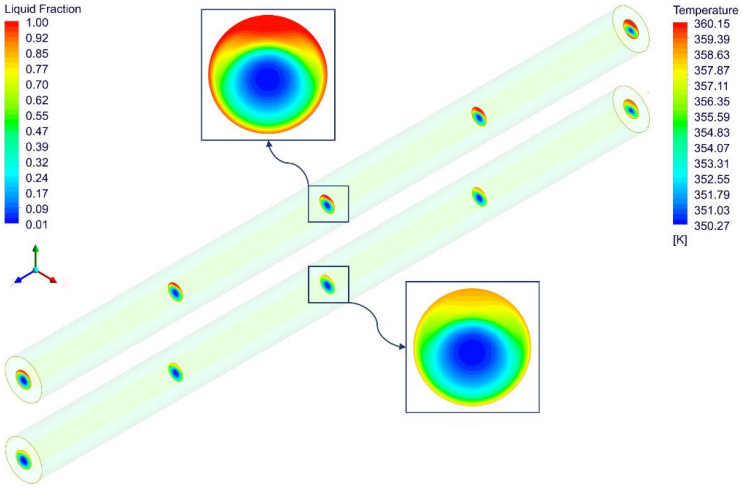

Ste= 0.113

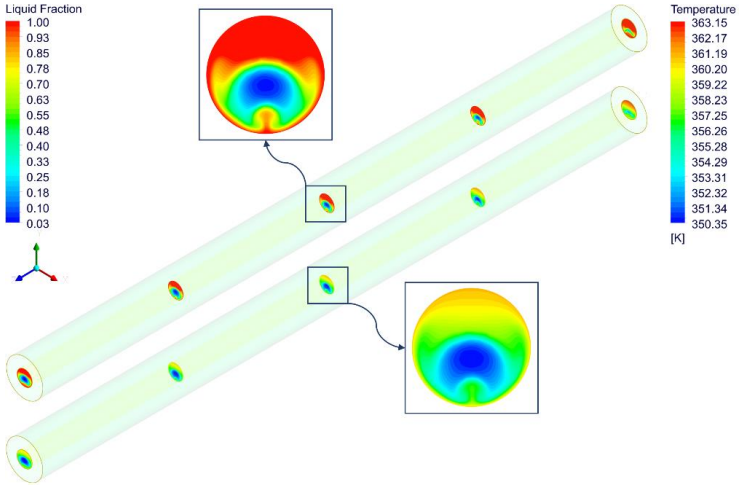

Ste= 0.147

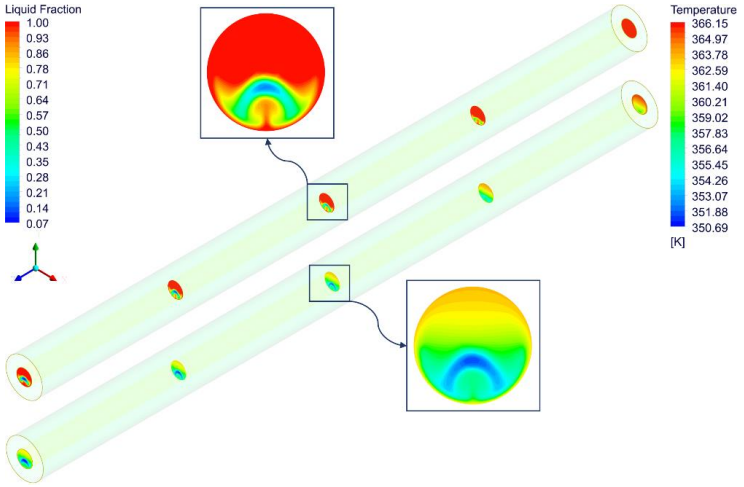

Ste= 0.181

Fig. 4.10. Liquid fraction (top of each subfigure) and temperature fields (bottom of each subfigure) for Case A with-Pure PCM at 20 min with different Ste numbers

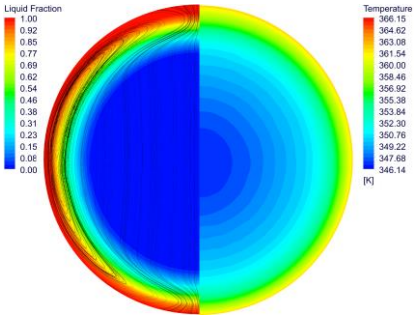

5 min-Ste= 0.181

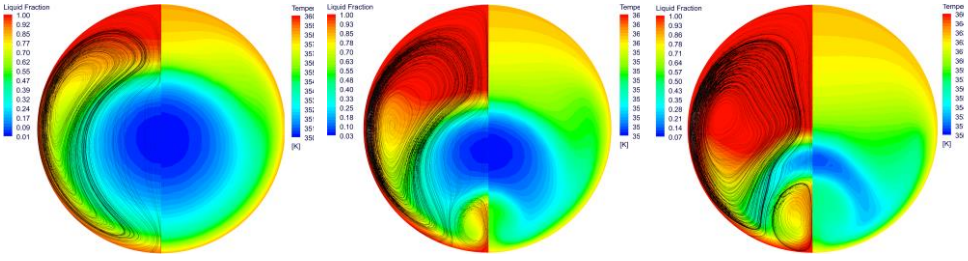

20 min-Ste= 0.113 20 min-Ste= 0.147 20 min-Ste= 0.181

Fig. 4.11. Contour plots of liquid fraction, and streamlines (left), and thermal fields (right), for $z = L/2$ and Case A with-Pure PCM

4.4.1.2 Heat exchanger geometry: Optimization of the lobes number

Fig. 4.12 displays the simulation outcomes of one to six-lobed DPHX as melting time, energy storage, time-saving, and heat transfer rate. In this figure, the effect of the lobed DPHX on the PCM melting process can be seen. The result indicated that the amount of heat absorption for case F with a six-lobed cross-section is higher than in other cases for both 5 and 20 minutes, while the melting time becomes smaller if higher number of lobes are considered. This can be mainly attributed to the fact that the heat transfer area is improved if more lobes are considered. The outcomes showed that changing from a one to six-lobed DPHX reduces the melting time by 18.32%.

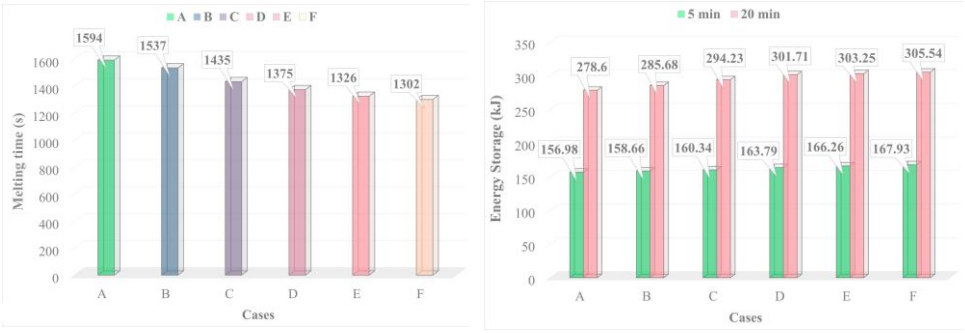

(a) (b)

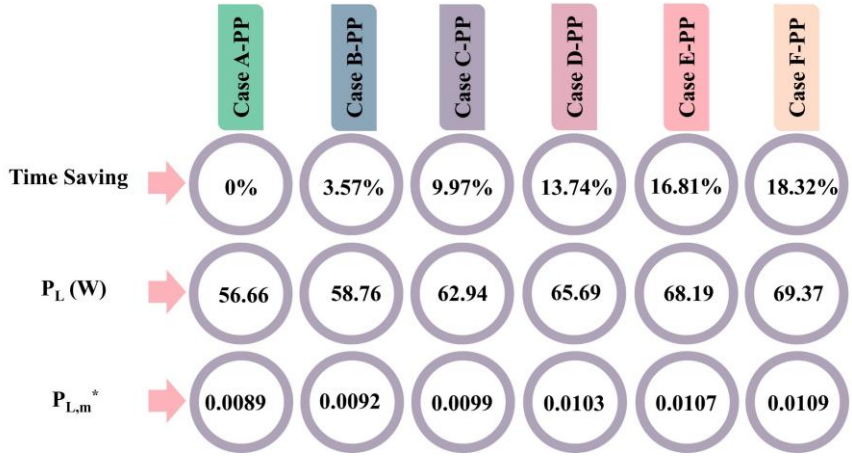

(c)

Fig. 4.12. A comparison between various configuration double-pipe heat exchangers on instantaneous (a) melting time, (b) stored energy (after 5 and 20min), and (c) time saved and heat transfer rates

Fig. 4.13 shows the simulated DPHX results for one to six lobes in the form of temperature and liquid fraction contours at t = 20 min and Ste = 0.181. As shown in **Fig. 4.13** under the same conditions, when increasing the lobed number from one to six, the melting process speeds up. This occurs because, when the geometry of the inner tube's cross-section is changed from Case A (one-lobed DPHX) to Case F (six-lobed DPHX), there is more heat transfer area that allows more penetration for the heat. Furthermore, there is no liquid PCM natural convection dumping that might allow to reduce the thermal enhancement effect with more lobes. Thus, the completion time of the melting process in Case F (six-lobed heat exchanger, LDPHX) will be less than in Case A (one- LDPHX). Cross-section plots for $z = L/2$ are also shown to underline liquid PCM natural convection. As it is clear, in Case F-PP a larger amount of PCM has been melted in the section of $z = L/2$ compared to Case A-PP. The fact that the liquid fraction is not symmetric is attributed to some natural convection that arises with lobed heat exchanger too.

Fig. 4.14 depicts contour plots of liquid fraction, thermal field, and streamlines at t = 20 min for all cases. For all cases, heat transfer by the hot HTF from the outer tube to the solid PCM in the inner tube is carried out and the PCM starts transitioning from the solid to the liquid phases. Natural convection (NC) heat transfer starts to develop at this stage and eventually gets stronger time after time. The fluid moves upwards as a result of the buoyancy force and the density difference between phases. This cycle is completed by the opposing gravitational force, which generates a vortex that is repeated until the entire solid PCM melts. The comparison of LDPHXs also shows that adding lobed pipe leads to higher melting rates which can be inferred from the larger liquid zones. In cases A-F, where the same volume of PCM was used, increasing the number of lobes in the heat exchanger led to a faster rate of heat transfer. This is because the additional lobes provide more surface area for heat transfer, allowing for more efficient heat transfer between the fluids and PCM. Indeed, it is clear that after Case B melting is almost or completely done. As a result, the temperature difference between the two fluids decreases; the overall heat transfer rate increases since at this point complete melting has been reached from a while. By increasing the number of lobes, these heat exchangers can enhance their heat transfer efficiency and, therefore, increase their overall performance.

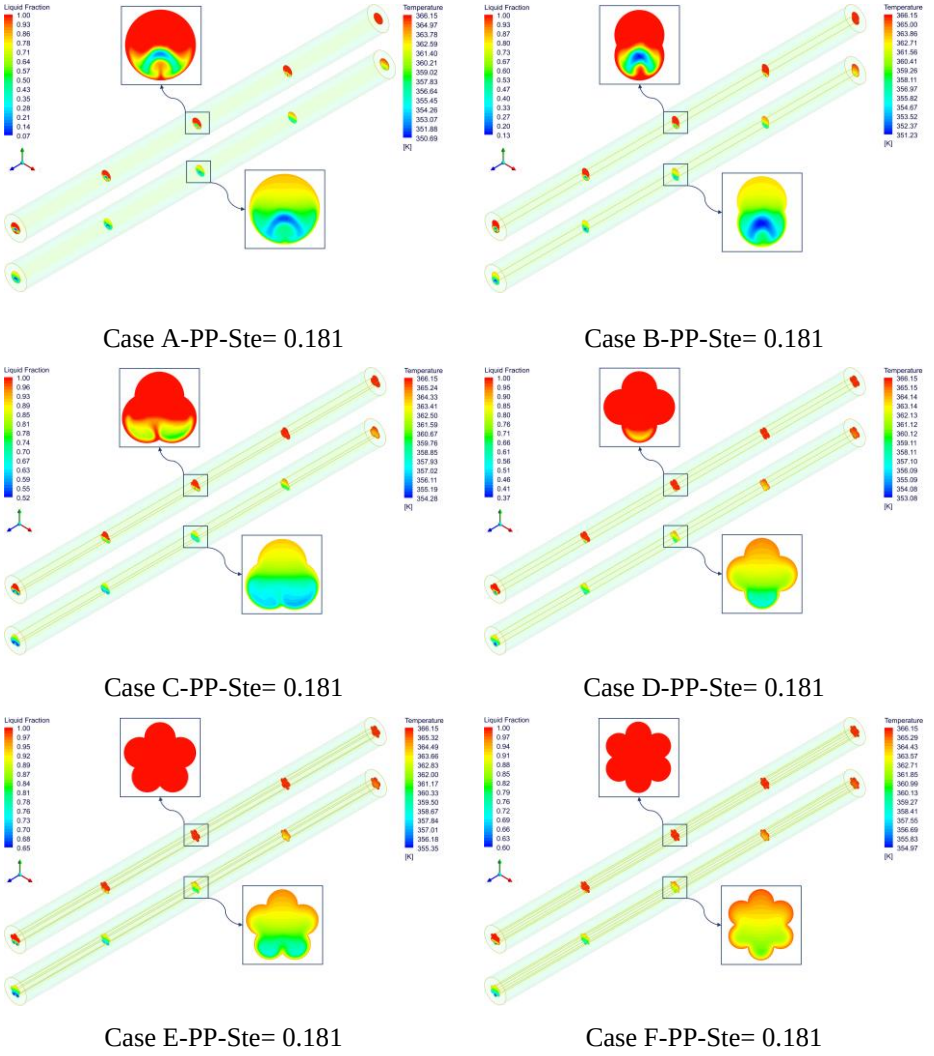

Case A-PP-Ste= 0.181 Case B-PP-Ste= 0.181

Case C-PP-Ste= 0.181 Case D-PP-Ste= 0.181

Case E-PP-Ste= 0.181 Case F-PP-Ste= 0.181

Fig. 4.13. Liquid fraction (top of each subfigure) and temperature fields (bottom of each subfigure) of the lobed DPHX-LHTES for different lobed cross-sections after 20 min

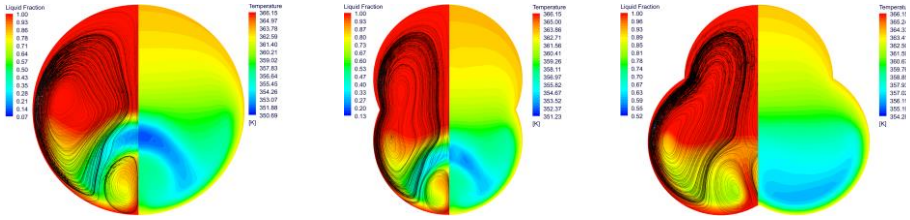

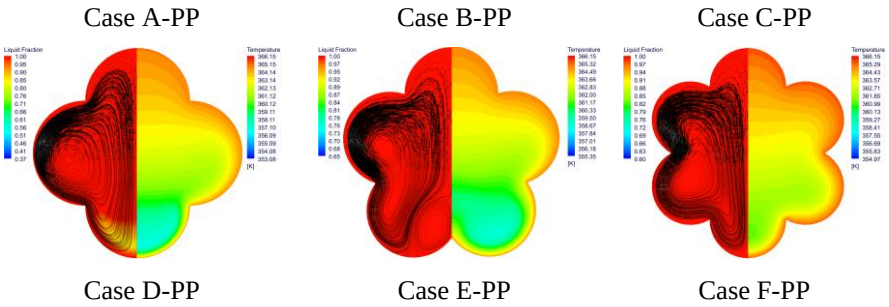

Fig. 4.14. Contour plots of liquid fraction and liquid PCM streamlines (left), and thermal field (right) at Z=L/2 section and for all cases Pure PCM

4.4.1.3 Nanoparticle: the effect of both NEPCM and hybrid nanofluid

Fig. 4.15 illustrates melting time, energy storage, time-saving, and heat transfer rate for case F with dispersing Al_2O_3 nanoparticles in the pure PCM, and Al_2O_3-MWCNT nanoparticles into H_2O (HTF). When comparing PP with NP, NP-HNF in Case F, the figure shows that the former system is the case in which the melting time is the shortest. On the other hand, energy stored after 5 minutes looks more or less similar for all the cases investigated. This happens because NP has a lower energy storage capacity than pure PCM, thus the overall heat capacity becomes smaller, while there is no huge advantage in terms of melting time. The case that presents slightly higher stored energies are the ones with pure PCM because of this reason. According to the available data, with dispersing combining NP in PCM with a HNF in water in Case F-NP-HNF, the melting time is decreased by 3.6 % and 21.41% when compared to Case F-PP and Case A-PP, respectively. The heat storage rate $P_{L,m}$ is always higher for all the cases F within this subsection than Case A-PP. However, all these cases present a heat transfer rate of about 70 W. Again, this parameter looks to be really important here since it weighs the stored energy with the melting time for each case to appreciate how fast melting is.

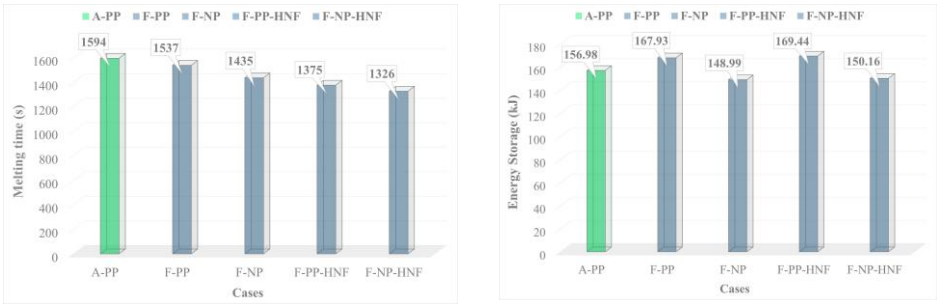

(a) (b)

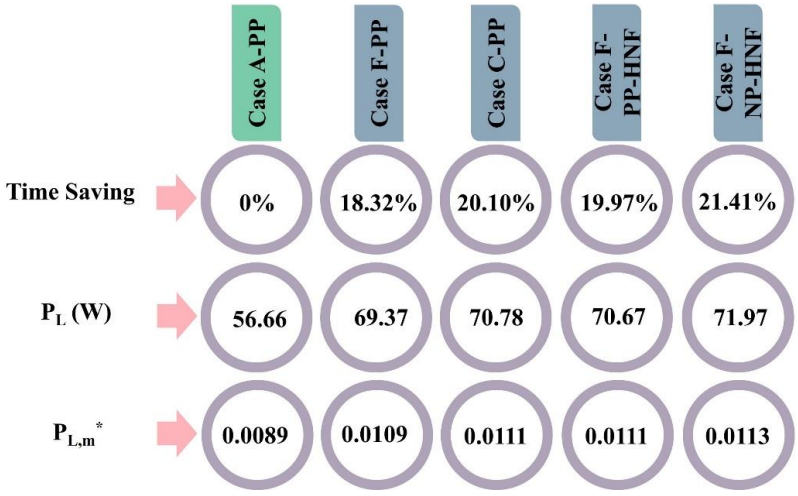

(c)

Fig. 4.15. A comparison between Case A-PP and Case F-PP/NP/HNF instantaneous (a) melting time, (b) stored energy (after 5 minutes), and (c) time saving and heat transfer rate

4.4.1.4 Metal foam: Analysis of different porosities

In **Fig. 4.16**, melting time, energy storage, time-saving percentage, and heat transfer rate, are presented for Case F of investigated solutions referred to PP, PP-MF, NP-MF, and NP-HNF-MF ($\varepsilon = 0.92$). Percentages are referred to Case A-PP. From **Fig. 4.16**, it is shown that the best solution, which is case F-NP-HNF-MF that considers NP, HNF, and foam together, allows reducing the melting time by 56.22 % and 64.30% when compared to Case F-PP and Case A-PP respectively. When compared with pure PCMs, employing MFs drastically improves both $P_{L,m}$ and $P_{L,m}^*$. This means that combined solutions

allow to have a strong increase in terms of stored energy velocity, especially due to the inclusion of MF.

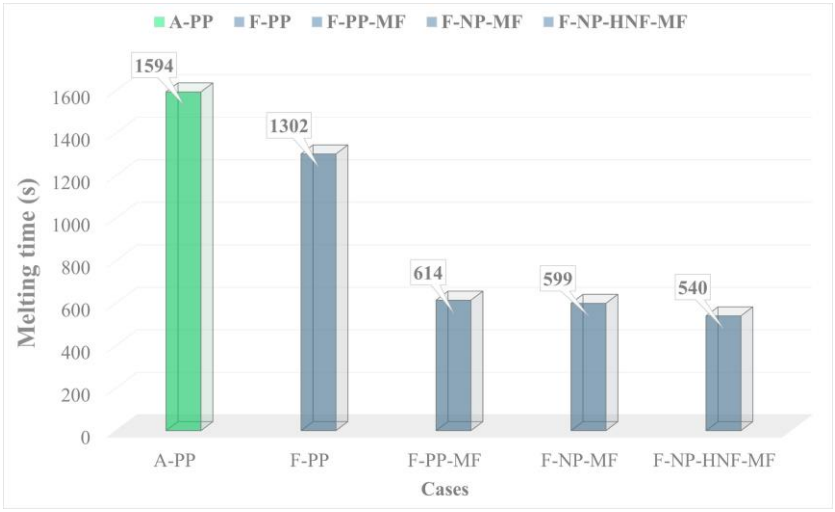

(a)

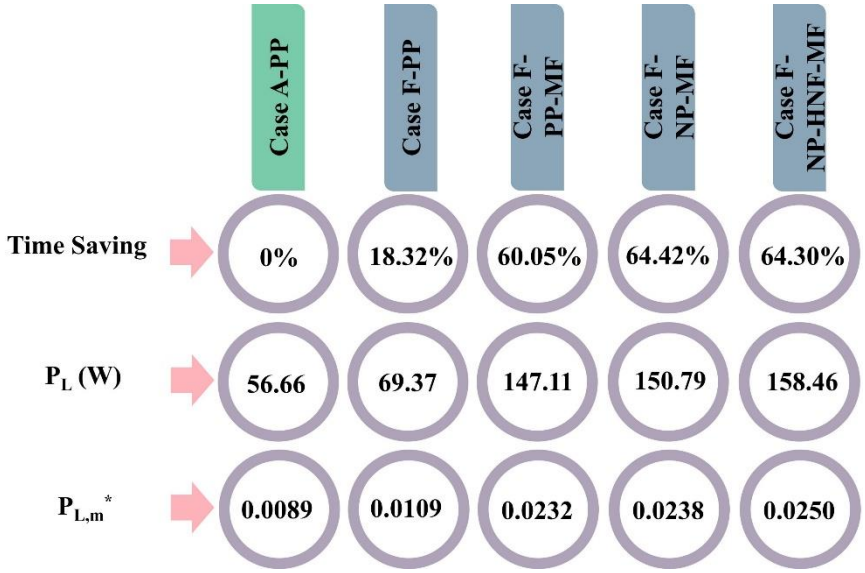

(b)

Fig. 4.16. A comparison between Case A-PP and Case F-PP/NP/HNF/MF (Ɛ=0.92) instantaneous (a) melting time, and (b) time saving and heat transfer rates

A summary of melting time, energy storage, time-saving percentage, and heat transfer rate, is shown in **Fig. 4.17** to underline how relevant is porosity on the thermal performances of the device proposed as Case F. Here, four distinct porosities (say, from 0.88 to 0.95) are employed at equal PPIs (say, 20) since it has been shown that porosity has a greater impact than PPIs throughout the period of the research [46, 62-66]. Time saving and rate of energy released for the porosity of 0.88 is almost higher than all the other cases, even if foams reduce some volume to the PCM. In comparison with the pure PCM system, the effect of porous foam and NP is significant on system, where foams show to have a primary role in these thermal performance enhancements. Also, lowering porosity would reduce melting time. From **Fig. 4.17**, it is shown that the best solution, which is case F-NP-HNF-MF with porosity of 0.88 considers NP, HNF, and foam together, allow reducing the melting time by 59.14% and 66.68% compared to Case F-PP and Case A-PP, respectively. The thermal conductivity of the metal foam can affect the rate of heat transfer between the PCM and the metal foam; indeed, the overall thermal conductivity of the system is increased because of the metal matrix included within the PCM. A lower porosity metal foam also provides a higher surface contact area between the PCM and the metal foam, which results in improved heat transfer. The higher surface area, together with the higher overall thermal conductivity, facilitates more effective heat transfer, leading to a faster charging time for the PCM. This might be the reason why metal foams have the highest impact on heat transfer so far.

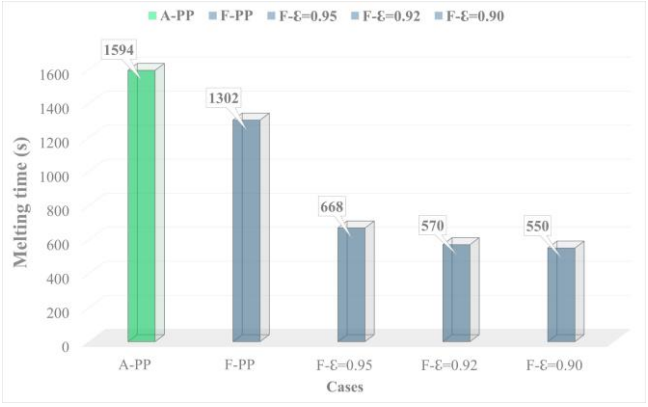

(a)

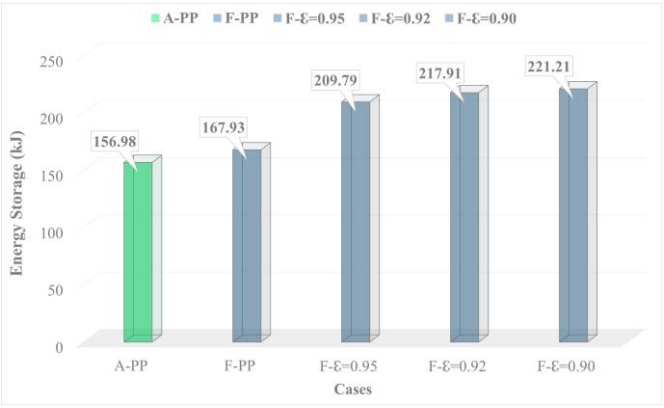

(b)

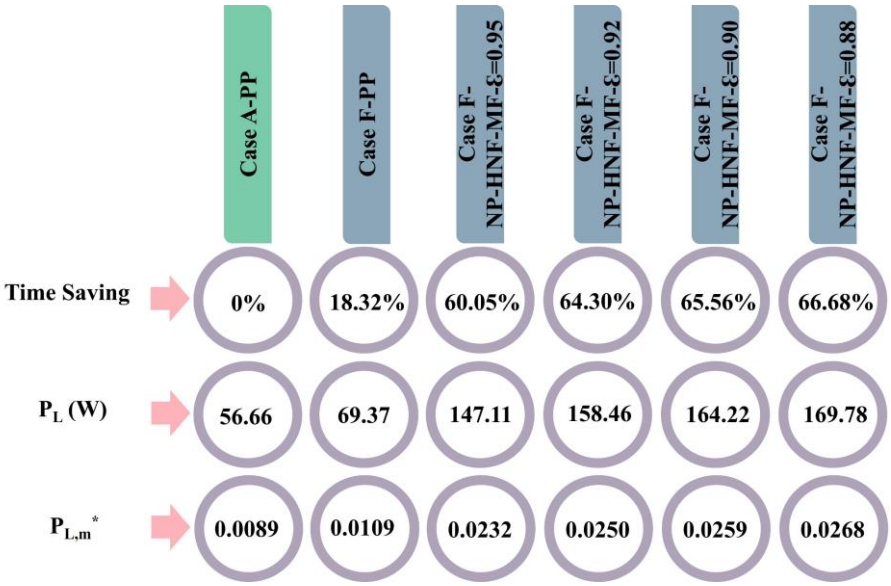

(c)

Fig. 4.17. A comparison between Case A-PP and Case F-NP-HNF-MF instantaneous (a) melting time, (b) stored energy (after 5), and (c) time saving and heat transfer rates

A comparison among two cases, namely cases A-PP as references case, and Case F-NP-HNF-MF, that in turn is the one that provides the best performances, is presented in **Figs. 4.18** in terms of liquid fraction and temperature evolution after 20 minutes. From the figures, it is shown that when the DPHX coupled with the six-lobed with combined NP-HNF-MF to be used, the core of the lobed tube is reached by the heat propagation just after 5 min. On the other hand, there is still a large region in Case A-PP. This demonstrates the advantages due to the

fact that a combined solution is here proposed. The addition of metal foam with high thermal conductivity improves the overall thermal conductivity of metal foam with PCM composite, leading to enhanced conduction heat transfer in both the solid and liquid zones of the PCM. However, the insertion of metallic foam in the base PCM leads to flow blockage in the liquid zone, impeding upward movement and weakening buoyancy force. This results in suppressed convection heat transfer in the melted zone. By increasing the lobed of inner tubes in the composite metal foam with PCM melting, similar to PP melting, the melting rate is accelerated due to the increase in heat transfer surfaces. The temperature of the NP-HNF-MF composite is higher than that of pure PCM, indicating that inserting foam in the base PCM reduces thermal stratification and creates a uniform temperature distribution in NP-HNF-MF.

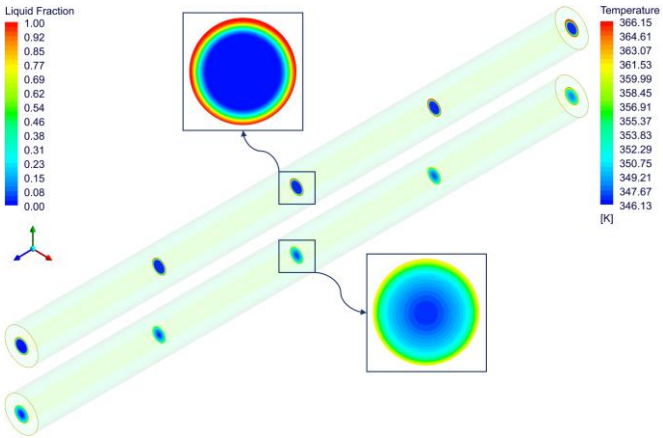

Case A-PP-Ste= 0.181

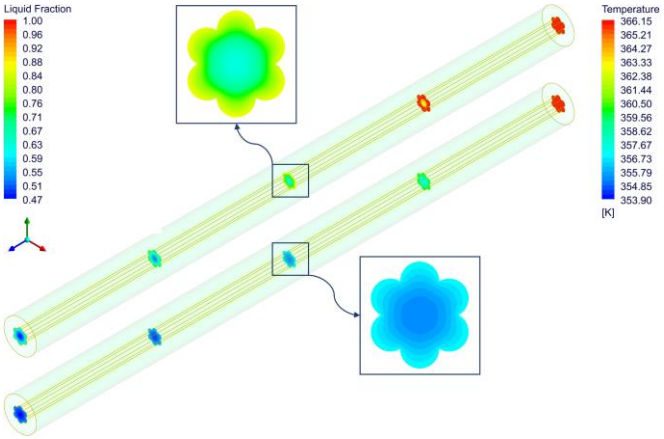

Case F-HNF-MF(0.88)-NEPCM-Ste= 0.181

Fig. 4.18. Liquid fraction (top of each subfigure) and temperature fields (bottom of each subfigure)) of the lobed DPHX-LHTES for lobed cross- sections at after 5 min

4.4.2. Solidification scenario

Bar chart comparisons in terms of solidification time, energy harvesting, time-saving percentage, and heat transfer rate are shown in **Fig. 4.19** with references to the solidification case. Since it has been shown in subsection 4.1 which are the best conditions for melting, it is here assumed that these conditions are the best for the solidification scenario; therefore, in this subsection, we will quantify these conditions improvements. Heat transfer performances in terms of both solidification time and heat storage rate look to be far better if NP, MF, and lobed geometry are employed, which means that far more PCM is frozen at an equal time by adding NP and MF. When comparing Case F- NP-HNF-MF with a porosity of 0.88 to Case A-PP, a reduction of 81.62% in terms of solidification time has been found. The heat transfer rate for NP-HNF-MF, is drastically higher than for PP, say 198.95 W *vs.* 36.56 W. This makes freezing velocity to be much higher if combined solutions are considered.

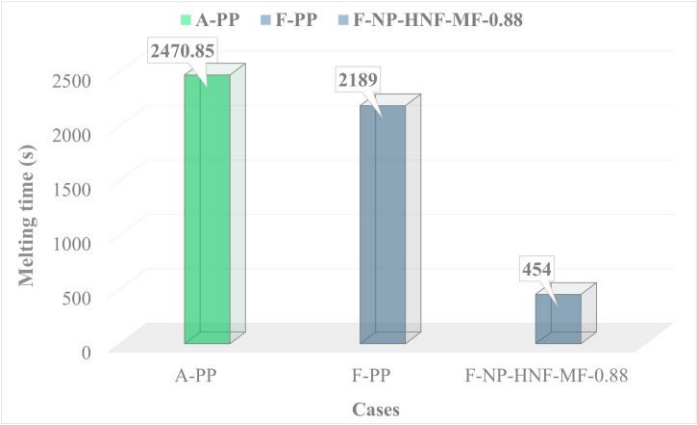
A-PP
F-PP
F-NP-HNF-MF-0.88
2470.85
2189
454
2500
2000
1500
1000
500
0
Melting time (s)
A-PP
F-PP
F-NP-HNF-MF-0.88
Cases

(a)

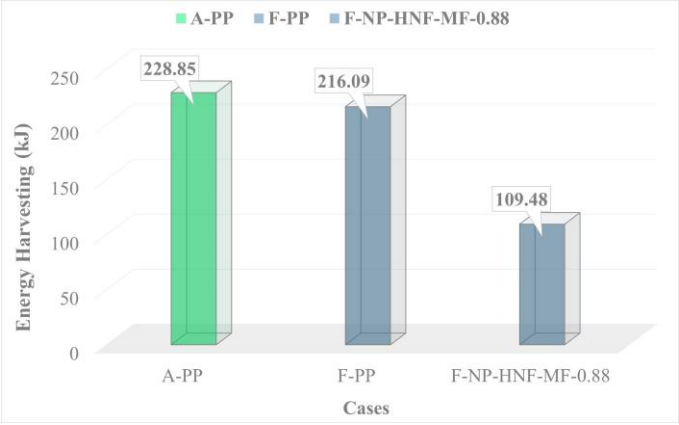
A-PP
F-PP
F-NP-HNF-MF-0.88
228.85
216.09
109.48
250
200
150
100
50
0
Energy Harvesting (kJ)
A-PP
F-PP
F-NP-HNF-MF-0.88
Cases

(b)

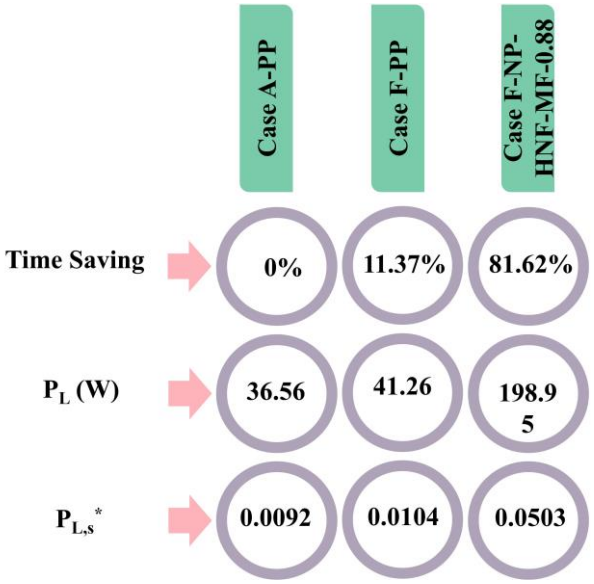

(c)

Fig. 4.19. A comparison between Case A-PP and Case F-PP/NP/HNF instantaneous (a) solidification time, (b) energy harvesting (after 5 min), and (c) time saving and heat transfer rates

Contour plots of liquid fraction, thermal field, and liquid PCM streamlines, after 5 and 20 minutes are shown in **Fig 4.20**. Natural convection is more significant in the early phases of the discharge process; as time passes, the impacts of free convection diminish. The lower part of the storage unit seems to benefit from weak natural convection during the solidification phase, in contrast to the melting process. Comparing Case F-NP-HNF-MF and Case A-PP, it can be shown that Case F-NP-HNF-MF outperforms Case A-PP in the early first 5 minutes. It was discovered that the discharge process in the system's lower zone becomes quicker than that in the upper portion because of the natural convection that causes quicker solidification in the lower half of the HX. It was also demonstrated that adding NP-HNF-MF boosts the heat exchange rate.

In **Fig. 4.20.a,** the liquid fraction, streamlines, thermal field contours at at z= L/2 cross-sections of heat exchangers filled with pure PCM are depicted. During the early stage of the solidification process, the large temperature difference between the cold HTF and hot PCM leads to a high heat transfer rate. The initial temperature of pure PCM is 366 K, which is higher than the melting point. Natural convection is important in the solidification process, just as in melting. After 5 minutes, a thin layer of solid PCM is observed around the cold HTF

tubes. The temperature difference between the solid and liquid phases of the PCM generates natural convection flow in the liquid phase. The cold PCM moves downward and pushes warm PCM to the upper region. It can be noted that the thickness of the solid layer in the lower section of the HTF tubes is slightly greater than that in the upper section due to buoyancy effects. As solidification progresses, two phenomena occur simultaneously: the solid PCM around the cold HTF tubes becomes thicker, resulting in an increase in thermal resistance and a reduction in solidification rate. Additionally, the temperature of the liquid phase is lower than the initial temperature of pure PCM due to heat exchange with solid PCM at the solid-liquid interface. Therefore, the temperature gradient between the solid and liquid phases of pure PCM decreases, weakening the natural convection flow. As time elapses, the solidification rate is reduced significantly until the final moments.

As shown in **Fig. 4.20.b**, the amount of solidified PCM in NP-HNF-MF composites is significantly greater than that in PP in each case, as the overall thermal conductivity of NP-HNF-MF composites is higher. Solidification rates in all regions of NP-HNF-MF composites are uniform. Conversely, in solidifying PP, the solidification rate is higher at the bottom section of the cold tubes than at their top section. There is no liquid zone in the solidifying NP-HNF-MF composites, unlike in PP. However, a large region of NP-HNF-MF composites is similar to a mushy zone since the coolness of HTF is transferred to all regions of the NP-HNF-MF composite through the metal ligament. Hence, solidification starts everywhere in NP-HNF-MF composites. In contrast, in PP, the solidified zone grows gradually and layer by layer where there is persistent thermal stratification.

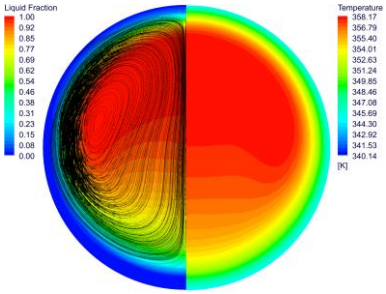

Case A-PP-5min

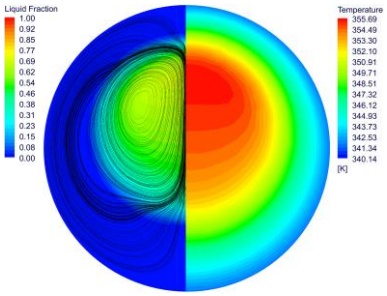

Case A-PP-20min

(a)

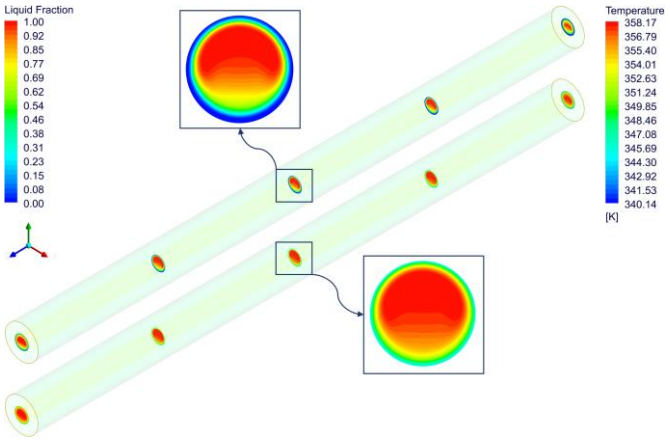

A-PP-5min

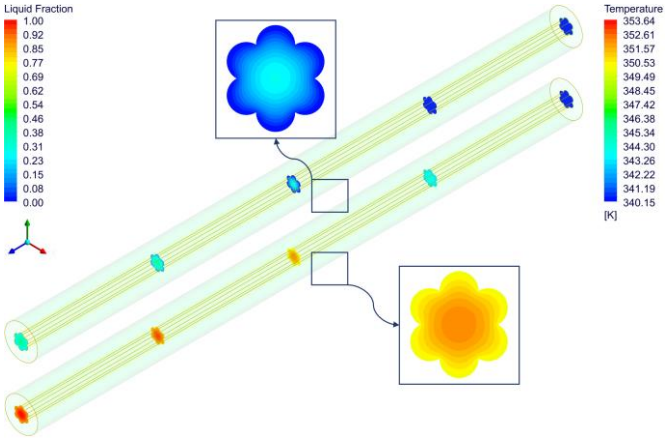

F-NP-HNF-MF-5min

(b)

Fig. 4.20. Contour plots of the (a) liquid fraction and 0 (right) at z=L/2, (b) Liquid fraction (top of each subfigure) and temperature fields (bottom of each subfigure) of solidification process in the lobed DPHX-LHTES for Case A-PP and Case F-PP-NP-HNF-MF at 5 min and 20 min

4.4.3. Economic assessment

Within the present analysis, it is really important to understand the economical feasibility of a solution. Even if a throughout economical analysis might be a future plan for the present research, a discussion of this aspect is here reported. The cost of a thermal storage system that includes metal foam,

nanoparticle and in general a heat exchanger, several factors must be considered, including both initial and operating costs. While the cost of metal foam, nanoparticles and PCM may be higher than that of traditional materials, their superior heat transfer properties and smaller size can balance out these expenses. In a study by Yang et al. [75], the use of metal-foam-cored phase change heat exchangers was examined, revealing potential yearly cost savings of 2139 $/year thanks to the higher heat exchanger efficiency. Thus, a single metal-foam-cored heat exchanger would require approximately 4.5 years to recoup the initial investment costs for fabrication. Over the system's 30-year lifespan, a metal-foam-cored plate heat exchanger could potentially save roughly 56683 $ if one uses a conventional plate heat exchanger as a reference case. These results indicate that metal foam can offer an economically feasible solution for improving heat transfer in thermal storage systems. Bianco et al. [76] utilized a mathematical model that was based on volume-averaged porous media equations to analyze the cost and operational time of a finned heat sink that incorporated both phase change material and metal foam. They employed a multi-objective Pareto optimization approach using a genetic algorithm to achieve their research objectives. The authors emphasized the importance of using appropriate values for porosity, pore density, fin thickness, number of fins, and device height to enhance heat transfer performance, minimize cost, and maximize operational time. The study conducted by Yang et al. [77] focused on the solidification behavior of metal foam composite PCM for refrigeration purposes. Furthermore, the research also evaluated the technical and economic aspects of employing composite PCM for cold storage. The economic analysis conducted as a part of the research demonstrated that the payback period for implementing PCM was less than 2 years.

To summarize, the research findings highlight the optimal solutions in terms of cost and operation time for designing heat management devices. These outcomes are expected to be beneficial for individuals who are involved in the design of such devices, especially in situations where cost or operation time constraints exist.

4.4.4. Practical significance and usefulness

From the results, it has been clearly shown that mixing different thermal enhancement techniques might be helpful to improve the thermal performances of a thermal energy storage system coupled with a concentrated solar source. These techniques are based on using lobed configurations for the tube-in-tube heat exchangers, as well as using nanoparticles and/or metal foams. In

particular, we suggest a uniform variation of foam porosity to facilitate conduction heat transfer during the initial phase of heat transfer when the PCM is in a solid state. Subsequently, the porosity can be increased to allow natural convection flows to take effect. Our results indicate that the porosity parameter can influence the isotherm and melting behavior within the enclosure. On the other hand, including other enhancement solutions might be helpful for a further improvement of the system performances. Based on our findings, it can be inferred that porosity variation and the use of nanoparticles may have a more significant impact on the melting and solidification process in large-scale thermal energy storage/harvesting systems. In such systems, the molten region can be extended, resulting in greater distances between the heated surface and solid PCM. This necessitates the conduction of heat through longer distances to reach the cold PCM. In other words, such solutions might be really helpful for large scale system, since the performance index like stored energy in kWh are really high if scaled with the volume of the system in m^3. Moreover, the larger molten region enables the hot liquid PCM to move more easily from the heated surface to reach the cold PCM, potentially leading to significant natural convection flows in large-scale systems. While the scope of our research was limited to smaller-scale systems, our findings suggest avenues for future investigation in the context of larger systems. If one considers smaller-scale systems, since the stored energy per unit volume, in kWh/m^3, at constrained times, becomes much higher because of the improved thermal performances, one might consider to design smaller thermal energy storage systems that are still able to guarantee large amounts of stored energy.

4.5. Conclusions

4.5.1. The Key Findings

In this work, a lobed double-pipe heat exchanger with a solar parabolic system that can store and release energy, to provide hot water, have been proposed to increase the rate of charging and discharging in thermal storage/harvesting units. To improve the low conduction mode of RT82 and increase efficiency systems, some enhancing methods have been used separately or together; 1) Lobed-heat exchanger geometry; 2) Dispersing Aluminium oxide nano-sized powders into RT82 as Phase Change Material; 3) Dispersing Aluminium oxide- carbon nanotubes into water; 4) Adding metal foam with different porosity (Aluminum foam). A 3-dimensional Local Thermal Non-Equilibriumporous-media volume-averaged model is used to estimate melting

time, solidification time, energy storage, time-saving percentage, and heat transfer rates by taking into account both nanoparticles and the Phase Change Materials in a single-phase equivalent medium with water/water with nanoparticles is used as the working heat transfer fluid. Either melting or solidification have been investigated here by considering different heat transfer fluid inlet temperatures. The objective of the present study is to have a throughout comparison of all these solutions in order to appreciate which one could be the best for thermal energy storage/harvesting and melting/solidification fraction evolution when a lobed double-pipe heat exchanger is used in combination with a solar parabolic system. The main conclusions from the present work are listed as follows:

- When changing the heat transfer fluid temperature from 360.15 to 363.15, and 360.15 K (Ste numbers 0.113, 0.147, and 0.181), the melting time was reduced by 37.82% and 52.53%, respectively;

- By using different lobes for the heat exchanger, both melting, and solidification times were significantly reduced, so that Case F (six-lobed surfaces) has the best performance among other cases of the lobed pipe heat exchanger energy storage system. The reason for higher performance is mainly due to heat transfer surface area improvement, and also some increase due to higher liquid PCM natural convection. Case F (six-lobed surfaces) compared to Case A (one-lobed surfaces) decreases the melting and solidification times by 18.32% and 11.37%, respectively; this underlines that even changing just the geometry might have an impact;

- For Case F, the addition of both nanoparticle to RT82 and hybrid nanoparticle to water reduces the melting time by 21.41%, compared to the reference case with Case A-pure RT82; employing nanoparticle to RT82 allows to reach a 20.10% saving;

- Still for Case F with both nanoparticle and metal foam (0.92 porosity), a melting time reduction of 62.42% can be achieved compared to Case A-pure RT82; if only the metal foam is used, the save becomes 60.05%;

- The addition of all methods (nanoparticle, hybrid nanofluid, and metal foam), with porosities of 0.88, 0.90, 0.92, and 0.95, for Case F, reduces the melting time of 66.68%, 65.56%, 64.30%, and 60.52%, respectively, when compared to the Case A-pure RT82; these are slight changes that confirm the fact that foam alone might have more impact than changing its porosity;

- Employing all methods with porosities of 0.88 reduces the solidification time of 81.62% saving; because conduction heat transfer has a bigger effect, the solid component expands more quickly. As a result, every segment's RT82 approaches the phase-change point more quickly.

- With the addition of all methods (nanoparticle, hybrid nanofluid, and metal foam) with porosities of 0.88, in Case F, the rate of heat energy harvesting, and storage has been 198.95 W and 169.78 W, respectively; on the other hand, dimensionless heat rates are 0.0503 and 0.0268, respectively; these numbers are relevant since they quantify how fast is charging/discharging within the presented solutions

After considering the evidence, it can be concluded that metal foams provide the most significant impact on reducing PCM melting/solidification time in flat plate solar collectors. This aspect can be further improved by implementing nanoparticles and lobed surfaces. The authors suggest exploring the following directions for future research in thermal management storage systems:

- Using other types of cellular structures to further improve thermal performance.
- Perform an overall system analysis, including the life-cycle analysis, exergy, economic, and enviroeconomic to assess pros and cons of the proposed system.

In the upcoming Chapter 5 of this thesis, our overarching objective will be meticulously pursued through a comprehensive experimental and numerical approach. This entails the systematic application of a diverse array of existing methodologies and materials previously elucidated in the preceding chapter. These experiments will be conducted across various systems and diverse applications, allowing for a nuanced exploration of the efficacy and adaptability of the discussed methods. By undertaking this multifaceted experimental journey, we aim to glean valuable insights and empirical evidence that not only validate the applicability of the proposed methods but also contribute to a deeper understanding of their versatility and potential impact in diverse contexts.

References

[1] Martin-Escudero K, Salazar-Herran E, Campos-Celador A, Diarce-Belloso G, Gomez-Arriaran I. Solar energy system for heating and domestic hot water supply by means of a heat pump coupled to a photovoltaic ventilated façade. Solar Energy. 2019 May 1;183:453-62.

[2] Yeh CY, Boonk KJ, Sadeghi G, Mehrali M, Shahi M, Brem G, Mahmoudi A. Experimental and numerical analysis of thermal performance of shape stabilized PCM in a solar thermal collector. Case Studies in Thermal Engineering. 2022 Feb 1;30:101706.

[3] Alomar OR, Salih MM, Abd HM. Performance analysis of single-pass solar air heater thermal collector with adding porous media and finned plate. Energy Storage. 2023 Aug;5(5):e447.

[4] Alomar OR, Abd HM, Salih MM. Efficiency enhancement of solar air heater collector by modifying jet impingement with v-corrugated absorber plate. Journal of Energy Storage. 2022 Nov 15;55:105535.

[5] Salih MM, Alomar OR, Yassien HN. Impacts of adding porous media on performance of double-pass solar air heater under natural and forced air circulation processes. International Journal of Mechanical Sciences. 2021 Nov 15;210:106738.

[6] Abd HM, Alomar OR, Ali FA, Salih MM. Experimental study of compound parabolic concentrator with flat plate receiver. Applied Thermal Engineering. 2020 Feb 5;166:114678.

[7] Yassien HN, Alomar OR, Salih MM. Performance analysis of triple-pass solar air heater system: effects of adding a net of tubes below absorber surface. Solar Energy. 2020 Sep 1;207:813-24.

[8] Salih MM, Alomar OR, Ali FA, Abd HM. An experimental investigation of a double pass solar air heater performance: A comparison between natural and forced air circulation processes. Solar Energy. 2019 Nov 15;193:184-94.

[9] Lamrani B, Kuznik F, Draoui A. Thermal performance of a coupled solar parabolic trough collector latent heat storage unit for solar water heating in large buildings. Renewable Energy. 2020 Dec 1;162:411-26.

[10] Gorzin M, Hosseini MJ, Ranjbar AA, Bahrampoury R. Investigation of PCM charging for the energy saving of domestic hot water system. Applied Thermal Engineering. 2018 Jun 5;137:659-68.

[11] Wang Z, Qiu F, Yang W, Zhao X. Applications of solar water heating system with phase change material. Renewable and Sustainable Energy Reviews. 2015 Dec 1;52:645-52.

[12] Nkwetta DN, Haghighat F. Thermal energy storage with phase change material—A state-of-the art review. Sustainable cities and society. 2014 Feb 1;10:87-100.

[13] Jian-you L. Numerical and experimental investigation for heat transfer in triplex concentric tube with phase change material for thermal energy storage. Solar Energy. 2008 Nov 1;82(11):977-85.

[14] Baran G, Sari A. Phase change and heat transfer characteristics of a eutectic mixture of palmitic and stearic acids as PCM in a latent heat storage system. Energy Conversion and Management. 2003 Dec 1;44(20):3227-46.

[15] Stritih U. An experimental study of enhanced heat transfer in rectangular PCM thermal storage. International Journal of Heat and Mass Transfer. 2004 Jun 1;47(12-13):2841-7.

[16] Joybari MM, Haghighat F, Seddegh S, Al-Abidi AA. Heat transfer enhancement of phase change materials by fins under simultaneous charging and discharging. Energy Conversion and Management. 2017 Nov 15;152:136-56.

[17] Rennie TJ, Raghavan VG. Effect of fluid thermal properties on the heat transfer characteristics in a double-pipe helical heat exchanger. International Journal of Thermal Sciences. 2006 Dec 1;45(12):1158-65.

[18] Ahmadi R, Hosseini MJ, Ranjbar AA, Bahrampoury R. Phase change in spiral coil heat storage systems. Sustainable cities and society. 2018 Apr 1;38:145-57.

[19] Najafabadi MF, Rostami HT, Farhadi M. Analysis of a twisted double-pipe heat exchanger with lobed cross-section as a novel heat storage unit for solar collectors using phase-change material. International Communications in Heat and Mass Transfer. 2021 Nov 1;128:105598.

[20] Mahdi MS, Mahood HB, Khadom AA, Campbell AN. Numerical simulations and experimental verification of the thermal performance of phase change materials in a

tube-bundle latent heat thermal energy storage system. Applied Thermal Engineering. 2021 Jul 25;194:117079.

[21] Mahdi MS, Mahood HB, Campbell AN, Khadom AA. Experimental study on the melting behavior of a phase change material in a conical coil latent heat thermal energy storage unit. Applied Thermal Engineering. 2020 Jul 5;175:114684.

[22] Suresh C, Saini RP. Review on solar thermal energy storage technologies and their geometrical configurations. International Journal of Energy Research. 2020 May;44(6):4163-95.

[23] Dhaidan NS. Thermal performance of constrained melting of PCM inside an elliptical capsule of two orientations. Iranian Journal of Science and Technology, Transactions of Mechanical Engineering. 2021 Jun;45:515-21.

[24] Anish R, Mariappan V, Suresh S. Experimental investigation on melting and solidification behaviour of erythritol in a vertical double spiral coil thermal energy storage system. Sustainable Cities and Society. 2019 Jan 1;44:253-64.

[25] Kabbara M, Groulx D, Joseph A. A parametric experimental investigation of the heat transfer in a coil-in-tank latent heat energy storage system. International Journal of Thermal Sciences. 2018 Aug 1;130:395-405.

[26] Khedher NB, Bantan RA, Kolsi L, Omri M. Performance investigation of a vertically configured LHTES via the combination of nano-enhanced PCM and fins: Experimental and numerical approaches. International Communications in Heat and Mass Transfer. 2022 Oct 1;137:106246.

[27] Khedher NB, Mahdi JM, Majdi HS, Khosravi K, Al-Azzawi WK, Al-Qrimli FA, Dhahbi S, Talebizadehsardari P. CFD analysis of phase-change material-based heat storage with dimple-shaped fins: evaluation of fin configuration and distribution pattern. Journal of Computational Design and Engineering. 2022 Oct;9(5):2055-72.

[26] Elarem R, Alqahtani T, Mellouli S, Aich W, Khedher NB, Kolsi L, Jemni A. Numerical study of an Evacuated Tube Solar Collector incorporating a Nano-PCM as a latent heat storage system. Case Studies in Thermal Engineering. 2021 Apr 1;24:100859.

[28] Mehrali M, ten Elshof JE, Shahi M, Mahmoudi A. Simultaneous solar-thermal energy harvesting and storage via shape stabilized salt hydrate phase change material. Chemical Engineering Journal. 2021 Feb 1;405:126624.

[29] Zhang Y, Wang J, Qiu J, Jin X, Umair MM, Lu R, Zhang S, Tang B. Ag-graphene/PEG composite phase change materials for enhancing solar-thermal energy conversion and storage capacity. Applied energy. 2019 Mar 1;237:83-90.

[30] Abdulateef AM, Mat S, Abdulateef J, Sopian K, Al-Abidi AA. Thermal performance enhancement of triplex tube latent thermal storage using fins-nano-phase change material technique. Heat Transfer Engineering. 2018 Jul 21;39(12):1067-80.

[31] Li B, Zhai X. Experimental investigation and theoretical analysis on a mid-temperature solar collector/storage system with composite PCM. Applied Thermal Engineering. 2017 Sep 1;124:34-43.

[32] Sushobhan BR, Kar SP. Thermal modeling of melting of nano based phase change material for improvement of thermal energy storage. Energy Procedia. 2017 Mar 1;109:385-92.

[33] Arıcı M, Tütüncü E, Kan M, Karabay H. Melting of nanoparticle-enhanced paraffin wax in a rectangular enclosure with partially active walls. International Journal of Heat and Mass Transfer. 2017 Jan 1;104:7-17.

[34] Naghavi MS, Ong KS, Badruddin IA, Mehrali M, Metselaar HS. Thermal performance of a compact design heat pipe solar collector with latent heat storage in charging/discharging modes. Energy. 2017 May 15;127:101-15.

[35] Mehrali M, Sadeghinezhad E, Akhiani AR, Latibari ST, Talebian S, Dolatshahi-Pirouz A, Metselaar HS, Mehrali M. An ecofriendly graphene-based nanofluid for heat transfer applications. Journal of cleaner production. 2016 Nov 20;137:555-66.

[36] NematpourKeshteli A, Iasiello M, Langella G, Bianco N. Enhancing PCMs thermal conductivity: A comparison among porous metal foams, nanoparticles and finned surfaces in triplex tube heat exchangers. Applied Thermal Engineering. 2022 Jul 25;212:118623.

[37] Li Z, Shahsavar A, Al-Rashed AA, Talebizadehsardari P. Effect of porous medium and nanoparticles presences in a counter-current triple-tube composite porous/nano-PCM system. Applied Thermal Engineering. 2020 Feb 25;167:114777.

[38] Yang X, Wei P, Cui X, Jin L, He YL. Thermal response of annuli filled with metal foam for thermal energy storage: An experimental study. Applied Energy. 2019 Sep 15;250:1457-67.

[39] Yang X, Yu J, Guo Z, Jin L, He YL. Role of porous metal foam on the heat transfer enhancement for a thermal energy storage tube. Applied Energy. 2019 Apr 1;239:142-56.

[40] Yang X, Guo Z, Liu Y, Jin L, He YL. Effect of inclination on the thermal response of composite phase change materials for thermal energy storage. Applied energy. 2019 Mar 15;238:22-33.

[41] Kuruneru ST, Sauret E, Vafai K, Saha SC, Gu Y. Analysis of particle-laden fluid flows, tortuosity and particle-fluid behaviour in metal foam heat exchangers. Chemical Engineering Science. 2017 Nov 23;172:677-87.

[42] Chen X, Tavakkoli F, Vafai K. Analysis and characterization of metal foam-filled double-pipe heat exchangers. Numerical Heat Transfer, Part A: Applications. 2015 Nov 17;68(10):1031-49.

[43] Al-Abidi AA, Mat S, Sopian K, Sulaiman MY, Mohammad AT. Internal and external fin heat transfer enhancement technique for latent heat thermal energy storage in triplex tube heat exchangers. Applied thermal engineering. 2013 Apr 29;53(1):147-56.

[44] Khetib Y, Sedraoui K, Melaibari AA, Alsulami R. The numerical investigation of spherical grooves on thermal–hydraulic behavior and exergy efficiency of two-phase hybrid MWCNT-Al2O3/water nanofluid in a parabolic solar collector. Sustainable Energy Technologies and Assessments. 2021 Oct 1;47:101530.

[45] Ilyas SU, Pendyala R, Narahari M. Stability and thermal analysis of MWCNT-thermal oil-based nanofluids. Colloids and Surfaces A: Physicochemical and Engineering Aspects. 2017 Aug 20;527:11-22.

[46] Iasiello M, Mameli M, Filippeschi S, Bianco N. Metal foam/PCM melting evolution analysis: Orientation and morphology effects. Applied Thermal Engineering. 2021 Mar 25;187:116572.

[47] Arasu AV, Mujumdar AS. Numerical study on melting of paraffin wax with Al2O3 in a square enclosure. International Communications in Heat and Mass Transfer. 2012 Jan 1;39(1):8-16.

[48] Brent AD, Voller VR, Reid KT. Enthalpy-porosity technique for modeling convection-diffusion phase change: application to the melting of a pure metal. Numerical Heat Transfer, Part A Applications. 1988 Apr 1;13(3):297-318.

[49] Calmidi VV, Mahajan RL. Forced convection in high porosity metal foams. J. Heat Transfer. 2000 Aug 1;122(3):557-65.

[50] Boomsma K, Poulikakos D. On the effective thermal conductivity of a three-dimensionally structured fluid-saturated metal foam. International Journal of Heat and Mass Transfer. 2001 Feb 1;44(4):827-36.

[51] Tian Y, Zhao CY. A numerical investigation of heat transfer in phase change materials (PCMs) embedded in porous metals. Energy. 2011 Sep 1;36(9):5539-46.

[52] Li WQ, Qu ZG, He Y, Tao W. Experimental and numerical studies on melting phase change heat transfer in open-cell metallic foams filled with paraffin. Applied Thermal Engineering. 2012 May 1;37:1-9.

[53] Churchill SW, Chu HH. Correlating equations for laminar and turbulent free convection from a horizontal cylinder. International journal of heat and mass transfer. 1975 Sep 1;18(9):1049-53.

[54] Žkauskas A. Heat transfer from tubes in crossflow. InAdvances in heat transfer 1987 Jan 1 (Vol. 18, pp. 87-159). Elsevier.

[55] Zhang P, Meng ZN, Zhu H, Wang YL, Peng SP. Melting heat transfer characteristics of a composite phase change material fabricated by paraffin and metal foam. Applied Energy. 2017 Jan 1;185:1971-83.

[56] Yao Y, Wu H, Liu Z. Direct simulation of interstitial heat transfer coefficient between paraffin and high porosity open-cell metal foam. Journal of Heat Transfer. 2018 Mar 1;140(3).

[57] Yapici K, Osturk O, Uludag Y. Dependency of nanofluid rheology on particle size and concentration of various metal oxide nanoparticles. Brazilian Journal of Chemical Engineering. 2018 Apr;35:575-86.

[58] Ahammed N, Asirvatham LG, Wongwises S. Entropy generation analysis of graphene–alumina hybrid nanofluid in multiport minichannel heat exchanger coupled with thermoelectric cooler. International Journal of Heat and Mass Transfer. 2016 Dec 1;103:1084-97.

[59] Maxwell JC. A treatise on electricity and magnetism. Oxford: Clarendon Press; 1873.

[60] Adine HA, El Qarnia H. Numerical analysis of the thermal behaviour of a shell-and-tube heat storage unit using phase change materials. Applied mathematical modelling. 2009 Apr 1;33(4):2132-44.

[61] Xu Y, Ren Q, Zheng ZJ, He YL. Evaluation and optimization of melting performance for a latent heat thermal energy storage unit partially filled with porous media. Applied energy. 2017 May 1;193:84-95.

[62] Madruga S. Modeling of enhanced micro-energy harvesting of thermal ambient fluctuations with metallic foams embedded in Phase Change Materials. Renewable Energy. 2021 May 1;168:424-37.

[63] Carmona M, Rincón A, Gulfo L. Energy and exergy model with parametric study of a hot water storage tank with PCM for domestic applications and experimental validation for multiple operational scenarios. Energy Conversion and Management. 2020 Oct 15;222:113189.

[64] Dardir M, Roccamena L, El Mankibi M, Haghighat F. Performance analysis of an improved PCM-to-air heat exchanger for building envelope applications–An experimental study. Solar Energy. 2020 Mar 15;199:704-20.

[65] Mallow A, Abdelaziz O, Graham S. Thermal charging performance of enhanced phase change material composites for thermal battery design. International Journal of Thermal Sciences. 2018 May 1;127:19-28.

[66] Lafdi K, Mesalhy O, Shaikh S. Experimental study on the influence of foam porosity and pore size on the melting of phase change materials. Journal of Applied Physics. 2007 Oct 15;102(8):083549.

[67] Patankar S. Numerical heat transfer and fluid flow. Taylor & Francis; 2018 Oct 8.

[68] Liu Z, Yao Y, Wu H. Numerical modeling for solid–liquid phase change phenomena in porous media: Shell-and-tube type latent heat thermal energy storage. Applied energy. 2013 Dec 1;112:1222-32.

[69] Mahdi JM, Nsofor EC. Melting enhancement in triplex-tube latent heat energy storage system using nanoparticles-metal foam combination. Applied energy. 2017 Apr 1;191:22-34.

[70] Zhao CY, Lu W, Tian Y. Heat transfer enhancement for thermal energy storage using metal foams embedded within phase change materials (PCMs). Solar energy. 2010 Aug 1;84(8):1402-12.

[71] Atal A, Wang Y, Harsha M, Sengupta S. Effect of porosity of conducting matrix on a phase change energy storage device. International Journal of Heat and Mass Transfer. 2016 Feb 1;93:9-16.

[72] Ho CJ, Viskanta R. Heat transfer during melting from an isothermal vertical wall.

[73] Shatikian V, Ziskind G, Letan R. Numerical investigation of a PCM-based heat sink with internal fins. International journal of heat and mass transfer. 2005 Aug 1;48(17):3689-706.

[74] Kamkari B, Shokouhmand H. Experimental investigation of phase change material melting in rectangular enclosures with horizontal partial fins. International Journal of Heat and Mass Transfer. 2014 Nov 1;78:839-51.

[75] Yang X, Feng S, Zhang Q, Chai Y, Jin L, Lu TJ. The role of porous metal foam on the unidirectional solidification of saturating fluid for cold storage. Applied energy. 2017 May 15;194:508-21.

[76] Bianco N, Busiello S, Iasiello M, Mauro GM. Finned heat sinks with phase change materials and metal foams: Pareto optimization to address cost and operation time. Applied Thermal Engineering. 2021 Oct 1;197:117436.

[77] Yang X, Bai Q, Zhang Q, Hu W, Jin L, Yan J. Thermal and economic analysis of charging and discharging characteristics of composite phase change materials for cold storage. Applied Energy. 2018 Sep 1;225:585-99.

Chapter 5. EXPERIMENTAL THERMAL ENHANCEMENT TECHNIQUES THERMAL STORAGE SYSTEM

5.1. Research Objectives

There is a scarcity of comparative studies, either theoretical or experimental, on the melting and solidification processes of PCM with a constant heat flux heat source. This highlights the need for experimental data to comprehend the efficacy and comparison of the different methods of enhancing PCM heat transfer. Furthermore, experimental studies can illuminate the physical obstacles linked with various enhanced PCM composites, which are not considered in theoretical studies. Therefore, the objective of this study is to bridge the aforementioned gap by investigating and comparing the enhancement of PCM heat transfer during both melting and solidification processes through the addition of nanoparticles, metal foam, or a combination of both to a pure PCM.

The primary objective of this research is to propose a new energy storage system that can enhance the thermal performance of PCMs used in solar collectors and heat exchangers. The research aims to overcome the challenges of existing latent heat energy storage systems by introducing nanoparticle and porous medium enhancers to improve the heat transfer performance of PCMs. To achieve this goal, we will conduct experimental investigations into several methods for enhancing the thermal performance of PCMs, including optimizing the contact surface between the working hot fluid and the PCM domain, incorporating metal foams, and adding nanoparticles. These methods have shown promising results in previous studies, and we aim to build upon their findings by further exploring their impact on the thermal performance of PCM-based energy storage systems. In summary, this research proposes a novel energy storage system that aims to address the thermal issues of latent heat energy storage systems. By optimizing the contact surface between the hot fluid and PCM domain, incorporating metal foams, and adding nanoparticles, we aim to improve the thermal performance of PCM-based energy storage systems for solar collectors and heat exchangers. The experimental procedures entail the use of both constant heat flux and constant temperature heat sources. Nonetheless, during the solidification process, a constant heat flux heat sink was not employed. This is because constant-flux cooling typically necessitates a refrigeration cycle, and cases that utilize PCM as a direct heat source in such cycles are rare. Normally, a heat transfer fluid is utilized to extract the thermal energy stored in PCM. The findings of this study can establish a robust reference point for assessing performance.

This study involved conducting experiments with a pure PCM and three distinct PCM compositions. The primary aims of this research are to model and

experimentally analyze the transport processes of NanoPCM inside both porous and non-porous media, with experimental validation. The objective is to better comprehend and demonstrate the potential application of PCM with nanoparticles and porous media. The study will concentrate on four key areas: **1) Pure PCM (PP)**; **2) PCM composition with nanoparticles (NP)**; **3) PCM composition with metal foam (MFP)**; and **4) PCM composition with metal foam and nanoparticles (MFNP)**. These areas will be investigated to achieve the desired research objectives.

5.2. Materials used in the experiments

The PCM, nanoparticles, and metal foam used in this study were RT35HC, Graphite (Gr), and Aluminum (Al6061), respectively. To ensure that the PCM fully penetrated the metal foam and made full contact with its metallic body, an open-cell type of metal foam was utilized. The aluminum foam investigated in this study was manufactured by ERG Aerospace. Literature suggests that common compositions tested are metal foam porosities of 85-95% and nanoparticle concentrations of 0.1-5.0 w%. For this study, the metal foam porosity was 94%, with a 10 PPI and a nanoparticle concentration of 0.4 w%.

5.2.1. Thermophysical properties of PCM

The RUBITHERM® RT is a type of pure PCM that makes use of the phase change processes between the solid and liquid states (melting and congealing) to store and release significant amounts of thermal energy at nearly constant temperatures. Although the latent heat of fusion is a crucial feature of a PCM, it is not the only criterion for selecting a PCM for specific applications. Other important factors include small volume expansion throughout the phase change process, high density, long-term chemical stability, non-corrosiveness, and non-toxicity. The RT-line of PCMs possess these features and boasts of high thermal energy storage capacity, heat storage and release at relatively constant temperatures, no supercooling effect, chemical inertness, long product life, and stable performance through the phase change cycles. It has a wide melting temperature range, between -9°C and 100°C, which makes it a versatile material suitable for various applications that require efficient and dependable thermal energy storage. The use of PCM has gained significant attention among researchers as a means of latent heat storage due to its ability to transfer heat by changing phase without raising temperature. However, the poor thermal conductivity of PCM is a major challenge in its effective use as a latent heat energy storage device. Thus, efforts have been made to enhance the thermal

conductivity of PCM to improve its heat transfer performance, with the focus being on addressing the charging/discharging rate and the amount of energy stored during the phase change. Initially, thermal conductivity enhancement techniques focused on the use of highly conductive fixed structures such as metallic extended surfaces. However, the use of fixed structures occupies a considerable amount of space and reduces the effective volume of PCM for phase change, thereby limiting the amount of metallic insert that can be used for a particular application to avoid reducing the volume of PCM. Therefore, alternative techniques are being explored that do not affect the amount of phase change material or the latent heat energy storage device.

Table 5.1 presents the thermophysical properties of RT35HC, which were determined through direct measurements in the Thermal Engineering Lab and Chemical Lab. The process of melting PCM is demonstrated in **Figure 5.1**, which provides a clear representation of the various stages involved in transforming a solid state to a liquid state. Melting a PCM with an oven is a common method used to transition a solid-state PCM to a liquid state. To effectively melt a PCM using an oven, an appropriate oven with adjustable temperature control should first be selected. The PCM should then be prepared by transferring it to a clean, dry, and heat-resistant container. Subsequently, the oven should be preheated to the recommended melting temperature, and the container with the PCM should be placed in the center of the oven. The temperature and the PCM should be monitored frequently to ensure even melting without overheating or burning. When melting begins, the PCM should be gently stirred with a clean and dry stirrer to distribute the heat evenly and ensure complete melting. Finally, the oven should be turned off, and the container with the melted PCM should be carefully removed and allowed to cool before use. It is crucial to follow the manufacturer's instructions for both the PCM and the oven and to take the necessary safety precautions when working with high temperatures. By adhering to these steps, successful melting of a phase change material with an oven can be accomplished [2]. In this report, **Figure 5.2** displays the enthalpy-temperature relationship of the PCM in question [1].

Table 5.1. Thermophysical properties of RT35HC [1]

The most important data	**Unite**	**Typical Values**
Melting area	[°C]	34-36
Congealing area	[°C]	36-34

Heat storage capacity ± 7,5%	[kJ/kg]	240
Combination of latent and sensible heat	[Wh/kg]	67
Specific heat capacity	[kJ/kg.K]	2
Density solid	[kg/l]	0.88
Density liquid	[kg/l]	0.77
Heat conductivity (both phases)	[W/(m.K)]	0.2

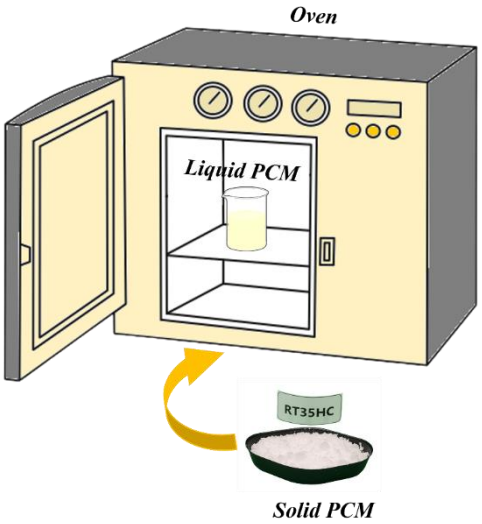

Fig. 5.1. A visual guide to melting PCMs (RT35HC) using an Oven

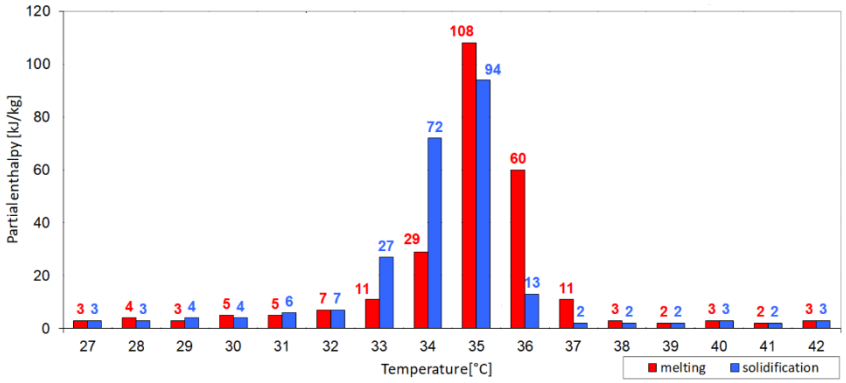

Fig. 5.2. Partial enthalpy distribution of PCM (RT35HC) [1]

2.1.1. Differential scanning calorimetry analyses (DSC) analysis

Differential scanning calorimetry (DSC) is an important technique used for thermal analysis, which allows for the measurement of heat flow or energy changes as a material undergoes heating or cooling [3]. DSC finds extensive applications in various fields of science, such as materials science, chemistry, and biology, for studying the thermal properties of different materials. The primary purpose of DSC is to investigate phase transitions, melting points, and reaction energies in materials. In a typical DSC experiment, a sample material and a reference material are subjected to a constant rate of heating or cooling while measuring the heat flow between them. As the sample undergoes a thermal event, such as a phase transition or chemical reaction, the heat flow changes, and this is recorded as a peak in the DSC trace. The shape and position of the peak can be analyzed to obtain valuable information about the thermal behavior of the material, including the onset and completion temperatures of phase transitions, the enthalpy of melting or reaction, and the heat capacity. **Figure 5.3** illustrates the analysis of the DSC data to obtain information about the thermal properties of the material under investigation. DSC is a powerful and versatile technique that can provide a wealth of information about the thermal behavior of materials, making it a valuable tool for scientific research and industrial applications .

Paraffin RT35HC undergoes two thermal cycles, and **Figure 5.4** displays and examines the DSC curves of both cycles. The most significant peak in the curves is attributed to the phase change from solid to liquid during the heating process and from liquid to solid during the cooling process. Furthermore, it is evident from **Figure 5.4** that RT35HC exhibits only two distinct peaks during both the heating and cooling processes. These peaks are related to the amount of heat absorbed during the solid-liquid phase transition, which is 238.3 J/g with a melting temperature of 36.0 °C, and the amount of heat released during the liquid-solid phase transition, which is 235.5 J/g with a solidification temperature of 30.6 °C and 26.9 °C. These values demonstrate the efficient energy storage capability of RT35HC and the potential for its use in thermal energy storage applications. It is important to note that the accurate measurement of these thermophysical properties using DSC is crucial for the optimal design and utilization of the PCM. The DSC curves of RT35HC indicate the absence of a minor peak during the heating transition, which can be attributed to the molecular length and composition of n-alkanes Cn H_{2n+2} that form the paraffin wax. Studies have reported that n-alkanes with a value of n

less than 20 and paraffin molecules with n values lower than 50 exhibit only one peak that corresponds to the solid-liquid phase change, and they do not exhibit a solid-solid transition. In **Figure 5.4**, the minor peaks observed in the DSC curves of RT35HC are related to the cooling phase change, where the heat is released during the liquid-solid transition. This behavior is expected for a pure paraffin wax material and can be attributed to the intermolecular forces between the paraffin molecules. The absence of a minor peak during the heating process suggests that RT35HC has a relatively short n-alkane chain length and a simple paraffin composition, which is consistent with the manufacturer's specifications. The main peak observed in the DSC curves corresponds to the heat absorbed during the solid-liquid phase change and has a melting temperature of 36.0 °C with an enthalpy of 238.3 J/g. The second peak observed during the cooling process corresponds to the heat released during the liquid-solid phase change and has a solidification temperature of 30.6 °C and 26.9 °C with an enthalpy of 235.5 J/g, as shown in **Figure 5.4**. The heat capacity of power compensating DSC's can achieve an accuracy of up to 0.5% under ideal testing circumstances. Under normal operating circumstances, it is possible to achieve errors of 2% depending on factors such as temperature range and external variables (such as ambient-sub-ambient operation). These devices achieve precision of less than 1% when operating in temperature-modulated mode. Temperature accuracy and heat flow accuracy are ±1°C and ±2%, respectively, based on metal melting standards.

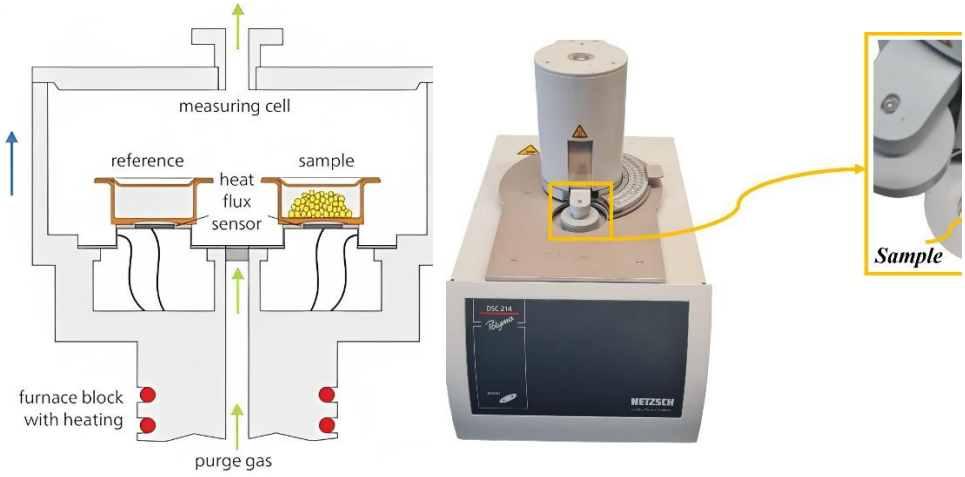

Fig. 5.3. Block diagram of Heat Flux DSC (left), and DSC 214 Polyma system (right)

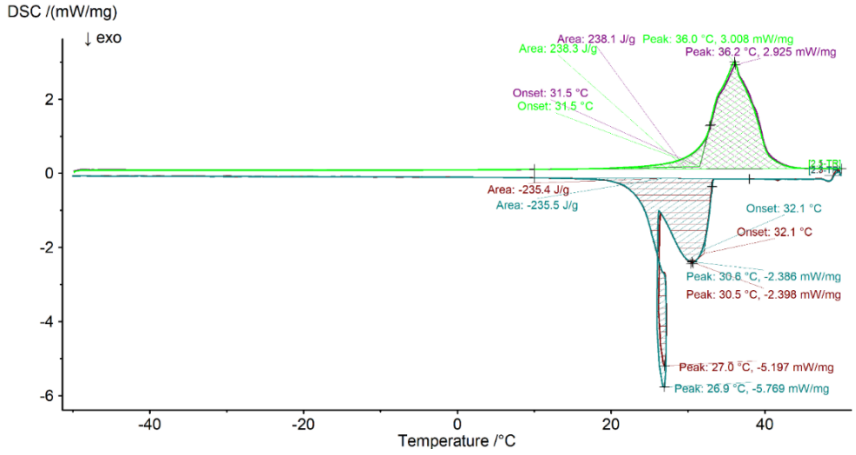

Fig. 5.4. DSC curve for the heating and cooling for two thermal cycles of of RT35HC

The paper presents an analysis of two thermal cycles of paraffins, with the average DSC results summarized in **Table 5.2**. The DSC curves of RT35HC during the heating and cooling process were overlaid for each paraffin. It was found that the latent heat of melting of RT35HC had a maximum variation of 0.2 J/g, while the latent heat of solidification had a maximum variation of 0.1J/g within the cycles. The maximum variation of the melting temperature during the two cycles was found to be only 0.2 for RT35HC. However, the maximum discrepancy between the solidification temperatures during the cycles was 0.1°C for RT35HC. These results indicate that RT35HC is stable over the two thermal cycles, and it does not exhibit significant changes in its thermal behavior.

Table 5.2. Phase change properties of RT35HC

	Heating				**Cooling**			
	Solid-Solid		Solid-Liquid		Liquid-Solid		Solid-Solid	
RT35HC	T (˚C)	ΔH(J/g)	T (˚C)	ΔH(J/g)	T (˚C)	ΔH(J/g)	T (˚C)	ΔH(J/g)
	-	-	36.0	238.3	30.6	235.5	26.9	235.5

5.2.2. Thermophysical properties of Nanoparticle

The use of nanofluids, which are nanomaterials dispersed in PCM, has generated significant interest among researchers as a means of avoiding volume reduction of PCM while enhancing its thermal performance. By introducing

highly conductive nanoparticles into PCM, researchers aim to improve its melting and freezing rates. However, the extent to which thermal enhancement can be achieved is limited by the loading of nanoparticles. Heavy loading can lead to heavier nanofluids and sedimentation, both of which significantly affect convection heat transfer. It is worth noting that the focus of research in this area has been on enhancing thermal conductivity, rather than heat transfer characteristics. Furthermore, there is some disagreement among researchers regarding the heat transfer characteristics of nanoparticles in PCM. Finding literature that accurately characterizes the heat transfer behavior of nanoparticles with PCM is quite challenging. In fact, some researchers have treated the mixture of nanoparticles with PCM as a single-phase fluid instead of a two-phase mixture. However, the interaction between particles and liquids, as well as their movement, are crucial factors that can impact heat transfer performance. Only a few researchers have attempted to study the effects of Brownian and thermophoresis motion on thermal conductivity enhancement resulting from convection heat transfer. Despite these efforts, there is still insufficient agreement among researchers, and experimental validation remains limited. In summary, the accurate characterization of heat transfer behavior in nanoparticles with PCM is a complex and ongoing research area. The addition of nanoparticles with high thermal conductivity to pure PCM can effectively enhance the thermal conductivity of the resulting nano-PCM. This increase in thermal conductivity can improve the rate of heat transfer, a crucial factor in various industrial and scientific applications. In this regard, a nano-PCM composite was synthesized through direct addition of nanoparticles to the PCM. To achieve a desired nanoparticle concentration, the mass of nanoparticles was carefully determined. Specifically, the NP sample was formulated to contain 0.4 w% of nanoparticles.

To disperse nanoparticles inside melted PCM, a heated magnetic stirrer was utilized. This type of stirrer is commonly used for mixing and heating aqueous solutions in a wide range of chemical reactions, including synthesis. In this study, the researchers synthesized NEPCMs by dispersing a mass fraction of Graphite particles in pure paraffin (RT35HC). To avoid particle agglomeration and excessive material costs, it is recommended that nanoparticles be dispersed in concentrations ranging from 0.1 to 5%. The NEPCM samples were prepared in several steps, as depicted in **Figure 5.5**. First, the paraffin was heated to 60 °C on a hot plate and then transferred to the magnetic stirrer. Next, the required mass concentration of nanoparticles was gently added to the melted paraffin wax while simultaneously heating and stirring the nanocomposite PCM for 30

minutes. To ensure a uniform homogeneous mixture and prevent nanoparticle agglomeration, the mixture was then placed in an ultrasonic vibrator and sonicated for an additional 30 minutes at 60 °C. The experimental procedure is illustrated in **Figure 5.6**. Overall, the use of a heated magnetic stirrer and ultrasonic vibrator enabled the researchers to disperse nanoparticles effectively within the melted PCM, resulting in the synthesis of NEPCMs with improved thermal properties. Accuracy in a heated magnetic stirrer is often specified in terms of temperature control, with the temperature display accuracy set at ±0.1°C. This indicates that the actual temperature of the solution being stirred will be within 0.1 degree Celsius of the set temperature on the stirrer [4, 5].

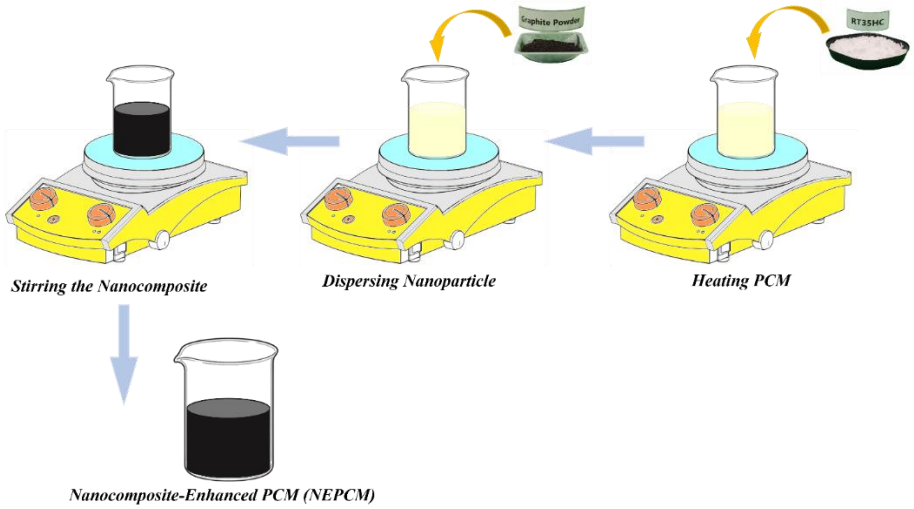

Fig. 5.5 Schematic diagram of nano-PCM samples preparation method

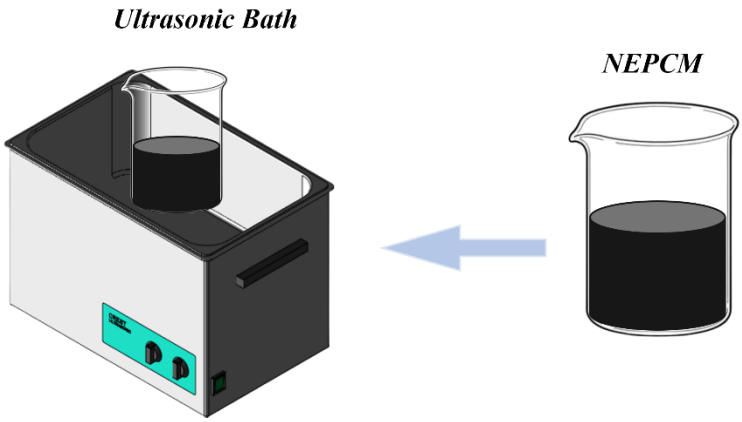

Fig. 5.6 Preparation of RT35HC-Graphite composite PCM using bath ultrasonicator.

5.2.3. Thermophysical properties of Metal foam

The performance of a composite metal-foam PCM system is influenced by a range of factors. Several key factors that play a crucial role include the thermo-physical properties of both the foam material and PCM, the structure of the foam, the porosity of the foam, and the size and aspect ratio of the storage unit. Each of these factors is discussed in more detail in the following sub-sections. It is important to carefully consider all of these factors when designing and optimizing composite metal-foam PCM systems to ensure that they operate efficiently and effectively. Factors such as foam structure and porosity can significantly impact the overall heat transfer rate and thermal storage capacity of the system, while the size and aspect ratio of the storage unit can influence the ease of deployment and overall system efficiency. Therefore, a comprehensive understanding of these factors is crucial for developing high-performance composite metal-foam PCM systems that can be utilized in a variety of industrial and scientific applications.

5.2.3.1 Thermo-physical Properties of Foam Material

The foam material is a crucial component of the composite metal-foam PCM system and its properties play a vital role in determining the performance of the storage unit. In order to optimize the system, the foam material should possess several key characteristics. For example, high thermal conductivity and high specific heat are desirable to promote efficient heat transfer and sensible energy storage. Additionally, a low density material is preferable for reducing the overall weight of the system, but it's important to note that low density can also

result in lower sensible heat storage, which may reduce the energy storage capacity of the system. It is also important that the foam material has a low thermal coefficient of expansion so that the foam structure does not change significantly during the charging or discharging process. Furthermore, good mechanical properties such as strength are desirable to maintain the integrity of the system during use. It is also important that the foam material and PCM combination have high wettability to prevent the formation of air pockets due to the shrinkage of the PCM during solidification. By considering all of these factors and optimizing the properties of the foam material, it is possible to develop high-performance composite metal-foam PCM systems that are well-suited to a range of industrial and scientific applications.

5.2.3.2 Thermophysical properties of paraffin

The critical property of PCM that determines the overall energy storage capacity of the system is its high latent heat of fusion. PCM should also possess relatively high thermal conductivity to enable better heat transfer to the interior regions and high specific heat for improved sensible heat storage. As noted previously, PCM should have high wettability with the metal foam structure to prevent air pockets formation due to PCM shrinkage during solidification. Another significant property is the change in density during solidification and melting. Typically, PCMs undergo volume contraction during solidification, leading to shrinkage. Ideally, the shrinkage should be as minimal as possible, as it can significantly impair the performance of the energy storage system by creating air pockets between the metal foam and PCM, which can reduce the effective thermal conductivity of the system. In addition to these properties, chemical inertness and stability are also important characteristics of PCM. Furthermore, lower viscosity is a necessary property of PCM for initial filling up of the metal foam.

5.2.3.3 Foam Porosity

It is important to meticulously evaluate and select the appropriate overall porosity of the metal foam based on a comprehensive analysis. The selection of the right porosity level will play a significant role in determining the heat transfer rates in the system, which in turn will influence the speed of charging and discharging of energy. The lower the porosity, the higher the heat transfer rate will be, leading to faster energy exchange. Conversely, a higher porosity level will result in a larger volume fraction of PCM and consequently, a higher overall energy storage capacity. To determine the ideal porosity level, the

sensible heat capacity of both the metal foam and the PCM must be taken into consideration. This is necessary to accurately calculate the necessary porosity level for the system. Ultimately, the careful selection of porosity will determine the performance of the energy storage system and ensure its effective and efficient operation.

5.2.3.4 Foam Structure

The performance of a metal foam-PCM energy storage system is greatly influenced by the structure of the metal foam. Recent studies have demonstrated that the heat transfer rates in such systems can be enhanced by utilizing foams with smaller pore sizes and higher pore densities. This is due to the more intricate network of metal structure that allows for more efficient heat transfer. Furthermore, open cell foams with high porosity can significantly enhance convective heat transfer, thereby contributing to the overall heat transfer rate. In contrast, closed foams or nearly closed foam structures tend to rely more on conduction as the primary heat transfer mechanism. It is worth noting that foams with regular and irregular structures may exhibit different heat transfer characteristics. Therefore, selecting the appropriate metal foam structure is a critical factor in optimizing the performance of metal foam-PCM energy storage systems. Careful consideration and analysis of the foam's characteristics are crucial in determining the optimal design for a specific application.

5.2.3.5 Overall Size and Aspect Ratio

When designing a storage unit for energy storage, it is essential to ensure that its overall dimensions are sufficient to accommodate the required charging and discharging time. However, if the storage unit is too small, the need for a large number of units can arise, ultimately increasing the overall cost of the system. It is crucial to strike a balance between size and efficiency. Aspect ratio is another crucial factor to consider when designing a storage unit. This parameter defines the farthest distance of the PCM from the heat transfer surface. A broad and shallow design that positions the wall opposite to the heat transfer surface relatively near is more effective as energy can be transported to the entire PCM in a shorter amount of time. By optimizing the size and aspect ratio of the storage unit, we can ensure that the system operates efficiently and meets the required energy storage needs within the desired time frame. Ultimately, careful consideration and analysis of these factors are necessary for the effective design of an energy storage unit. Combining a PCM with a metal foam structure can increase the surface area to volume ratio of the material,

resulting in greater contact between the PCM and its surroundings. This enhances heat transfer rates and improves overall heat storage capacity. The metal foam acts as a supportive structure, preventing damage or leakage of the PCM, and its porous nature improves thermal conductivity. The combination of metal foam with PCMs has numerous applications, including in building insulation, thermal energy storage systems, and electronic cooling. Studies have shown that metal foam significantly improves heat transfer during solid-liquid transitions, indicating conduction and local free convection mechanisms in melted PCMs. The effectiveness of the composite PCM is largely dependent on the metal foam's structural parameters, such as pore size, porosity, material, and effective thermal conductivity.

The previously reported investigation involved aluminum foam produced by ERG Aerospace. **Table 5.3** summarizes the thermophysical properties of the metal foam, with the investigated foams having 0.94 porosities and 10 PPIs. The experiment details will be presented later. The combination of metal foam with PCMs has attracted attention in thermal management. To achieve this combination, the foam can be impregnated with the PCM and cured under vacuum conditions using a vacuum oven. To create the metal foam and PCM composite material, a process is followed which involves several steps. Firstly, the metal foam is placed inside a vacuum oven. The chamber is then evacuated to eliminate any moisture or air that may be present in the foam. Secondly, the PCM is prepared by melting and degassing it. Once ready, the liquid PCM is introduced into the chamber to impregnate the metal foam. Following the impregnation process, the composite material is cured and cooled under vacuum conditions. This results in the elimination of any trapped air or moisture from both the metal foam and the PCM. The removal of these impurities creates a uniform distribution of the PCM within the material and enhances the thermal properties of the composite material. **Fig. 5.7** illustrates the process involved in creating the metal foam and PCM composite material. This process is crucial in achieving a high-quality and effective composite material that is useful in various applications such as thermal energy storage systems, building insulation, and electronic cooling systems. These versions have a vacuum rating of less than 133, making them suitable for precision vacuum drying applications. These devices have a time range of 0 to 999 minutes and provide an accuracy of ± 1 minute with a ± 2% variation. This level of precision makes them suitable for use in intense labs, and temperature control accuracy is +/- 1°C.

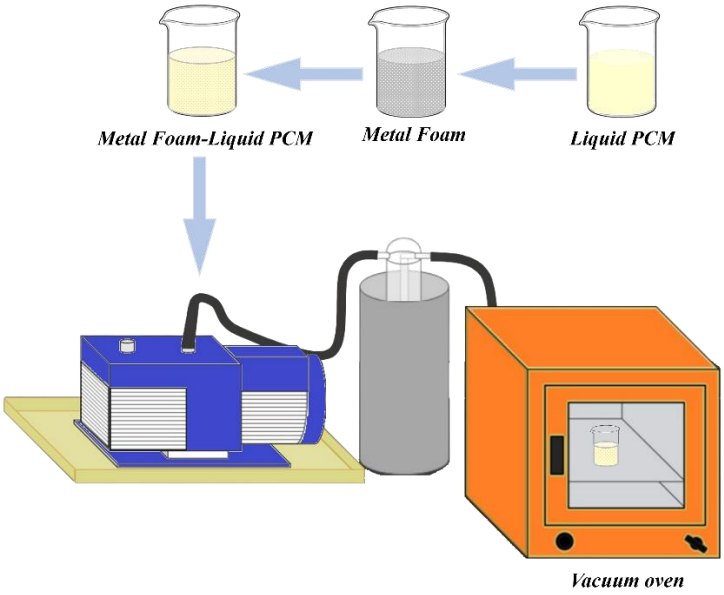

Fig. 5.7. Schematic diagram of combination of metal foam with RT35HC using a vacuum oven

Table. 5.3. Thermophysical properties of metal foam Al6061 [6]		
The most important data	**Unite**	**Typical Values**
Density solid	[kg/m^3]	2700
Thermal conductivity	[W/m·K]	220
Specific heat capacity	[J/kg.K]	900

5.2.4 Porosity measurements

X-ray computed microtomography (Micro-CT) is a non-destructive imaging technique that allows for the visualization and analysis of internal structures of an object in 3D. It is similar to medical CT scanning, but with much higher resolution, typically in the range of micrometers to sub-micrometers. The Micro CT system works by rotating an object and capturing a series of 2D X-ray images at different angles. These images are reconstructed into a 3D volume using computer algorithms that can differentiate between different materials within the object based on their X-ray attenuation properties. This allows for the visualization and analysis of the internal structure and composition of the object, without the need for physical sectioning or destructive testing. Micro CT

is widely used in various fields, including material science, engineering, biology, and medicine, for applications such as quality control, defect analysis, morphology characterization, and structural analysis. It is a powerful tool for investigating the microstructure and properties of complex materials and components and has become increasingly important in research and industrial applications. In the μCT technique, X-rays are used to provide high-resolution images of geometry and microstructures. X-ray μ-CT is a non-invasive X-ray-based method that allows the 3D reconstruction of an opaque sample by illuminating it from different directions. From this perspective, X-ray computed microtomography (μ CT) seems to be a promising and appealing approach for characterizing the 3D foam structure at the pore level [7].

Figure 5.8 displays the vertical and horizontal slices of the 3D and 2D volumes of independent porosity measurements on paraffin and a combination of paraffin and metal foam. The high-resolution X-ray μ-CT imaging was performed at the University of Twente. This paper presents the results of microtomography conducted on open-cell aluminum foam samples with varying pore density (10 PPI). The object is imaged from several angles, and radiographs are recorded corresponding to the projection of the linear attenuation coefficient. In this activity, absorption μ-CT is employed, where the contrast of the sample is determined by the difference between the linear attenuation coefficients of the two phases. A suitable algorithm is used to reconstruct a 3D image of the object. In the case of two-phase materials, such as metallic foams, a segmentation process can be applied to distribute the voxels, which are the elemental digital units forming the reconstructed volume, into only two kinds of elements: solid and void. This is achieved by selecting a proper threshold value in the histogram of the intensities.

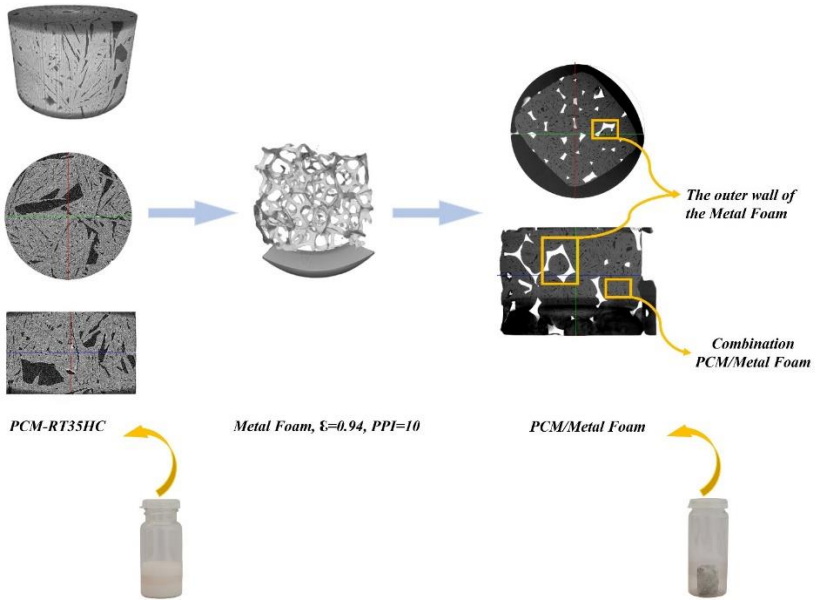

Fig. 5.8. RT35HC and Aluminum foam samples employed in the μ-CT analyses: photographies of the specimens and reconstructed volume for the 10 PPI sample

5.3. First Experimental study

5.3.1 Aim and novelty of the present study

The primary objective of this study is to investigate the effectiveness of various techniques for enhancing the heat transfer performance of PCMs during both melting and solidification processes. Specifically, the study aims to compare the performance of four different types of composite materials, namely pure PP, NP, MFP, and MFNP, in terms of their heat transfer properties. The experimental setup involves the use of constant temperature heat sources to facilitate the melting process, while the solidification process does not include a constant heat flux heat sink. The reason for this is that constant-flux cooling typically requires a refrigeration cycle, and such cycles with PCM as the direct heat source are rare. By comparing the heat transfer performance of different PCM enhancement methods, this study aims to provide a reliable benchmark for future research in this area. The results of this study will be useful in designing more efficient and cost-effective thermal energy storage systems that can be used in a variety of applications, including solar energy conversion, waste heat recovery, and thermal management systems.

5.3.2. Experiments on melting with constant temperature heat source

In the initial stage of the study, a series of experiments were performed to investigate the heat transfer performance of the PCM composites using a constant temperature heat source. The schematic diagram of the experimental setup is presented in **Figure 5.9**. The heat source was heated from below using an electric heater, which was connected to a temperature controller to maintain the plate temperature at approximately 50 °C and 60 °C. The modified Stefan numbers (Ste*) were calculated for each temperature condition, taking into account the sensible heating effects of the solid and liquid states of the PCM. The results of the calculation revealed that the $Ste^{*} = (c(T_m - T_{ini}) + c(T_{inlet} - T_m))/L_f$ values for wall temperatures of 50 °C and 60 °C were 0.358 and 0.275, respectively. These values will be useful in analyzing the performance of the PCM composites under different temperature conditions and can provide valuable insights into the heat transfer behavior of the composites. The results of these experiments can serve as a useful reference for future research in this area and can aid in the development of more efficient and effective thermal energy storage systems for a range of applications. The melting process of the PCM was primarily driven by the bottom plate, which served as the main heat source, and thus an electric heater was utilized with temperature control. A temperature sensor was installed at the surface midpoint of the plate to monitor the plate temperature, which was regulated by the heater controller. The ambient temperature was found to be between 18-20 °C during the experiments, which is a typical range for laboratory procedures and provides suitable temperature stability for experiments. The heat source temperature was set at 50–60 °C because this range is representative of the hot water supplied from a solar thermal collector, which is expected to have an average temperature within this range. Moreover, the RT35HC was selected as the PCM because its melting point of 34–35 °C falls within a reasonable range for integration with solar hot water systems. The ambient temperature was maintained at 18–20 °C to ensure that it would not interfere with the main heat source, while values lower than this range would result in significant heat losses from the PCM. Conversely, values higher than this range would also interfere with the primary heat source. For the experiments, cylindrical containers were used to hold the PCM samples, with each container having a uniform mass of 30.458 g of PCM. The NP and MFNP samples were prepared by adding 0.158 g of Gr nanoparticles, equivalent to 0.4 w% of the PCM mass. On the other hand, the MFP and MFNP samples contained 1.898 g of Al foam. It is worth noting that the same mass of

PCM was used for all samples to avoid any potential impact on the overall thermal performance. This is because changes in the PCM mass can alter the amount of energy required for the phase change process and lead to variations in melting or solidification behavior. As a result, the thermal performance of different compositions would be affected by the mass of PCM, and a comparison under such conditions would not accurately reflect the effects of adding nanoparticles and/or metal foam on the sample performance. In addition, it should be mentioned that RT35HC experiences a 12% volume expansion during the phase change process. Therefore, empty space was intentionally left in the containers to prevent any overflow of PCM. A photograph of the samples is shown in **Fig. 5.9** to provide a visual representation of the experimental setup.

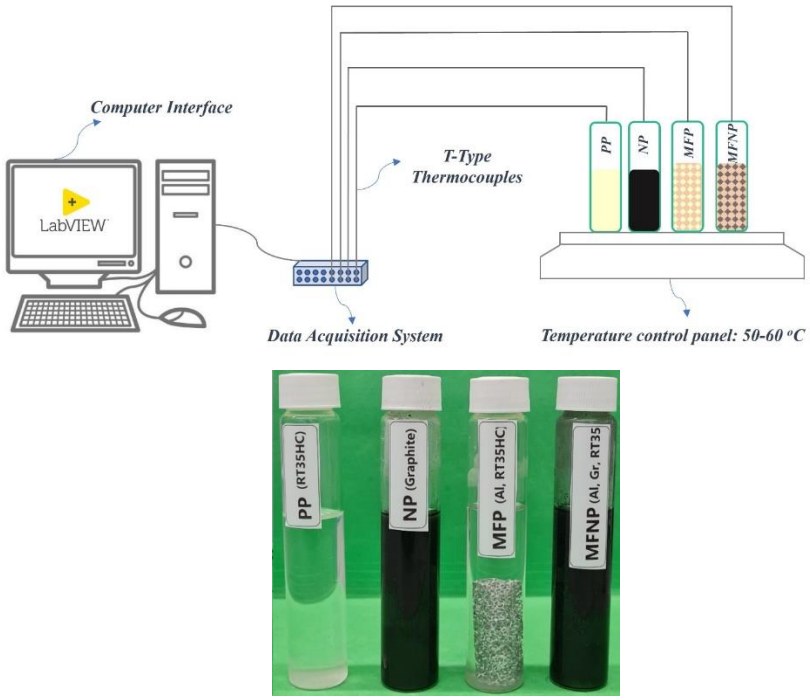

Fig. 5.9. Schematics of the melting experiments with constant temperature heat source (top). Photo of tested samples for constant temperature experiment (bottom).

The experimental setup was equipped with multiple T-type temperature sensors, including one in each test sample, one in the hot plate, and another in the surrounding air. **Fig. 5.10** displays the dimensions of the pure PCM sample in the liquid state and the locations of the temperature sensors inside it, which are marked with crosses. It is worth emphasizing that the total height of the

sample and the heights at which the temperature sensors were placed in **Fig. 5.10** correspond to all samples. This is because the same amount of PCM was used in all samples. The addition of nanoparticles had minimal effects on the heights, while the addition of metal foam increased them considerably. Additionally, there were two temperature sensors positioned at the midpoint of the hot surface and the surrounding air. At the outset of the experiment, all four samples were placed in the primary container and separated into two groups, with one group containing PP and MFP and the other containing NP and MFNP. The heater was then activated and began to warm the plates. While the heater was warming up, the temperature of the heater and the temperature of the samples and their surroundings were recorded. To maintain the heater's temperature between 50 and 60 °C, a temperature controller was employed, which switched the heater on and off as required. Throughout this process, temperature data was collected, and recordings were made until all the samples were entirely melted, after which their temperature was increased with the PCM in a liquid state.

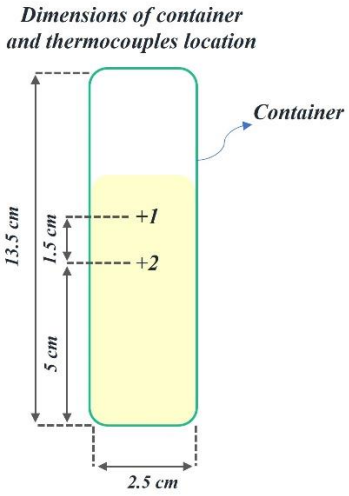

Fig. 5.10. Schematic dimensions of the container and the placement of thermocouple sensors

5.3.2 Melting experiments

As mentioned previously, to maintain a constant temperature during the experiments, a temperature-controlled heater was utilized to maintain the plate

temperature at approximately 50 °C and 60 °C. Additionally, the air temperature within the container was regulated to approximately 18-20 °C. Four temperature sensors were placed inside each of the PP, NP, MFP, and MFNP samples, and their respective locations were described in the preceding section. The experiments were conducted thrice, and the average differences between the recorded data for the PP, NP, MFP, and MFNP samples were 0.3 °C, 0.2 °C, 0.6 °C, and 0.3 °C, respectively. Nevertheless, all the experiments showed a similar trend in their findings.

5.3.2.1 Pure PCM (PP)

To ensure that all the samples had the same initial temperature, they were kept in the laboratory environment for an extended period. When they were placed inside the container, they were left there for a brief period before the electric heater was turned on. Additionally, the temperature log was initiated approximately 2 minutes before heating up the samples. Since the ambient temperature was around 18 °C, both samples had a uniform initial temperature of approximately 18 °C, as shown in **Figure 5.11**. For all samples, the temperature began to rise sharply once the water was hot enough. This temperature increase was from an initial temperature of approximately 18 °C to the PCM melting point, which is a temperature range of 34-36 °C. At this point, the PCM began to melt, and there were slight temperature changes inside it until it was fully melted. Then, significant temperature changes were observed inside the PCM. These changes occurred more quickly in the bottom parts of the samples because they were closer to the heat source. There was a delay, and the temperatures recorded by the top sensor exhibited similar behavior for the top parts of the PCM. The most critical difference between our sample (PP) and the plate was the temperature fluctuations. This is one of the desirable characteristics of PCMs, making them capable of storing heat and releasing it almost isothermally. It was also observed that the fluctuations had less effect on the top parts of the samples that were further from the heat source. This suggests that the more thermal energy passes through the samples, the more stable they become.

The variation of the temperature of thermocouple number 1 (T_1) with time is shown in **Fig. 5.11**. A modified Stefan number ($Ste^* = c_p(T_m - T_i) + c_p(T_{in} - T_m)/L_f$) is used, which considers the sensible heating effects of the solid and liquid states of the PCM. The Stefan number represents the ratio between sensible to latent heat. By assuming linear heat

conduction, phase change at a fixed temperature, and negligible density differences between the phases, this number describes how sensitive is the thermal process compared to the reference latent heat. Thus, increasing Ste means that the relative weight of sensible heating compared to latent one is increased; this is obvious if one considers higher inlet temperatures. Here, modified Stefan numbers of 0.275, and 0.358 correspond to wall temperatures of 50 °C and 60 °C, respectively. The results presented in **Figure 5.11** demonstrate that the temperature (melting time decreases) increase as the modified Stefan number increases. Convective flow amplification is related to heat transfer enhancement and, as a result, melting time decrease in enclosures. Moreover, with the aim of providing clearer illustrations, the temperature values at the location of the top sensors are shown in **Fig. 5.12** and discussed further.

Table 5.4 presents the timings for temperature readings at 20000 seconds for the PP samples in liquid form, where the corresponding Ste^{*} numbers vary.

In order to provide a clearer representation of the results, **Figure 5.12** displays the temperature values at the top sensor locations and further discusses their implications. The figure labeled as **Fig. 5.12** illustrates the impact of different inlet temperatures (also referred to as Ste numbers) on the charging process, including the melting process of PCM-PP at different points in time. Upon examination, it becomes clear that more PCM has melted after a period of 20 minutes. The results indicate that the liquid percentage behaves differently for each Ste value scenario, with it appearing and growing from the outer tube towards the inner tube as heat comes from the bottom side. Furthermore, the thermal distribution follows the same pattern as the liquid fraction, with the temperature of the PCM increasing as it moves from the outer tube towards other areas of the container. The growth of the liquid-solid fraction and the location of the liquid-solid interface (mushy zone) correspond with the thermal fields. As the hot fluid temperature used for work is higher than the melting point of the PCM, heat will begin to seep through the outer surfaces, causing the PCM to melt in the form of a layer adjacent to the inner surface. If one restricts the cross-sectional location, a higher amount of PCM will melt if the inlet temperature is higher (Ste=0.358).

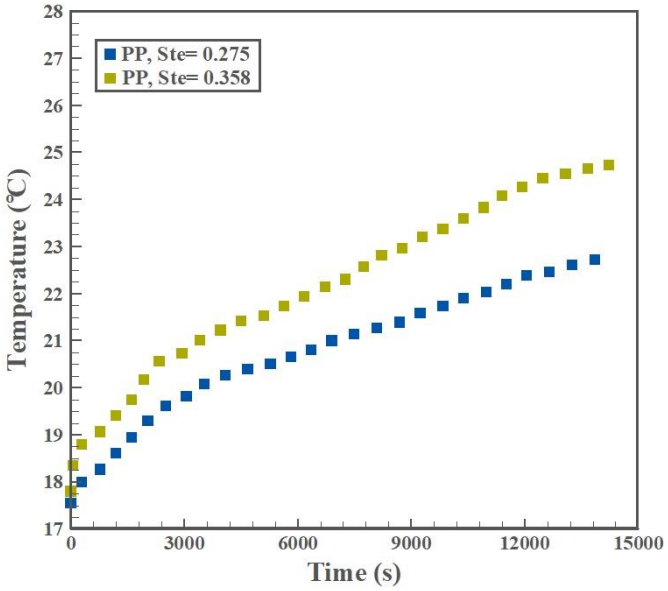

Fig. 5.11 Comparison of sample (PP) temperature (T_1) during the whole constant temperature melting experiment for T_{in}=60°C (Ste=0.358) and T_{in}=50°C (Ste=0.275)

Table. 5.4. Summarized temperature data for the melting experiments with constant temperature heat source for PP sample and different Ste numbers		
	Ste=0.358	**Ste=0.275**
PP (Time= 0s - 20000s)	25.00°C	22.99°C

t=60 min t=120 min t=180 min t=240 min

Ste=0.358

t=60 min t=120 min t=180 min t=240 min

Ste=0.275

Fig. 5.12 Evolution of melting process of pure PCM (PP) at T_{in}=60°C (Ste=0.358) and T_{in}=50°C (Ste=0.275)

5.3.2.2 Metal Foam-pure PCM (MFP)

The primary objective of this analysis is to observe how these porosity levels affect the overall performance of the system. **Figures 5.13** and **5.14** show the variation of the temperature of thermocouples (T1 and T2) for two cases: PP and MFP of investigated solutions referred to as PP and MFP, respectively. The investigated solutions had a porosity of 10 PPI and an emissivity of 0.94%. The numbers T1 to T2 given in the graphs of **Figure 5.13** indicate the location of the temperature sensors, with 1 at the highest and 2 at the lowest heights, as shown schematically in **Figure 5.10**. Therefore, closer lines on the graph mean a more uniform temperature distribution inside the sample. The sudden local changes recorded for some of the temperature sensors (for example, the sensor No. 1 for the MFP sample and around 1000s in **Figure 5.13**) must be due to the creation of hollow spaces inside the PCM, as explained in the previous section. It is noteworthy that for the preparation of the samples, the PCMs were firstly melted, then poured into the sample container, and put in a vacuum oven. Then, the samples were left in an off-vacuum oven to solidify and reach a uniform temperature. Hence, there was no chance of void creation inside the samples during solidification. As the samples were placed in the lab environment, their initial temperature was equal to the ambient temperature. However, since the tests were conducted on different days, there were slight differences in the samples' initial temperature.

Table 5.5 provides the timings for the two heating steps involved in melting the solid samples, as well as the PCM melting time, for cases MFP with Tin=60°C (Ste=0.358) and two different locations of sensors (T1 and T2). The data presented in the table shows that the heating process is critical for the successful melting of the solid samples and efficient thermal energy storage. The second thermocouple (T2) registers a higher temperature reading than the first (T1) because it is located in closer proximity to the heat source. This observation is consistent with the principles of heat transfer, which dictate that temperature gradients are steeper closer to the source of heat. This is because the heat transfer was directed upwards, and the higher points had a larger amount of melted PCM beneath them. The convection heat transfer mechanism within the melted PCM is faster when it is in the liquid state than when it is in the solid state. Therefore, as the PCM melts, its heat transfer rate increases, and in this experiment, the higher points experienced a shorter melting period.

Fig. 5.14 illustrates a comparison in terms of average temperature evolution between Case PP and Case MFP with distinct PPI and porosities of $\omega = 10$ PPI,

and ε=0.94% at Tin=60°C (Ste=0.358) and Tin=50°C (Ste=0.275). The full melting process of MFP with ε = 0.94 is less than that of Case PP. **Figure 5.14** indicates that combining paraffin and foam with pure PCM is the one effective approach for reducing melting time. These results clearly demonstrate the significant impact that integrating foam can have on the performance of the system and highlight the importance of considering both factors when optimizing thermal behavior. By improving the heat transfer performance in MFP sample, the solid section will be melted faster providing less chance for the heat to be trapped in the melted section, resulting in a slower increase in the temperature of the melted section. At a higher temperature (T_{in}=60°C Ste=0.358), the use of metal foam led to the almost complete melting of all the PCM, as opposed to the other models where a large portion of the material remained solid. This indicates that the addition of metal foam to the PCM can significantly enhance its melting performance, especially at higher temperatures. Also, it is shown that the best solution, which is case MFP which considers metal foam and PCM together, allows reducing the melting time when compared to Case PP. When compared with PP, employing MFP can drastically improve the rate of energy storage. This means that combined solutions allow a strong increase in terms of stored energy velocity, especially due to the inclusion of MF.

Table 5.6 presents the timing data for the heating steps involved in melting the solid samples for cases PP and MFP with T_{in}=60°C (Ste=0.358) and T_{in}=50°C (Ste=0.3275), as well as the locations of the sensor (T1) used to record the temperature. The results demonstrate that the heating process plays a critical role in achieving effective melting of the solid samples and efficient thermal energy storage. Notably, the MFP with T_{in}=60°C (Ste=0.358) exhibits a higher temperature reading than the other cases, indicating superior thermal conductivity and energy storage capacity. These findings are significant for the design and operation of thermal energy storage systems and provide valuable insights into the thermal behavior of metal foam/PCM composites under different heating conditions.

Figures 5.15 and **5.16** provide a comparison between Case PP and Case MFP in terms of the melting process at different times, with T_{in}=60°C (Ste=0.358) and T_{in}=50°C (Ste=0.275). By examining the melting process at different times, it becomes clear that the results differ between PP and MFP. This indicates that the temperature of the metal foam/pure PCM composite is higher than that of pure PCM alone. Furthermore, the addition of aluminum foam in the base PCM reduces thermal stratification and creates a more uniform

temperature distribution in the metal foam/pure PCM. The figures demonstrate that melting occurs faster in MFP with 0.94 porosity and T_{in}=60°C (Ste=0.358) compared to the other cases, especially in comparison to PP. This suggests that the use of aluminum foams with Tin=60°C improves heat transfer, thereby increasing melting velocity. Overall, these results provide valuable insights into the advantages of using metal foam/pure PCM composites for thermal energy storage applications. By examining **Figures 5.15**, and **5.16**, it becomes clear that the temperature of the metal foam/PCM composite for example at t=240 min is higher than that of pure PCM. This suggests that the addition of metal foam increases the amount of PCM that is melted, resulting in more effective thermal energy storage. The enhanced thermal performance of the metal foam/PCM composite can be attributed to the high thermal conductivity of the metal foam, which facilitates the transfer of heat from the surrounding environment to the PCM. Overall, these findings highlight the potential of metal foam/PCM composites as a promising solution for thermal energy storage applications, particularly in situations where high thermal performance is essential.

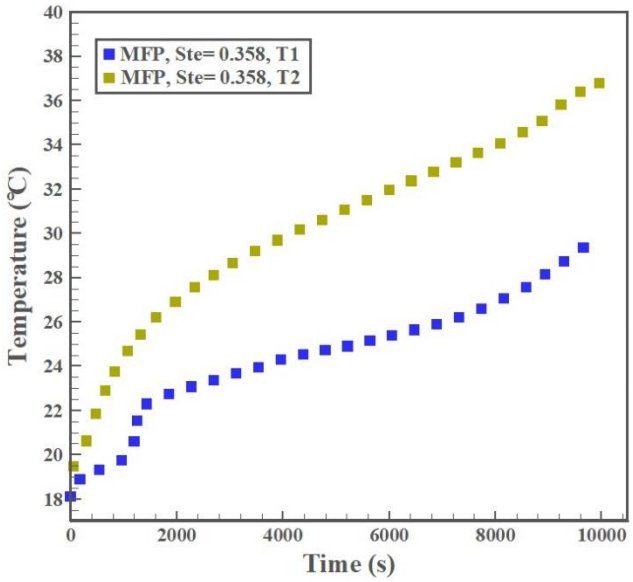

Fig. 5.13 Comparison of metal foam (MFP) (ω = 10 PPI, and ε =0.94%) temperature (T_1) and temperature (T_2) and during the whole constant temperature melting experiment

Table 5.5. Summarized temperature data for the melting experiments with constant temperature heat source for MFPP sample and different locations of sensors			
Sample-PP		**Ste=0.358 (T1)**	**Ste=0.358 (T2)**
Heating up (solid state Temperature change ºC)	20-34 ºC	0s - 12285s	0s –s
Melting Temperature change ºC)	34-36 ºC	12285 - 13249s	0s - s

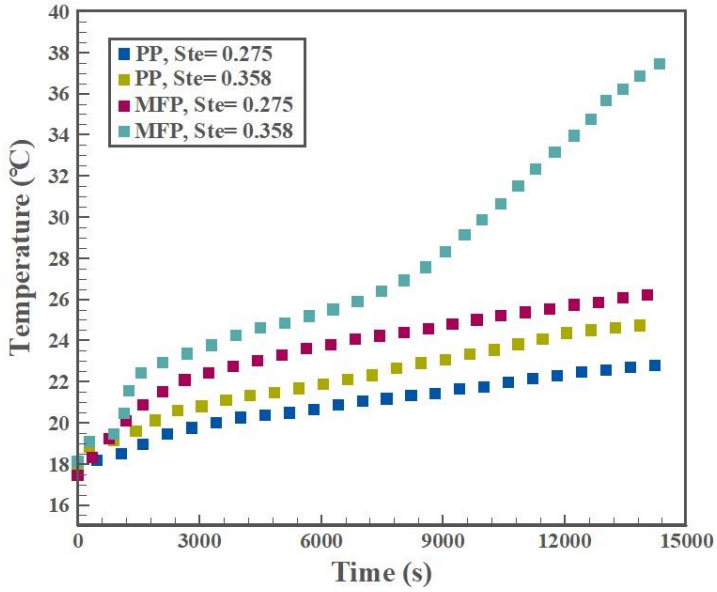

Fig. 5.14 Comparison of sample (PP) and metal foam (MFP) (ω = 10 PPI, and ε =0.94%) temperature (T_1) during the whole constant temperature melting experiment for T_{in}=60°C (Ste=0.358) and T_{in}=50°C (Ste=0.275)

Table 5.6. Summarized temperature data for the melting experiments with constant temperature heat source for MFPP sample and different Ste number		
Sample (0s - 15000s)	**PP**	**MFP**
T_{in}=50°C (Ste=0.275)	22.99 °C	26.40 °C
T_{in}=60°C (Ste=0.358)	24.97 °C	37.74 °C

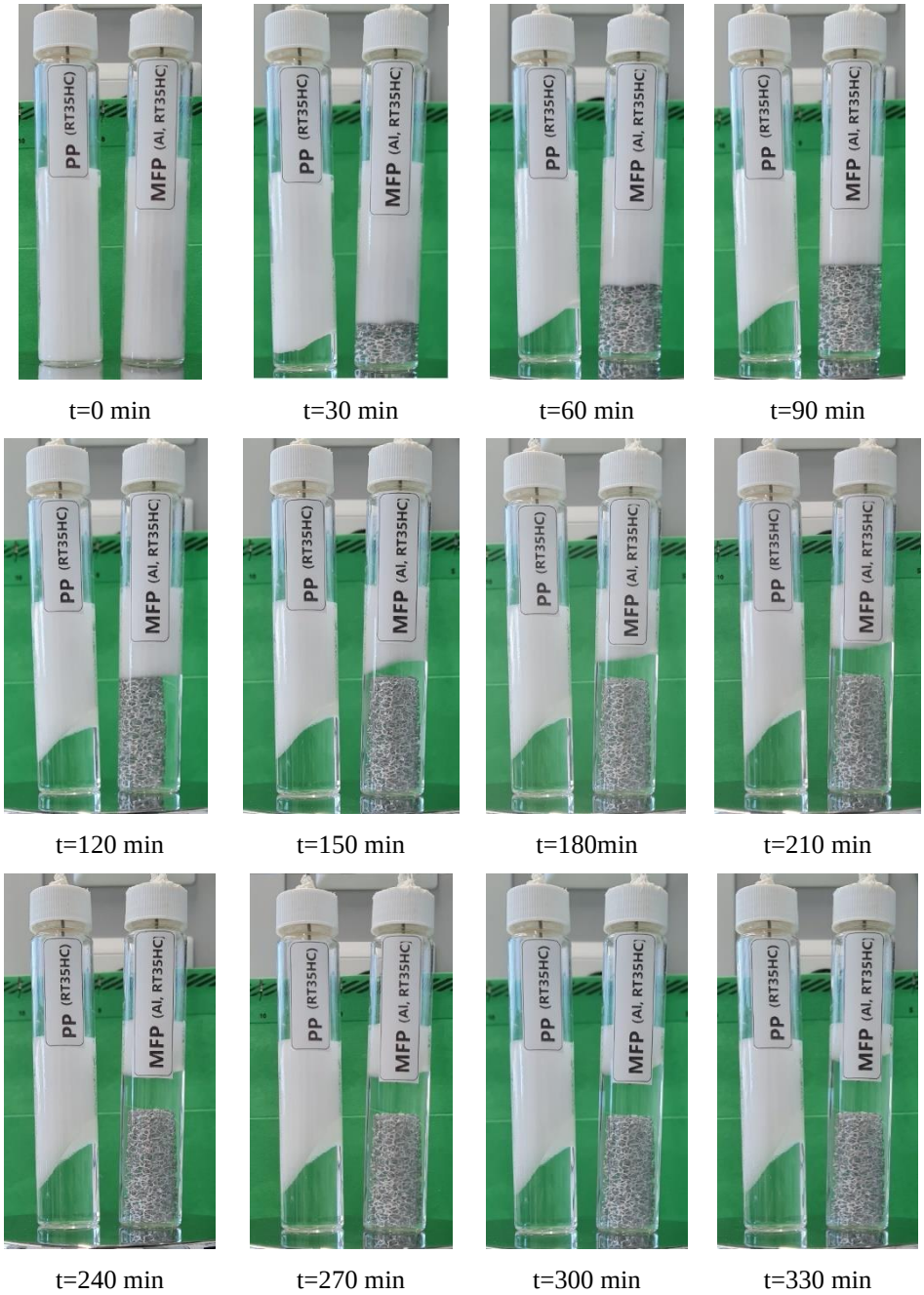

Fig. 5.15 Evolution of melting process of PP and MFP ($\omega = 40$ PPI, and $\varepsilon = 93.5\%$) temperature (T_1) during the whole constant temperature (at T_{in}=60°C, Ste=0.358) melting experiment

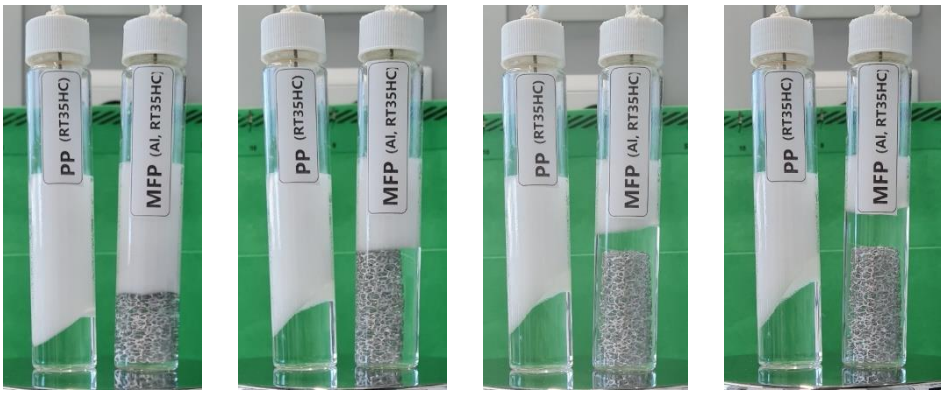

t=60 min t=120 min t=180 min t=240 min

Ste=0.358

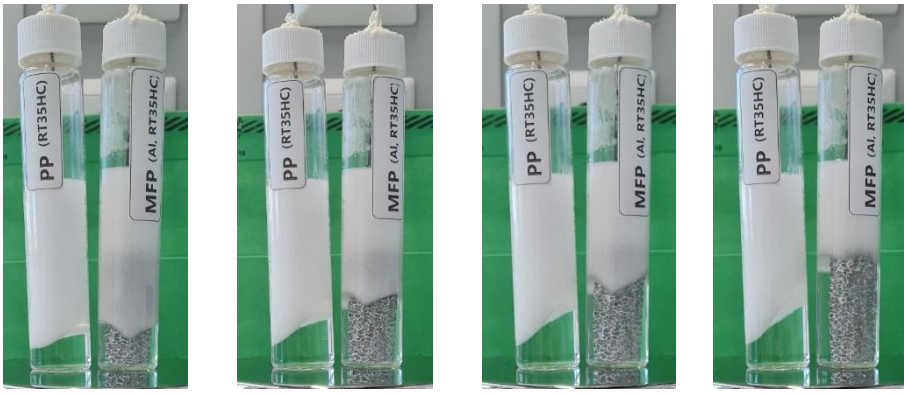

t=60 min t=120 min t=180 min t=240 min

Ste=0.275

Fig. 5.16 Evolution of melting process of PP and MFP (ω = 10 PPI, and ε = 94%) temperature (T_1) during the melting experiment whole constant temperature (top) T_{in}=60°C, Ste=0.358, and (bottom) T_{in}=50°C, Ste=0.275

5.3.2.3. NanoPCM (NP) and Metal Foam-NanoPCM (MFNP)

The paper discusses the physical issues observed during the monitoring of heat transfer performance for some samples. **Fig. 5.17** displays photographs of these issues, which show that after the PCM is fully melted, the nanoparticles in the NP and MFNP samples began to settle, especially after several solidification/melting cycles. A significant portion of the nanoparticles

dispersed in the PCM settled at the bottom of the sample. **Fig. 5.17** (left) demonstrates this phenomenon in the melted NP sample after one to three solidification/melting cycles, while **Fig. 5.17** (right) shows the solid NP after three cycles. Even though the metal foam was an open-cell type and the PCM and nanoparticles could move inside the porous medium, the settlement issue was observed for the MFNP sample as well. Consequently, the MFNP sample melted and solidified much quicker than the MFP sample. The nanoparticles enhanced heat transfer during the solidification process, speeding up the solidification process. However, once the PCM became liquid, the nanoparticles began to settle, contributing little to the heat transfer inside the sample. Nanoparticle sedimentation is a major drawback of NP composites. However, the stability of the NP sample was not investigated as it requires a dedicated study, which was beyond the scope of this research.

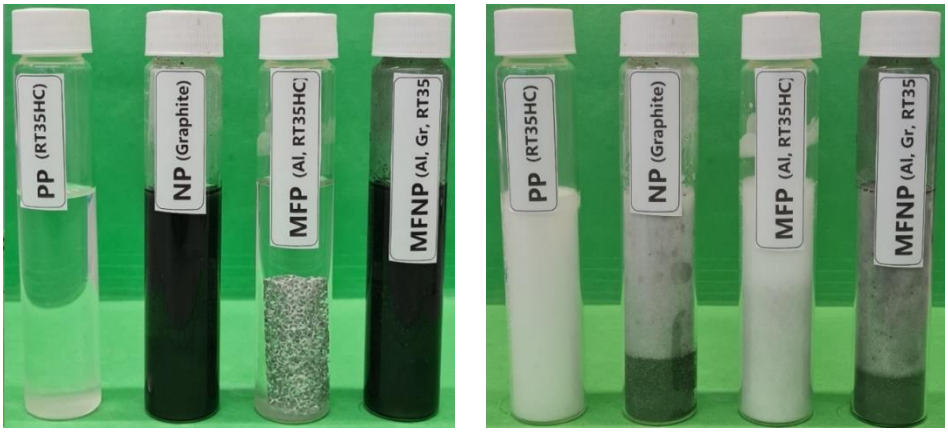

Fig. 5.17. Photos of the (left) melted NP after 1 to 3 solidification/melting cycles, and (right) solid NP after the third solidification/melting cycle.

This section compares four different cases, namely PP, NP, MFP, and MFNP, in terms of temperature evolution, aiming to investigate the impact of metal foams and nanopowder on the properties of PP cases. The primary objective of this analysis is to observe how variations in porosity and nanoparticle levels affect the overall system's performance. Metal foams provide a network of interconnected pores that facilitate heat transfer and reduce melting time, while nanopowder reinforces the matrix, resulting in improved mechanical properties and stability. As shown in **Figure 5.18**, the results demonstrate that the combination of metal foam and nanopowder, referred to as the MFNP case, is the best solution. The experimental results

reveal that the addition of metal foams and nanopowder significantly enhances the thermal conductivity and mechanical properties of the PP cases. The MFNP case exhibited the best overall performance, which can be attributed to the synergistic effects of metal foams and nanopowder. This approach resulted in a reduction in melting time compared to the PP, NP, and MFP cases (See **Figure 5.18**). The combination of metal foams and nanopowder provides a promising strategy for enhancing the performance of PP cases, and further research is necessary to explore the potential of this approach in other applications. The MFNP case is regarded as the most effective case since it delivers the best performance compared to the other cases, as shown in **Figure 5.18**. The temperature evolution of the four cases was analyzed using a data logger on LabView software. The MFNP case demonstrated the highest temperature increase among all cases, which can be attributed to the synergistic effects of metal foam and nanopowder. The metal foam provides a network of interconnected pores that facilitate heat transfer, while the nanopowder enhances the reactivity and mechanical properties of the material. The combination of these two materials resulted in improved thermal conductivity, reduced melting time, and increased stability. The NP case showed a higher temperature increase compared to the PP case due to the presence of nanopowder, which has a high surface area to volume ratio and therefore enhances heat transfer. The MFP case also exhibited a higher temperature increase, which can be attributed to the presence of metal foam, providing a network of interconnected pores that facilitate heat transfer.

The results presented in **Figure 5.19** demonstrate a similar trend to that observed in previous experiments, wherein the addition of nanoparticles and/or metal foam has an impact on the behavior of the system. The addition of metal foam was found to be more effective than that of nanoparticles. The lines in the graphs for the MFP and MFNP samples are much closer together than those for the PP and NP samples, indicating that the addition of metal foam has a greater impact on the overall performance of the system. Furthermore, it was observed that the addition of nanoparticles had a greater effect on the heat transfer in the MFP sample as compared to the PP sample, as shown in **Table 5.7**. Upon starting the heating process, the temperature at different heights increased rapidly, reaching approximately 38.53 °C for MFP and 39.48°C for MFNP samples, while it reached around 25.51 °C for PP and 26.03°C for NP samples.

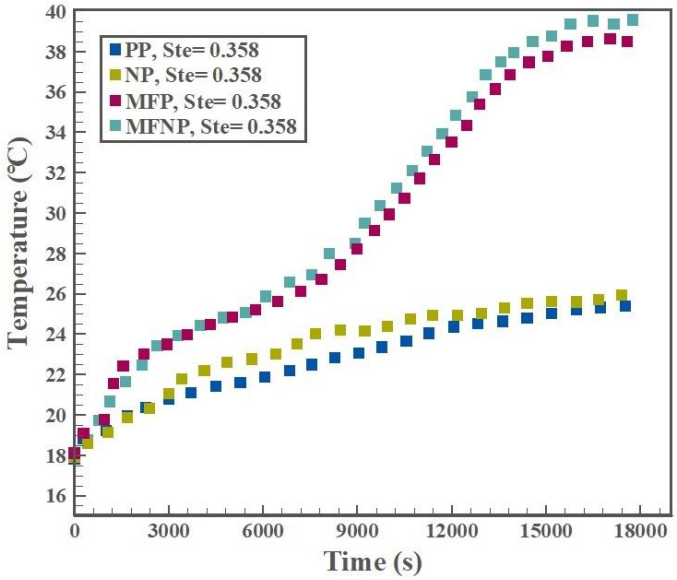

Fig 5.18 Comparison of all samples PP, NP (0.4w%), MFP, and MFNP (ω = 10 PPI, and ε =0.94%) temperature (T_1) during the whole constant temperature melting experiment

Table 5.7. Summarized temperature data for the melting experiments with constant temperature heat source for all samples at T_{in}=60°C (Ste=0.358)				
Sample (0s - 18000s)	**PP**	**NP**	**MFP**	**MFNP**
Tin=60°C (Ste=0.358)	25.51 °C	26.03°C	38.53 °C	39.48°C

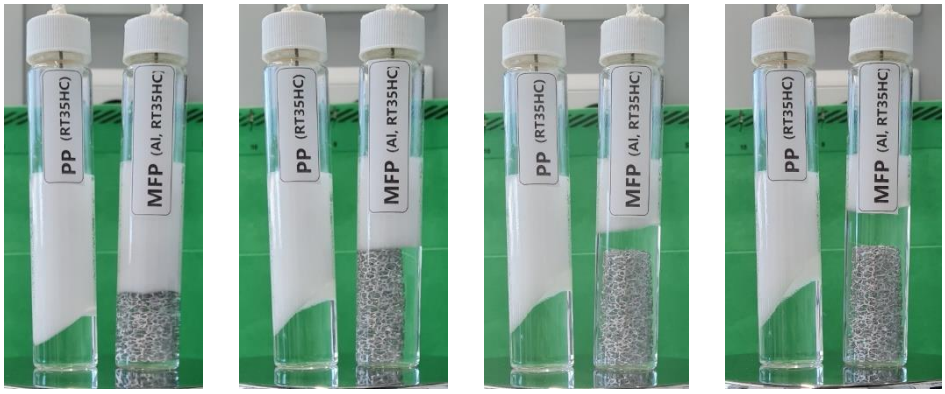

t=60 min t=120 min t=180 min t=240 min

PP, MFPP, Ste=0.358

t=60 min t=120 min t=180 min t=240 min

NP, MFNP, Ste=0.358

Fig. 5.19 Evolution of melting process of all samples at temperature (T1) during the melting experiment whole constant temperature at T_{in}=60°C (Ste=0.358)

5.3.3. Summary of first test

With the aim of comparing the methods for heat transfer enhancement of PCMs, the melting and solidification performance of pure PCM and three enhanced PCM compositions were experimentally tested. The two common enhancement methods of adding nanoparticles and adding metal foam to PCM were investigated in this study, and the three enhanced samples were PCM-nanoparticle (NP), PCM-metal foam (MFP), and PCM-nanoparticle-metal foam (MFNP) composites. Based on the heat source type, a main experimental melting setups were designed, i.e. one with a constant temperature. Below the results of each experiment are summarized:

• When the heat source temperature was increased from 50°C to 60°C (Ste numbers 0.358 and 0.275), the melting time decreased, and the temperature rose. This effect was more pronounced in MFP systems than in PP systems.

• The type of foam material used in a system has a significant impact on its heat transfer characteristics. Comparing PP and MFP systems, the use of metal foam greatly improves heat transfer, and the effective thermal conductivity of the composite structure is much higher than that of the PCM.

• In all cases tested, the addition of nanoparticles reduced the melting time compared to the reference case using PP.

• When all methods were used with MFNP at porosities of 0.94, the melting times decreased drastically compared to the other cases. This suggests that using high-porosity MFNP is an effective way to improve the performance of thermal energy storage systems.

5.4. Second Experimental study

5.4.1 Aim and novelty of the present study

The primary objective of this project is to develop a storage-integrated solar thermal collector that has a compact design and is equipped with a compatible PP and MFP. To achieve this goal, the project begins with an experimental study of a simple collector to analyze the behavior of the developed PCM and metal foam as light absorbers and storage mediums. The results of the experiment are then compared with the predicted outcomes, and a validated model is established to investigate the heat transfer characteristics of a solar collector with PCM and metal foam. The validated model is then used to design a heat exchanger that considers both the discharging and charging modes. The purpose of the experimental work is to understand the behavior of the developed PCMs and metal foam-Pure PCM when exposed to solar irradiance. The experiment involves heating and cooling phases, for which a lab-sized collector is designed and exposed to solar irradiance emitted by a solar simulator. The solar simulator used is manufactured by Newport (Type 94023A), and a 470W Xenon lamp is positioned inside it. Once the PCM is melted completely, the solar simulator is switched off to allow the collector to cool naturally via convection and radiation.

5.4.2 Geometry and material of the collector

The lab-sized collector utilized in the experiment is 3D printed and constructed using ABS and PLA materials due to their high melting temperature that can withstand the high flux of solar irradiance during the experiment. Two collectors were designed, one using pure PCM (Case PP) and the other using a combination of metal foam and pure PCM (Case MFP), with the aim of improving heat transfer within the PCM blocks. The incorporation of metal foam is intended to enhance heat transfer within the collector, enabling the observation of a desired temperature gradient. **Figure 5.20** displays an actual

image of the system equipped with PP and MFP. The rectangular enclosure had interior dimensions of 5 cm x 5 cm x 5 cm, with all sides measuring the same length. This compact size was beneficial for storing small objects or conducting experiments that required a confined space. To absorb heat flux effectively, a copper plate that has been sprayed with graphite is placed on top of the container. By using this technique, the heat energy from the container can be transferred to the plate and dissipated efficiently, preventing any potential damage or overheating. This approach is commonly utilized in various industries where heat management is crucial to maintain safe and efficient operation. Three T-type thermocouples were utilized for temperature measurement purposes. During melting, these thermocouples were inserted into three holes that were drilled on the side surface of the enclosure, positioned 1.5 cm, 3 cm, and 4.5 cm away from the bottom side of the enclosure. Moreover, the aluminum plate thermocouples were placed 1.5 cm apart from each other, and each one of them was positioned 2.5 cm away from both the right and left surfaces of the plate. This setup allowed for precise temperature readings at multiple points throughout the experiment, providing valuable data for analysis and comparison. The use of thermocouples is a common practice in many fields of research, including material science, chemistry, and engineering. A vacuum oven can be utilized to achieve a combination of Pure PCM (RT35HC) and metal foam (with $\omega = 10$ PPI and $\varepsilon = 0.94\%$). The process involves impregnating the foam with PCM and curing it under vacuum conditions.

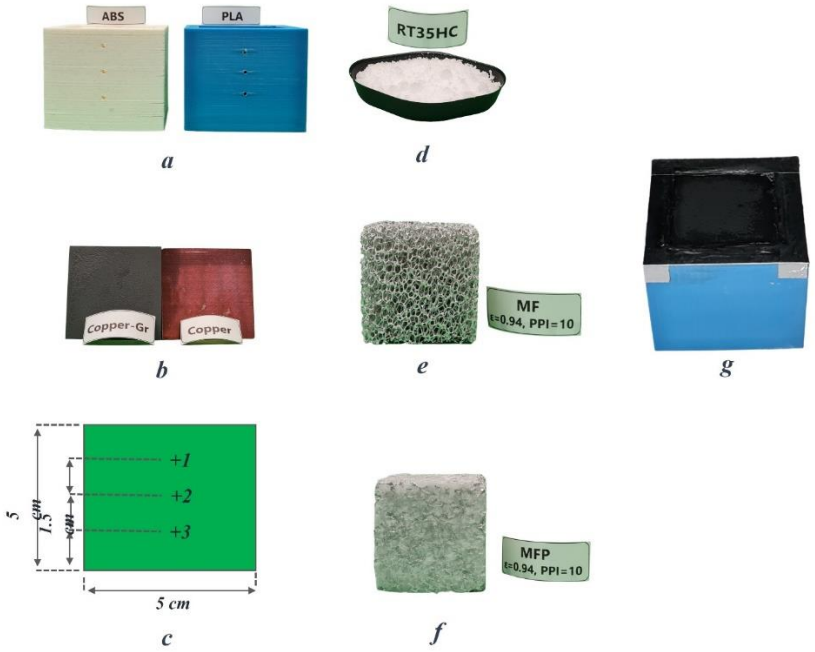

Fig. 5.20. (a) Various types of 3D printed containers, (b) copper plate and graphite copper plate with a thickness of 1 mm, (c) a schematic representation of the thermocouple placement, (d) solid pure PCM (RT35HC), (e) metal foam having a cell density of 10 PPI and porosity of 94%, (f) combination PCM with metal foam in a vacuum oven, and (g) the assembled collector.

Figures 5.21 and **5.22** provide an overview of the solar energy system and the related equipment and software used in the experiment. The diagram illustrates the various components that constitute the system, including the computer interface, temperature controller, power supply, Data Acquisition System (DAQ), holder plate, thermocouples, lamp, and heat flux sensors. It also highlights the interconnections between these components and how they function together to capture and store solar energy. The collector was placed inside the solar simulator cabin at a height where the irradiance reached up to 1200 W/m^2 after passing through the copper plate. To support thermocouple input, a compact 10-Channel DAQ system from National Instrument (NI-9211) was used as the data acquisition system. The temperature data were recorded and processed using LabVIEW software from National Instruments. The captured data were stored on a laptop computer, with data points recorded at 1-second intervals until full melting was achieved. The use of LabVIEW software

and a DAQ system allowed for precise and accurate data acquisition and analysis, providing valuable insights into the behavior of the storage-integrated solar thermal collector. Overall, the experimental setup was well-designed and allowed for a comprehensive investigation of the system's performance under different conditions.

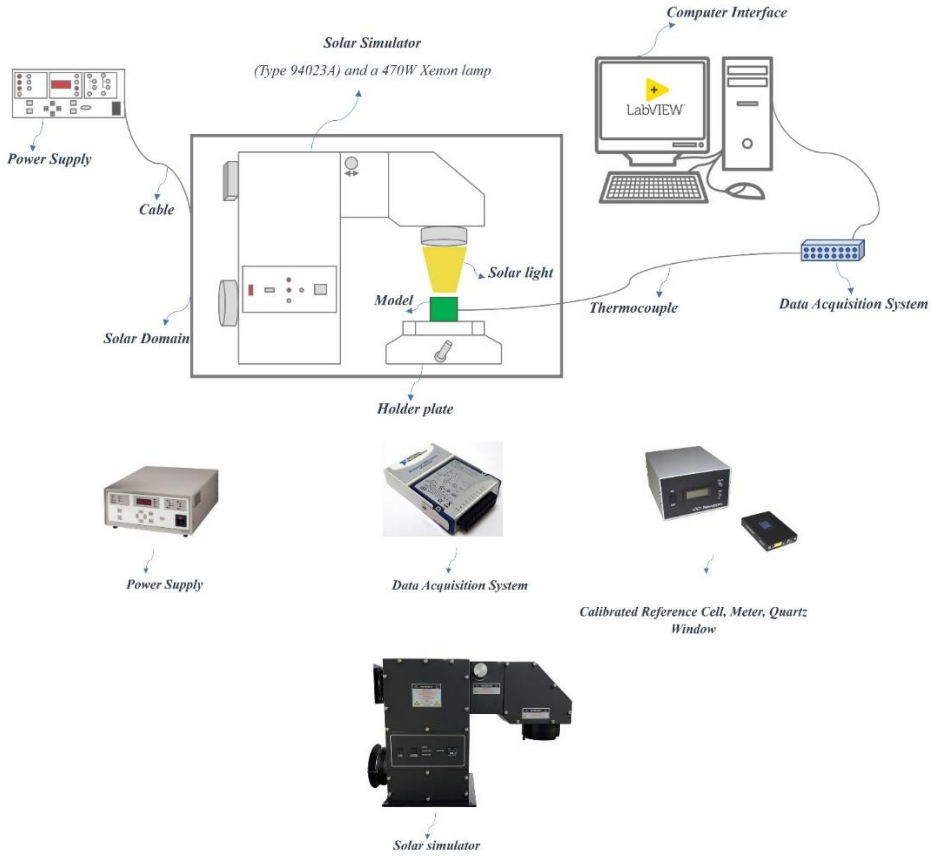

Fig. 5.21. Schematics of the complete experimental setup and equipment

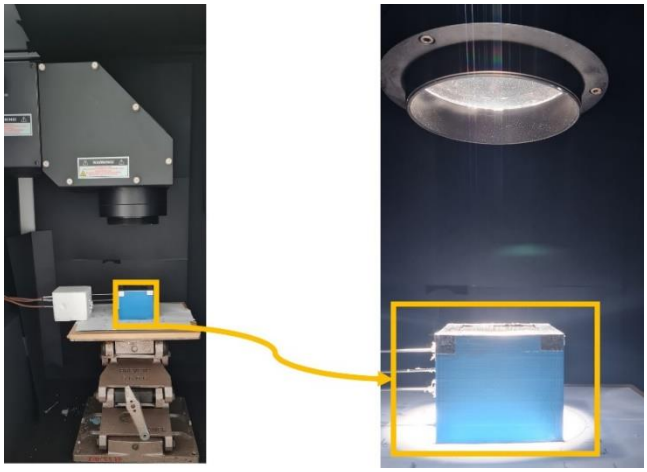

Fig. 5.22. Thermal energy storage configuration. Pure PCM and metal foams are placed inside container; the constructed experimental unit.

5.4.3. Effect of PP on solar system

The experiment aimed to observe the changes in temperature of the thermocouples placed in the PP collector over a span of 30,000 seconds (8.33 hours). The methodology included maintaining controlled conditions while monitoring the temperature variations using thermocouples. **Fig. 5.23** illustrates the results obtained, which depict a gradual rise in temperature over time (up to 10,000 seconds). The temperature-time plots are shown for three different thermocouple numbers that are obtained by maintaining a constant wall heat flux. The temperature probe point is strategically placed to observe the effect of different melting stages, as explained previously. In all cases, the temperature varies almost linearly from its initial value towards the melting point as time progresses, owing to the continuous sensible heating in the solid phase of PCM. For a heat flux value of 1250 W/m^2, the linearity of the temperature curve persists beyond the melting point, indicating the impact of conduction on heat transfer. As anticipated, for higher thermocouple numbers (T1>T2>T3) and applied heat flux, the temperature at the probe point reaches the melting point earlier, as the heat penetrates the PCM faster. Moreover, as time advances, the magnitude of the melt fraction increases from zero. The melting process further accelerates with increasing heat time, as discussed earlier.

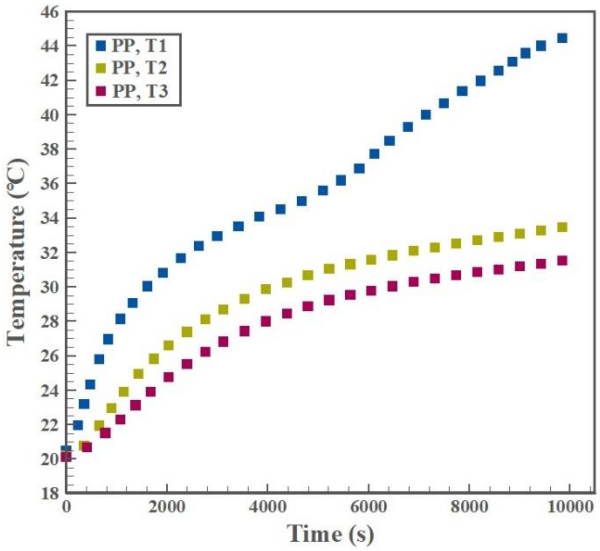

Fig. 5.23. Comparison of sample (PP) temperature (T1, T2, and T3) at heat flux (q'' =1250 W/m^2)

Table 5.8 presents the duration of the three stages of the experiment for the three thermocouples. The first stage involved heating the solid samples, followed by the second stage of melting the PCM, and finally, the third stage of heating the samples in their liquid state. The temperature increased gradually from the initial temperature of approximately 20 °C until it reached the melting point of the PCM, which was within the temperature range of 34-36 °C. The temperature continued to rise above this range during the third stage. The duration of each stage varied depending on the thermocouple used and the applied heat flux. At this point, the PCM started melting, and there were large temperature changes inside it until it was fully melted. According to the results presented in **Table 5.8**, it can be concluded that T1 exhibits better heat transfer than T2 and T3. The thermocouple measurements indicate that T1 reached the melting point at 3798 s, whereas T2 and T3 reached it at 11398s and 26518 s, respectively. Furthermore, T1 fully melted at 5357 s, while T2 melted at 17795 s. At the 30000 s point, T1 had a temperature of 48.61°C, which was higher than T2 (38.36°C) and T3 (34.23°C).

Table 5.8. Summarized temperature data for the temperature (T1, T2, and T3) at heat flux (q" =1250 W/m^2)				
Sample-PP		**T1**	**T2**	**T3**
Heating up (solid state Temperature change ^oC)	**20-34 ^oC**	0s - 3798s	0s – 11398s	0s – 26518 s
Melting Temperature change ^oC)	**34-36 ^oC**	3798s - 5357s	0s - 17795s	-
Heating up (liquid state Temperature change ^oC)	**Max**	48.61 ^oC at= 30000s	38.36 ^oC at= 30000s	34.23 ^oC at= 30000s

5.4.4. Effect of MFP on solar system

Figure 5.24 illustrates the temperature variations over time for the combination PCM with metal foam at constant heat fluxes of 1250 W/m^2. The graphs display the change in temperature at three different heights, with sensor 1 located at the highest height and sensor 3 at the lowest height, as depicted in **Fig. 5.20**. The closer the lines are to each other, the more uniform the temperature distribution within the sample. As time advances, the magnitude of the melt fraction increases gradually, indicating the melting of the PCM. Similar to the previous experiments, a general pattern of behavior was observed. However, the addition of metal foam was much more effective in enhancing the thermal performance of the PCM compared to the addition of pure PCM alone. **Figure 5.24** illustrates that for the MFP sample, the lines depicting the temperature changes are much closer together than those in the PP sample. A similar pattern was observed for the constant temperature heat source, indicating the warming up of the solid, melting of PCM, and heating up of the liquid phases. In all the samples, the thermocouples located at higher positions recorded shorter constant temperature periods, which correspond to the melting of PCM. This can be attributed to the convection heat transfer mechanism inside melted PCM, where the heat transfer rate is much faster in the liquid state than in the solid state. As the PCM melts, its heat transfer rate increases, resulting in shorter melting periods at higher points, as observed in our experiment. The overall trends of the graphs for all three thermocouples in the MFP samples

were similar, but different from those observed in the PP samples. This suggests that the addition of metal foam was much more effective than the addition of pure PCM in enhancing the thermal performance of the system.

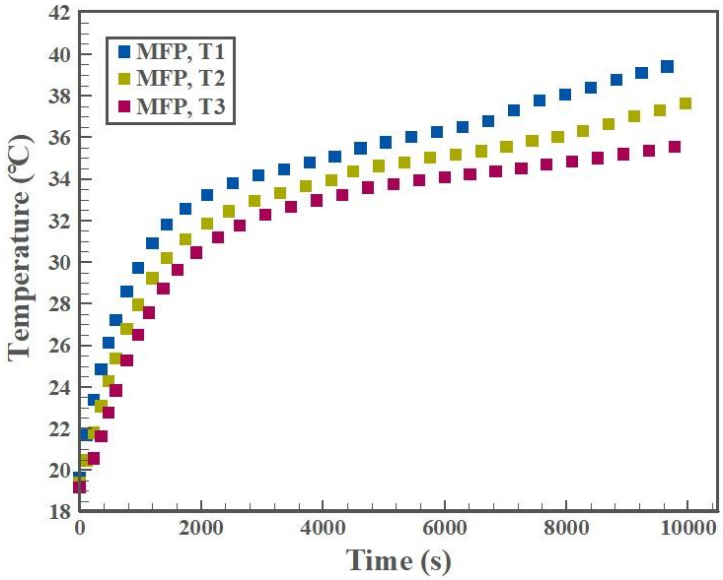

Fig. 5.24. Comparison of sample MFP (ω=10 PPI, and ε=94%) temperature (T1, T2, and T3) at heat flux (q'' =1250 W/m^2)

The timings for the three steps of heating the solid samples, PCM melting, and heating the samples when being in liquid form for three thermocouples are given in **Table 5.9**. At this point, the PCM started melting, and there were large temperature changes inside it until it was fully melted. According to the results presented in **Table 5.9**, it can be concluded that T1 exhibits better heat transfer than T2 and T3. The thermocouple measurements indicate that T1 reached the melting point at 2273 s, whereas T2 and T3 reached it at 4276s and 265185731s, respectively. Furthermore, T1 fully melted at 5315 s, while T2 melted at 7789s. At the 10000s point, T1 had a temperature of 39.57°C, which was higher than T2 (37.64°C) and T3 (35.59°C).

Table 5.9. Summarized temperature data for the temperature (T1, T2, and T3) at heat flux (q" =1250 W/m^2)				
Sample-MF		**T1**	**T2**	**T3**
Heating up (solid state Temperature change ^oC)	**20-34 ^oC**	0s - 2773s	0s – 4276s	0s – 5731s
Melting Temperature change ^oC)	**34-36 ^oC**	2773s – 5415s	4276s - 7789s	-
Heating up (liquid state Temperature change ^oC)	**Max**	39.57 ^oC t= 10000s	37.64 ^oC t= 10000s	35.59 ^oC t= 10000s

Fig. 5.25 provides a detailed analysis of the behavior of the temperature at the top parts of the samples once they were melted, and to better describe the behavior, trendlines were also drawn in the graph. It can be observed that the melted section of the PP sample experienced a quicker temperature rise than the other samples, despite being measured in the same point. However, this does not indicate that the heat transfer performance of the PP sample is better than the other samples, but rather the opposite. This is due to the fact that the layers above the melted section of the PP sample, where the temperature sensor records the temperature of the melted PCM, are still in solid form, resulting in poor heat transfer performance of this sample. As the heat transfer in solid PCM is much slower than in liquid PCM, it slows down the heat transfer process and causes the heat to be trapped in the melted section, resulting in a quicker temperature rise in this section compared to the same point in other samples. Improving the heat transfer performance in the MFP sample will result in the solid section melting faster, leaving less chance for the heat to be trapped in the melted section. Consequently, the temperature of the melted section will increase at a slower rate. Therefore, by enhancing the heat transfer performance in the MFP sample, a slower increase in the temperature of the melted section can be achieved.

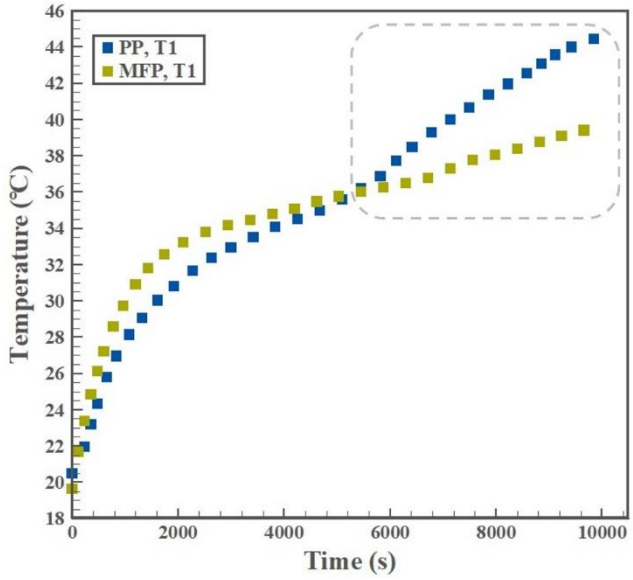

Fig. 5.25. Comparison of samples of PP and MFP(ω=10 PPI, and ε=94%) temperature (T1) at heat flux (q" =1250 W/m^2)

In order to evaluate the melting performance of the samples, a comparison was made between the total duration of each step from the beginning to the end of the experiment for the MFP and PP. This analysis was conducted for each point within the samples where temperature sensors were placed between 20°C to 34°C, as indicated in **Table 5.10**. The results showed that the addition of metal foam panels resulted in a significant decrease in melting time. Specifically, for sensors T1, T2, and T3, the melting time was reduced by 26.99%, 62.48%, and 73.38%, respectively. These findings suggest that the use of metal foam can be a valuable strategy to improve melting performance in similar experimental settings.

Table 5.10. Summarized temperature data for the temperature (T1, T2, and T3) at heat flux (q" =1250 W/m^2)

Sample- PP & MFP	**T1**	**T2**	**T3**
Time-saving compared to PP 20 °C - 34 °C	26.99%	62.48%	78.38%

Figure 5.26 depicts the changes in temperature over time for a combination of PCM with metal foam, while maintaining a constant heat flux of 1250 W/m^2 during melting, and 0 W/m2 during solidification. The samples were initially at a temperature slightly above 35°C and were placed in an ambient environment with a consistent temperature of around 21°C for solidification. It should be noted that the initial temperature of the samples was not standardized, as temperature measurements were taken at three different points within the samples and the presence of metal foam could have affected the temperature profile during the melting process. Therefore, the solidification experiments began immediately after the PCM inside the samples had completely melted, marking the onset of the solidification process. As each sample had a different melting time, they were placed in the ambient temperature individually, and temperature logging commenced as soon as each sample was introduced to the ambient environment. The temperature sensors were placed in the same positions as shown in **Fig. 5.20**, except for the bottom surface, and the samples were in full contact with the surrounding environment, which was expected to create a more uniform temperature profile at various levels in the sample container. The temperature measurements for all sensors for all the MFP samples are graphically displayed for both melting and solidification in **Fig. 5.26**.

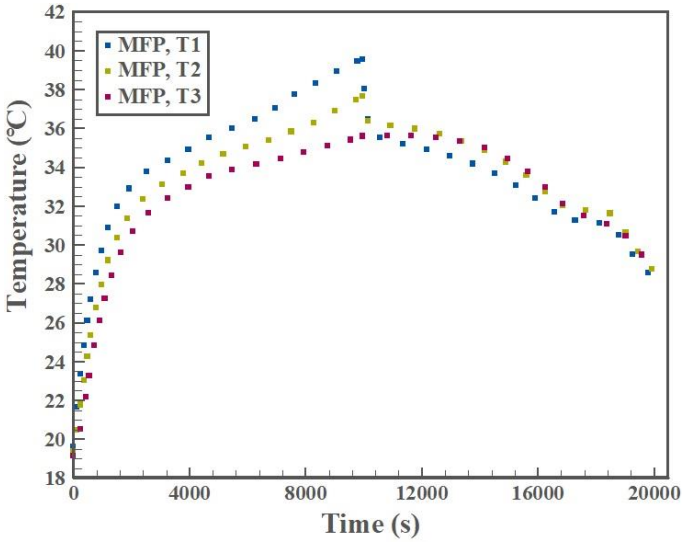

Fig. 5.26. Comparison of sample MFP (ω=10 PPI, and ε=94%) temperature (T1, T2, and T3) at heat flux (q" =1250 W/m^2) during melting time and at heat flux (q" =0 W/m^2) during solidification time

5.4.5. Summary of the second test

The goal of this research is to evaluate the effectiveness of a solar thermal collector that incorporates energy storage for heating domestic water. Initially, the study involved testing the RT35H material's thermal energy charging and discharge efficiency using lab-sized collectors and solar irradiance experiments. As solar radiation can be unreliable, the use of PCMs in thermal energy storage systems can help balance the energy supply and demand. However, PCMs have low thermal conductivity, which can be improved by adding thermal enhancement solutions, such as metal foams. The study aims to provide a comprehensive comparison of these solutions and identify the best option for a solar thermal energy storage system based on factors like thermal energy storage and melting fraction evolution. The findings suggest that the addition of metal foam with ω=10 PPI and ε=94% can reduce melting time by 26.99%, 62.48%, and 78.38% for T1, T2, and T3, respectively, when compared to the PP samples of the solar collector.

5.5. Third Experimental study

5.5.1 Aim and novelty of the present study

Based on the literature survey conducted above, it has been observed that both porous foams and nanoparticles have the potential to significantly improve the performance of TES units. In this study, we investigate the effect of a U-shaped heat exchanger and porous material on accelerating the energy-storing process in PCMs through experimental analysis. For practical applications, it is crucial to increase the charge/discharge rate of the TES unit initially, followed by a lower rate for optimal usage. Although previous studies have shown remarkable improvements in heat storage, managing the release of stored heat based on system requirements is equally important. In some applications, the duration of the charge/discharge process is critical, and it can be regulated by controlling heat storage. Thus, it is necessary to evaluate heat storage management methods experimentally, which has not been done before. To address this issue, we propose a novel design for a multi-purpose TES unit with two energy storage regions featuring different charge/discharge rates. This design allows for better control of energy storage and usage. Specifically, we designed a U-shaped HX TES unit with two separate LHTES regions: a region with porous metal foam and another with pure PCM and/or nanoPCM. Both regions are in contact with the copper pipe, and their charge/discharge rates can support the required energy based on its need.

This work is novel because it presents an experimental application of a PCM in a tankless direct-absorption heat exchanger. The use of this technology not

only addresses the issue of leakage in solar collectors but also allows for the direct absorption and storage of input heat. The proposed heat exchanger design features a single U-shaped pipe, aluminum metal foam with a porosity of 10 PPI and and porosities of 94%, and 0.4% graphite nanoparticles to meet the heat demand of domestic applications. By comparing the heat transfer performance of different PCM enhancement methods (such as the addition of metal foam and nanoparticles), this study aims to provide a reliable benchmark for future research in this field.

5.5.2 Experimental design

The chosen TES configuration is a shell with a U-shaped heat exchanger, depicted in **Figure 5.27**. The shell was produced by 3D printing using PLA material that is 0.5 cm thick. The heat exchanger has a unique design with U-pipes, known as U-pipe HEX, which are situated inside a PLA container as illustrated in **Figure 5.27**. The U-shaped tube is constructed of copper, as it has high thermal conductivity and is easily formed. To reduce heat losses during system operation, a cap made of Plexiglas was utilized. When comparing Plexiglas and glass of the same thickness, it is essential to note that Plexiglas conducts slightly less heat. Additionally, Plexiglas was necessary to use for the LHTES tank since it provided clear pictures using a camera. The experimental setup was equipped with multiple T-type temperature sensors, including one in each test sample, two in the container, and another in the surrounding air**. Fig. 5.27** displays the dimensions of the pure PCM sample in the liquid state and the locations of the temperature sensors inside it. For all experiments, PLA containers were used to hold the PCM samples, with each container having a uniform mass of 108.59 g of PCM. The NP and MFNP samples were prepared by adding 0.4343 g of Gr nanoparticles, equivalent to 0.4 w% of the PCM mass, and aluminum metal foam with a porosity of 10 PPI and porosities of 94% [8, 9, 10].

Fig. 5.27. Schematic dimensions of the container, U-shaped pipe and the placement of thermocouple sensors

Figure 5.28 depicts the experimental arrangement used to test the U-shaped heat exchanger fitted with the newly developed PCM and PCM-Metal foam as a single unit. The U-shaped heat exchanger was tested in the thermal bath located at Kleinhorst Laboratory in the University of Twente. The pipes and water hose were efficiently insulated with an elastomeric material, and aluminum tape was wrapped around the insulation to ensure the apparatus accessories were maintained at lower operational temperatures. Additionally, polyethylene foam was utilized to insulate the pipes and water hose to reduce heat losses during the heat exchanger's thermal system operation. To regulate the water flow rate provided by a thermal bath, two ball valves were installed. It should be noted that the geometrical parameters of the LHTES tank were determined based on the manufacturing limitations of the metal foams. Therefore, the design and geometrical parameters of the experimental setup were established with these limitations in mind. For more detailed information about the test rig and materials employed, refer to **Figure 5.28**. To evaluate the thermal efficiency of the proposed U-shaped heat exchanger, three T-type thermocouples were employed to measure the temperatures of the heat exchanger components. Two thermocouples were placed at the top and bottom sections of the tube to determine the temperatures of the PCM and MFP, and they were positioned 1.5 and 4.5 cm away from the bottom surface of the heat exchanger. The temperature profiles of the PCM and MFP, which show the exact positions of the thermocouples within these materials, have been presented in the results section. Additionally, another thermocouple was used to monitor the ambient temperature throughout the experiments. The connectors of the thermocouples were properly insulated to prevent them from being affected by any temperature changes. The experiments were performed at a volume flow rate of 0.01 LPS to investigate the impact of varying volume flow rates on the heat extraction from the PCM and MFP.

In the initial stage of the study, a series of experiments were performed to investigate the heat transfer performance of the PCM composites using a constant temperature. The schematic diagram of the experimental setup is presented in **Figure 5.28**. The heat source was heated from thermal bath, which was connected to a temperature controller to maintain the plate temperature at approximately 40 °C, 50 °C and 60 °C. The results of the calculation revealed that the Ste* values for wall temperatures of 40 °C, 50 °C, and 60 °C were 0.191, 0.275 and 0.358, respectively. Two temperature sensor was installed at the surface midpoint of the heat exchanger to monitor the PP and MFP temperature, which was regulated by the thermal bath controller. The ambient

temperature was found to be between 18-20 °C during the experiments, which is a typical range for laboratory procedures and provides suitable temperature stability for experiments.

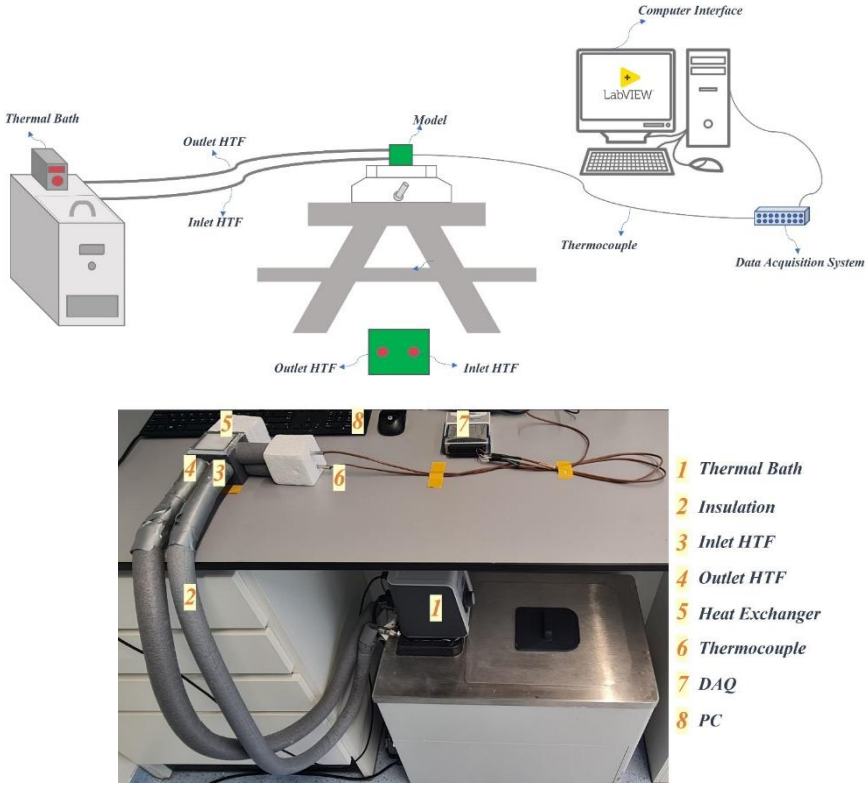

Fig. 5.28. Experimental setup of the PPHX and MFPHX tested under the thermal bath in the laboratory

5.5.3. Melting process- Case Pure PCM (PP)

In this study, we investigated the thermal behavior of single PP, NP, MFP, and MFNP through experimental work. When Hot Thermal Fluids (HTF) are used at temperatures higher than the initial temperature of PCM, the PCM undergoes melting. To establish a baseline for comparison, we first examined and evaluated a basic U-Shaped-Tube Heat Exchanger (UTHX) without NPs or MF. The obtained results, presented in **Fig. 5.29,** show a gradual temperature increase over time (up to 10,000 seconds). Temperature-time plots are shown for two different thermocouple points (T1 and T2) and three different inlet temperatures (40°C, 50°C, and 60°C) that were obtained by maintaining a

constant wall heat flux. The temperature probe location was strategically selected to observe the effect of different melting stages. In all cases, the temperature rises almost linearly from its initial value towards the melting point over time due to continuous sensible heating in the solid phase of PCM. The simulation terminates when all PCM is melted, resulting in a significant rise in temperature due to a large amount of sensible heat. This phenomenon occurs in all cases, leading to average PCM temperatures much higher than melting temperatures. As expected, for higher thermocouple numbers (T1>T2>T3), the temperature at the probe point reaches the melting point earlier, and the melting fraction increases from zero as time passes. The melting process is further accelerated by longer heating times.

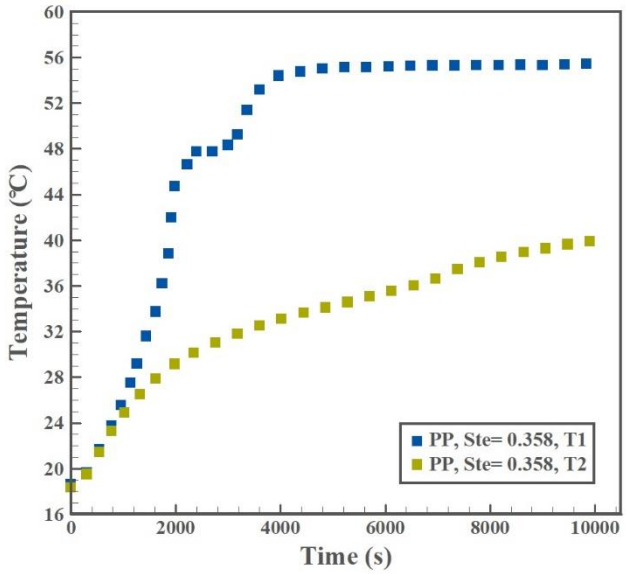

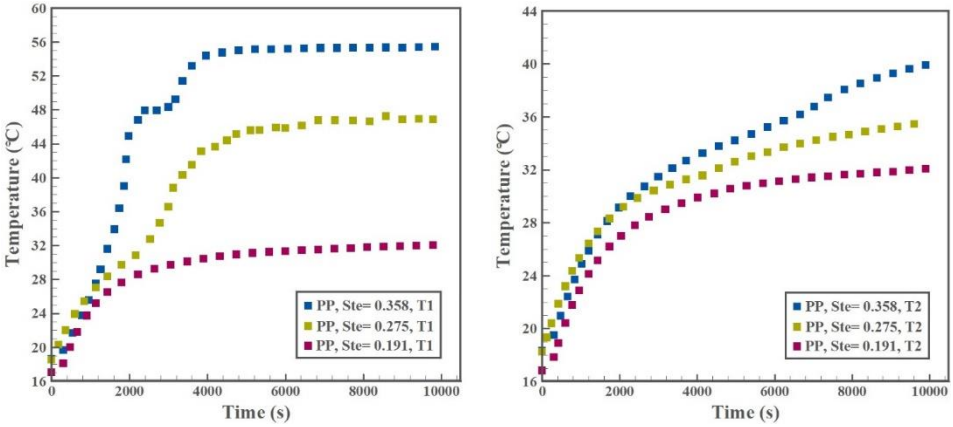

Fig. 5.29. Single pure PCM (PP) during melting (charging) process: T_{in}=60°C (Ste*=0.358), T_{in}=50°C (Ste*=0.275), and T_{in}=40°C (Ste*=0.191) at two different thermocouple sensor locations.

Figure 5.30 provides a comparative analysis of the melting evolution time between two different thermocouple points (T1 and T2) and three different inlet temperatures (40°C, 50°C, and 60°C) during the charging process. The plot clearly indicates that the melting time varies significantly with increasing inlet temperatures due to the lower temperature difference between the HTF and the melting PCM temperature. It is noteworthy that T1 exhibits a faster melting time compared to T2, and the variation is more pronounced at higher inlet temperatures. The full melting time of T1 for Ste*=0.358, Ste*=0.275, and Ste*=0.191 is 1641s, 2713s, and 19998s, respectively. Similarly, the full melting time of T2 for Ste*=0.358, Ste*=0.275, and Ste*=0.191 is 4749s, 6711s, and 36560s, respectively. The non-linear enhancement in melting time is attributed to the overall increase in conduction with higher inlet temperature, and the closer proximity of thermocouple T1 to the heat source from solar radiation, as depicted in **Figure 5.29**. The results suggest that selecting an appropriate inlet temperature is crucial for optimizing the melting performance of the PCM. A resume of melting time, and time-saving compared with reference pure PCM (Ste*=0.191) case for two different sensor numbers, is shown in **Table 11**.

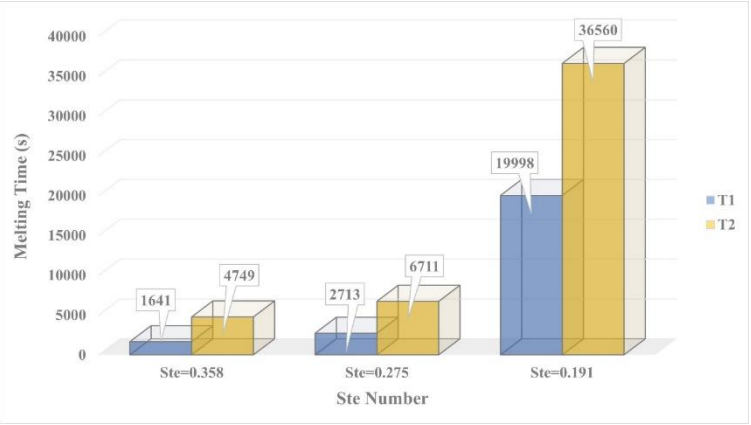

Fig. 5.30. A comparison between various solutions (PP) that consider pure PCM in terms of melting: T_{in}=60°C (Ste*=0.358), T_{in}=50°C (Ste*=0.275), and T_{in}=40°C (Ste*=0.191) at two different thermocouple sensor locations (T1 and T2).

Table. 5.11. A resume of melting time and time saving for PCM without nanoparticle and metal foam for different Ste numbers

Cases	**Melting time (s)**	**Time-saving (%)**	**Cases**	**Melting time (s)**	**Time-saving (%)**
Case-PP, Ste=0.358, T1	1641	91.79%	Case-PP, Ste=0.358, T2	4749	87.01%
Case-PP,Ste=0.275, T1	2713	86.40%	Case-PP, Ste=0.275, T2	6711	81.64%
Case-PP,Ste=0.191, T1	19998	0	Case-PP, Ste=0.191, T2	36560	0

5.5.4. Solidification process- Case Pure PCM (PP)

Fig. 5.31 demonstrates the behavior of RT35 during the solidification process for two different thermocouple points (T1 and T2) and three different inlet temperatures (40°C, 50°C, and 60°C), which have a solidification temperature of 36°C. The graph shows a steep slope at the beginning of the solidification process, followed by a significant decrease in the solidification rate as the PCM temperature approaches its solidification temperature. The steep slope at the beginning is due to the release of latent heat during the solidification process, which causes a rapid decrease in the PCM temperature.

However, as the PCM temperature approaches its solidification temperature, the release of latent heat decreases, which results in a slower rate of solidification. At the solidification temperature, the PCM releases all of its latent heat, and the temperature difference between the PCM and its surroundings reduces, which ultimately causes the solidification rate to decrease significantly. This phenomenon occurs because, at the melting temperature, the PCM absorbs a large amount of latent heat, which reduces the temperature difference between the PCM and its surroundings, and consequently, the rate of solidification decreases.

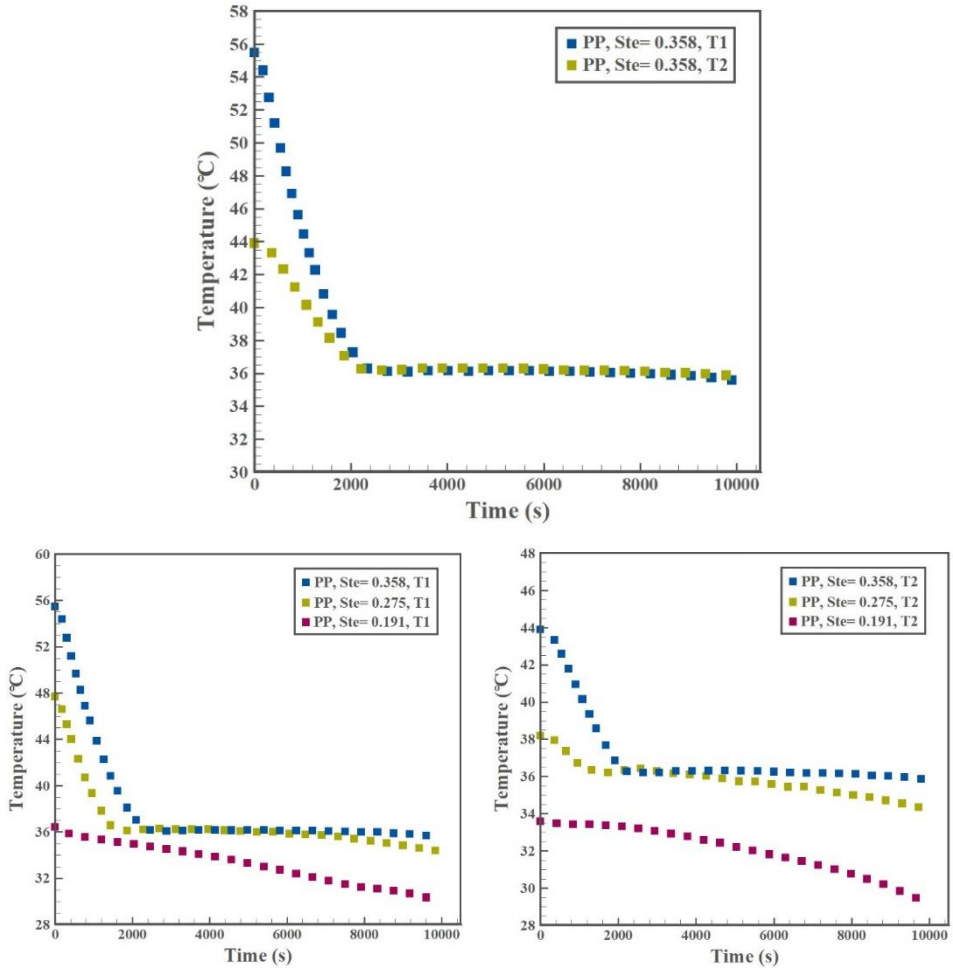

Fig. 5.31. Single pure PCM (PP) during solidification process: T_{in}=60°C (Ste*=0.358), T_{in}=50°C (Ste*=0.275), and T_{in}=40°C (Ste*=0.191) at two different thermocouple sensor locations.

5.5.5. Melting process- Nano Pure PCM (PP)

The comparison of the PCM-averaged temperature between Case PP and Case NP during the solidification process at two different thermocouple points (T1 and T2) and an inlet temperature of 60°C is presented in **Fig. 5.32**. The NEPCM volume percentage assumed in this study is 0.4%. The figures indicate that the melting and solidification time is slightly reduced for the NP case, which exhibits lower liquid and solid fractions and a faster evolution of the solid and liquid front compared to the PP case.

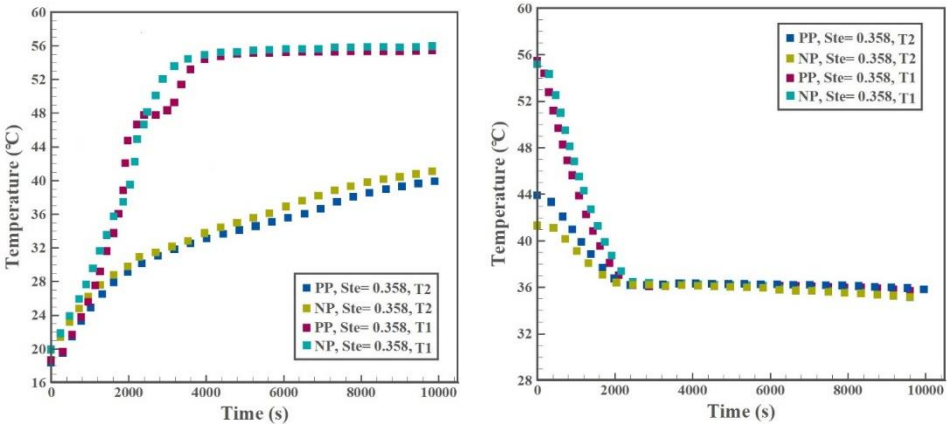

Fig. 5.32. Single pure PCM (PP) during melting and solidification process: T_{in}=60°C (Ste*=0.358) at two different thermocouple sensor locations.

Based on the data shown in **Fig. 5.33**, the NP sample proves to be more advantageous for melting and solidification, with the lowest required time reported as 1521s for T1 and 4113s for T2 during the melting process. The temperature graphs presented in **Figure 5.33** indicate that the use of nanoPCM (NP) configuration results in similar temperatures with a slight reduction in melting time, i.e., a reduction of 7.31% for thermocouples number 1 (T1), and 13.39% for thermocouples number 2 (T2) during the melting process (see **Table 5.12** for further details). In summary, **Fig. 5.33** demonstrates that the NP sample is superior for both melting and solidification processes, as it requires less time to complete the phase change. The temperature graphs in **Fig. 5.32** also confirm that the use of nanoPCM configuration results in a slight reduction in melting and solidification time. These findings suggest that the use of NP can be a promising approach to improve the efficiency of the phase change process in thermal energy storage systems.

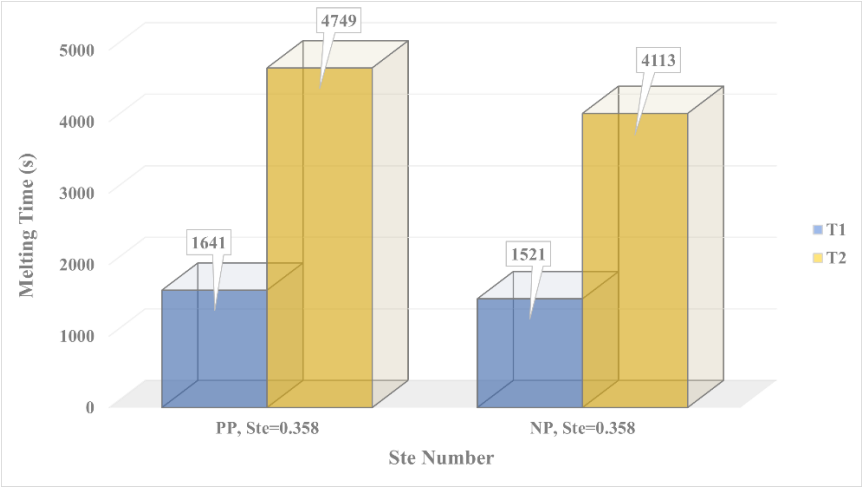

Fig. 5.33. Effects of nanoparticle on instantaneous melting time Case Pure PCM (PP) and Case nanoPCM

Table 5.12. A resume of melting time and time saving for PCM without nanoparticle for different Ste numbers

Cases	**Melting time (s)**	**Time-saving (%)**	**Cases**	**Melting time (s)**	**Time-saving (%)**
Case-NP, Ste=0.358, T1	1521	0%	Case-NP, Ste=0.358, T2	4113	0%
Case-PP, Ste=0.358, T1	1641	7.31%	Case-PP, Ste=0.358, T2	4749	13.39%

The data collected and illustrated in **Figure 5.34** exhibits a steady elevation in temperature as time progresses, spanning a duration of 10,000 seconds, for both the comparison of PP and MFP cases. To provide a comprehensive understanding of the temperature changes, temperature-time graphs for two distinct thermocouple points (T1 and T2) and three varying inlet temperatures (40°C, 50°C, and 60°C) were plotted. These inlet temperatures were achieved by upholding a constant wall heat flux. The selection of the temperature probe's placement was carefully considered to observe and analyze the impacts of various melting stages. The results obtained from the data collected and illustrated in **Figure 5.34** indicate a consistent rise in temperature over a duration of 10,000 seconds for both PP and MFP cases. To facilitate a thorough comprehension of the temperature fluctuations, temperature-time graphs were

plotted for two distinct thermocouple points (T1 and T2) and three varying inlet temperatures (40°C, 50°C, and 60°C), with the inlet temperatures achieved by maintaining a constant wall heat flux. The selection of the temperature probe's placement was carefully considered to assess the effects of various melting stages. The study employed distinct porosity of $\varepsilon = 0.94$ at equal PPIs (e.g., 10). The results indicate a significant variation in melting time with porosity due to the increased amount of metal, leading to enhanced overall thermal conduction. It was observed that the MFP Foam exhibited higher temperatures overall. This can be attributed to the faster melting rate of the PCM with foam, resulting in the other cases and pure PCM still undergoing the melting fraction evolution even after complete melting in the PCM/Porous Foam case.

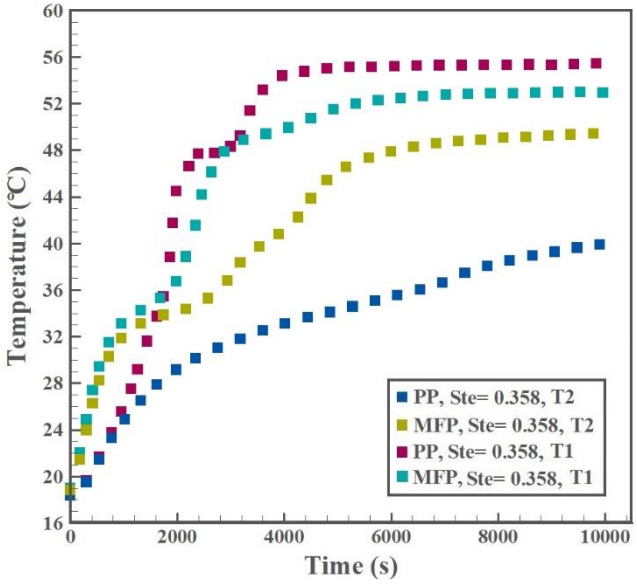

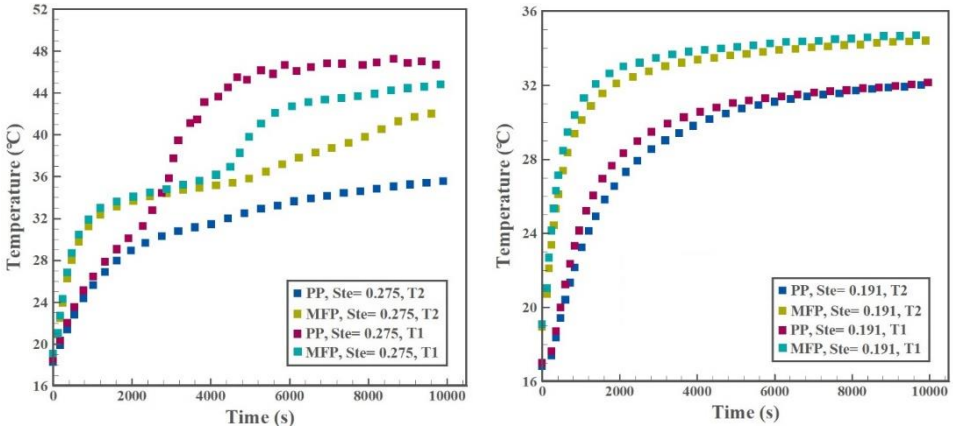

Fig. 5.34. Effects of metal foam on instantaneous melting time Cases PP and MFP

The results in **Fig. 5.35** demonstrate the melting time and time saving for Case PP, which pertains to pure PCM, and Case MFP, which involves pure PCM with metal foam, with the utilization of two distinct thermocouple points and three varying Ste numbers. The bar chart depicts that the inclusion of PCM-Metal Foam leads to a significant improvement in the melting (charging) rate and a decrease in melting time in reference to the required time. It was observed that the melting time for $\varepsilon = 0.94$ and 10 PPI is almost 26.02% (Ste=0.358), 25.69% (Ste=0.275), and 77.07% (Ste=0.275) at T1 and almost 60.77% (Ste=0.358), 64.97% (Ste=0.275), and 81.68% (Ste=0.275) at T2 higher than PP, respectively. These results indicate that foams are the primary reason for the observed improvement in thermal behavior. The inclusion of metal foam in PCM-Metal Foam significantly enhances the melting rate and saves time. Therefore, it can be concluded that the use of metal foam can effectively enhance thermal performance of PCM-based energy storage systems.

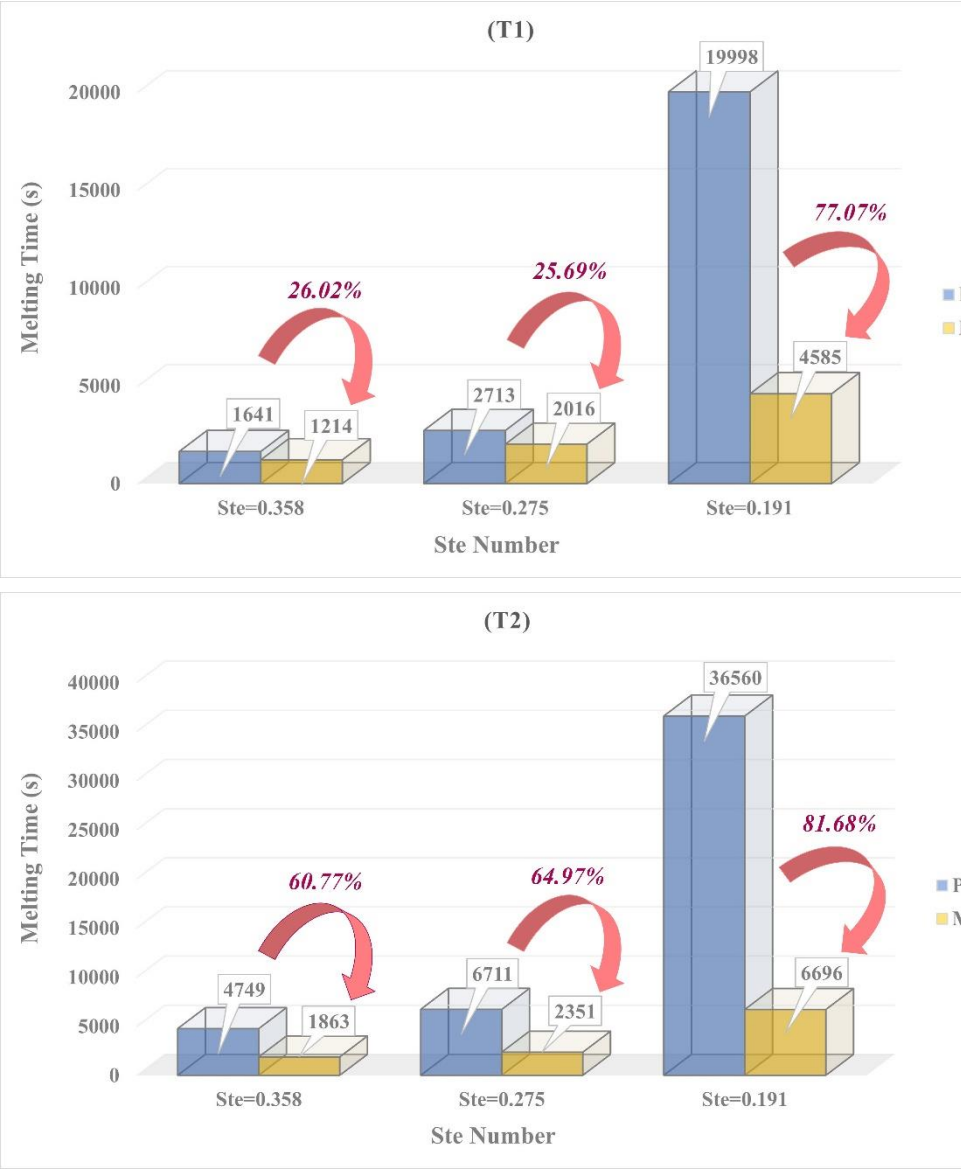

Fig. 5.35. A comparison between various solutions that consider pure PCM and metal foams; Tin=60°C (Ste*=0.358), Tin=50°C (Ste*=0.275), and Tin=40°C (Ste*=0.191) at two different thermocouple sensor locations.

The data presented in **Figure 5.36** illustrates the behavior of two different cases, Case PP and Case MFP, during the solidification process. Case PP pertains to pure PCM, while Case MFP involves the addition of metal to the phase change material. The solidification process was monitored at two

different thermocouple points, T1 and T2, and at three different inlet temperatures, 40°C, 50°C, and 60°C, which all have a solidification temperature of 36°C.The graph in **Figure 5.36** shows a sharp decline in temperature at the beginning of the solidification process for both cases, followed by a significant decrease in the solidification rate as the PCM temperature approaches its solidification temperature. This initial drop in temperature is due to the release of latent heat during the solidification process, which causes a rapid decrease in the PCM temperature. However, as the PCM temperature approaches its solidification temperature, the release of latent heat decreases, which results in a slower rate of solidification. It is observed that the addition of metal to the PCM in Case MFP results in a much higher heat transfer rate compared to Case PP. Consequently, the solidification time is significantly reduced, indicating better heat transfer performance. This means that a larger amount of PCM is frozen in a shorter period of time by adding metal to the phase change material. The steep slope at the beginning and end of the solidification process for Case MFP is due to the addition of metal, which enhances the heat transfer rate. In summary, the results indicate that adding metal to the PCM can improve the heat transfer performance during the solidification process, resulting in faster solidification times.

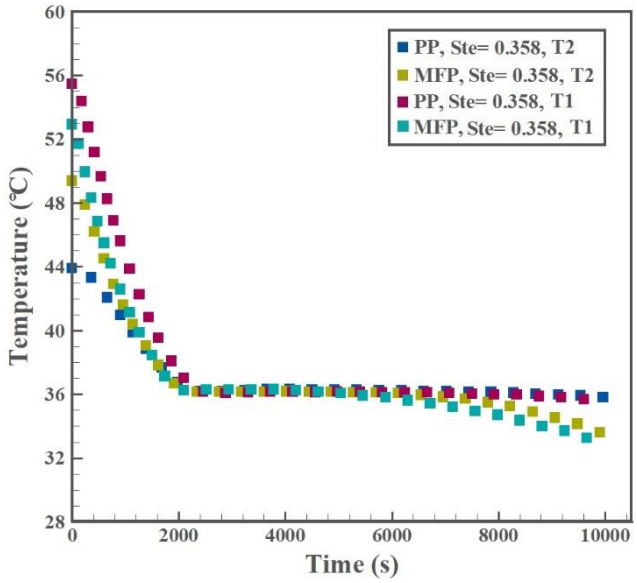

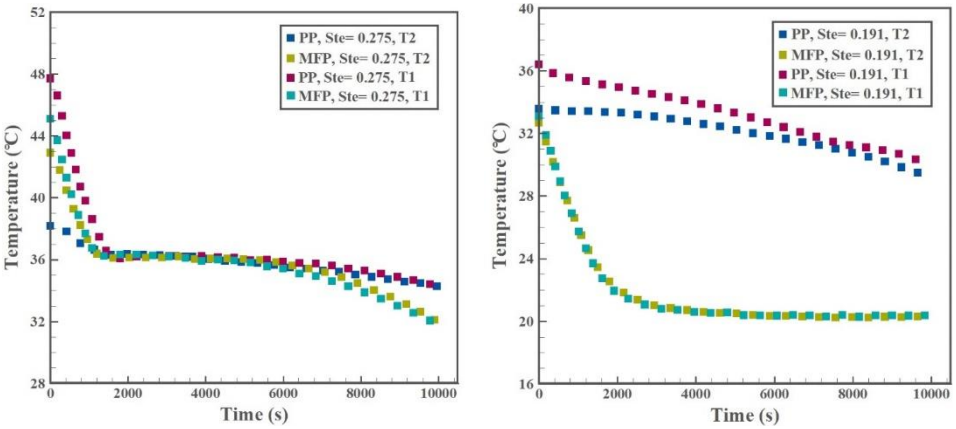

Fig. 5.36. Effects of metal foam on instantaneous solidification time for cases PP and MFP: Tin=60°C (Ste*=0.358), Tin=50°C (Ste*=0.275), and Tin=40°C (Ste*=0.191) at two different thermocouple sensor locations.

In **Figure 5.37**, a comparison between Case MFP and Case MFN during the melting process is presented, based on the PCM-averaged temperature at an inlet temperature of 60°C and two different thermocouple points, T1 and T2. The results indicate that the MFNP case exhibits a shorter melting time than the MFP case, owing to the lower liquid fractions and faster evolution of the solid front observed in the former. The melting process involves the transition of the PCM from a solid to a liquid state, which is accompanied by the absorption of latent heat. During this process, the temperature of the PCM changes, and the PCM-averaged temperature can be used to assess the performance of different cases. In the case of MFNP, the addition of nanoparticles to the PCM results in a faster evolution of the solid front and lower liquid fractions, leading to a shorter melting time compared to MFP. This indicates that the presence of nanoparticles enhances the heat transfer performance during the melting process.

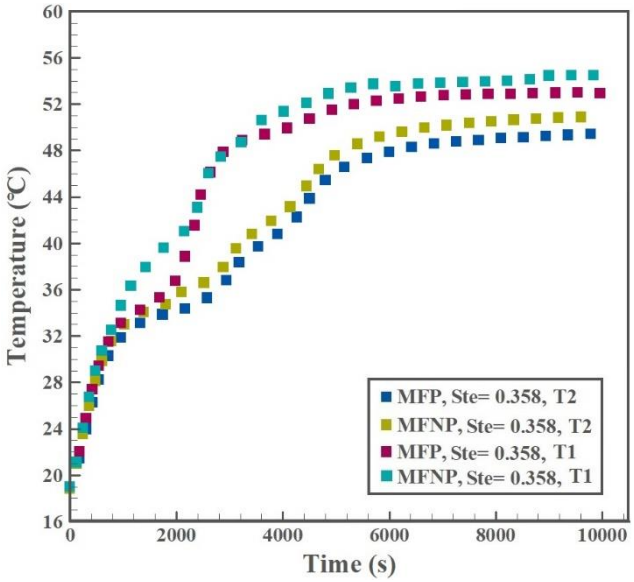

Fig. 5.37. Effects of metal foam and nanoparticels on instantaneous solidification time for cases MFP and MFNP: Tin=60°C (Ste*=0.358), and at two different thermocouple sensor locations.

Figure 5.38 and the **Table 5.13** present the melting time and the percentage of time saved for various solutions investigated in this study, including PP, NP, MFP, and MFNP. The percentage values are compared with Case A-PP for different sections of Thermocouples (T1 and T2). According to the results obtained from **Figure 5.38**, the best solution is case MFNP, which combines the use of nanoparticles and foam. This solution allows for a reduction in melting time of 43.57% and 71.93% for T1 and T2, respectively, when compared to the use of only PP. In other words, the incorporation of both nanoparticles and foam in the PP matrix leads to a significant reduction in melting time, particularly for T2. These findings suggest that the MFNP solution could be a promising approach for enhancing the thermal conductivity and reducing the melting time of PP-based materials.

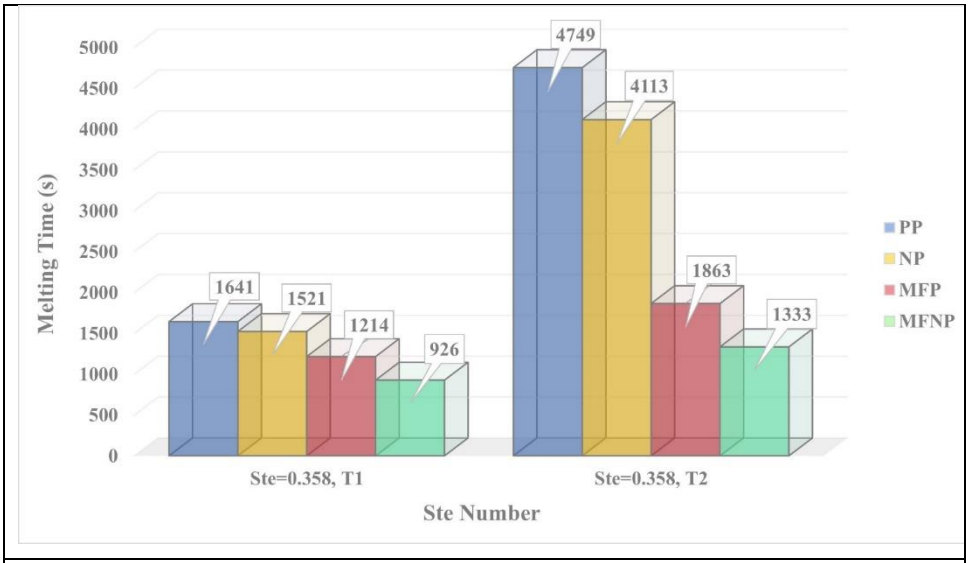

Fig. 5.38. A comparison between all methods PP, NP, MFP, and MFNP; Tin=60°C (Ste*=0.358), and at two different thermocouple sensor locations.

Table. 5.13. A comparison between various methods: melting time, and timesaving

Cases	Melting time (s)	Time-saving (%)	Cases	Melting time (s)	Time-saving (%)
Case-PP, Ste=0.358, T1	1641	0%	Case-NP, Ste=0.358, T2	4749	0%
Case-NP, Ste=0.358, T1	1521	7.31%	Case-PP, Ste=0.358, T2	4113	13.39%
Case-MFP, Ste=0.358, T1	1214	26.02%	Case-MFP, Ste=0.358, T2	1863	60.77%
Case-MFNP, Ste=0.358, T1	926	43.57%	Case-MFNP, Ste=0.358, T2	1333	71.93%

5.5.6. Uncertainty of measurements

The T-type thermocouples are pre-calibrated for the temperature range of 0–100 °C. The uncertainty in temperature measurement is found to be ±0.2 °C. On the other hand, the repeatability of the temperature sensors was ensured by observing a negligible deviation in temperature through comparison between four runs of experiments (See **Table 5.14**).

Table 5.14. Accuracy of instruments and Error analysis	
Parameter	Error
T-type thermocouples	±0.2
Hot water bath temperature T_{hot} / ◦C	±0.1
Porosity ε	±0.4
Flow rate L/min	0.02

5.7. Experimental results and model validation

With the use of numerical validation, several essential pieces of information that were not easily obtainable from the experiment were able to be retrieved, such as the melting percentage and the temperature distribution. **Figure 5.39** displays the liquid fraction and average temperature of the PCM for Case A utilizing pure PCM (Case A-PP). The average temperature is referred to the PCM average temperature during the melting process. The models accurately anticipated the temperature variations at various locations of the collectors throughout a certain time period. **Figure 5.39** illustrates the mean temperature derived from the experimental data, represented by solid lines, as well as the validation findings, shown by dotted lines, pertaining to the HX with a PP under the specified conditions of an inlet temperature (Tin=40°C, Ste*=0.191). The simulation is performed for 1 hour and 3 hours for Case PP. The models produced accurate projections for the temperature that would be experienced at T1 of USHX as time progressed, and the graphs' behavior and melting durations demonstrate a very excellent agreement with one another. On the USHX with PP and Tin=40°C, the average temperature from the trials is presented in **Figure 5.40** as red lines, and the validation results are shown as blue lines.

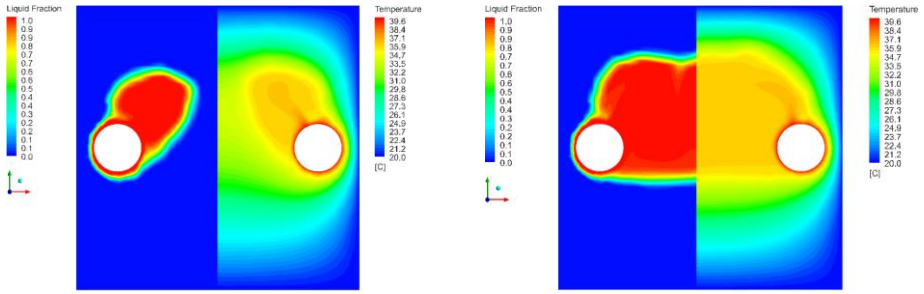

(a) 1 hours (b) 3 hours

Fig. 5.39. Liquid fraction and temperature fields for Pure PCM at different times: (a) 3600 s and (b) 10800 s

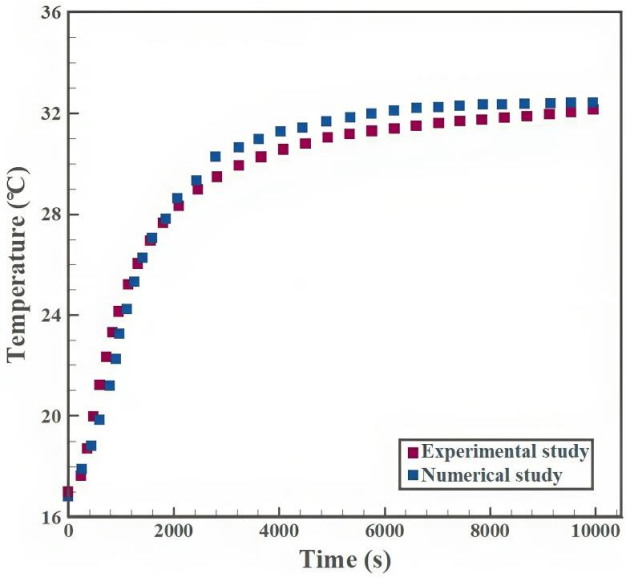

Fig. 5.40. Validation findings for Case A, specifically the average temperature of the pure PCM for both the experimental and simulation phases at T_{in}=40°C(Ste*=0.191)

5.5.8. Summary of the third test

To improve the low conduction mode of RT35HC and increase efficiency systems, some enhancing methods have been used separately or together; 1) U-shaped heat exchanger geometry; 2) Dispersing graphite nano-sized powders intoPCM; 3) Adding MF with different porosity (Aluminum foam). The objective of the present study is to have a throughout comparison of all these solutions in order to appreciate which one could be the best for thermal energy storage/harvesting and melting/solidification fraction evolution when a U-shaped pipe heat exchanger is used in combination with a solar system. The main conclusions from the present work are listed as follows:

- When the heat source temperature was increased from 40°C to 50°C and 60°C (Ste numbers 0.191, 0.275, and 0.358), the melting time decreased and the temperature rose. The melting time was reduced by 91.79% (Ste=0.358) and 86.40%(Ste=0.275) for T1 and reduced by 87.01% (Ste=0.358) and 81.64% (Ste=0.275) for T2 in PP systems

- For Case-PP (Ste=0.358), the addition of NP to PCM reduces the melting time by 7.31% for T1 and 13.39% for T2, compared to the reference case with Case PP;

- Still for Case PP with MF (ε = 0.94 and 10 PPI), a melting time reduction almost 26.02% (Ste=0.358), 25.69% (Ste=0.275), and 77.07% (Ste=0.275) at T1 and almost 60.77% (Ste=0.358), 64.97% (Ste=0.275), and 81.68% (Ste=0.275) at T2 compared to Case A-PP;

- The addition of all methods NP, MF, and MFNP, with porosities of 0.4% and 0.94, reduces the melting time by 7.31%, 26.02%, and 43.57% at T1. It also reduces the melting time by 13.39%, 60.77%, and 71.93% at T2 when compared to the Case PP.

References

[1] https://www.rubitherm.eu/en/

[2] Kalidasan B, Pandey AK, Saidur R, Kothari R, Sharma K, Tyagi VV. Eco-friendly coconut shell biochar based nano-inclusion for sustainable energy storage of binary eutectic salt hydrate phase change materials. Solar Energy Materials and Solar Cells. 2023 Oct 15;262:112534.

[3] Sreenath VR, Chanda S. Thermal performance evaluation of PCM-MF composite heat sinks under varying ambient conditions. International Journal of Heat and Mass Transfer. 2023 Jun 1;206:123927.

[4] Elarem R, Alqahtani T, Mellouli S, El Awadi GA, Algarni S, Kolsi L. Experimental investigations on thermophysical properties of nano-enhanced phase change materials for thermal energy storage applications. Alexandria Engineering Journal. 2022 Sep 1;61(9):7037-44.

[5] Kalidasan B, Pandey AK, Rahman S, Yadav A, Samykano M, Tyagi VV. Graphene–Silver Hybrid Nanoparticle based Organic Phase Change Materials for Enhanced Thermal Energy Storage. Sustainability. 2022 Oct 14;14(20):13240.

[6] Iasiello M, Mameli M, Filippeschi S, Bianco N. Metal foam/PCM melting evolution analysis: Orientation and morphology effects. Applied Thermal Engineering. 2021 Mar 25;187:116572.

[7] Confalonieri C, Boller E, Cheng Y, Gariboldi E. Synchrotron radiation micro-CT with phase contrast for high-temperature in-situ microstructural characterization of AlSn composite phase change materials. Materials Characterization. 2022 Nov 1;193:112302.

[8] Iasiello M, Mameli M, Filippeschi S, Bianco N. Metal foam/PCM melting evolution analysis: Orientation and morphology effects. Applied Thermal Engineering. 2021 Mar 25;187:116572.

[9] NematpourKeshteli A, Iasiello M, Langella G, Bianco N. Thermal enhancement techniques for a lobed-double pipe PCM thermal storage system. Applied Thermal Engineering. 2023 Oct 1;233:121139.

[10] Zhou T, Yan J. Glass molding process for microstructures. In Micro fabrication and Precision Engineering 2017 Jan 1 (pp. 213-262). Woodhead Publishing.

6.

Conclusions and Future Study

6.1. Conclusion

Based on the previous research works, the main aim of this work was to explore the thermal characteristics of an energy storage systems that incorporates a composite phase change material (PCM). This research employed a blend of experimental and numerical, including Porous Metal Foam (PMF), Nanoparticles (NP), and Optimization Systems (OP). The results of this study highlight that the incorporation of PMF, NP, and OP techniques can effectively minimize the time needed for both charging and discharging the PCM, resulting in a faster energy storage and release process.

6.1.1. Numerical Study

- With the addition of nanoparticles with different volume fractionin melting and solidification time is reduced, when compared to the systems with pure PCM without nanoparticles and metal foam, since thermal conductivity in the PCM will be enhanced by adding nanoparticles.

- The addition of both nanoparticles and metal foam with various porosities reduces the melting and solidification time, when compared to the systems with only pure PCM. The reason for this is that the use of nanoparticles and metal foam improves thermal conductivity in the PCM.

- Adding a Multilayer-PCM with the addition of nanoparticles and metal foam with a various porosity has a significant impact on reducing melting and solidification time. This effect results in an alteration of the time required for the entire PCM to transition from its solid to liquid state, ultimately affecting the efficiency and performance of the energy storage system. The presence of nanoparticles introduces intricate thermal dynamics and interaction mechanisms within the multilayer PCM, leading to changes in its melting kinetics. This, in turn, prompts a need for a comprehensive analysis of these interrelated factors to optimize the design and operation of energy storage systems utilizing such enhanced PCM formulations.

- Incorporating finned surfaces into a system facilitates more efficient heat transfer. The introduction of fins results in a substantial reduction in the time required for the phase change material to melt. This enhanced heat transfer capacity, achieved through the strategic use of fins, plays a pivotal role in expediting the melting process. Consequently, the integration of fins emerges as

a crucial factor for optimizing the efficiency of heat exchange and thermal management systems.

- Adding nanoparticles and foam, combined with a Y-shaped fin, significantly shorten the melting solidification time in Flat Plat Solar Collector Systems (FPSCS). From all the observations and arguments, it can be realized that the best configuration of FPSC occurs when nanoparticles and metals foam with wavy wall and Y-shaped fin are used, with foams that have the main role in this performance's improvement. These thermal enhancement techniques would be really helpful to reduce sizes of these thermal energy storage devices, as well as to improve their capability or absorbing/releasing it from/to the working fluid, and potential benefits due to aspects like system cost reduction would allow to also apply this technology to high-capacity storage systems.

- By using different lobes for the heat exchanger, both melting, and solidification times were significantly reduced, so that six-lobed surfaces has the best performance among other cases of the lobed pipe heat exchanger energy storage system. The reason for higher performance is mainly due to heat transfer surface area improvement, and also some increase due to higher liquid PCM natural convection. Six-lobed surfaces compared to one-lobed surface) decreases the melting and solidification times; this underlines that even changing just the geometry might have an impact. After considering the evidence, it can be concluded that metal foams provide the most significant impact on reducing PCM charching/discharging time in solar systems.

- Adding a finned surface together with the addition of nanoparticles and foam has a significant impact on reducing melting time. For example, in the triplex tube heat exchanger (with longitudinal fin), the inclusion of NPs with foam reduced the melting durations by 53.17% compared to the TTHX (simple-TTHX) without NEPCM. On the other hand, melting time is reduced by 20.70% if we compared the Triplex Tube Heat Exchanger (simple) without NEPCM.

- A combination of all the solutions investigated, which means metal foam, nanoparticles, wavy wall, and Y-shaped fin, makes melting time smaller than a 87.21% compared to the Case with pure PCM in flat plate solar collectors. Also, inclusion of nanoparticles with foam 0.95 and 0.92 reduced the solidification time durations by 84.49% and 89.18% compared to the Case with pure PCM.

• The addition of all methods (nanoparticle, hybrid nanofluid, and metal foam), with porosities of 0.88, 0.90, 0.92, and 0.95, for double pipe heat exchnager with six-lobed, reduces the melting time of 66.68%, 65.56%, 64.30%, and 60.52%, respectively, when compared to the simple double pipe heat exchnager with pure RT82. Also, employing all methods with porosities of 0.88 reduces the solidification time of 81.62% saving

6.1.2. Experimental study

• When the heat source temperature was increased from 50°C to 60°C (Ste numbers 0.358 and 0.275), the melting time decreased and the temperature rose. This effect was more pronounced in MFP systems than in PP systems.

• The type of foam material used in a system has a significant impact on its heat transfer characteristics. Comparing PP and MFP systems, the use of metal foam greatly improves heat transfer, and the effective thermal conductivity of the composite structure is much higher than that of the PCM.

• In all cases tested, the addition of nanoparticles reduced the melting time compared to the reference case using PP.

• When all methods were used with MFNP at porosities of 0.94, the melting times decreased drastically compared to the other cases. This suggests that using high-porosity MFNP is an effective way to improve the performance of thermal energy storage systems.

• The findings suggest that the addition of metal foam with ω=10 PPI and ε=94% can reduce melting time, when compared to the PP samples of the solar collector.

• When the heat source temperature was increased from 40°C to 50°C and 60°C (Ste numbers 0.191, 0.275, and 0.358), the melting time decreased and the temperature rose. Also, employing all methods NP, MFP, MFNP with porosities of 0.94 reduces the melting and solidification time.

• Comparison with experimental and numerical results during melting process are here presented in order to validate the code. The same initial conditions, boundary conditions, and thermal physical properties in the studies

were adopted in the current study to validate the code. The graphs, behavior and melting durations are nearly identical, concluding that the code here shown is considered to be validated.

- In experimental work, the findings suggest that the addition of metal foam with ω=10 PPI and ε=94% can reduce melting time by 78.38% when compared to the PP samples of the solar collector.

- In experimental work, the addition of all methods nanoparticle, metal foam, and metal foam/nanoparticle with porosities of 0.4% and 0.94, reduces the melting time by 7.31%, 26.02%, and 43.57% at thermocouple 1. It also reduces the melting time by 13.39%, 60.77%, and 71.93% at thermocouple 2 when compared to the Case with pure PCM.

6.2. Outlook for Future Research

In the realm of future research, several key areas warrant exploration:

- Advancements in Porous Metal Foam: The potential for enhancing the properties of porous metal foam with graded porosity is a promising avenue. Employing 3D printing to create molds with varying porosities offers the opportunity to fabricate porous metal foam with graded porosity through casting methods. Further research is essential to uncover the thermal characteristics of this innovative material.

- Optimizing Energy Release: The energy release process holds paramount significance in energy storage systems. It is conceivable that foam could enhance this process. To exert precise control over this phenomenon, adjustments in various composite parameters are requisite, including container geometry, the choice of materials for the cold wall, and the structural configuration of the foam. Exploring these modifications could lead to notable improvements in energy release efficiency.

- In the realm of future research, the optimization of PCMs extends beyond their mere categorization to encompass a nuanced exploration of thermal properties, particularly focusing on parameters like melting temperature.

- Multi-objective optimization offers a powerful and demanding method for designing and operating latent heat thermal energy storage systems. It allows for the simultaneous consideration of various objectives, such as reducing

charging/discharging time, minimizing costs, or maximizing stored energy. Topology optimization may be used to improve the thermal performance and efficiency of various components, including heat exchangers, thermal storage units, and related devices.

• Implementing innovative enhancement techniques like metal foams and optimizing geometric configurations in full-scale applications, such as Photovoltaic-Thermal (PVT) systems, heat pumps, and heat exchangers, offers a promising avenue for real-world energy systems. This approach involves the integration of advanced materials like metal foams and a meticulous fine-tuning of geometric parameters within the PCMs.

• Performing Numerical and Experimental validation in a 3D framework to conduct energetic analysis, emphasizing the consideration of the storage system as a lumped model for comprehensive energy storage and release in PVT and PVT-PCM systems, incorporating metal foam and nanoparticles.

• Undertaking multi-objective optimization and conducting exergoeconomic evaluations for a hybrid geothermal-PVT system that is seamlessly integrated with PCM and metal foam technologies.

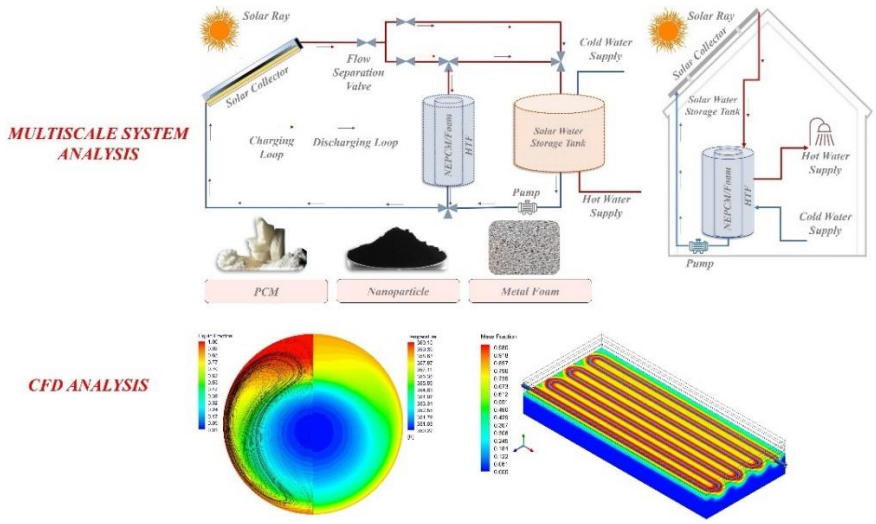

Fig. 6.1. Integration energy storage with solar thermal collector